國立臺灣大學理學院物理學系

博士論文

Department of Physics

College of Science

National Taiwan University

Doctoral Dissertation

化學氣相沉積之二硫化鉬表面及界面特性研究:由成長控制至潛在應用

Surface and Interfacial Properties on CVD-grown MoS_2: From Growth Control to Potential Applications

林裕凱

Yu-Kai Lin

指導教授：陳永芳 博士

林麗瓊 博士

陳貴賢 博士

Advisor: Yang-Fang Chen, Ph.D.

Li-Chyong Chen, Ph.D.

Kuei-Hsien Chen, Ph.D.

中華民國 105 年 7 月

July 2016

doi:10.6342/NTU201603487

Acknowledgement

First of all, I would like to thank my advisors, Prof. Li-Chyong Chen and Prof. Kuei-Hsien Chen, for the strong support and guidance in the experimental design and completion during my PhD career. They also build a pluralist environment and provide abundant resources for me to do research. Without their endless patience and encouragement, this thesis would not have been completed. I also want to thank my co-advisor, Prof. Yang-Fang Chen, for his insight of the different point of views in reading data. Special thanks to Prof. Ruei-San Chen, who has spent a lot of time to help me clarify physical meanings behind the experimental phenomena.

I would like to express my greatest thank to my dearest lab mates and friends: Prof. Yu-Kuei Hsu, Dr. Yan-Gu Lin, Dr. Sheng-Bo Wang, Dr. Cheng-Kai Chang, Dr. Cheong-Wei Chong, Dr. Deniz Wong, Dr. Lian-Ming Lyu, Dr. Ding-Shiun Tu, Dr. Yi-Fang Huang, Dr. Tsu-Chin Chou, Dr. Cheng-Ying Chen, Dr, Hsian-Ting Lien, and so on. They are very kind to share their own knowledge either on research or on life. Their passion and attitude also inspire me a lot. I also deeply appreciate my juniors in the AML: Ying-Chu Chen, Wei-Lun Chien, Pei-Hsuen Shih, I-Nan Chen, Pei-Chun Chiang, Chyong-Yi Chen, Pei-Ling Lee, Po-Shien Kuo, Meng-Chia Hsieh, Cheng-En Chang, and Huei-Pin Liou, etc. Although they are younger than me, they have taught me a lot and hang out with me to enrich my life. I really cherish the connection in this big family.

I would like to express my gratitude to TIGP for the financial support in the early stage of my PhD study, and the program assistant, Flora, who has simplified much paperwork for me. Besides, I am appreciate that my friends, Iris, Steven, Shuo-Wei, William, Yi-Han, and Evelyn, etc., always stand on my side and bring smiles to me.

Last but not least, I would like to express my special thanks to my family, who gives me endless love and silent support so that I can pursue my degree without pressure.

The present thesis is dedicated to those who have ever concerned and taken care of me.

Y. K. Lin

doi:10.6342/NTU201603487

中文摘要

本研究論文主要探討二維層狀材料二硫化鉬的成長機制、表面與界面特性及相關應用。首先，二硫化鉬以兩段式化學氣相沉積的方式成長於氧化矽(SiO_2-Si)基板上，之後主要以光電子能譜研究其表面特性。結果顯示當二硫化鉬的厚度由十層遞減為三層時，殼層價電子之束縛能會向高能量偏移約 0.2 eV，其原因可歸因於材料費米能階隨厚度的變化。由原子力顯微圖譜與價帶光電子能譜可發現，實驗所得的二硫化鉬屬多晶態的 n 型半導體且於價帶能量最高處前端有一缺陷能帶，此缺陷能帶主要是由材料表面的硫空缺所造成，進而形成類施體表面態而導致表面能帶往低能量彎曲。此外在較厚的二硫化鉬中，其塊材內的缺陷也可能形成類受體的缺陷能階而降低材料費米能階，故費米能階的變化來自於表面態及塊材缺陷的複合影響。當沉積奈米金於二硫化鉬表面，其價電子束縛能降低約 0.3 eV，顯示高功函數金屬的 p 型摻雜特性及其與二硫化鉬間有電荷交換行為，且隱含表面修飾能調變二硫化鉬費米能階及其觸媒方面的應用潛力。當進行電化學催化產氫測試，其反應起始電位隨材料厚度漸少而降低，且阻抗分析也顯示較薄的二硫化鉬具有更為優異的電荷交換效率，進一步驗證了費米能階與材料厚度的關係。

二硫化鉬晶體的異向性及材料邊緣與基平面特性的差異促進了其廣泛的應用。本研究同時藉由熱力學分析及實驗驗證進行不同二硫化鉬前驅物的硫化速率調控，且同時控制二硫化鉬的晶體排列方向。結果顯示在相同硫化條件下，三氧化鉬的硫化速率遠大於鉬金屬，原因主要來自於結晶結構的不同，造成反應機制及活化能的差異，進一步於硫化氫硫化過程中引入氫氣可擴大硫化速率的差異。此外，拉曼圖譜及 X 光吸收圖譜均顯示三氧化鉬傾向形成平行基板排列的二硫化鉬，而鉬金屬則傾向形成垂直基板排列的二硫化鉬，此晶體排列方向的差異也是前驅物晶體結構及反應機制不同的結果。因此同時使用兩種前驅物即可得結合兩種異向排列之二硫化鉬，其中垂直排列的二硫化鉬能提供優異的電子傳導率而成為金屬電極及水平排列二硫化鉬之間的歐姆接觸橋樑，進而能應用於電子元件上。另外，沉積三氧化鉬於鉬金屬上也發現其能作為硫化犧牲層，而抑制鉬金屬的進一步硫化，使其能應用於以銅鋅錫硫為吸收層的薄膜太陽能電池。

為了製備一個以二硫化鉬為基礎的垂直異相結構元件，本研究選擇氧化鋅作為與其搭配的材料，因為氧化鋅為三維六方晶型半導體而二硫化鉬則為二維六方晶型半導體，兩材料間的晶格不匹配程度只有約 2.8%，且兩者界面的能帶位置能形成 n-n$^+$異相接面而有更廣泛的應用。元件中氧化鋅採用原子層沉積的方式成長於二氧化鉬表面，上電極則以微影製程控制白金或金電極尺寸，並量測元件之電阻切換特性。電性量測結果顯示氧化鋅與垂直排列二硫化鉬之界面並不穩定，其電流電位曲線隨掃描圈數增加而改變，推測原因為二硫化鉬之晶體邊緣具高活性，易於高電流密度下與氧化鋅進行化學反應而部分氧化，進而增加元件電阻；反之，具雙重晶向排列的二硫化鉬有相當穩定的電流電位曲線，因在界面處的二硫化鉬為水平排列，其基平面有較高的化學惰性。當使用白金為上電極時，其電阻切換特性為雙極性，且具有良好的循環掃描穩定性與電阻持久性。由電流電位曲線適配及變溫電性量測結果，可推論其電子傳輸機制由空間電荷限制電流所主導，而氧空缺則扮演離子傳輸及形成導電通道切換電阻的角色。此外，於反向偏壓出現微分負電阻及重置電位主導設定電位之特性，可歸因於二硫化鉬與氧化鋅界面存在硫空缺及氧原子間之交互作用。二硫化鉬光電子能譜進一步驗證了界面態的存在，而穿透式電子顯微影像與電子色散 X 光譜則顯示氧空缺的存在及氧原子分布的梯度，最後對元件完整的電阻切換機制有詳盡的探討。

藉由兩段式化學氣相沉積法，二硫化鉬能成功成長於二氧化矽、鉬玻璃及石墨烯紙等基板上，其中石墨烯紙的基板造成二硫化鉬具有拉伸應力。本研究發現此種基板引發之應力會影響原子層沉積製程中水分子於二硫化鉬表面的吸附，進而影響氧化鋅的成核過程，推論原因為二硫化鉬的壓電特性形成一垂直基板的電場，其方向與水分子之偶極矩方向相反，阻礙了水分子於二硫化鉬基平面的凡得瓦吸附。此外石墨烯紙的超輕薄特性亦使其不易固定於真空系統中進行材料成長，使用有機物如真空膠帶、銀膠或金屬夾均無法成功成長氧化鋅。本研究應用靜電力與表面臭氧處理，同時解決石墨烯紙基板的固定問題及二硫化鉬表面輕水性的改善，最後能成功於具拉伸應力之二硫化鉬表面成長均勻的氧化鋅薄膜。

關鍵字： 二硫化鉬、表面及界面特性、厚度效應、費米能階、晶向控制、電阻切換特性、應力

ABSTRACT

In this study, the growth mechanism, surface/interface properties, and potential applications of MoS_2 are demonstrated. The thickness-dependent surface states of MoS_2 thin films grown by the CVD process on the SiO_2-Si substrates are investigated by XPS. Both the core levels and valance band edges of MoS_2 shift downward ~0.2 eV as the film thickness increases from 3 to 10 layers, which can be ascribed to the variations of Fermi level. Grainy features observed from the AFM topographies, and defect states illustrated at the valance band spectra indicate the influences of both surface states and bulk defects, which lead to the variations of Fermi level in n–type MoS_2 with thickness. When Au contacts with our MoS_2 thin films, the binding energy reduces due to the hole-doping characteristics of Au, and easy charge transfer from the surface defect sites of MoS_2. HER performance also exhibits that the easy charge transfer and the decrease in reaction barrier at the thin MoS_2 surface.

The anisotropic crystal structure and different properties between edge and basal plane of MoS_2 have given rise to versatile applications. Here, we are able to manipulate the orientations of MoS_2 by controlling the sulfurization kinetics in both MoO_3 and Mo precursors. Thermodynamic information and SEM observations indicate that MoO_3 has much higher sulfurization rate than Mo metal in H_2S. Introducing H_2 with H_2S is able to enlarge the rate difference between these two precursors. Raman and XAS studies further reveal the orientation evolution of MoS_2 is related to the MoO_3/Mo ratio in the precursor, so that MoO_3-derived MoS_2 is terrace-terminated whereas Mo-derived one is edge-terminated. The differences in the orientation of MoS_2 and sulfurization rate between MoO_3 and Mo metal are attributed to the crystal structures of the Mo precursors and the reaction routes with H_2S. The formation of terrace-terminated MoS_2 on the Mo surface is also expected to suppress sulfurization of the bottom Mo metal.

The hybrid hexagonal material of 2D-MoS_2 and 3D-ZnO is utilized as a memristor. The microstructure of this hybrid material was analyzed by Raman, XRD, and HRTEM. ZnO grown by atomic-layer deposition shows *c*-axis preferred orientation on terrace-terminated MoS_2 and stable I-V behavior at the ZnO/MoS_2 interface, while edge-terminated MoS_2 results in randomly oriented ZnO and unstable I-V characteristics, which could arise from the chemical reaction at the interface. The device with dual-oriented MoS_2 on Mo metal is demonstrated by employing both MoO_3 and Mo precursors. The MoS_2/ZnO interface plays an important role for the resistive switching behaviors. Good retention and endurance of the device is achieved, which could be attributed to the formation of dual-oriented MoS_2 on the Mo back contact that offers a stable interface with ZnO. The negative differential resistance (NDR) characteristics and voltage-dependent HRS are observed at the reverse bias, which could be related to the surface properties of MoS_2. The shift in binding energy after the formation of MoS_2/ZnO n-n$^+$ heterojunction indicates the generation of interface states. Temperature-dependent I-V measurement illustrates that carrier transport mainly follows the trapping/detrapping controlled SCL process accompanying with ionic transportation. The complete switching mechanism is also proposed. This work demonstrates that the combination of oxide with TMD could be a potential configuration for electronic applications.

Keywords: MoS_2, surface/interface properties, thickness, Fermi level, orientation, resistive switching, strain

CONTENTS

doi:10.6342/NTU201603487

doi:10.6342/NTU201603487

LIST OF FIGURES

doi:10.6342/NTU201603487

doi:10.6342/NTU201603487

doi:10.6342/NTU201603487

doi:10.6342/NTU201603487

doi:10.6342/NTU201603487

doi:10.6342/NTU201603487

doi:10.6342/NTU201603487

doi:10.6342/NTU201603487

doi:10.6342/NTU201603487

doi:10.6342/NTU201603487

LIST OF TABLES

doi:10.6342/NTU201603487

Chapter 1 Introduction

1.1 General background

Since the single-atom-thick graphene crystallite was extracted from bulk graphite and transferred onto the SiO_2-Si substrate with the scotch tape technique in 2004, new physical properties emerge when a bulk crystal of macroscopic dimension is thinned down to one atomic layer.[1, 2] Although graphene has many fascinating properties, such as ultrahigh mobility, high transparency and long spin relaxation time, the lack of bandgap limits its applications in the electronics and optoelectronics.[3-5] As a result, two-dimensional transition metal dichalcogenides (TMDs) becomes an alternative series of material for practical applications because this family can perform not only metallic but also insulating, semiconducting, superconducting behaviors by changing the composed elements, as illustrated in the Table 1.1.[6, 7]

Table 1.1 Electronic character of different layered TMDs.

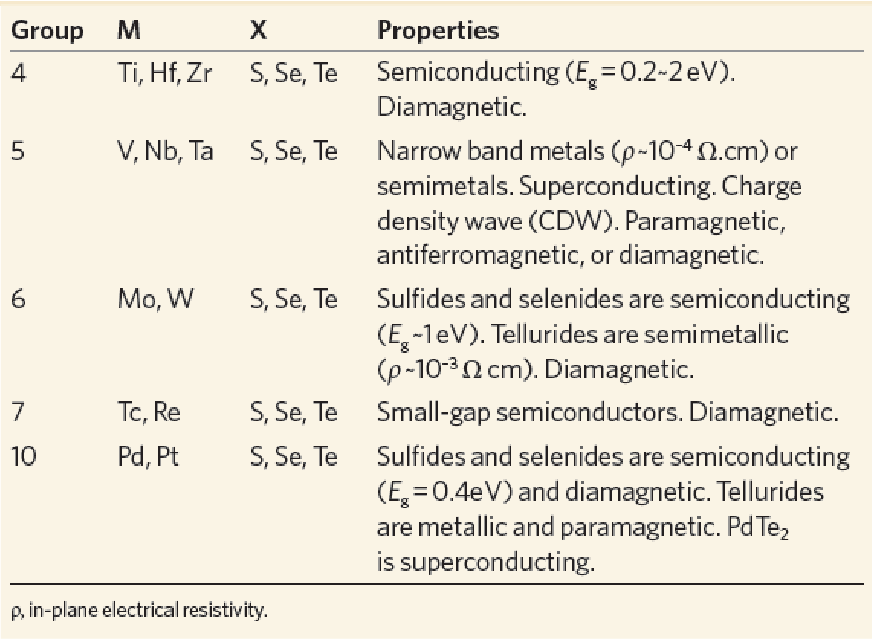

Group	M	X	Properties
4	Ti, Hf, Zr	S, Se, Te	Semiconducting ($E_g = 0.2\text{~}2$ eV). Diamagnetic.
5	V, Nb, Ta	S, Se, Te	Narrow band metals ($\rho \sim 10^{-4}$ Ω.cm) or semimetals. Superconducting. Charge density wave (CDW). Paramagnetic, antiferromagnetic, or diamagnetic.
6	Mo, W	S, Se, Te	Sulfides and selenides are semiconducting ($E_g \sim 1$ eV). Tellurides are semimetallic ($\rho \sim 10^{-3}$ Ω cm). Diamagnetic.
7	Tc, Re	S, Se, Te	Small-gap semiconductors. Diamagnetic.
10	Pd, Pt	S, Se, Te	Sulfides and selenides are semiconducting ($E_g = 0.4$eV) and diamagnetic. Tellurides are metallic and paramagnetic. $PdTe_2$ is superconducting.

ρ, in-plane electrical resistivity.

TMD has the general chemical composition of MX_2 (M = Mo, W, etc. and X = S, Se, etc.), and most of them crystallized in a graphite-like layered structure, where one M layer is sandwitched between two X layers.[8] Each MX_2 layer is typically 6~7 Å in thickness. The intra layer M-X bonds are predominantly covalent in nature, whereas the sandwich layer are coupled by weak van der Waal forces thus allowing the crystal to readily cleave along the layer surface. The strong anisotropy in the bonding nature gives rise to the significantly different electrical, chemical, mechanical, and thermal properties between basal plane and cross-plane of MX_2.[9]

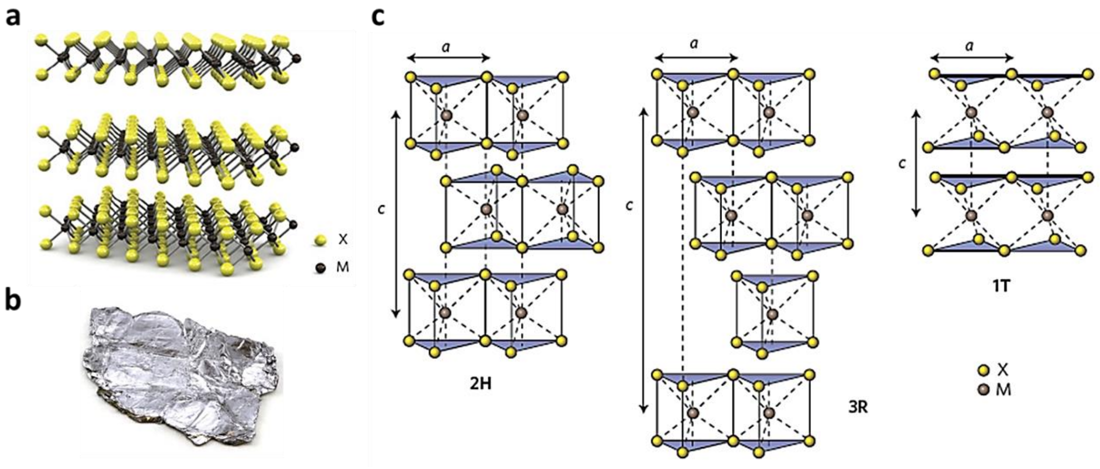

Figure 1.1 (a) A typical MX_2 structure with the chalcogen atoms (X) in yellow and the transition metal atoms (M) in grey; (b) Photograph of a bulk MoS_2 crystal; (c) Schematic crystal structures of bulk MX_2. The lattice constants *a* are in the range 3.1~3.7 Å for different materials. The stacking index *c* represents the layer number per repeating unit, and the interlayer spacing is ~6.5 Å.

Monolayer TMDs exhibit only either trigonal prismatic (D_{3h} group) or octahedral (D_{3d} group) phases. On the other hand, bulk TMDs may have three structural polytypes: 2H (hexagonal symmetry, two layers per repeat unit, D_{3h} coordinate), 3R (rhombohedral symmetry, three layers per repeat unit, D_{3h} coordinate), and 1T (tetrahedral symmetry, one layer per repeat unit, D_{3d} coordinate), as illustrated in Figure 1.1.[8] The electronic structure of TMDs strongly depends on the coordination environment of the transition metal and its *d*-orbital characteristics. According to ligand field theory, D_{3h} compounds exhibit three splitting *d* orbitals whose character is predominantly d_{z^2} (A_1), $d_{x^2-y^2,xy}$ (E), and $d_{xz,yz}$ (E') (from bottom to top), while D_{3d} compounds form degenerate d_{z^2,x^2-y^2} (e_g) and $d_{yz,xz,xy}$ (t_{2g}) that accommodate the TMDs' *d* electrons as illustrated in Figure 1.2.[10] In both D_{3h} and D_{3d} coordinates, the non-bonding *d* bands of the TMDs are located within the gap between the bonding (σ) and antibonding (σ*) bands. The diverse electronic properties of TMDs arise from the progressive filling of the non-bonding *d* bands from group 4 to group 10 species.[7]

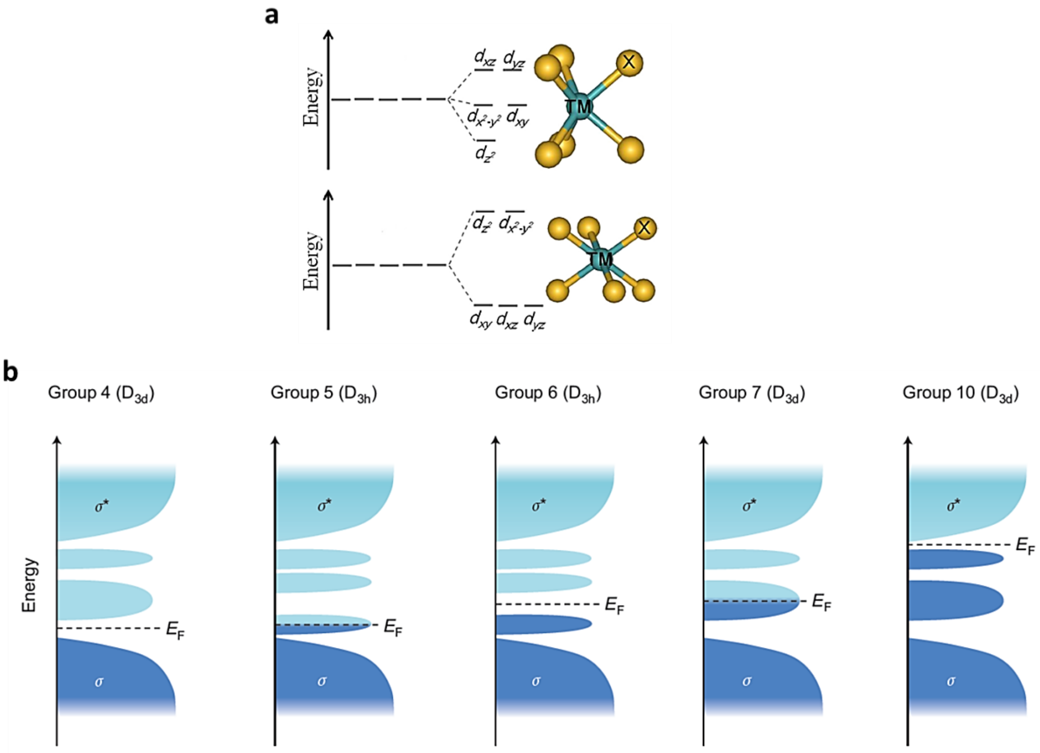

Figure 1.2 (a) *d*-orbital splittings in trigonal prismatic (top, D_{3h}) and octahedral (bottom, D_{3d}) crystal field; (b) Qualitative schematic illustration showing progressive filling of *d* orbitals that are located within the bandgap of bonding (σ) and anti-bonding states (σ*) in group 4, 5, 6, 7 and 10 TMDs.

Intercalating materials into layered TMDs generally alters the electronic structures and induces new physical properties different from the original host material. For example, when SnS inserts into the van der Waal gaps of TiS_2, a natural superlattice of $(SnS)_{1.2}(TiS_2)_2$ is formed, which weakens interlayer bonding, decreases transverse sound velocity, and reduces thermal conductivity, as depicted in Figure 1.3(a).[11] Intercalation-induced instability in electronic structures of TMDs may also result in higher temperature of charge-density-wave (CDW) phase due to the Jahn-Teller distortion in which the splitting of partially filled degenerate orbitals causes a reduction of the free energy.[7] Moreover, a new superconducting state is discovered near x = 0.04 in the Cu-intercalated $TiSe_2$ (Cu_xTiSe_2), and the CDW transition is continuously suppressed as illustrated in **Figure 1.3**(b).[12]

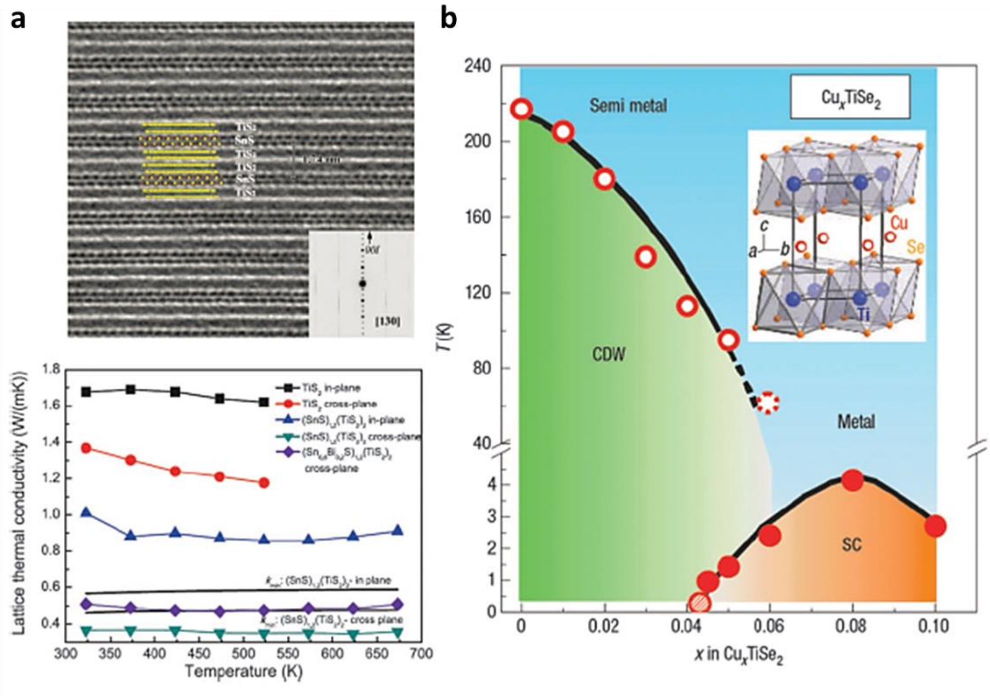

Figure 1.3 (a) HRTEM image (top) and corresponding lattice thermal conductivity (bottom) of TiS_2 layer after SnS intercalation; (b) Phase diagram of Cu-intercalated $TiSe_2$, where transition among metal, CDW, and superconducting (SC) phases is presented.

1.2 Fundamental properties of MoS_2

MoS_2 as one of the TMD family has exhibited its unique properties based on its layered structure, especially when the size reduces from bulk (three dimensions) to monolayer (two dimensions). Bulk MoS_2 is a semiconductor with indirect bandgap of about 1.29 eV. Theoretical calculation has predicted an indirect to direct bandgap transition when the bulk MoS_2 is thinned down to a single layer, as illustrated in Figure 1.4(a).[13]

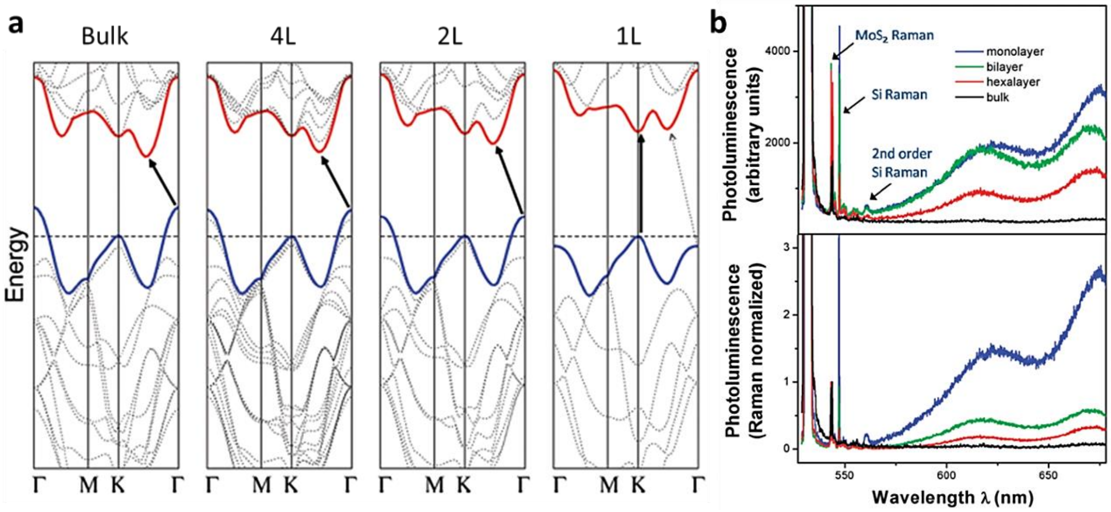

Figure 1.4 (a) Calculated band structures of MoS_2 evolving with layer number; (b) Photoluminescence spectra normalized by Raman intensity for MoS_2 with various layer numbers.

The evolution of electronic structures of MoS_2 with various thicknesses is also reflected on the photoluminescence (PL) spectra (Figure 1.4(b)), where the pronounced emission can be observed at ~670 and ~627 nm for monolayer MoS_2 arising from the direct excitonic transitions at the Brillouin zone *K* point. The emission intensity is inversely proportional to the thickness of MoS_2. The energy difference between these two peaks is attributed to the spin-orbit splitting of the valence band energy.

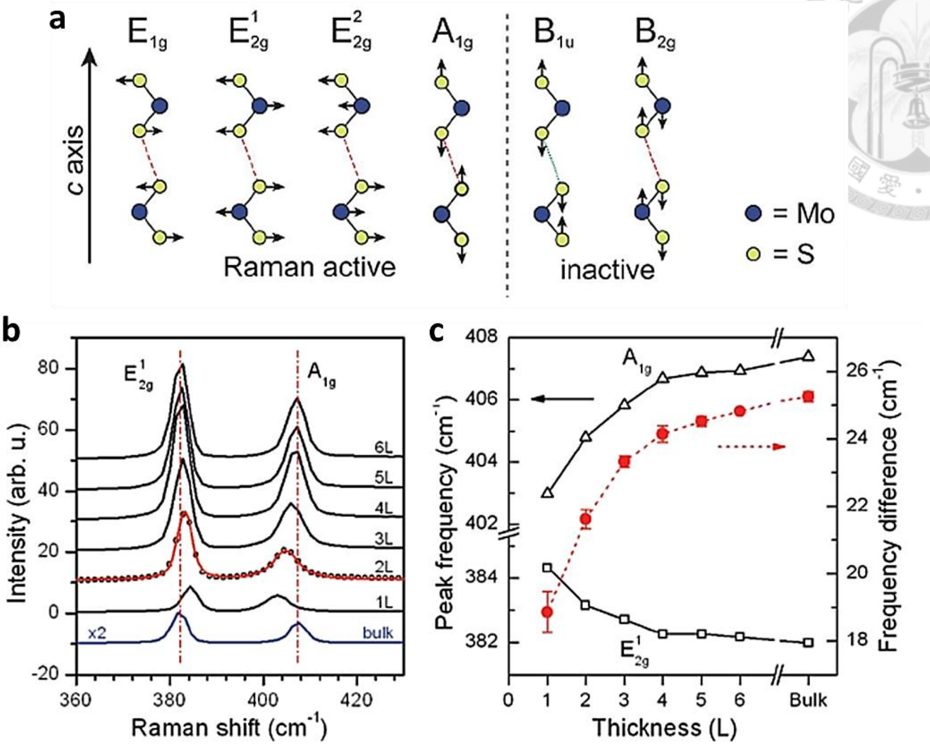

Figure 1.5 (a) Schematic drawing of the four Raman active and two inactive modes for MoS_2; (b) Raman spectra of MoS_2 with various layer numbers; (c) Frequencies of A_{1g} and E_{2g}^1 Raman modes and their difference as a function of layer number.

Raman spectroscopy has been widely used to determine the number of layers in two dimensional (2D) materials, as well as to examine the changes in material properties with thickness.[14] Theoretical calculation predicts four Raman active modes in TMDs, including one out-of-plane mode A_{1g} and three in-plane modes E_{1g}, E_{2g}^1, and E_{2g}^2, as shown in Figure 1.5(a).[15] Experimentally, E_{2g}^1 mode is at very low frequencies (~30 cm^{-1}), and E_{1g} mode is forbidden in back-scattering geometry on a basal plane. Only A_{1g} and E_{2g}^1 modes are accessible in measurement, which exhibit sensitive thickness dependence (Figure 1.5(b)). The frequency difference between the two modes increases with increasing the material thickness, which is an excellent

doi:10.6342/NTU201603487

indicator for the layer number of MoS_2. The opposite direction of frequency shifts can be related to the interlayer coupling, Coulombic interactions, and perhaps stacking-induced changes of the intralayer bonding.[16]

When the MoS_2 thins down to atomic thick, it breaks the structural centrosymmery that makes piezoelectric effect achievable in this material. Applying uniaxial tensile strain on monolayer MoS_2 alters its electronic structure, which is observed both in the PL and Raman spectra, as shown in Figure 1.6(a).[17] The pronounced strain-induced decrease in the PL intensity and optical bandgap indicates the direct-to-indirect transition. With increased strain, the A_{1g} peak shows no measurable shift in position while the degenerate E_{2g}^1 peak splits into two sub-peaks.

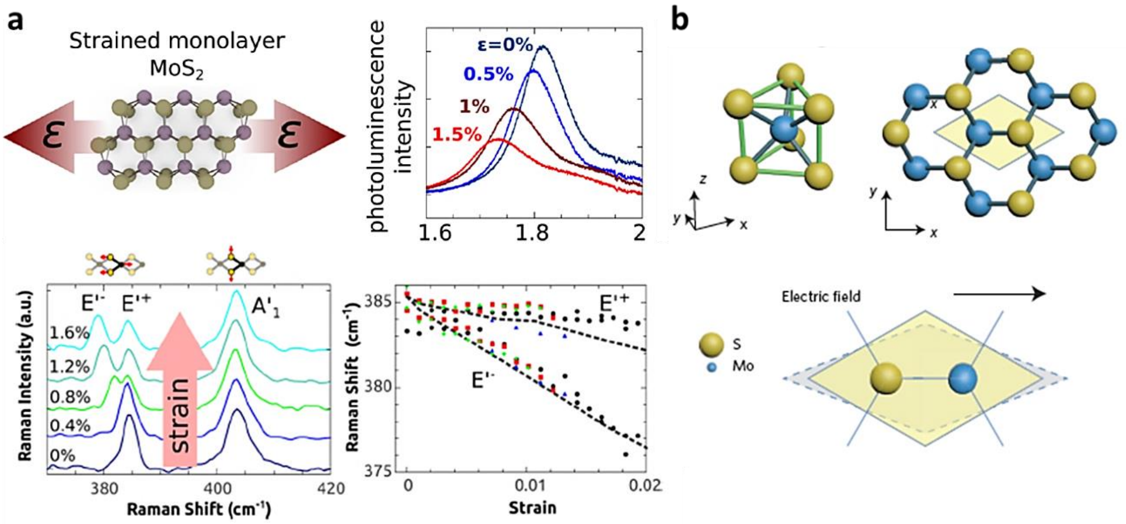

Figure 1.6 (a) The influence of uniaxial tensile strain on the phonon spectra and band structures of monolayer MoS_2; (b) Schematic diagram depicts inverse piezoelectric effect via applying electric field along S to Mo direction.

The strain in MoS_2 can also be induced by applying external electric field from S site to Mo site. This inverse piezoelectric effect stretches the Mo-2S dipole and elongates the unit cell of MoS_2, creating compressive stress in the *x* direction and tensile stress in the *y* direction, as shown in Figure 1.6(b).[18] The robust piezoelectricity of MoS_2 has exhibited its potential in atomically thin piezoelectric device which will make profound impacts in ultrasensitive sensors, nanoscale electromechanical systems, and the next generation of low-power electronics.

The other unique property corresponding to the single layer of MoS_2 is the inversion symmetry breaking together with spin-orbit coupling (SOC), leading to coupled spin and valley at the valence band edges, as illustrated in Figure 1.7.[19] The difference between MoS_2 and graphene is the strong SOC originating from the metal *d* orbitals.

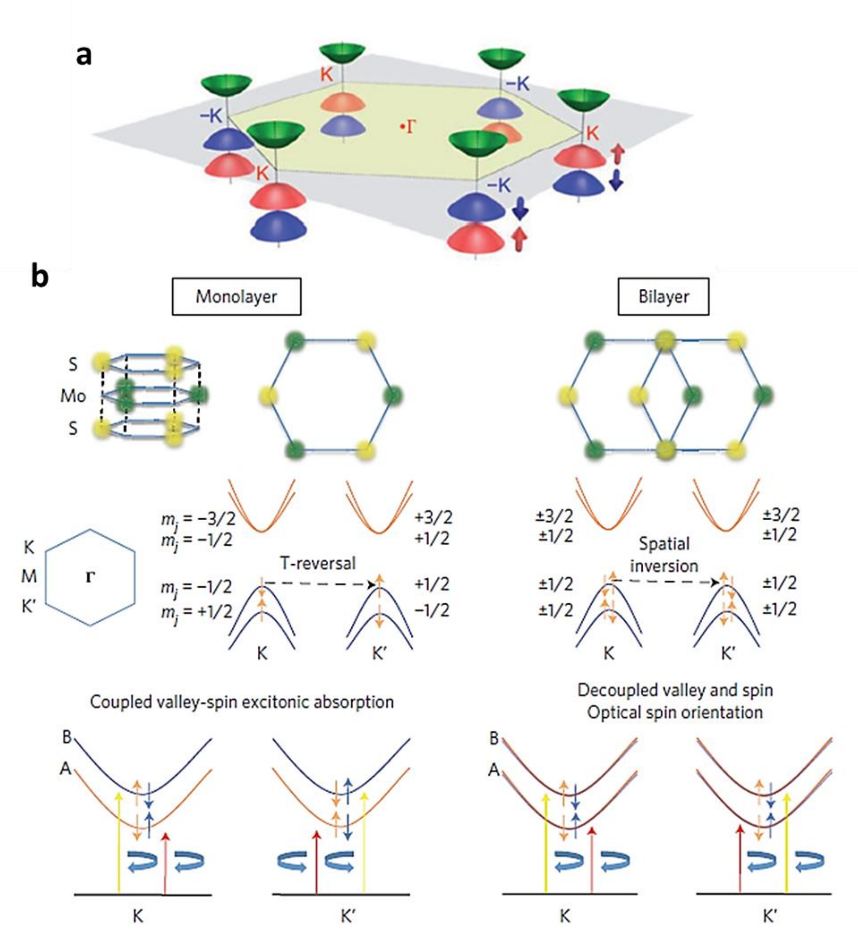

Figure 1.7 (a) Schematic drawing of the band structure at the band edges located at the *K* points; (b) Illustration of spin-valley coupling in monolayer (left) and bilayer (right) MoS_2 under circularly polarized excitation.

It is demonstrated that optical pumping with circularly polarized light can achieve complete dynamic valley polarization in monolayer MoS_2, while both *K* and *K*' valleys are equally populated in bilayer MoS_2 and only a net spin orientation is produced.[20] The viability of optical valley control suggests the possibility of valley-based electronic and optoelectronic applications in monolayer MoS_2.

1.3 Preparation of MoS_2

1.3.1 Top-down process

Mechanical cleavage has been a traditional method to obtain 2D flakes containing tens to hundreds of crystal layers. Since Novoselov *et al*. successfully produced various single-layer 2D crystals from the bulk with the aid of scotch tape in 2004, people apply this approach to study the fundamental properties of TMDs varying with thickness because the sample quality is similar to its bulk form, as illustrated in Figure 1.8(a).[1, 21] However, this method only produces small pieces of crystals with poor control in layer number, which limits the practical applications.

The other top-down approach is chemically exfoliating TMD sheets in the solution assisted either by sonication process or by ion intercalation (Figure 1.8(b) and Figure 1.8(c)).[22, 23] The former process requires a proper solvent whose surface energy is similar to that of the layered material to prevent the exfoliated crystals from aggregation, such as dimethylformamide (DMF) or N-methyl-pyrrolidone (NMP). The electrochemical lithiation is originally a half reaction in a battery test process. Here the insertion of lithium ions can weaken the interlayer van der Waal force, as well as react with water to form Li(OH) and H_2 gas and further push the layers apart. Although the

doi:10.6342/NTU201603487

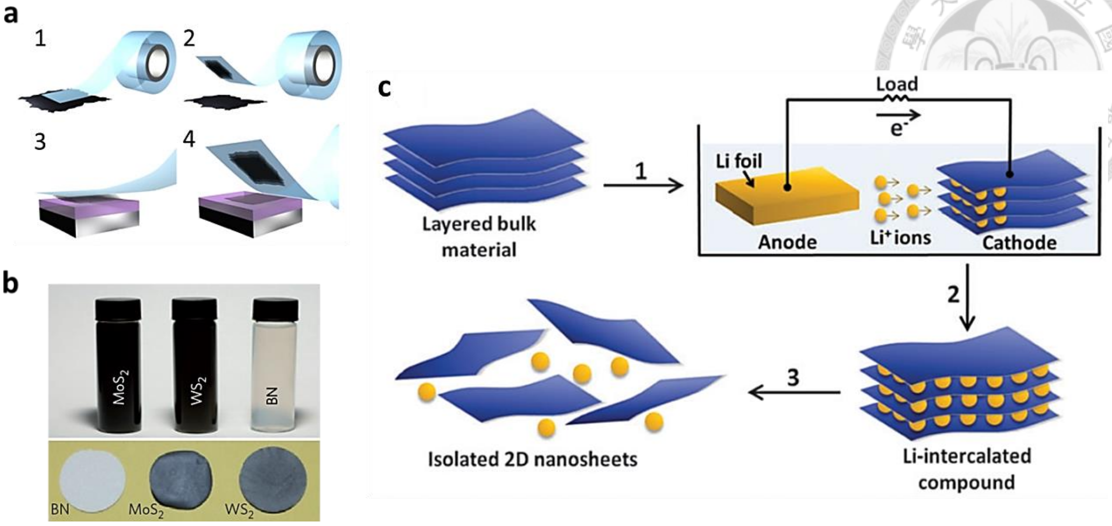

Figure 1.8 (a) Schematic drawing of mechanical exfoliation for layered materials; (b) Stable suspensions of layered materials from sonication-assisted exfoliation of MoS_2 (in NMP), WS_2 (in NMP), and BN (in IPA). (c) Electrochemical lithiation and exfoliation process for producing 2D crystals from the layered bulk materials.

solution process can provide high yield to solve the scalable problem in mechanical exfoliation process, the surface contamination and structure distortion or damage are inevitable, which varies the material properties from expectation and is difficult for electronic devices. Therefore, bottom-up approach, especially vapor phase process, is regarded as the most reliable procedure for producing high quality monolayer or few-layer MoS_2 in a large scale so far.

1.3.2 Chemical vapor deposition (CVD)

The synthesis of atomically thin TMDs in a large area with good layer controllability and uniformity has remained a challenge for a long time. Very recently, CVD technique has shown its promising ability to produce high quality MoS_2 with a scalable size, controllable thickness, low cost, and excellent electronic properties.

doi:10.6342/NTU201603487

- **Sulfurization from metal or metal oxide precursors**

A general strategy for producing wafer-scale MoS_2 is a two-step CVD process. Mo or MoO_2/MoO_3 precursors are pre-deposited on the substrate, followed by sulfurization in the sulfur vapor or H_2S (Figure 1.9(a) and Figure 1.9(b)).[24-26] Due to the simple reaction mechanism, the thickness and size of the as-grown MoS_2 can be determined by the precursors. However, the challenge for this approach is to obtain a uniform precursor film, especially when the target is less than 3 layers of MoS_2. Accordingly, atomic layer deposition (ALD) is an alternative technique to achieve thin and uniform precursor film even on the substrate of high aspect ratio (Figure 1.9(c)).[27]

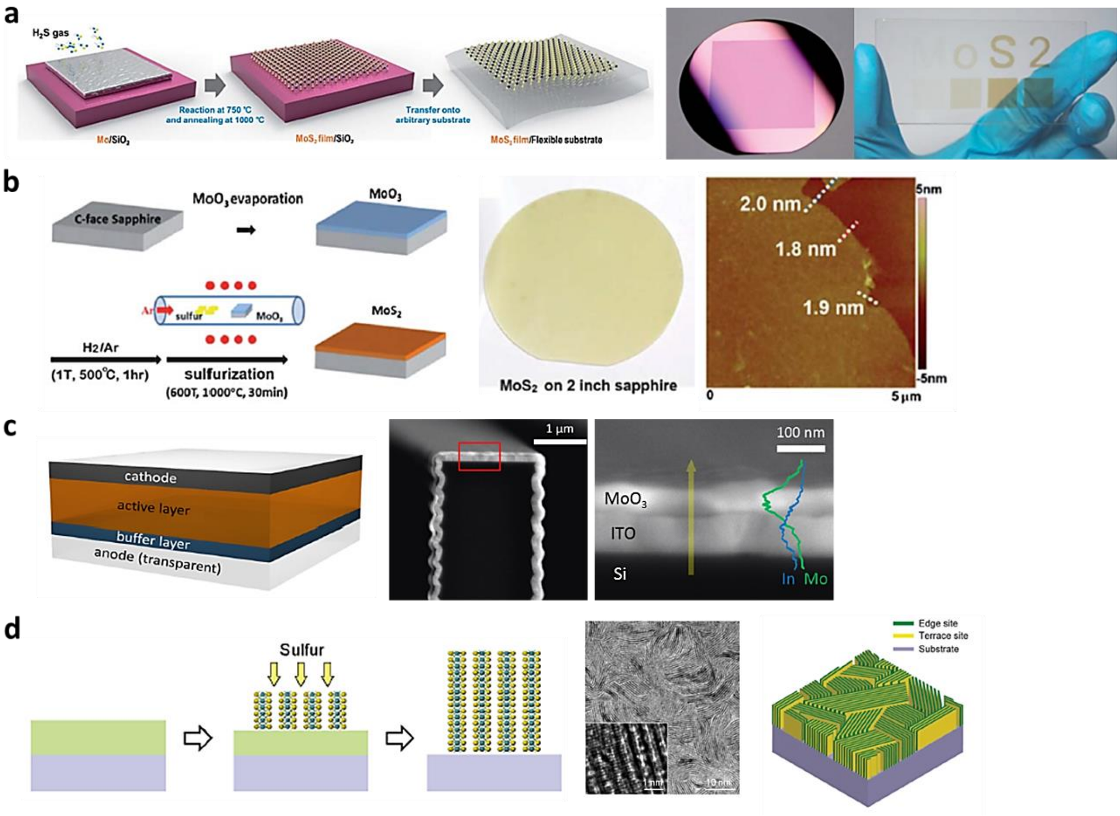

Figure 1.9 (a) Growth MoS_2 via Mo metal precursor on a SiO_2-Si substrate; (b) Growth MoS_2 via MoO_3 precursor on a sapphire substrate; (c) ALD-grown MoO_3 on ITO as the buffer layer in an organic photovoltaic device; (d) Rapid sulfurization to produce vertically aligned MoS_2.

Using metal precursor to produce MoS_2 may give rise to metallic transport behavior with a low o/off current ratio, which could be due to the presence of unreacted metal impurities. Rapid sulfurization on the metal precursor can further tune the orientation of MoS_2 to vertically aligned layers on the substrate (Figure 1.9(d)).[28] On the contrary, MoS_2 derived from oxide precursor exhibits a high on/off current ratio rather than the resistor-like behavior. The obtained MoS_2 is generally terrace-terminated and difficult to change the orientation.

- **Single vapor phase reaction and transport process**

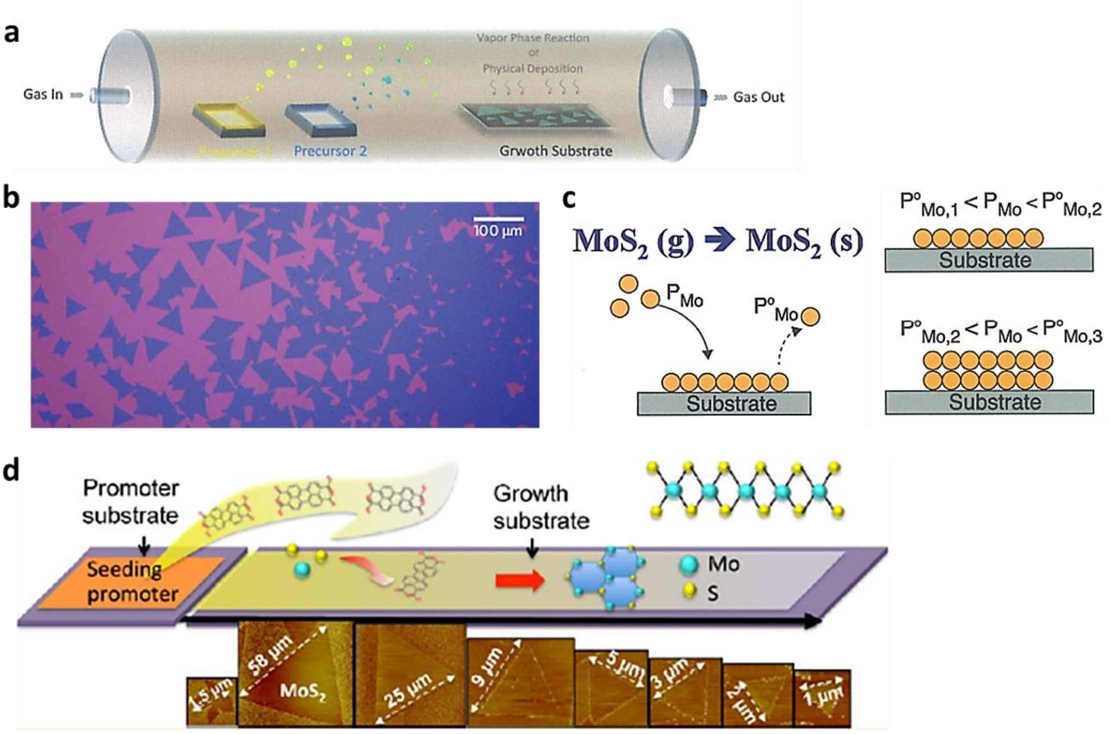

Figure 1.10 (a) Schematic diagram of the experimental setup for the single-step CVD process; (b) Optical reflection images of a typical large-grain MoS_2 on a SiO_2 grown by MoO_3 precursor; (c) Schematic illustration of the self-limiting growth with layer number control by using the $MoCl_5$ precursor; (d) Schematic drawing of the seeding promoter for MoS_2 growth.

Atomically thin MoS_2 can be synthesized by direct chemical vapor phase reaction of MoO_3 and S powders, where the two precursors are separately placed at two zones, as illustrated in Figure 1.10(a).[29] During this single-step process, MoO_{3-x} is likely formed as an intermediate phase and diffuse to the substrate, and further react with sulfur vapors to grow MoS_2 layers. This method allows the growth of single crystalline MoS_2 flakes on arbitrary substrates dependent on the nucleation density (Figure 1.10(b)).[30] The Mo source can be replaced with $MoCl_5$ to improve the reactivity. The balance between the partial pressure of the gaseous MoS_2 and the vapor pressure of the MoS_2 film provides the self-limiting growth mechanism to precisely control the layer number of MoS_2 on a large substrate.[31]

The growth of MoS_2 is very sensitive to the substrate chemistry. It has been discovered seeding the substrate with graphene-like species can promote the lateral growth of MoS_2 crystal to carry out the large area, continuous and high quality MoS_2 monolayer.[32] Direct growth of MoS_2 on an insulating substrate can also be achieved by ALD process or other vapor phase processes, such as physical vapor deposition (vapor phase transport method) and molecular beam epitaxy.[33-36] However, the cost, uniformity, and the control of layer number for producing high quality MoS_2 in a large scale still cannot compete with CVD process so far.

- **Bandgap and heterojunction engineering**

Bandgap engineering of MoS_2 is critical for the applications in electronics and optoelectronics. Although applying strain can tune the bandgap, it is not practical for real electronic device fabrication. Alternatively, the metallic or semiconducting behaviors of TMD family (MX_2) provide the degree of freedom to tune the intrinsic bandgap by partially substituting either transition metal or chalcogen for MoS_2.

doi:10.6342/NTU201603487

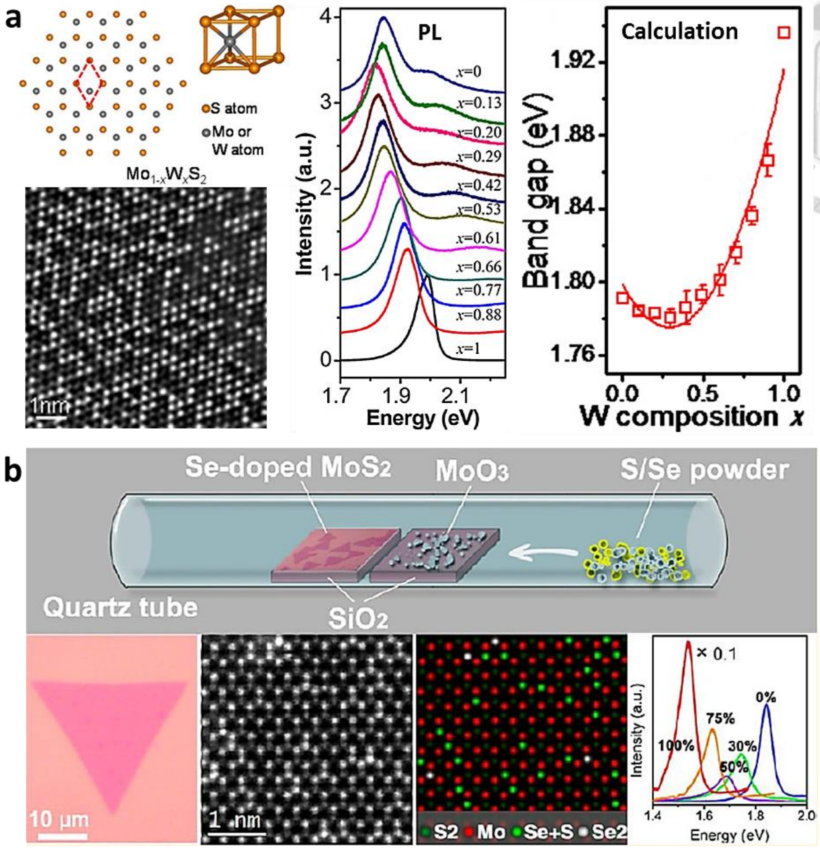

i

Figure 1.11 (a) Two-dimensional $Mo_{1-x}W_xS_2$ monolayer alloys show tunable bandgap in PL; (b) Monolayer $MoS_{2(1-x)}Se_{2x}$ (Se-doped MoS_2) shows over 10% optical bandgap modulation.

It has been reported both $Mo_{1-x}W_xS_2$ and $MoS_{2(1-x)}Se_{2x}$ exhibit their thermodynamic stability at room temperature to form ternary van der Waals alloys without phase separation.[37, 38] The bandgaps are modulated with the concentration of the dopants which can be observed from the PL measurement as illustrated in Figure 1.11. This strategy is also applied in CZTS-based thin film solar cell, where substitution of Se for S in CZTS adjusts the bandgap for light absorption.

The concept of the 2D materials as the building block, analogous to Lego blocks, for novel heterostructures has been first proposed by Geim *et al* (Figure 1.12(a)).[39]

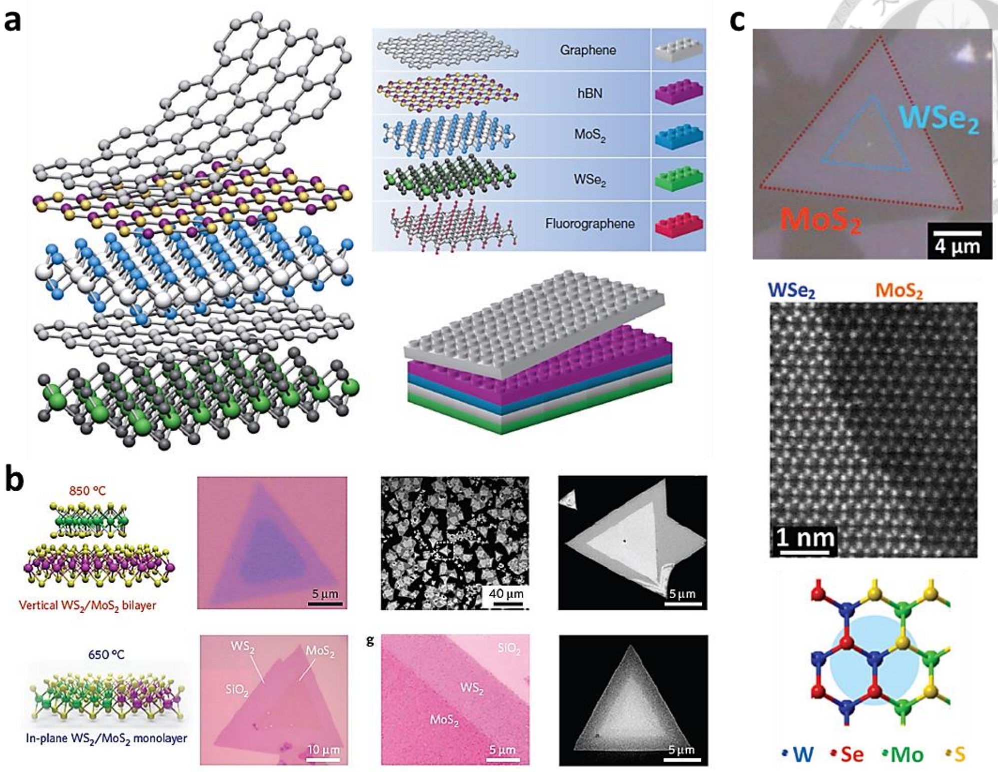

Figure 1.12 (a) Building van der Waal heterostructures as Lego blocks; (b) Schematic, optical and SEM images of the vertically (top) and in-plane (bottom) stacked WS_2/MoS_2 heterojunctions; (c) Optical (top), HR-STEM (middle) images, and atomic model (bottom) show the interface structure between WSe_2 and MoS_2.

This idea inspires a huge variety of designed van der Waal heterostructures assembled vertically to bring about new physical or chemical properties for applications. Very recently, bottom-up approach has achieved not only vertically stacked but also in-plane heterojunctions between WS_2 and MoS_2, which expands the junction design of 2D materials to another dimension (Figure 1.12(b)).[40] Moreover, the successful in epitaxial growth of a monolayer WSe_2-MoS_2 lateral p-n junction with an atomically sharp interface further demonstrated the possibility for fabricating lateral electronic or optoelectronic devices in an atomic level (Figure 1.12(c)).[41] All these efforts have shined the lights on the future material and device designs based on the TMD materials.

1.3.3 Transfer MoS_2 onto arbitrary substrates

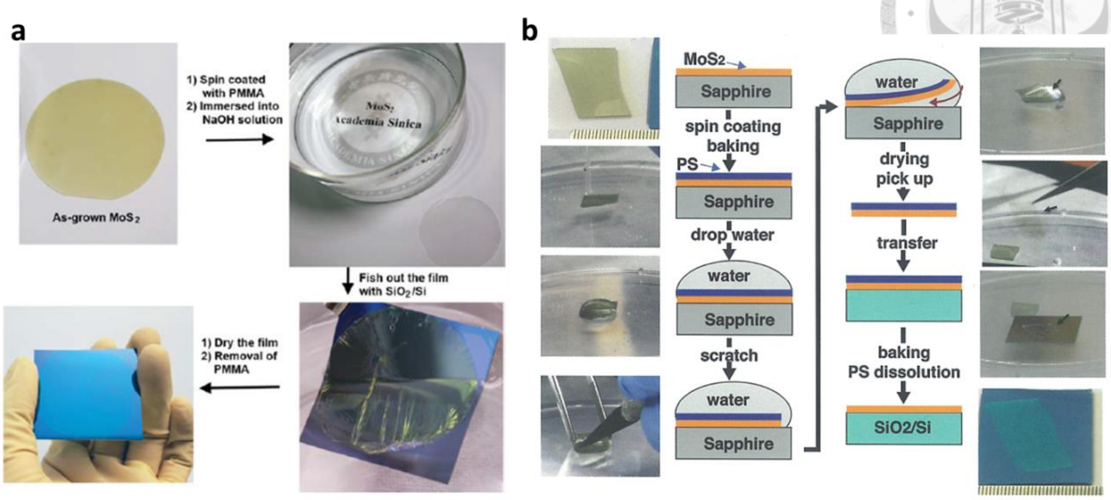

Figure 1.13 (a) General transfer process of MoS_2 from a sapphire substrate; (b) Surface-energy-assisted transfer process of MoS_2 onto arbitrary substrates.

Transferring an atomically thin TMD material from the original growth substrate without damaging its properties is critical for either fundamental studies or applied researches. The transfer process for MoS_2 is similar to that for graphene. General procedure is coating a polymer film on the MoS_2 (such as PMMA), etching out the bottom substrate (oxide layer) in a hot base solution, fishing out the film on the target substrate, and then remove the top polymer, as illustrated in Figure 1.13(a).[25] This process is effective, but is time-consuming. The properties of transferred MoS_2 may be altered due to the contamination from the etchant or the capillary-force-induced wrinkles. Recently, a simple, quick, and clean process is developed based on the surface energy difference between MoS_2 and sapphire.[42] By the assistance of water, the hydrophobic MoS_2 can be easily peeled off from the hydrophilic sapphire substrate and transferred to other desired substrates with no observable wrinkles, cracks, and polymer residues, which maintains similar properties as the as-grown one (Figure 1.13(b)).

1.4 MoS_2-based applications

MoS_2 is traditionally used for lubrication due to its anisotropic bonding nature of covalent at in-plane direction and weak van der Waal gaps between layers. The high chemical stability at the basal plane is also examined both by experiments and molecular-orbital calculations.[43] In MoS_2, the outer shell S-3*p* hybridizes with Mo-4*d* to form molecular orbitals, while the inner shell S-3*s* are buried in an atomic orbital that has low probability of electron density above the basal plane. Hence, those orbitals that are available for bonding are empty leading to chemically inert at the basal plane of MoS_2. The energy levels of antibonding orbitals are too high to involve the bonding behavior. Based on these two characters, MoS_2 is an excellent solid lubricant for high precision space-borne uses, such as satellite bearing, gears, and gimbals operating under extreme temperature ranges, as well as in microsystems, where the effects of surface forces are more significant than those of gravity.[44]

1.4.1 Field-effect transistor (FET) based electronics

One of the most important applications of semiconductors is for transistors in digital electronics, whose progress is driven by scaling down the size of transistors to extremely small dimensions. Subsequent reduction in scale will soon approach limits due to statistical and quantum effects and difficulty with heat dissipation, motivating the search for new device concepts and materials. On this point of view, the atomically thin 2D materials just match this demand to replace Si in CMOS-like digital logic devices. Semiconducting 2D TMDs have unique features that make them attractive as a channel material in FETs, such as the lack of dangling bonds, structural stability, and mobility comparable to Si.[8]

doi:10.6342/NTU201603487

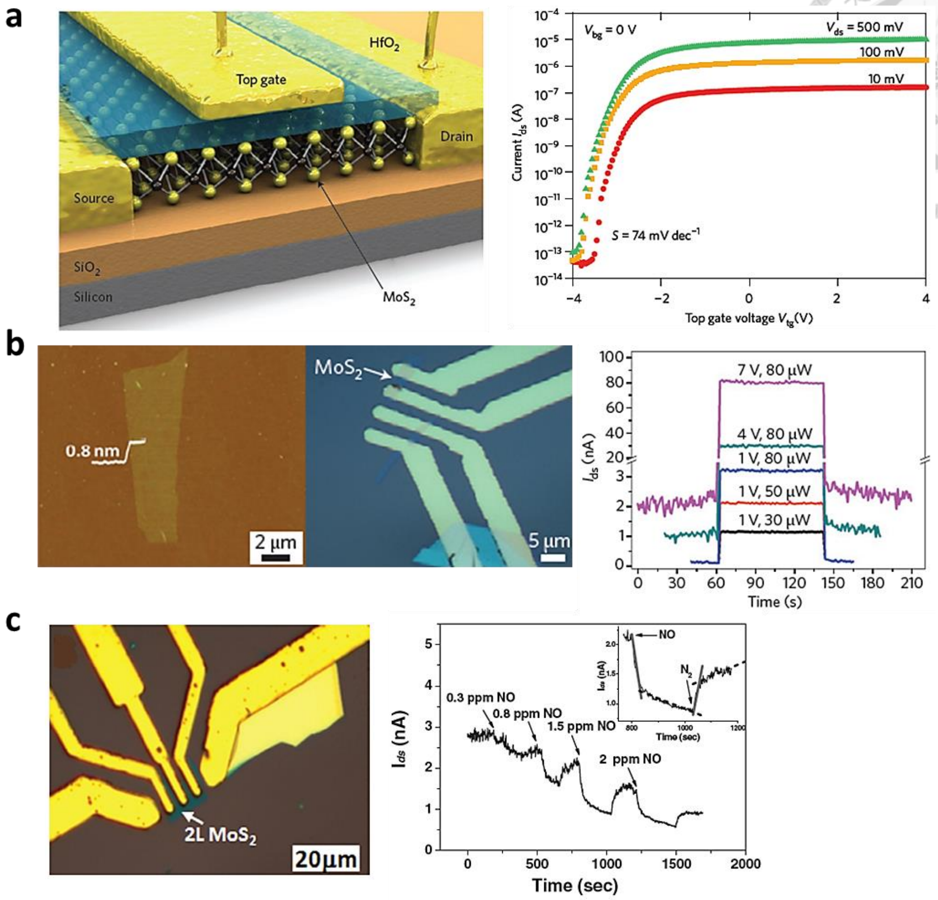

Figure 1.14 (a) Schematic illustration of HfO_2-top gated monolayer MoS_2 FET device and the source-drain current (I_{ds}) versus top gate voltage (V_{tg}) curve; (b) Photoswitching characteristics of single-layer MoS_2 phototransistor at different optical power (P_{light}) and drain voltage (V_{ds}); (c) Bilayer-MoS_2 FET device and real-time current response to NO exposure with increasing concentration.

The first top-gate transistor based on monolayer MoS_2 is demonstrated to have excellent on/off current ratio (~10^8), n-type conduction, room temperature mobility of >200 cm^2/V-s, and subthreshold swing of 74 mV per decade (Figure 1.14(a)).[45] Thin-film transistors made of MoS_2 from liquid exfoliation also have similar performance, suggesting possibilities for flexible and transparent electronics.[46] Other logic devices based on this configuration are also demonstrated in recent years.[47, 48]

Optoelectronic devices are electronic devices that can generate, detect, interact with or control light. Because single-layer MoS_2 has direct semiconductor bandgap, it is of great interest for applications in optoelectronics and because it is atomically thin and easily processed, it has great potential for flexible and transparent optoelectronics, such as displays and wearable electronics. Thickness-dependent bandgap variations within the visible range and the high photosensitivity make MoS_2 a good photodetector (Figure 1.14(b)).[49] The phototransistors based on the single-layer (Eg ~1.82 eV) and double-layer (Eg ~1.65 eV) MoS_2 are promising for the green light detection, while the triple-layer MoS_2 (Eg ~1.35 eV) is suitable for detection of the red light.[50] Incorporating materials of different bandgaps with MoS_2 may realize the concept of multi-junction solar cells that allow photons of different energies in the full solar spectrum to be efficiently absorbed.[51]

Chemical, biological and gas sensors based on FETs have been receiving continuous attention, which is realized by monitoring the change in conductance of the FET channel upon adsorption of target molecules. When NO gas exposes to the n-type MoS_2 based FET channel, the electron-withdrawing feature will cause p-doping of the channel, leading to an increase in channel resistance and a decrease in current (Figure 1.14(c)).[52] Further functionalization of the MoS_2 thin film with Pt nanoparticles (NPs) increases the sensing sensitivity by ~3 times with a detection limit of as low as 2 ppb for NO_2. Electrochemical sensing is another important strategy for detection of chemical and biological species. MoS_2 nanosheets have been used for glucose sensing, and selective detection of dopamine in the presence of uric acid and ascorbic acid.[53] Thus, it is expected that MoS_2 and other TMDs may represent new class of highly active electrochemical materials. Their composites with some types of catalytic nanostructures, such as noble metals, may further improve sensing performance.

doi:10.6342/NTU201603487

1.4.2 Energy storage

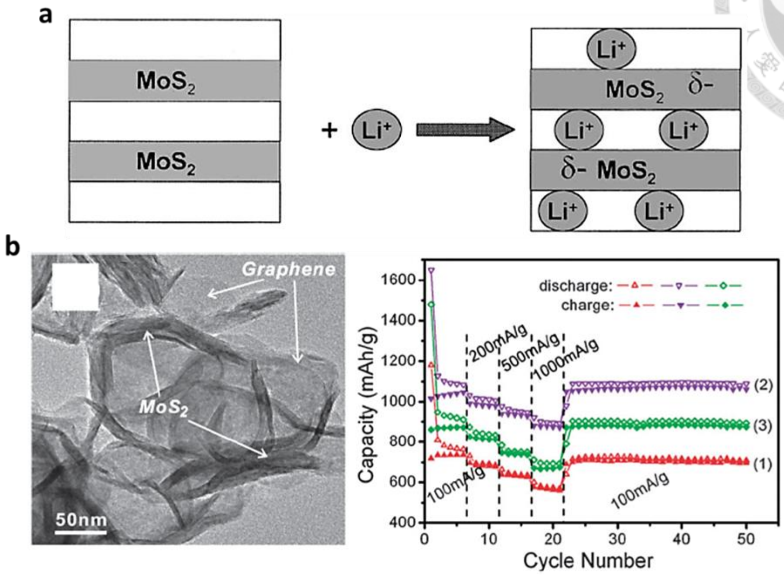

Figure 1.15 (a) Schematic representation of intercalation of lithium into MoS_2; (b) TEM image of MoS_2/rGO hybrid material and rate capability at different current density: (1) MoS_2/rGO (1:1), (2) MoS_2/rGO (1:2), (3) MoS_2/rGO (1:4).

Layered materials, such as graphite or TMDs, have been used for energy storage for decades. The electrical energy can be transformed into chemical energy for storage due to the ion intercalation into the layered materials and changes the valence states of transition metal in the host, as illustrated in Figure 1.15(a).[44] Lithium ion batteries (LIBs) and supercapacitors are two major applications in this electrochemical process. MoS_2 in a LIB system serves as an anode material, which undergoes lithiation and de-lithiation process driven by the electrochemical potential accompanying with the volume variations. A hybrid MoS_2 and carbon-related material (rGO) has been demonstrated to have high capacity of ~1100 mAh/g at a current of 100 mA/g, as well as excellent cycling stability and high-rate capability (Figure 1.15(b)).[54] This superior performance suggests the novel 2D composite holds great potential for LIBs.

1.4.3 Catalyst

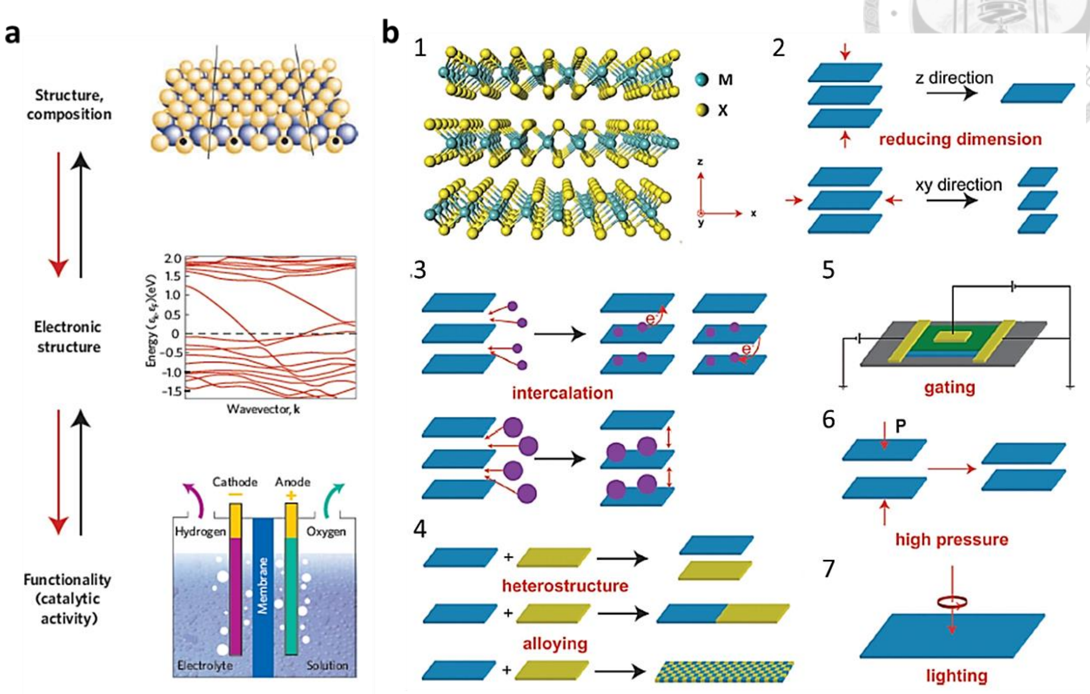

Figure 1.16 (a) Illustration of the way the electronic structure is the link between the structure and composition of a material and its functionality; (b) ① Schematic of 2D TMDs; Tuning 2D TMD properties by ② reducing dimension along the *z* direction and *xy* direction; ③ guest ion intercalation; ④ constructing heterostructures and alloying; ⑤ gating; ⑥ applying high pressure; ⑦ illuminating circular-polarized light.

Catalysis is a crucial technology that can positively influence the quality of our lives and the health of our environment. Currently, there is a significant drive to relinquish our dependence on fossil fuels and to minimize the emission of CO_2. Reducing environmental impact will require entirely new catalysts which are for new processes, more active and more selective, and made of earth abundant elements. In chemistry and biology, catalysis can accelerate the rate of a chemical reaction through providing an alternative mechanism involving a different transition state and lower activation energy, which accounts for its applications in diverse fields.[55] The catalytic properties of a material are in principle determined completely by its electronic structure, so the objective is the engineering of electronic structure by changing composition and physical structure (Figure 1.16 (a)).[56]

2D TMDs have wild range of electronic structures which not only boots the development of low-dimensional electronic and optoelectronic devices, but also facilitates the applications into catalysis due to the strong correlation between electronic and catalytic properties. These electronic structures can be effectively tuned through different methodologies, as illustrated in Figure 1.16(b).[9]

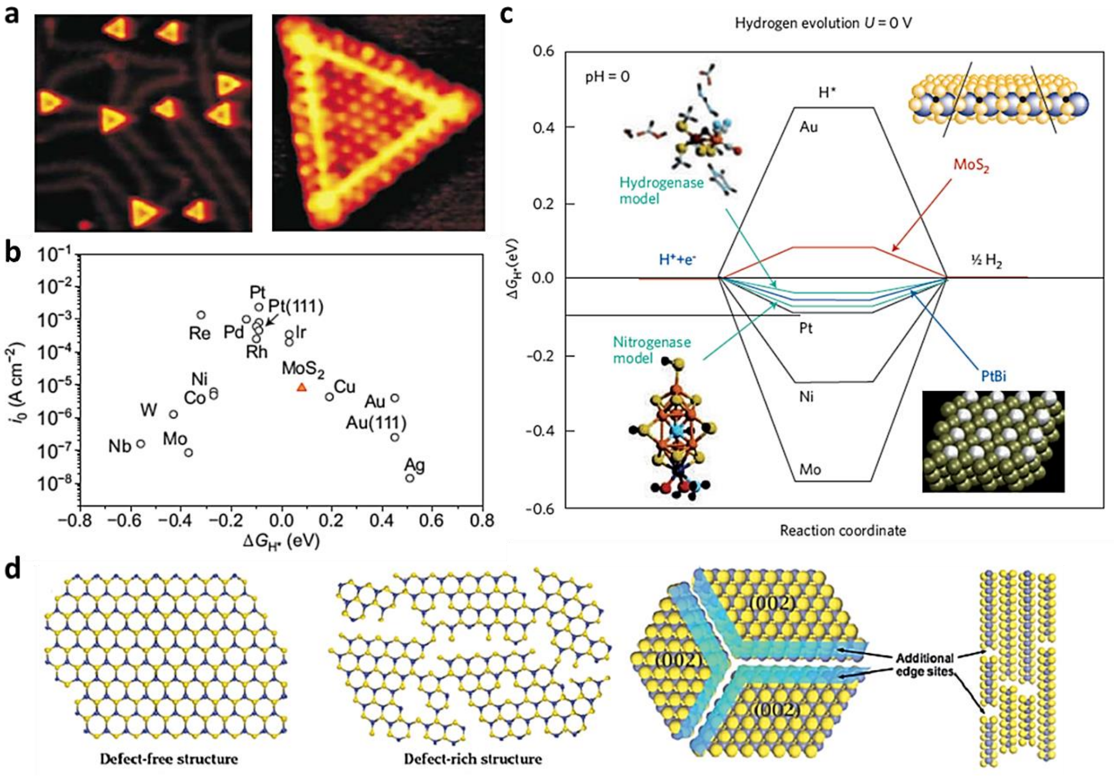

Figure 1.17 (a) STM images show one-dimensional metallic edge states in single MoS_2 cluster; (b) Volcano plot of exchange current density as a function of DFT-calculated Gibbs free energy of adsorbed atomic hydrogen for MoS_2 and pure metals; (c) The free energy diagram of hydrogen evolution at zero potential and zero pH for MoS_2 edge sites and some metals; (d) Schematic illustrations for defect-free, defect-rich, and atomic reconstruction of defect-rich MoS_2.

doi:10.6342/NTU201603487

Catalysis is a surface reaction process, in which the coordination number of surface atoms plays a crucial role in affecting their catalytic activities. In this regard, single layer of MoS_2 cluster has few dangling bond at the basal surface, while the edge of the cluster possesses unsaturated atoms that can serve as the active sites for catalytic reaction (Figure 1.17(a)).[57] The edge site of MoS_2 has been examined to have metallic properties that can easily transfer charges for catalytic reaction, such as hydrogen evolution reaction (HER).[58] The comparable activity of MoS_2 edges with noble metals in HER can be attributed to the low binding free energy of the intermediate, where H atoms are bound to the active sites, giving rise to high activity (Figure 1.17(b) and Figure 1.17(c)).[56] Although increasing the edge sites in MoS_2 seems to improve the HER activity, the disordered structure would block the electron transport along the collapse of 2D electron conjugation resulting in the poor overall electrical conductivity, which limits the HER process.[55] Therefore, MoS_2 with a moderate degree of disorder can provide both abundant active sites and high overall electrical conductivity, which ensures superior HER performance (Figure 1.17(d)).

Since the metallic behavior of MoS_2 is the key for the HER performance, many strategies have been developed to increase the number of active sites in MoS_2. One is increasing the exposure number of edges by the assistance of porous templates, such as double-gyroid structure (Figure 1.18(a)) and the porous Ni foam (Figure 1.18(b)).[59, 60] Another method is preparing the edge-terminated MoS_2 vertically aligned on the substrate (Figure 1.9(d)), followed by an intercalation process, as illustrated in Figure 1.18(c).[61] During the lithiation process, MoS_2 will transform from a semiconducting 2H phase to a metastable metallic 1T phase. The phase transformation will turn all the bulk MoS_2 to metallic behavior rather than edges only, which further boosts the HER activity due to the strains in the distorted 1T lattice help lower the reaction free energy.

doi:10.6342/NTU201603487

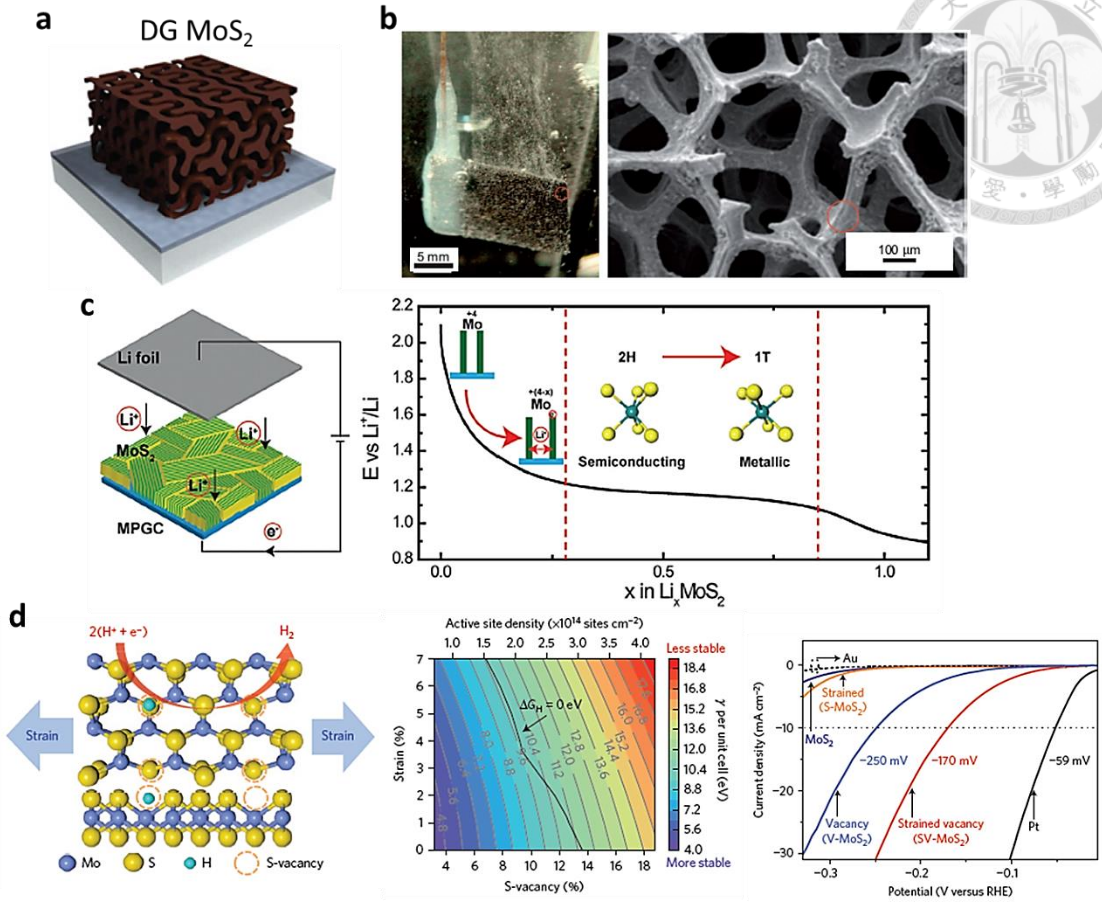

Figure 1.18 (a) Structural model for mesoporous MoS_2 with a double-gyroid (DG) morphology; (b) Optical and SEM images of MoS_2 grown on graphene-protected Ni foam; (c) Schematic of the edge-terminated MoS_2 lithiation process and galvanostatic discharge curve with schematic of charge transfer and phase transition; (d) Illustration of MoS_2 with strained S-vacancies on the basal plane that optimizes the thermodynamic requirement for HER activity.

The other strategy is to tune the electronic structure of MoS_2 by both creating plenty of S-vacancies on the basal plane and applying strains from the substrate, as illustrated in Figure 1.18(d).[62] By proper control of the amount of S-vacancies and the strain, the zero free energy for H atoms adsorption can be achieved, which is consistent to the simulated expectation (Figure 1.17(c)), and thus optimizes the HER performance.

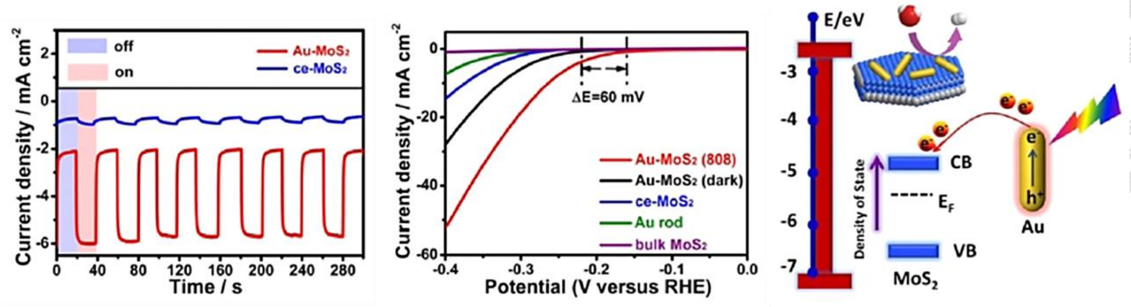

Figure 1.19 Hot electrons of Au nanorods activate the electrocatalysis of hydrogen evolution on MoS_2 nanosheets.

Traditional catalytic reaction, such as HER, requires charge transfer between active material and reactants, so metallic MoS_2 is essential as a mediate to deliver electrons for chemical reaction. On the other hand, MoS_2 is intrinsic a semiconductor with tunable bandgaps in the visible range and has good photo-response. The direct bandgap transition in monolayer MoS_2 makes it a potential photocatalyst. However, the limitation of this application for monolayer MoS_2 is the thickness, which is too thin to absorb enough light so as to generate enough electrons for catalytic reaction. To compromise the light absorption, plasmonic effect is introduced by fabricating Au nanorods and MoS_2 composites (Figure 1.19).[63] The increase of carrier density of MoS_2 induced by the injection of hot electrons from Au nanorods (plasmon-excited hot electrons injection mechanism) matches the energy level of HER leading to decrease the overpotential.

1.4.4 Heterojunction device for memory

Heterostructure devices composed of MoS_2 and other 2D materials have shown many extraordinary performances than an individual MoS_2 device because they provide different electronic structures for tuning the synergistic device behaviors. For example,

doi:10.6342/NTU201603487

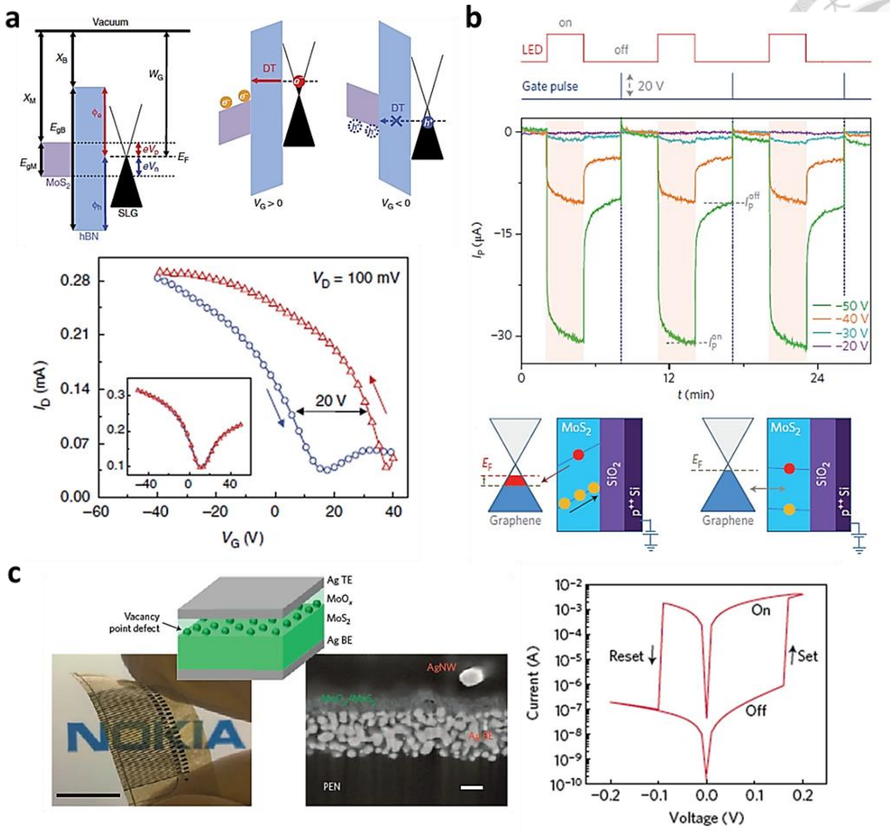

Figure 1.20 (a) Energy band diagrams and transfer curve of GBM heterostructured memory devices; (b) Gate voltage dependent photocurrent induction and switching operation of graphene-MoS$_2$ hybrid structure and schematic of charge exchange process; (c) Solution-processed MoO$_x$/MoS$_2$ memristors on a plastic foil and resistive switching characteristics.

fabricating semiconducting MoS$_2$ with semi-metal graphene and insulating BN with the floating gate configuration carries out a nonvolatile memory in atomic level (Figure 1.20(a)).[64] Hybrid graphene and MoS$_2$ can make a multifunctional photoresponsive memory device (Figure 1.20(b)).[65] Softly oxidizing the surface MoS$_2$ to MoO$_x$ also brings about significant resistive switching behaviors for the heterostructure (Figure 1.20(c)).[66] All these efforts suggest the modulation of charge trapping in MoS$_2$ and in corresponding heterojunctions is crucial for flexible and transparent memory devices.

1.5 Motivation

Although MoS_2 has versatile applications, it has been demonstrated that we cannot predict the contact properties of metal-MoS_2 by merely considering the work functions and the Schottky theory.[67-69] Au/MoS_2 interface is still in debate on the Schottky or ohmic behavior, and the formation mechanism of the contact is vague so far.[45, 69-72] The elusive surface properties of MoS_2 may result in the limited device performance and impede the development to compete with Si-based devices. This situation will become more complicated when the layer number of MoS_2 reduces because the electronic structure changes with the thickness.[13, 73, 74] The optical and the transport properties through the interface will then be affected. Therefore, the puzzles left on the surface or interface drive us to study the surface properties of MoS_2 especially when the thickness reduces from bulk to few layers.

To fit the practical demand, CVD process is the most efficient way to produce large-area MoS_2, where MoO_3 and Mo metal are two common precursors. Mo metal has revealed its flexibility to grow either terrace-terminated or edge-terminated MoS_2 on the SiO_2/Si substrate.[26, 28] On the other hand, it seems difficult to grow MoS_2 of different orientations from MoO_3 without the aid of a specifically oriented substrate.[75] Although utilizing Mo metal as a precursor can perform alternative orientations depending on the sulfurization conditions, the vertically aligned MoS_2 is generally applied for catalysts.[28, 61, 76, 77]

It was reported that Mo is a suitable contact metal to MoS_2 with zero tunnel and Schottky barrier under source/drain contact, as well as an ultra-low Schottky barrier (0.1 eV) at source/drain-channel junction due to strong Fermi level pinning.[67] Applying metallic 1T-MoS_2 as a contact for 2H-MoS_2 can further reduce the contact resistance to

doi:10.6342/NTU201603487

~200 Ω-μm at zero gate bias.[78] Since the edges of MoS_2 have metallic properties, the vertically aligned MoS_2 is probably able to bridge the Mo metal and in-plane MoS_2 to achieve low contact resistance in electronic devices. However, control of sulfurization kinetics is highly required to construct the sandwich configuration.

MoS_2-based heterojunction devices have exhibited promising applications in catalysis,[79] photovoltaic,[80] and nonvolatile memory.[64, 65] Selecting a proper material that has similar structure with MoS_2 and tunable electronic properties in the heterostructure brings about versatile material designs based on the applications. Two-dimensional TMDs are general selections for MoS_2. ZnO, on the other hand, is also a hexagonal material as MoS_2, but has three-dimensional lattice structure. The lattice mismatch is estimated to be small between ZnO and MoS_2 (~2.8%). Both ZnO and MoS_2 also have distinct photoresponse and have potentials in memory applications. Combining these two materials as a heteostructure material may give rise to extraordinary synergy effects.

1.6 Thesis layout

Chapter 2 introduces the procedures of sample preparation and device fabrication. Several tools and techniques I used to characterize samples are also presented. Chapter 3 discusses the variations in surface properties of MoS_2 thin films with various film thicknesses, which are observed from the XPS results. The growth conditions of MoS_2 thin films on SiO_2-Si substrate are optimized for the thickness and quality control. Potential application based on our findings is also demonstrated.

Chapter 4 compares the sulfurization kinetics between MoO_3 and Mo precursors from both the thermodynamic and experimental points of view. The orientations of

doi:10.6342/NTU201603487

MoS_2 derived from different oxide to metal ratio are analyzed by Raman and XAS techniques. ALD process is utilized for fabricating hybrid ZnO-MoS_2 vertically stacking device. The interface issue is also pointed out at the end of this chapter.

Chapter 5 continues the study of the ZnO/MoS_2 heterojunction by measuring the resistive switching behavior. Electrical measurements at various conditions are carried out to understand the device performance and junction properties. The possible mechanism for the carrier transport is also proposed.

In Chapter 6, Raman spectra of MoS_2 grown on various substrates are compared. Electrostatic force and surface treatment by ozone are introduced to improve the nucleation of ZnO on the MoS_2 surface in the ALD process. Finally, the conclusion of this thesis is presented in Chapter 7.

doi:10.6342/NTU201603487

References

[1] K. S. Novoselov, A. K. Geim, S. V. Morozov, D. Jiang, Y. Zhang, S. V. Dubonos, I. V. Grigorieva and A. A. Firsov, Science **306** (5696), 666-669 (2004).

[2] A. K. Geim and K. S. Novoselov, Nat. Mater. **6**, 183-191 (2007).

[3] K. S. Novoselov, A. K. Geim, S. V. Morozov, D. Jiang, M. I. Katsnelson, I. V. Grigorieva, S. V. Dubonos and A. A. Firsov, Nature **438** (7065), 197-200 (2005).

[4] N. Tombros, C. Jozsa, M. Popinciuc, H. T. Jonkman and B. J. van Wees, Nature **448** (7153), 571-574 (2007).

[5] X. Wang, L. J. Zhi and K. Mullen, Nano Lett. 8 (1), 323-327 (2008).

[6] J. A. Wilson and A. D. Yoffe, Adv. Phys. **18** (73), 193-335 (1969).

[7] M. Chhowalla, H. S. Shin, G. Eda, L. J. Li, K. P. Loh and H. Zhang, Nat. Chem. **5** (4), 263-275 (2013).

[8] Q. H. Wang, K. Kalantar-Zadeh, A. Kis, J. N. Coleman and M. S. Strano, Nat. Nanotechnol. **7** (11), 699-712 (2012).

[9] H. Wang, H. Yuan, S. Sae Hong, Y. Li and Y. Cui, Chem. Soc. Rev. **44** (9), 2664-2680 (2015).

[10] C. Gong, H. Zhang, W. Wang, L. Colombo, R. M. Wallace and K. Cho, Appl. Phys. Lett. **103** (5), 053513 (2013).

[11] C. Wan, Y. Wang, N. Wang, W. Norimatsu, M. Kusunoki and K. Koumoto, J. Electron. Mater. **40** (5), 1271-1280 (2011).

[12] E. Morosan, H. W. Zandbergen, B. S. Dennis, J. W. G. Bos, Y. Onose, T. Klimczuk, A. P. Ramirez, N. P. Ong and R. J. Cava, Nat. Phys. **2** (8), 544-550 (2006).

[13] A. Splendiani, L. Sun, Y. Zhang, T. Li, J. Kim, C. Y. Chim, G. Galli and F. Wang,

Nano Lett. **10** (4), 1271-1275 (2010).

[14] A. C. Ferrari, J. C. Meyer, V. Scardaci, C. Casiraghi, M. Lazzeri, F. Mauri, S. Piscanec, D. Jiang, K. S. Novoselov, S. Roth and A. K. Geim, Phys. Rev. Lett. **97** (18), 187401 (2006).

[15] T. P., R. Schmidt, B. J., L. A., A. M., K. C., G. O., Z. D. R. T., V. S. M. and B. R., Optics Express **21** (4), 4908-4916 (2013).

[16] C. Lee, H. Yan, L. E. Brus, T. F. Heinz, J. Hone and S. Ryu, ACS Nano **4** (5), 2695-2700 (2010).

[17] H. J. Conley, B. Wang, J. I. Ziegler, R. F. Haglund, Jr., S. T. Pantelides and K. I. Bolotin, Nano Lett. **13** (8), 3626-3630 (2013).

[18] H. Zhu, Y. Wang, J. Xiao, M. Liu, S. Xiong, Z. J. Wong, Z. Ye, Y. Ye, X. Yin and X. Zhang, Nat. Nanotechnol. **10** (2), 151-155 (2015).

[19] D. Xiao, G. B. Liu, W. Feng, X. Xu and W. Yao, Phys. Rev. Lett. **108** (19), 196802 (2012).

[20] K. F. Mak, K. He, J. Shan and T. F. Heinz, Nat. Nanotechnol. **7** (8), 494-498 (2012).

[21] K. S. Novoselov and A. H. Castro Neto, Phys. Scripta **T146**, 014006 (2012).

[22] Z. Zeng, Z. Yin, X. Huang, H. Li, Q. He, G. Lu, F. Boey and H. Zhang, Angew. Chem. Int. Ed. Engl. **50** (47), 11093-11097 (2011).

[23] J. N. Coleman, M. Lotya, A. O'Neill, S. D. Bergin, P. J. King, U. Khan, K. Young, A. Gaucher, S. De, R. J. Smith, I. V. Shvets, S. K. Arora, G. Stanton, H. Y. Kim, K. Lee, G. T. Kim, G. S. Duesberg, T. Hallam, J. J. Boland, J. J. Wang, J. F. Donegan, J. C. Grunlan, G. Moriarty, A. Shmeliov, R. J. Nicholls, J. M. Perkins, E. M. Grieveson, K. Theuwissen, D. W. McComb, P. D. Nellist and V. Nicolosi, Science **331** (6017), 568-571 (2011).

[24] Y. Zhan, Z. Liu, S. Najmaei, P. M. Ajayan and J. Lou, Small **8** (7), 966-971 (2012).

[25] Y. C. Lin, W. Zhang, J. K. Huang, K. K. Liu, Y. H. Lee, C. T. Liang, C. W. Chu and L. J. Li, Nanoscale **4** (20), 6637-6641 (2012).

[26] Y. Lee, J. Lee, H. Bark, I. K. Oh, G. H. Ryu, Z. Lee, H. Kim, J. H. Cho, J. H. Ahn and C. Lee, Nanoscale **6** (5), 2821-2826 (2014).

[27] Y.-C. Tseng, A. U. Mane, J. W. Elam and S. B. Darling, Sol. Energ. Mat. Sol. C. **99**, 235-239 (2012).

[28] D. Kong, H. Wang, J. J. Cha, M. Pasta, K. J. Koski, J. Yao and Y. Cui, Nano Lett. **13** (3), 1341-1347 (2013).

[29] Y. H. Lee, X. Q. Zhang, W. Zhang, M. T. Chang, C. T. Lin, K. D. Chang, Y. C. Yu, J. T. Wang, C. S. Chang, L. J. Li and T. W. Lin, Adv. Mater. **24** (17), 2320-2325 (2012).

[30] A. M. van der Zande, P. Y. Huang, D. A. Chenet, T. C. Berkelbach, Y. You, G. H. Lee, T. F. Heinz, D. R. Reichman, D. A. Muller and J. C. Hone, Nat. Mater. **12** (6), 554-561 (2013).

[31] Y. Yu, C. Li, Y. Liu, L. Su, Y. Zhang and L. Cao, Sci. Rep. **3**, 1866 (2013).

[32] X. Ling, Y. H. Lee, Y. Lin, W. Fang, L. Yu, M. S. Dresselhaus and J. Kong, Nano Lett. **14** (2), 464-472 (2014).

[33] L. K. Tan, B. Liu, J. H. Teng, S. Guo, H. Y. Low, H. R. Tan, C. Y. Chong, R. B. Yang and K. P. Loh, Nanoscale **6** (18), 10584-10588 (2014).

[34] Z. Jin, S. Shin, H. Kwon do, S. J. Han and Y. S. Min, Nanoscale **6** (23), 14453-14458 (2014).

[35] S. Wu, C. Huang, G. Aivazian, J. S. Ross, D. H. Cobden and X. Xu, ACS Nano **7** (3), 2768-2772 (2013).

doi:10.6342/NTU201603487

[36] Y. Zhang, T. R. Chang, B. Zhou, Y. T. Cui, H. Yan, Z. Liu, F. Schmitt, J. Lee, R. Moore, Y. Chen, H. Lin, H. T. Jeng, S. K. Mo, Z. Hussain, A. Bansil and Z. X. Shen, Nat. Nanotechnol. **9** (2), 111-115 (2014).

[37] Y. Gong, Z. Liu, A. R. Lupini, G. Shi, J. Lin, S. Najmaei, Z. Lin, A. L. Elias, A. Berkdemir, G. You, H. Terrones, M. Terrones, R. Vajtai, S. T. Pantelides, S. J. Pennycook, J. Lou, W. Zhou and P. M. Ajayan, Nano Lett. **14** (2), 442-449 (2014).

[38] Y. Chen, J. Xi, D. O. Dumcenco, Z. Liu, K. Suenaga, D. Wang, Z. Shuai, Y. S. Huang and L. Xie, ACS Nano **7** (5), 4610-4616 (2013).

[39] A. K. Geim and I. V. Grigorieva, Nature **499** (7459), 419-425 (2013).

[40] Y. Gong, J. Lin, X. Wang, G. Shi, S. Lei, Z. Lin, X. Zou, G. Ye, R. Vajtai, B. I. Yakobson, H. Terrones, M. Terrones, B. K. Tay, J. Lou, S. T. Pantelides, Z. Liu, W. Zhou and P. M. Ajayan, Nat. Mater. **13** (12), 1135-1142 (2014).

[41] M. Y. Li, Y. Shi, C. C. Cheng, L. S. Lu, Y. C. Lin, H. L. Tang, M. L. Tsai, C. W. Chu, K. H. Wei, J. H. He, W. H. Chang, K. Suenaga and L. J. Li, Science **349** (6247), 524-528 (2015).

[42] A. Gurarslan, Y. Yu, L. Su, Y. Yu, F. Suarez, S. Yao, Y. Zhu, M. Ozturk, Y. Zhang and L. Cao, ACS Nano **8** (11), 11522-11528 (2014).

[43] J. R. Lince, D. J. Carré and P. D. Fleischauer, Phys. Rev. B **36** (3), 1647-1656 (1987).

[44] E. Benavente, M. A. Santa Aan, F. Mendizabal and G. Gonzalez, Coord. Chem. Rev. **224**, 87-109 (2002).

[45] B. Radisavljevic, A. Radenovic, J. Brivio, V. Giacometti and A. Kis, Nat. Nanotechnol. **6** (3), 147-150 (2011).

[46] K. Lee, H. Y. Kim, M. Lotya, J. N. Coleman, G. T. Kim and G. S. Duesberg, Adv. Mater. **23** (36), 4178-4182 (2011).

doi:10.6342/NTU201603487

[47] H. Wang, L. Yu, Y. H. Lee, Y. Shi, A. Hsu, M. L. Chin, L. J. Li, M. Dubey, J. Kong and T. Palacios, Nano Lett. **12** (9), 4674-4680 (2012).

[48] B. Radisavljevic, M. B. Whitwick and A. Kis, ACS Nano **5** (12), 9934-9938 (2011).

[49] Z. Yin, H. Li, H. Li, L. Jiang, Y. Shi, Y. Sun, G. Lu, Q. Zhang, X. Chen and H. Zhang, ACS Nano **6** (1), 74-80 (2012).

[50] H. S. Lee, S. W. Min, Y. G. Chang, M. K. Park, T. Nam, H. Kim, J. H. Kim, S. Ryu and S. Im, Nano Lett. **12** (7), 3695-3700 (2012).

[51] A. Polman and H. A. Atwater, Nat. Mater. **11** (3), 174-177 (2012).

[52] H. Li, Z. Yin, Q. He, H. Li, X. Huang, G. Lu, D. W. Fam, A. I. Tok, Q. Zhang and H. Zhang, Small **8** (1), 63-67 (2012).

[53] S. Wu, Z. Zeng, Q. He, Z. Wang, S. J. Wang, Y. Du, Z. Yin, X. Sun, W. Chen and H. Zhang, Small **8** (14), 2264-2270 (2012).

[54] K. Chang and W. CHen, ACS Nano **5** (6), 4720-4728 (2011).

[55] Y. Sun, S. Gao, F. Lei and Y. Xie, Chem. Soc. Rev. **44** (3), 623-636 (2015).

[56] J. K. Norskov, T. Bligaard, J. Rossmeisl and C. H. Christensen, Nat. Chem. **1** (1), 37-46 (2009).

[57] M. V. Bollinger, J. V. Lauritsen, K. W. Jacobsen, J. K. Nørskov, S. Helveg and F. Besenbacher, Phys. Rev. Lett. **87** (19) (2001).

[58] T. F. Jaramillo, K. P. Jorgensen, J. Bonde, J. H. Nielsen, S. Horch and I. Chorkendorff, Science **317** (5834), 100-102 (2007).

[59] J. Kibsgaard, Z. Chen, B. N. Reinecke and T. F. Jaramillo, Nat. Mater. **11** (11), 963-969 (2012).

[60] Y. H. Chang, C. T. Lin, T. Y. Chen, C. L. Hsu, Y. H. Lee, W. Zhang, K. H. Wei and L. J. Li, Adv. Mater. **25** (5), 756-760 (2013).

doi:10.6342/NTU201603487

[61] H. Wang, Z. Lu, S. Xu, D. Kong, J. J. Cha, G. Zheng, P. C. Hsu, K. Yan, D. Bradshaw, F. B. Prinz and Y. Cui, Proc. Natl. Acad. Sci. U. S. A. **110** (49), 19701-19706 (2013).

[62] H. Li, C. Tsai, A. L. Koh, L. Cai, A. W. Contryman, A. H. Fragapane, J. Zhao, H. S. Han, H. C. Manoharan, F. Abild-Pedersen, J. K. Norskov and X. Zheng, Nat. Mater. **15** (1), 48-53 (2016).

[63] Y. Shi, J. Wang, C. Wang, T. T. Zhai, W. J. Bao, J. J. Xu, X. H. Xia and H. Y. Chen, J. Am. Chem. Soc. **137** (23), 7365-7370 (2015).

[64] M. S. Choi, G. H. Lee, Y. J. Yu, D. Y. Lee, S. H. Lee, P. Kim, J. Hone and W. J. Yoo, Nat. Commun. **4**, 1624 (2013).

[65] K. Roy, M. Padmanabhan, S. Goswami, T. P. Sai, G. Ramalingam, S. Raghavan and A. Ghosh, Nat. Nanotechnol. **8** (11), 826-830 (2013).

[66] A. A. Bessonov, M. N. Kirikova, D. I. Petukhov, M. Allen, T. Ryhanen and M. J. Bailey, Nat. Mater. **14** (2), 199-204 (2015).

[67] J. Kang, W. Liu and K. Banerjee, Appl. Phys. Lett. **104** (9), 093106 (2014).

[68] J. Kang, W. Liu, D. Sarkar, D. Jena and K. Banerjee, Phys. Rev. X **4** (3) (2014).

[69] S. McDonnell, R. Addou, C. Buie, R. M. Wallace and C. L. Hinkle, ACS Nano **8** (3), 2880-2888 (2014).

[70] S. Das, H. Y. Chen, A. V. Penumatcha and J. Appenzeller, Nano Lett. **13** (1), 100-105 (2013).

[71] I. Popov, G. Seifert and D. Tománek, Phys. Rev. Lett. **108** (15) (2012).

[72] C. Gong, L. Colombo, R. M. Wallace and K. Cho, Nano Lett. **14** (4), 1714-1720 (2014).

[73] K. F. Mak, C. Lee, J. Hone, J. Shan and T. F. Heinz, Phys. Rev. Lett. **105** (13) (2010).

doi:10.6342/NTU201603487

[74] X. Chen, Z. Wu, S. Xu, L. Wang, R. Huang, Y. Han, W. Ye, W. Xiong, T. Han, G. Long, Y. Wang, Y. He, Y. Cai, P. Sheng and N. Wang, Nat. Commun. **6**, 6088 (2015).

[75] Y. Sakashita and T. Yoneda, J. Catal. **185**, 487-495 (1999).

[76] H. Wang, Q. Zhang, H. Yao, Z. Liang, H. W. Lee, P. C. Hsu, G. Zheng and Y. Cui, Nano Lett. **14** (12), 7138-7144 (2014).

[77] H. Wang, C. Tsai, D. Kong, K. Chan, F. Abild-Pedersen, J. K. Nørskov and Y. Cui, Nano Res. **8** (2), 566-575 (2015).

[78] R. Kappera, D. Voiry, S. E. Yalcin, B. Branch, G. Gupta, A. D. Mohite and M. Chhowalla, Nat. Mater. **13** (12), 1128-1134 (2014).

[79] Y. Li, H. Wang, L. Xie, Y. Liang, G. Hong and H. Dai, J. Am. Chem. Soc. **133** (19), 7296-7299 (2011).

[80] M. Bernardi, M. Palummo and J. C. Grossman, Nano Lett. **13** (8), 3664-3670 (2013).

doi:10.6342/NTU201603487

Chapter 2 Experimental and Analysis Techniques

In this chapter, we introduce the experimental overview of this thesis, including the sample preparation on various substrates, properties characterization, and device fabrication for HER and resistive switching.

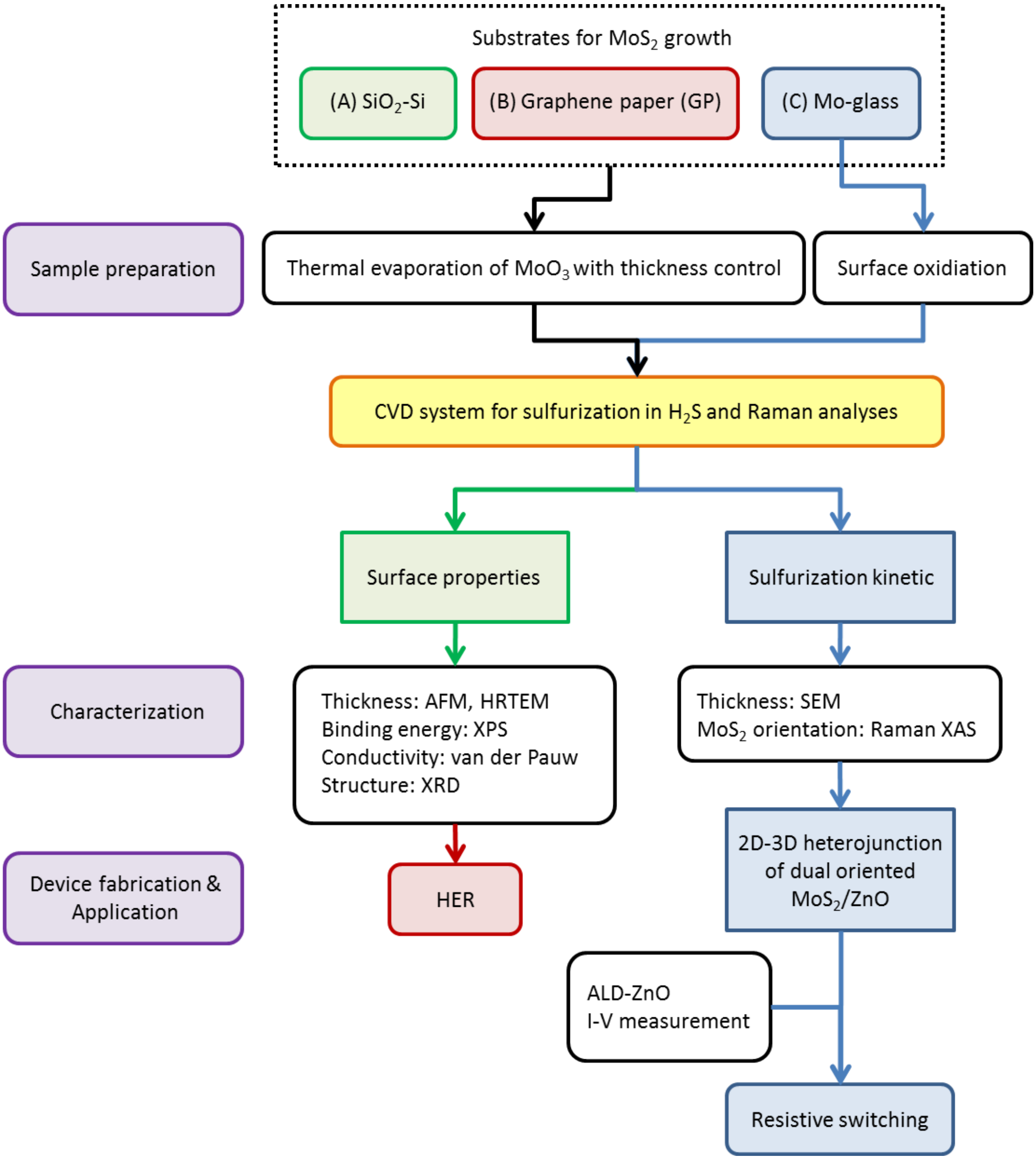

Figure 2.1 Schematic diagram illustrates the experimental procedure.

2.1 Sample preparation and device fabrication

Different thicknesses of MoS_2 thin films on various substrates were prepared via a two-step CVD process. First, a thin MoO_3 layer with controlled thickness was deposited by thermal evaporation process as a precursor. Then MoS_2 thin films were obtained after sulfurizing the precursor in a CVD system.

2.1.1 CVD process for sulfurization

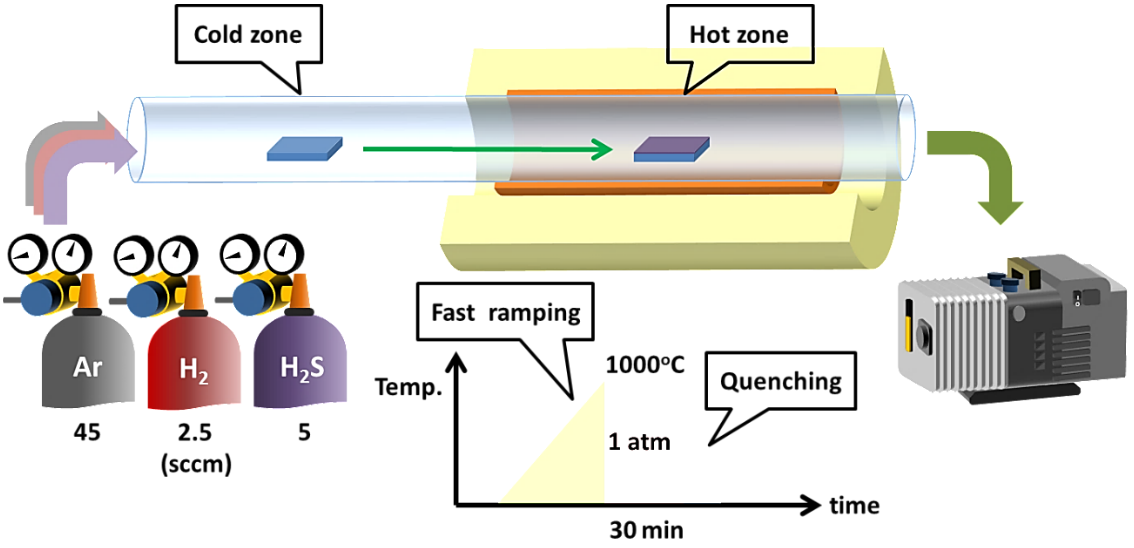

Figure 2.2 Schematic of the CVD system for sulfurization.

The CVD system utilized for sulfurization is illustrated as Figure 2.2. Initially, the system was vacuumed to below 1 mtorr to remove oxygen species. The MoO_3 precursor experienced a fast temperature ramp from room temperature to 1000^{o}C when it was transferred from the cold zone to the hot zone, and reacted with diluted H_2S (H_2S:H_2:Ar = 1:2:9) at 1 atm for 30 min to produce MoS_2. After sulfurization, the reactant gases were removed, and the sample was transferred to the cold zone and quenched down to room temperature with air blowing outside the quartz tube.

2.1.2 ALD process for ZnO growth

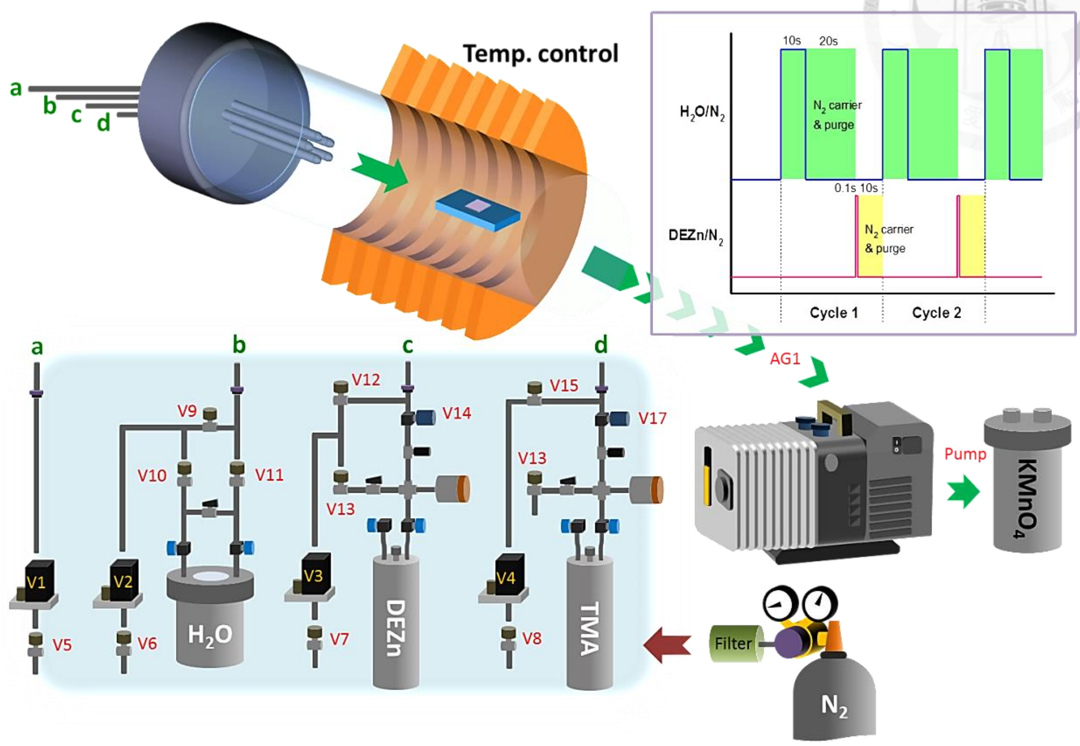

Figure 2.3 Schematic of the home-made ALD system for ZnO growth.

To fabricate the hybrid vertical heterostructure of ZnO and MoS_2, we adopt the ALD process to directly grow ZnO on the top surface of MoS_2. The system is illustrated in Figure 2.3, and the growth parameters are listed in Table 2.1. Zn precursor of diethyl zinc (DEZn, SAFC Hitech.) and H_2O were alternatively fed into the 150^{o}C reaction zone with the N_2 carrier gas to produce ZnO. The working pressure was controlled at few torr, and the growth rate was estimated as 2.75 Å /cycle.

Table 2.1 Controlled parameters for ZnO growth in the ALD process.

Precursor	N_2 carrier (sccm)	Dose time (sec)	Dose pressure (torr)	Purge time (sec)	Purge pressure (torr)
DeZn	100	0.1	2.2	10	0.7
H_2O	40	10	1.8	20	0.7

2.1.3 Device fabrication for resistive switching

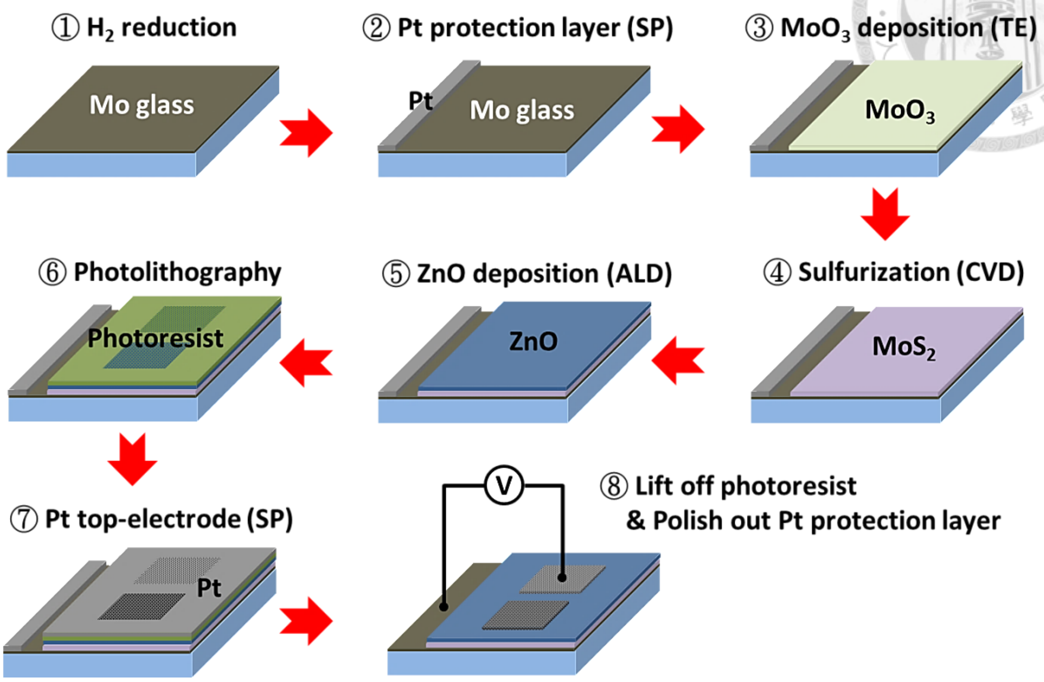

Figure 2.4 Schematic illustration of the fabrication process for the Pt/ZnO/MoS_2/Mo heterojunction device, where SP refers to sputtering and TE refers to thermal evaporation.

Mo-glass (MG, Junsun Tech.) of 1x1 cm in size was used for sulfurization, and the thickness of the Mo metal on the glass is 1 μm. After washing the MG sequentially by acetone, isopropyl alcohol (IPA), and de-ionized water, the substrate was put into a single zone CVD system, and annealed at 500°C for 1h in 10% H_2/Ar with the ramping rate of 30°C/min. A ~150 nm thick Pt layer was deposited on one side of the H_2-treated MG as a protection layer by sputtering. Thin MoO_3 layer with thicknesses ranging from 3 to 10 nm was deposited on the rest uncovered Mo surface via thermal evaporation. The MoO_3/MG specimen was sulfurized at 500°C for 10 min by CVD process. A ZnO of ~100 nm in thickness was directly grown on the MoS_2 via ALD and the deposition rate of 2.75 Å/cycle at 150°C. A photomask with the pad size of 100x100 μm (LxW) was fabricated on the ALD-ZnO surface by the conventional photolithography process. Top Ti/Au electrode (30:100 nm in thickness) was deposited by e-beam evaporation with the deposition rate of ~0.2 Å /sec. Pt top electrode was deposited by sputtering as previous conditions. After lifting off the photoresist and polishing away the Pt protection layer from the Mo surface, the electrical properties of the devices were measured. The whole process is illustrated in Figure 2.4.

2.2 Micro-Raman and micro-PL spectroscopy

Raman spectroscopy is the most powerful tool for analyzing 2D materials because it is highly sensitive to the short range order of crystal structure, layer number, and orientation of 2D materials, which can be revealed from the lattice vibration modes. PL spectroscopy here can provide supporting information about the bandgap of MoS_2, which is related to the layer number. In our work, Raman and PL spectra were recorded using a Jobin-Yvon LabRAM H800 with a 532 nm Nd:YAG laser as the excitation source and the spot size was ~1 μm (Figure 2.5). Spectra at several positions inside the continuous films were collected to check the uniformity of the films.

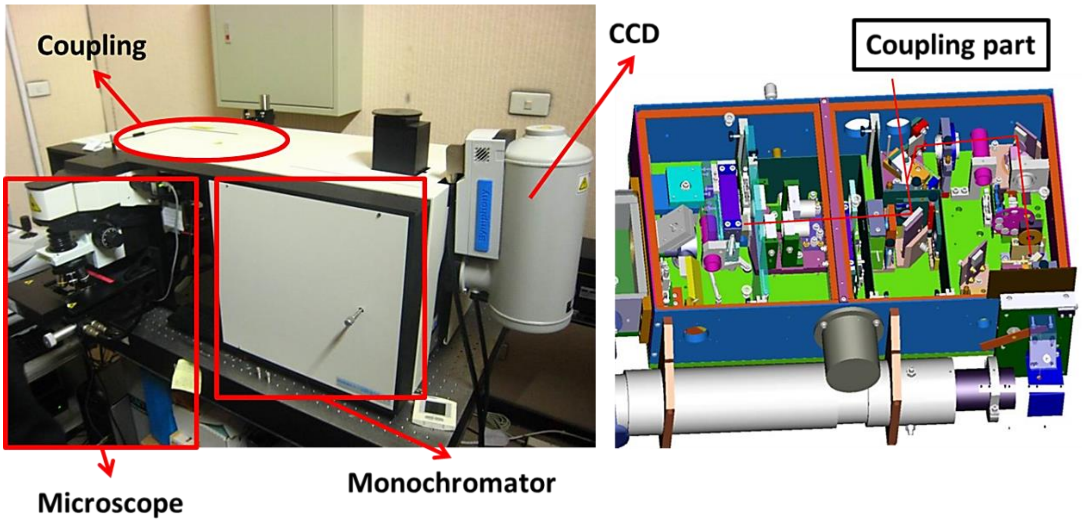

Figure 2.5 Overview of Raman system.

2.3 Interaction of x-ray with matter

X-ray is a sort of electromagnetic radiation with a wavelength smaller than UV radiation, and can be sub-divided into soft x-ray (100 eV ~ 3 kev), which does not penetrate air, and hard x-ray (above 3 keV). If an x-ray hits a solid material, the material starts to emit electrons. This is essentially the photoelectric effect that transfers energy from incident photons to excite electrons. This energy transfer process is not straight forward and has many consecutive effects that bring about versatile spectroscopic techniques (Figure 2.6 (a)). For example, when O-1*s* electrons in an oxide are collided with x-ray photons, the final states of excited photoelectrons will then be determined by the incident photon energy, as illustrated in Figure 2.6(b). If the energy is just sufficient for electron transition to unoccupied states, we may observe an absorption process; while if the energy is greater than the bound energy, photoelectrons will be ejected with a kinetic energy.

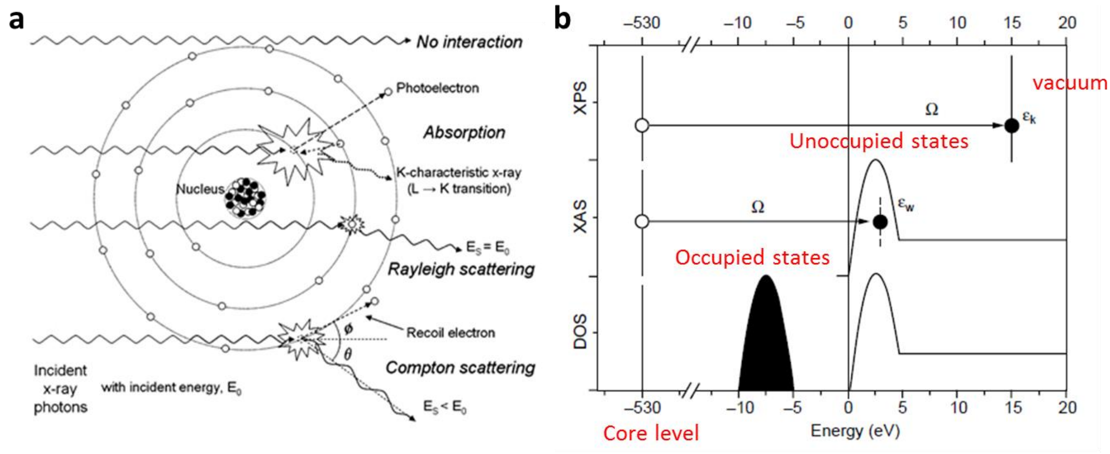

Figure 2.6 (a) Photons interact with inner shell electrons of oxygen atoms; (b) Schematic DOS of an oxide. The oxygen 1*s* electron at energy -530 eV is excited by an x-ray.

2.3.1 X-ray photoelectron spectroscopy (XPS)

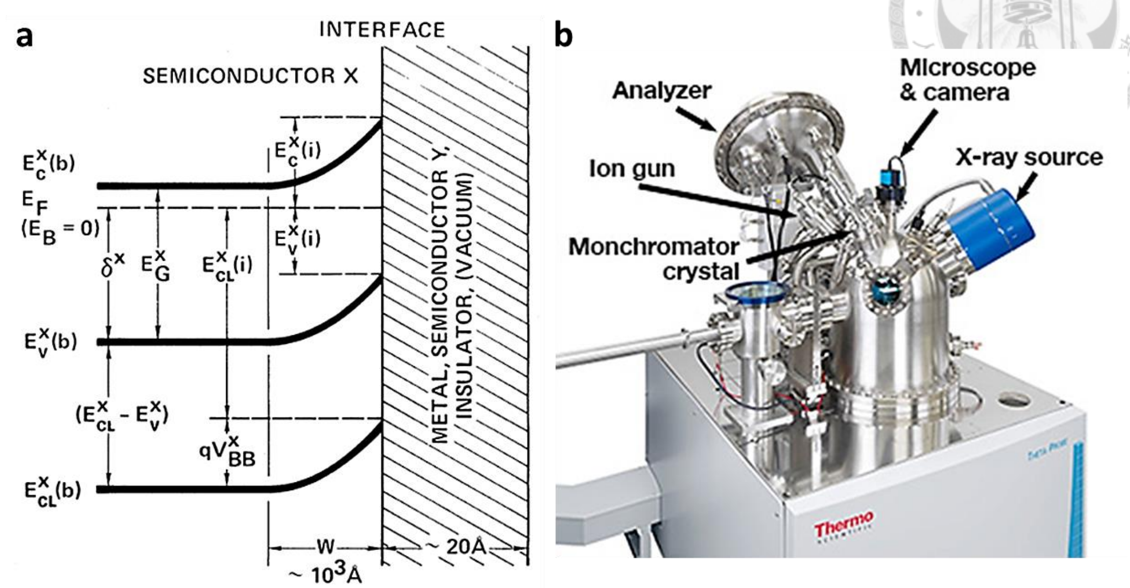

Figure 2.7 (a) Generalized energy-band diagram at an abrupt interface between a semiconductor and vacuum, metal, insulator, or a different semiconductor; (b) Overview of XPS system.

X-ray photoelectron spectroscopy (XPS) is a surface sensitive quantitative spectroscopic technique that analyzes the elemental composition, chemical and electronic states of the elements that exist within a material. According to the energy conservation, the electron binding energy can be calculated from the following equation:

$$E_B = h\nu - E_K - \phi \tag{2.1}$$

where E_B is the electron binding energy of a core level, $h\nu$ the is incident photon energy, $E_K = \hbar^2k^2/2m$ is the kinetic energy of the escaped photoelectron that can be detected by the spectrometer, and ϕ is the work function depending on both the spectrometer and the material. Photo-emitted electrons can undergo inelastic collisions, recombination, exicitation of the sample, recapture of trapping in various excited states within the material, all of which can reduce the number of escaping photoelectrons. Thus, the signal measured by XPS is an exponentially surface-weighted signal, and this fact can be used to estimate the surface band bending of a semiconductor, as illustrated in Figure 2.7(a).

In this work, the surface properties of MoS_2 thin films were characterized right after the CVD process with high-resolution XPS (Thermo Scientific Theta Probe) using Al K_α radiation (1486.6 eV) (Figure 2.7(b)). The spot size we used to probe the sample was fixed at ~400 μm. All XPS peaks were corrected for inelastic scattering by initially subtracting the Shirley background, followed by fitting the peaks with Voigt shape peaks. The peak positions were adjusted carefully with respect to C-1*s* and Au-4*f* core levels. The atomic sensitivity factors used in this work were 3.321 for Mo and 0.666 for S, respectively. Each specimen was measured five different points to confirm the spectra coherency. The deviation of measured binding energy (BE) between each point after calibration was around 0.02~0.04 eV. The spectra of valence band edges were recorded by fine scanning the energy range from -10 to 10 eV.

2.3.2 X-ray absorption spectroscopy (XAS)

The interaction of x-rays with matter is expressed by the Fermi-Golden Rule, which states the transition probability between a system in its initial state and final state by absorbing the incident photon with energy hν.[1]

$$I_{XAS} \sim \left| \langle \Phi_f | H | \Phi_i \rangle \right|^2 \delta(E_f - E_i - h\nu) \qquad (2.2)$$

doi:10.6342/NTU201603487

The initial and final state wave functions are built from an electron part and photon part, which can be regarded as core level and the empty state in the material, respectively. The delta function takes care of the energy conservation, and a transition takes place if the energy of the final state equals the energy of the initial state plus the x-ray energy. X-ray absorption process can be described with the dipole transition, thus the interaction Hamiltonian can be determined by the photon polarization and the electron position $(\hat{\varepsilon} \cdot \vec{r})$.

When x-rays are absorbed by the photoelectric effect, the excited core-hole will relax back to a “ground state” of the core atom. A higher level core electron drops into the core hole, and a fluorescent x-ray or Auger electron is emitted (Figure 2.8(a)).

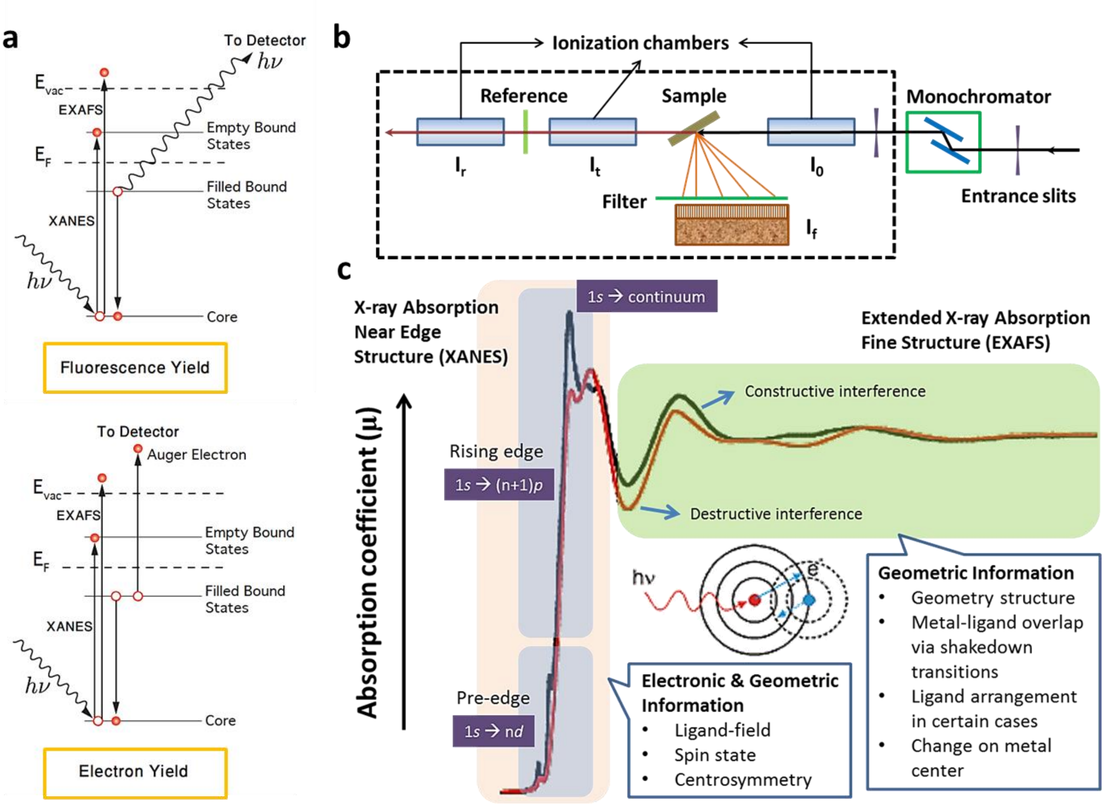

Figure 2.8 (a) Schematic of fluorescence yield and Auger effect for data collection; (b) Schematic of general experimental setup for XAS measurement; (c) Illustrations of three regions of a XAS spectrum.

doi:10.6342/NTU201603487

XAS is a widely used technique for determining the local geometric and electronic structure of matter. The experiment is usually performed with synchrotron radiation sources, which provide intense and tunable x-ray beams for energy scan. The general experimental setup is illustrated in Figure 2.8(b). The spectrum can be collected by transmission, fluorescence mode, or electron yield depending on the sample conditions. Transmission mode directly measures the signals after photons penetrate through the sample. The attenuation of the photon intensity follows the Beer’s law. Fluorescence mode measures the emitting x-ray energy which equals to the difference of the core level. Electron yield records the electron energy that is promoted to the continuum from another core-level. The radiative process of the fluorescence mode can provide more bulk information of the material than the electron yield which is non-radiative and surface sensitive.

A full XAS profile can be divided into three regions, pre-edge, near edge, and extended region, as illustrated in Figure 2.8(c). Each region can provide different information about the material. XANES is relatively sensitive to the electronic and structure symmetry of the core atom. EXAFS is the outcome of the interference between outgoing wave function from the core atom and backscattered wavelets from the surrounding atoms, which can be expressed as follows:[2]

$$\chi(k) \sim \sum_{j} \frac{N_j}{kR_j^2} S_j(k) F_j(k) e^{-\sigma_j^2 k^2} e^{-\frac{2R_j}{\lambda(k)}} \sin[2kR_j + \delta_{ij}(k)] \qquad (2.3)$$

where the scattering amplitude F(k) and phase shift δ(k) are photoelectron scattering properties and depend on atomic number Z of the scattering atom, so the neighboring atom can be determined. If we know F(k) and δ(k), we can also determine the distance R to neighboring atom, coordination number N of neighboring atom, and mean-square disorder σ^2 of neighbor distance.

In this work, Mo *K*-edge and S *K*-edge x-ray absorption spectra (XAS) of CVD-grown MoS_2 were recorded respectively at the Beamline 01C and Beamline 16A of the National Synchrotron Radiation Research Center (NSRRC) in Taiwan. The ring energy of NSRRC was operated at 1.5 GeV with a typical current of 360 mA. The spectra were taken in fluorescence mode with a constant incident angle of photons at 45^o and a Lytle detector for collecting the signals.

2.4 Hydrogen Evolution Reaction (HER)

Hydrogen has the largest energy density that other fuels in the world (like methanol) cannot compete with. When it reacts with oxygen, huge energy can be produced:[3]

$$2H_2(g) + O_2(g) \rightarrow 2H_2O(l) \quad (\Delta H = -286 \text{ kJ/mol}) \qquad (2.4)$$

Obviously, the energy density of hydrogen is E = 286 kJ/mol x 0.5 mol/g = 143 kJ/g. In a fuel cell, hydrogen acts as the anode and splits into protons and electrons under the assistance of catalyst. Protons move from anode towards cathode through a conductive electrolyte, and electrons go through external circuit and meet with protons and oxygen in cathode. The voltage of this cell can be calculated by the Gibbs free energy, $\Delta G = -237.1$ kJ/mol, which gives the voltage applying the Nernst equation $E = -\Delta G/nF = (237.1 \text{ kJ/mol})/(2 \times 96485 \text{ C/mol}) = 1.229$ V. This voltage is reversible, which indicates that 1.23 V is the lowest limit voltage we need to split water into hydrogen and oxygen. However, the voltage is calculated thermodynamically. Kinetically, higher voltage is needed depending on the electrode we use.

doi:10.6342/NTU201603487

For HER with acid electrolyte, hydrogen evolves from the reaction 2H + 2e → $H_2(g)$. The rate of this reaction is determined by the current through the circuit. The relationship between the current and the voltage we apply is known as the current-overpotential equation:[4]

$$i = i_0[\frac{C_O(0,t)}{C_O^*}e^{-\alpha nf\eta} - \frac{C_R(0,t)}{C_R^*}e^{(1-\alpha)nf\eta}] \tag{2.5}$$

where C_O and C_R represent the concentrations of participants, i_0 is the exchange current, α is the asymmetry coefficient, f = F/RT, and η = E - E_{eq} is overpotential. When the overpotential goes too negative, the left term in Eq. (2.5) is much larger than the right one, and the equation can be written as $i = i_0e^{-\alpha nf\eta}$. The current increases exponentially with overpotential, which is named as Tafel behavior. From this behavior, we can extract two important parameters, exchange current i_0 and Tafel slope $1/\alpha nf$ by fitting the linear relationship between log(i) and η. These two parameters are the criterions for the catalytic activity of catalyst. The best catalyst for HER should have the largest exchange current and the smallest Tafel slope. So far, platinum is the champion catalyst for HER which has the exchange current density of $4.5\text{x}10^{-4}$ A/cm^2, and the Tafel slope as small as 30 mV/decade.

However, platinum is very scarce in the earth and extremely expensive. Alternatively, MoS_2 has been estimated to have comparable performance with Pt for HER. The whole process of HER can be divided into two steps: First, the protons from the solution are attached onto the catalytic sites of the electrode. The electrons from the electrode combine with the protons to form hydrogen atoms. Two hydrogen atoms combine together to become a hydrogen molecule. Finally, the molecular hydrogen desorbs from the electrode. One of the two steps may be the rate determine step. For Pt,

doi:10.6342/NTU201603487

the rate determine step is the desorption step because the Gibbs free energy is uphill, while the rate determine step for MoS_2 is the absorption step. When the free energy approaches to zero, the catalyst becomes very active due to the rate determine step is also very fast.

In this work, the MoS_2 for electrochemical studies was grown on the 1 x 1.5 cm graphene paper (GP, AzTrong) with thickness control. HER was carried out in the 0.1 M $HClO_4$ solution by a three-electrode system with Ag/AgCl as the reference electrode and a graphite rod as the counter electrode. Linear sweep voltammetry with scan rate of 2 mV/s, and AC impedance spectroscopy with 0.1 to 100k Hz and amplitude of 10 mV were recorded by a Zahner Zennium workstation.

2.5 Resistive Switching Behavior

Resistance switching memory cells can be described as so-called memristors, which have been predicted by Leon Chua as the fourth basic circuit element because of the conceptional symmetry with the resistor, capacitor, and inductor, later extended to memristive devices (Figure 2.9).[5, 6] He described a generailized flux as time integral of voltage V(t) and relates this to the charge q as time intergral of current I(t). If the resistance representing the ratio V/I depends on the charge q(t) passed through the device, it becomes a memristance M(q(t)) according to

$$V(t) = M(q(t))/t \tag{2.6}$$

In this case, the memresistance shows hysteretic behavior with can be exploited as non-volatile resistance switching memory cell.

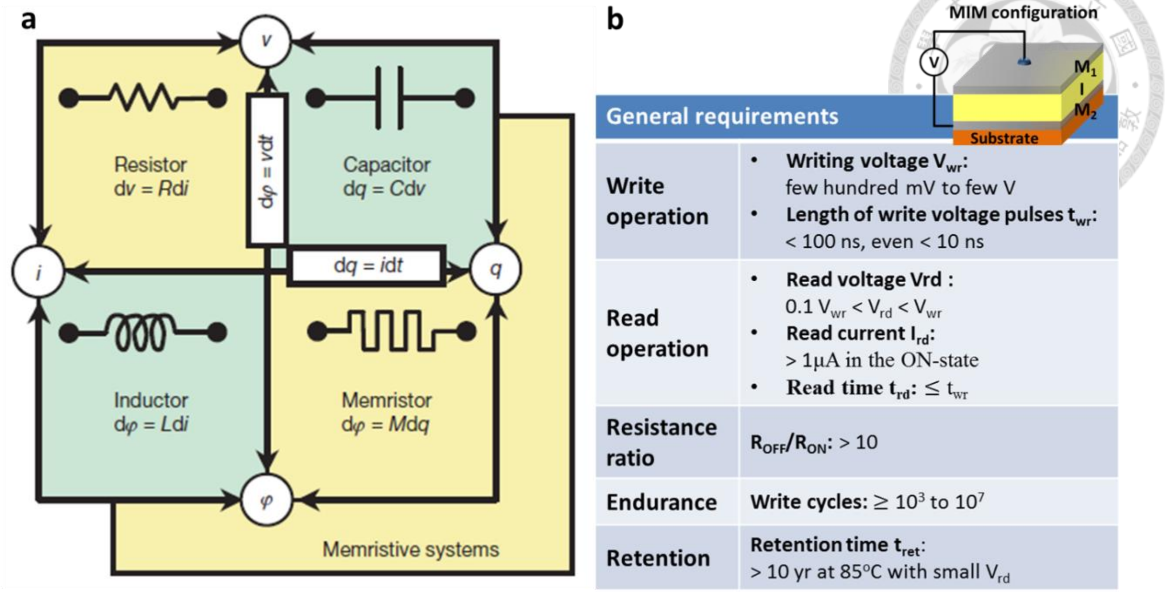

General requirements	
Write operation	• **Writing voltage V_{wr}:** few hundred mV to few V • **Length of write voltage pulses t_{wr}:** < 100 ns, even < 10 ns
Read operation	• **Read voltage Vrd :** $0.1 V_{wr} < V_{rd} < V_{wr}$ • **Read current I_{rd}:** > 1μA in the ON-state • **Read time t_{rd}:** $\leq t_{wr}$
Resistance ratio	**R_{OFF}/R_{ON}:** > 10
Endurance	**Write cycles:** $\geq 10^3$ to 10^7
Retention	**Retention time t_{ret}:** > 10 yr at 85°C with small V_{rd}

Figure 2.9 (a) The four fundamental two-terminal circuit elements: resistor, capacitor, inductor, and memristor; (b) MIM structure and general requirements of RRAM.

A non-volatile memory based on electrically switchable resistance has been named as resistance (switching) random access memory (RRAM or ReRAM). A resistive switching memory cell in a RRAM is generally built by a capacitor-like MIM structure, composed of an insulating or resistive material (I) sandwiched between two electron conductors (M). These MIM cells can be electrically switched between at least two different resistance states, after an initial electroforming cycle which is usually required to activate the switching property. To compete with the current commercial memories and satisfy the future technological progress, a number of requirements for RRAM shall be made, as illustrated in Figure 2.9(b).[7]

2.5.1 Working Principles

When applying an electric field to a resistive switching cell, there are two general schemes to switch the device resistance, as illustrated in Figure 2.10(a).[7]

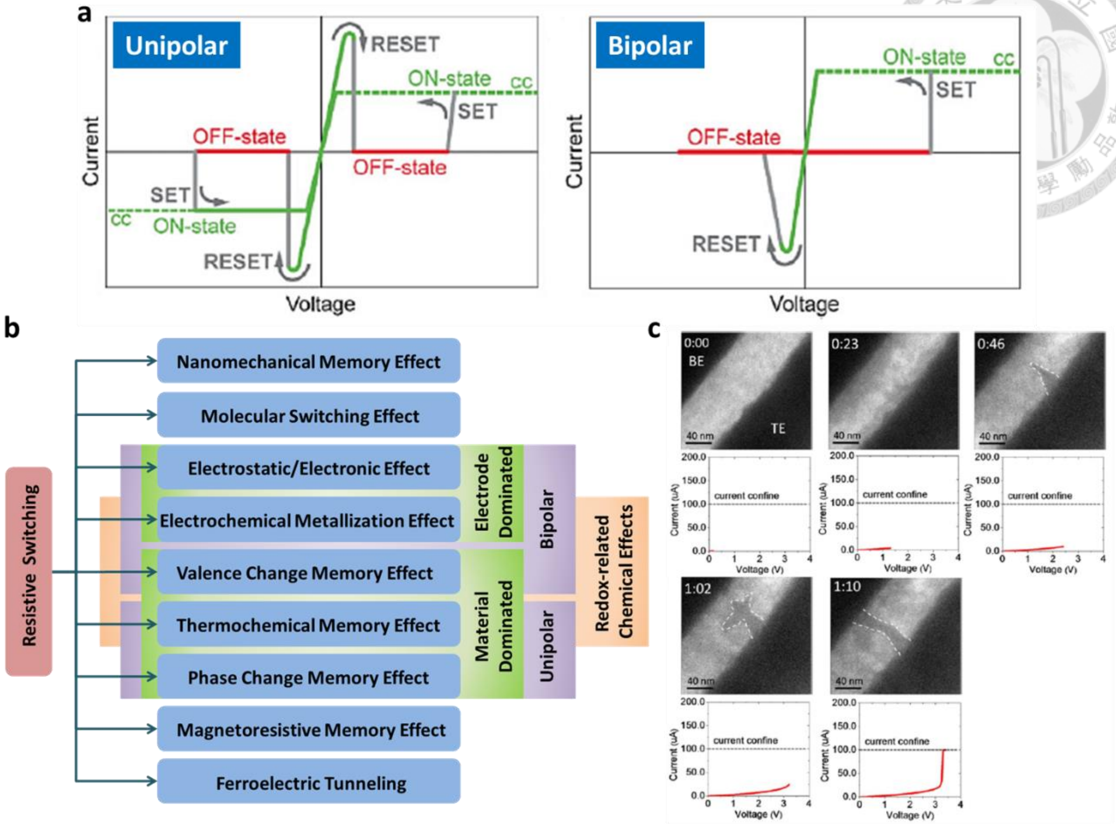

Figure 2.10 (a) Two basic operation schemes of resistance switching memory cells. cc denotes the compliance current; (b) Classification of the resistive switching effects which are considered for non-volatile memory applications; (c) A series of in-situ TEM images and the corresponding I-V measurements illustrate the formation of conducting filament in ZnO at SET process.

When the switching procedure is independent on the electrical polarity of the writing voltage, the operation is called unipolar. During the switching process, the SET voltage is always higher than the RESET voltage, and the RESET current is always higher than the compliance current of the control circuit. The switching operation is called bipolar when the SET to and ON-state occurs on one polarity of the voltage or current and the RESET operation requires the opposite polarity. In some systems, no current compliance is used. The MIM system needs to have some asymmetry, such as different electrode materials M, or a dedicated voltage polarity during the initial electroforming step, in order to show bipolar switching behavior.

A large variety of physical phenomena can lead to non-volatile resistive switching memory effect, as illustrated in Figure 2.10(b). The actual physical driving force of the resistance switching, though electrically induced in all case, is quite different. Here, we are more interesting in thermal, electrical, or ion-migration-induced switching mechanisms because they are more related to our research. The ion-migration effects are coupled to redox processes which cause the change in resistance. They are subdivided into cation-migration cells, based on the electrochemical growth and dissolution of metallic filaments, and anion-migration cells, typically realized with transition metal oxides as the insulator, in which electronically conducting paths of sub-oxides are formed and removed by local redox process.[8] Therefore, this resistance switching mechanism involves not only electrical carrier transport, but also ionic migration that varies local chemical composition. The most prominent characteristic in this mechanism is the formation and rapture of the conducting filament during the switching process, which has been directly observed in Pt/ZnO/Pt by the in-situ TEM technique (Figure 2.10(c)).[9]

2.5.2 Transport mechanism

An electrical bias generates two main effects in a switching material: an electric field and Joule heating, which is given by high current densities (> 10^6 A/cm^2). Electric field and Joule heating generally coexist in all memristive switching, though their relative importance varies depending on the device stacking, materials, electrical operation history and so on. This leads to four main classes of switching commonly observed in oxide-based switches, as shown in Figure 2.11(a) to Figure 2.11(d).[10]

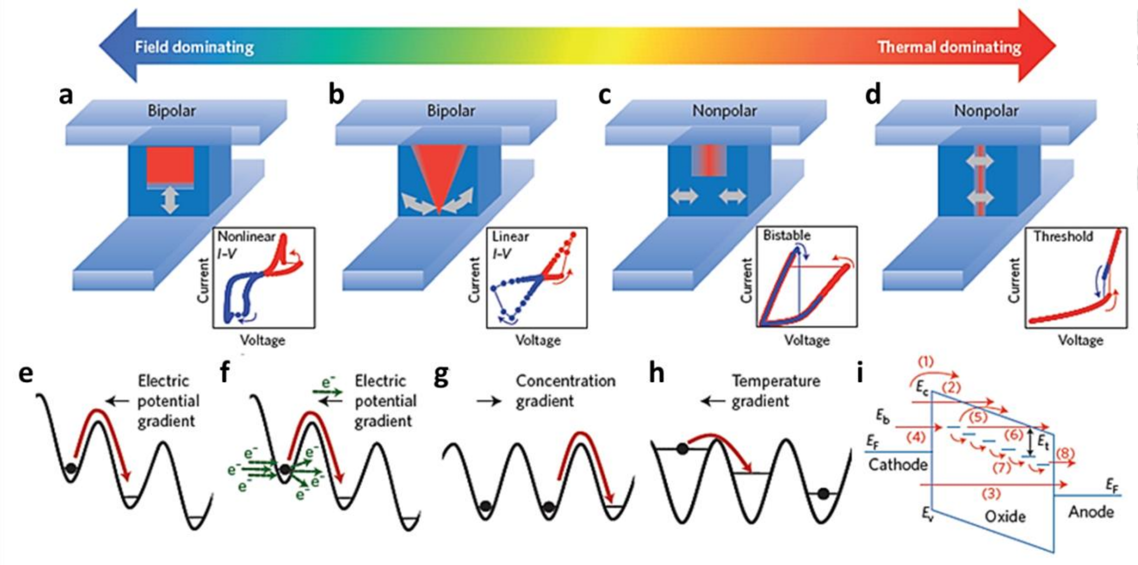

Figure 2.11 The driving forces, electrical characteristics, transport mechanisms of ions and electrons for the switching of anion-based device. (a)-(d) Simplified schematics of conduction channels (red) in switching matrix materials (blue) in four typical switching devices, where both electric field and Joule heating drive the switching. The grey arrows indicate the idealized ionic motion: (a) bipolar nonlinear switching, (b) bipolar linear switching, (c) unipolar non-volatile switching, and (d) unipolar threshold switching; (e)-(h) Schematic illustration of the factors that influence oxygen anion motion for drift: (e) electric potential gradient, (f) electromigration (electron kinetic energy), (g) Fick's diffusion (concentration gradient), and (h) thermophoresis (temperature gradient); (i) Schematic of the possible electron transport paths in the devices: (1) Schottky emission, (2) Fowler-Nordheim tunneling, (3) Direct tunneling, (4) tunneling from cathode to traps, (5) emission from traps to the conduction band (Frenkel-Poole emission), (6) tunneling from trap to conduction band, (7) trap-to-trap hopping or tunneling, ranging from Mott hopping between localized states to metallic conduction through extended states, and (8) tunneling from traps to anode. E_F, Fermi level; E_V, valence band; E_C, conduction band; E_b, Schottky barrier height; E_t, trap barrier height.

In all cases there are four main driving forces that work independently or together to influence atomic motion or rearrangement (Figure 2.11(e) to Figure 2.11(h)). Both electric field and electron kinetic energy are polarity dependent and can cause bipolar switching. Joule heating is more complicated and not fully understood yet. High temperatures induced from Joule heating significantly enhance drift and diffusion, and may also generate a high temperature gradient laterally. Drift and electromigration move dopants vertically along conducting channel, while the temperature gradient might contribute dopants diffusion in both vertical and lateral ways. The less polarity effect from Joule heating may induce unipolar switching, which is less stable in retention than the bipolar switching dominated by electric field.

2.5.3 Key challenges

The key challenges in a RRAM arise from the matrix material itself or the device performance. To form a resistance switching system, both conductive and insulating phases are required. Reliable switching requires these two phases do not react with each other chemically or form a new phase, even at the high temperatures induced by Joule heating, which is essentially unavoidable in the devices. This would require a simple material system, whose phase diagram is like the illustration in Figure 2.12(a).[10] Thermodynamically stable conductive and insulating phases with temperatures may give rise to stable switching performance.

Device variability (or reproducibility) and integrated device design are the two major obstacles that need to be overcome for RRAM development. Selecting a proper material can lead to a stable channel-materix system and thus reduce the variations in switching from cycle to cycle in a device. However, the variance from device to device stems mainly from the random formation of conducting filaments and their various

doi:10.6342/NTU201603487

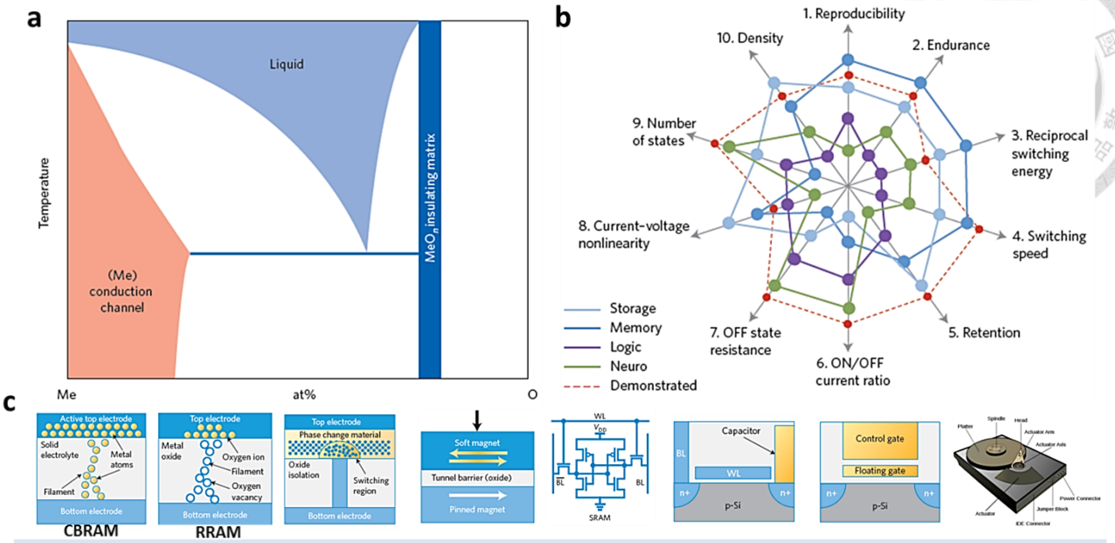

	Memristor	PCM	STTRAM	SRAM	DRAM	Flash (NAND)	HDD
		Prototypes		Commercialized technologies			
Reciprocal density (F^2)	<4	4-16	20-60	140	6-12	1-4†	2/3
Energy per bit (pJ)	0.1-3	2-25	0.1-2.5	0.0005	0.005	0.00002	1-10 × 10^9
Read time (ns)	<10	10-50	10-35	0.1-0.3	10	100,000	5-8 × 10^6
Write time (ns)	-10	50-500	10-90	0.1-0.3	10	100,000	5-8 × 10^6
Retention	years	years	years	As long as voltage applied	<<second	years	years
Endurance (cycles)	10^{12}	10^9	10^{15}	>10^{16}	>10^{16}	10^4	10^4

*The energy to operate NAND Flash is typically hundreds of picojoules per bit primarily because accessing the memory cells requires charging word and bit lines to high voltages. †Smaller number represents an effective area for multi-level cells. PCM, phase-change memory; STTRAM, spin torque transfer random access memory; SRAM, static RAM; DRAM, dynamic RAM; HDD, hard disk drive.

Figure 2.12 (a) Simplified schematic phase diagram of a metal-oxide (Me-O) system with only two solid-state phases at low temperature; (b) Device performance requirements for representative applications; (c) Schematic of devices and corresponding comparison of memory and storage technologies.

structures in different devices. Engineering control probably is the solution to reduce this variance. On the other hand, using a transistor as the select device at each crosspoint in a crossbar array limits the footpoint of each cell and its 3D stacking capability and would thus not realize the potential scalability of memristive devices. New circuit and system designs may be required for solving this problem. Memristive devices combining all the desired properties would be beneficial for many prospective applications as illustrated in Figure 2.12(b).[10] Compared with other types of memories, memristor has exhibited better or compatible performances (Figure

doi:10.6342/NTU201603487

2.12(c)).[10, 11] Once these drawbacks are overcome, it will soon replace all the other commercial memories.

In our work, the resistive switching behavior of the Pt/ZnO/MoS_2/Mo heterojunction device is studied by doing the current-voltage (I-V) sweeping measurement. Keithley 2400 is used as voltage source and current probe. All the measurements are done at room temperature in air ambient. Temperature-dependent I-V was also performed for MS5 device at the range of 80 K to 400 K.

2.6 Other characterizations

UV−visible absorption spectrometry was adopted by using a JASCO 670 spectrometer. Atomic force microscopy (AFM) images with height profiles were carried out by a Veeco Dimension-Icon system with the scan rate of 1 Hz and 1024 scanning lines to examine the thickness of MoO_3 precursors and the corresponding MoS_2 films. To observe the surface topographies of MoS_2 thin films, the tapping-mode AFM images were collected by a JPK NanoWizard II. The conductivities of MoS_2 films were calculated by van der Pauw method where Keithley 4200 was used to perform the I-V curves. High resolution cross-sectional image of grown MoS_2 thin film was performed by the field emission transmission electron microscope (FETEM, JEOL JEM-2100) to confirm the layer number of MoS_2. The specimens for TEM were prepared by focused-ion-beam (FIB) cutting with 50 nm BCP as a protection layer. TEM-EDX mapping with Quantmap adjustment and x-ray diffraction (XRD, Bruker D8) patterns were analyzed to identify the composition and structure of MoS_2 films. Top-view and cross-section images of oxidized MG and sulfurized specimens were performed by the field-emission scanning electron microscope (FESEM, JEOL 6700).

doi:10.6342/NTU201603487

References

[1] F. d. Groot and A. Kotani, *Core Level Spectroscopy of Solids*. (CRC Press, 2008).

[2] G. Bunker, *Introduction to XAFS*. (Cambridge University Press, 2010).

[3] H. Wang, *Hydrogen Evolution Reaction*. (Stanford University, 2012).

[4] A. J. Bard and L. R. Faulkner, *Electrochemical methods : fundamentals and applications*. (Wiley, New York, 2001).

[5] L. O. Chua, IEEE Trans. Circuit Theory **18** (5), 507-519 (1971).

[6] D. B. Strukov, G. S. Snider, D. R. Stewart and R. S. Williams, Nature **453** (7191), 80-83 (2008).

[7] R. Waser, R. Dittmann, G. Staikov and K. Szot, Adv. Mater. **21** (25-26), 2632-2663 (2009).

[8] R. Waser and M. Aono, Nat. Mater. **6**, 833-840 (2007).

[9] J. Y. Chen, C. L. Hsin, C. W. Huang, C. H. Chiu, Y. T. Huang, S. J. Lin, W. W. Wu and L. J. Chen, Nano Lett. **13** (8), 3671-3677 (2013).

[10] J. J. Yang, D. B. Strukov and D. R. Stewart, Nat. Nanotechnol. **8** (1), 13-24 (2013).

[11] H. S. Wong and S. Salahuddin, Nat. Nanotechnol. **10** (3), 191-194 (2015).

doi:10.6342/NTU201603487

Chapter 3 Thickness-Dependent Surface Properties

In this chapter, the surface properties of CVD-grown MoS_2 are studied. The defects in MoS_2 seem to affect the surface properties intensively, especially when the thickness of MoS_2 reduces, because the properties transit from bulk to surface dominant.

3.1 Preparation of MoS_2 from MoO_3

3.1.1 Optimize the sulfurization conditions

A schematic illustration for the preparation of MoS_2 thin films with different thicknesses is shown in Figure 3.1(a). In order to optimize the sulfurization conditions, samples of 10 nm MoO_3 layer were annealed in 10% H_2S/Ar mixture at various temperatures and time. Figure 3.1(b) shows the Raman spectra of samples sulfurized at temperatures ranging from 500°C to 1000°C. Two characteristic peaks at around 382 cm^{-1} and 407 cm^{-1} correspond to the E_{2g}^1 and A_{1g} vibrational modes, respectively. Obviously, the peak intensity enhances with annealing temperature; the peak width reduces instead. This indicates the improvement of the crystal quality and the grain growth of the MoS_2 particles at high temperature.

In addition, the peak ratio of A_{1g} to E_{2g}^1 decreases dramatically from 2.3 to 1.4 when the annealing temperature reaches 1000°C as shown in the inset figure of Figure 3.1(b). A_{1g} and E_{2g}^1 modes result from the atom displacements that are orthogonal to one another. The out-of-plane A_{1g} mode illustrates the symmetric vibration of S atoms along the *c*-axis, and the in-plane E_{2g}^1 mode illustrates the opposite vibration of two S atoms with respect to the Mo atom.[1] Q. Li *et al*. suggested that the peak ratio of A_{1g} to E_{2g}^1 may provide an indication for the degree of structural coherence along the *c*-axis

doi:10.6342/NTU201603487

direction in MoS_2 nanomaterials.[2] They also observed that the morphology of MoS_2 varied from agglomerated nanoparticles to ribbon-like flakes when the sulfurization temperature was above 800°C. This implies that the decrease of the intensity ratio, in our case, can be correlated to the morphology transformation due to the anisotropic growth rate of MoS_2 grains and the atomic rearrangement, similar to Q. Li's work, which affects the atom displacements especially along the in-plane direction.

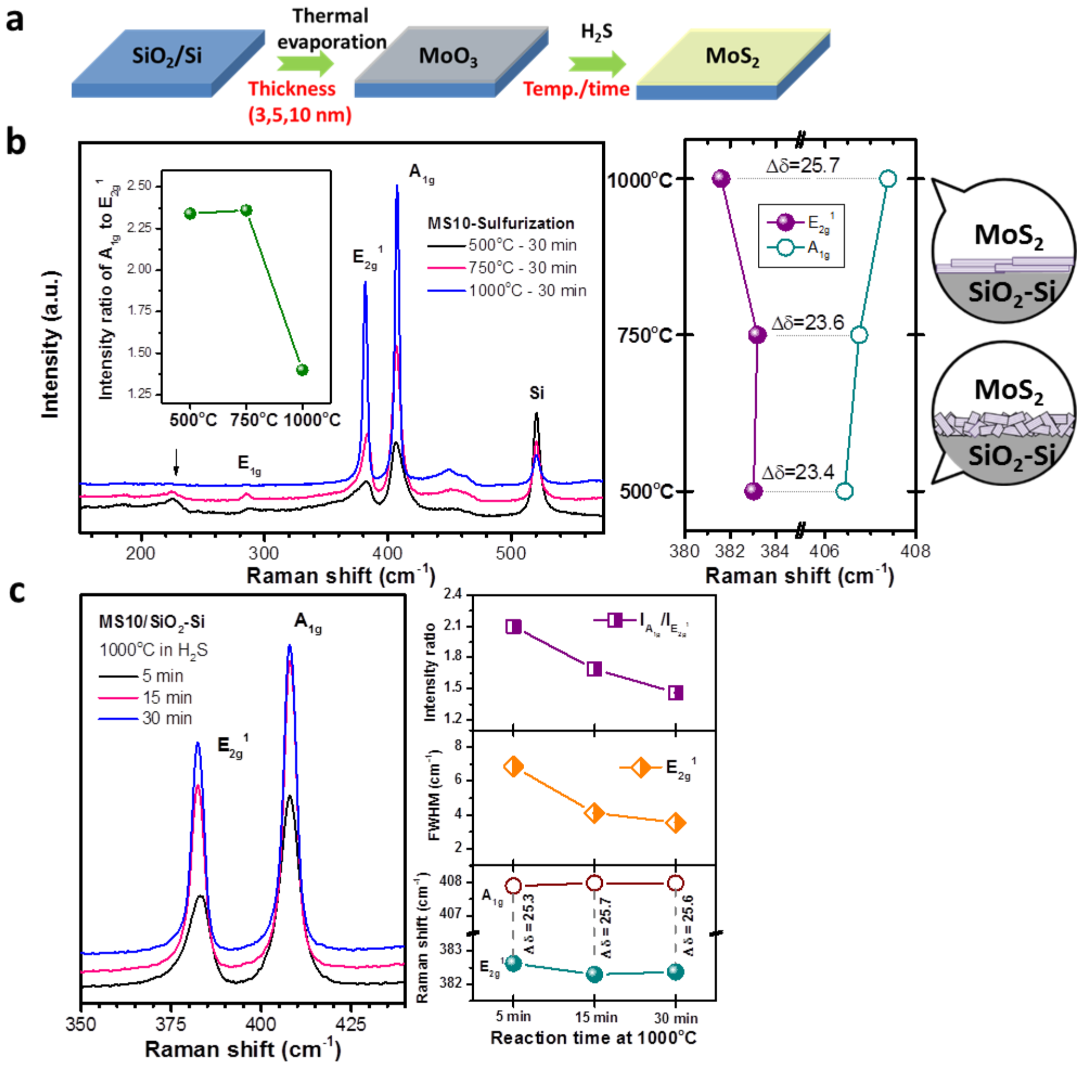

Figure 3.1 (a) A schematic diagram demonstrates the two-step process to produce the MoS_2 thin film with various thicknesses; (b) The Raman spectra of MoS_2 thin film grown at various sulfurization temperatures; (c) The Raman spectra of MoS_2 thin film grown at various sulfurization time.

doi:10.6342/NTU201603487

The Raman frequencies of A_{1g} and E_{2g}^1 peaks have been demonstrated to vary with the layer number of MoS_2.[3] In Figure 3.1(b), the frequency difference remains almost the same at 23.5 cm^{-1} as the temperature increases from 500^{o}C to 750^{o}C which corresponds to 4-5 layers of MoS_2. On the other hand, the frequency difference increases to 25.7 cm^{-1} at 1000^{o}C which is beyond 6 layers of MoS_2. The explicit increase in frequency difference at high temperature could be attributed to the grain growth of MoS_2 and the variation of the stacking orientation. This also implies the morphology of MoS_2 will change as the annealing temperature increases.

Except for the A_{1g} and E_{2g}^1, we also found E_{1g} mode at 285 cm^{-1}, and an unknown peak at 226 cm^{-1} at low temperature. It is worth to note that E_{1g} is forbidden for backscattering experiments on a basal plane,[4] which is just the major orientation that MoS_2 grows at high temperature. The disappearance of these two peaks at high temperature further indicates the morphology change and the improvement of the structure inhomogeneity in our MoS_2 thin film. Therefore, we believe that 1000^{o}C is a suitable temperature for our following material preparation.

Figure 3.1(c) shows the Raman spectra of 10 nm MoO_3 samples annealed at 1000^{o}C for various time. When the annealing time increases from 5 to 30 min, both the intensity ratio of A_{1g} to E_{2g}^1 and the peak width of E_{2g}^1 decrease, and they tend to reach a stable value after 30 min. On the other hand, the frequency difference between A_{1g} and E_{2g}^1 increases a little bit from 5 min to 15 min, but remains at 25.6 cm^{-1} after 15 min. These results demonstrate that prolonging the sulfurization time does not affect the thickness of MoS_2 much compared to the temperature effect, but it improves the crystal quality and the stacking orientation. Based on the Raman results of MoS_2 prepared at various temperature and time, we, thus, regard the best sulfurization condition as 1000^{o}C for 30min.

doi:10.6342/NTU201603487

3.1.2 Quantum confinement effects

After finding the optimized conditions for sulfurization, MoS_2 of various film thicknesses were prepared. For simplicity, MoS_2 samples are named as MS3, MS5, MS10, and MS20 corresponding to the original oxide layer of 3, 5, 10, and 20 nm, respectively. Figure 3.2 shows Raman spectra of the MoS_2 thin films prepared by sulfurization of MoO_3 with various thicknesses at 1000°C for 30 min. Intense E_{2g}^{1} at 382 cm^{-1} and A_{1g} at 407 cm^{-1} are observed. After normalization to the intensity of Si signal, the peak intensities of A_{1g} and E_{2g}^{1} increase from MS3 to MS20, merely reflecting the increase in the thickness of MoS_2.

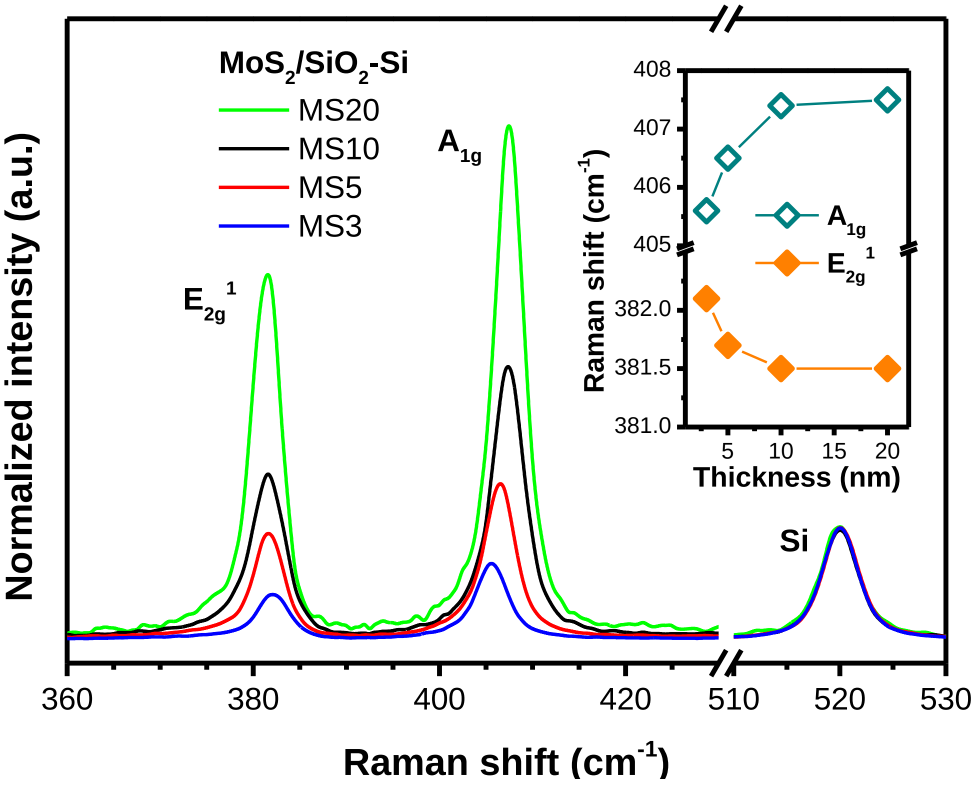

Figure 3.2 Raman spectra of MoS_2 with various film thicknesses. The inset figure illustrates the frequency evolutions of A_{1g} and E_{2g}^{1} modes with deposited MoO_3 thickness.

The Raman frequencies of A_{1g} and E_{2g}^1 peaks have been demonstrated to vary with the layer number of MoS_2 in the opposite way mainly due to the changes in the interlayer coupling.[3, 5] The frequency differences between A_{1g} and E_{2g}^1 from MS3 to MS10 are 23.5, 24.8, and 25.8 cm^{-1}, respectively, which correspond to around 3, 5, and 10 layers of MoS_2.[3, 6] On the other hand, MS20 does not show obvious peak shift compared to MS10, which indicates that MS10 has already possessed bulk properties of MoS_2. Thicker MoS_2 might show similar behaviors with MS10.

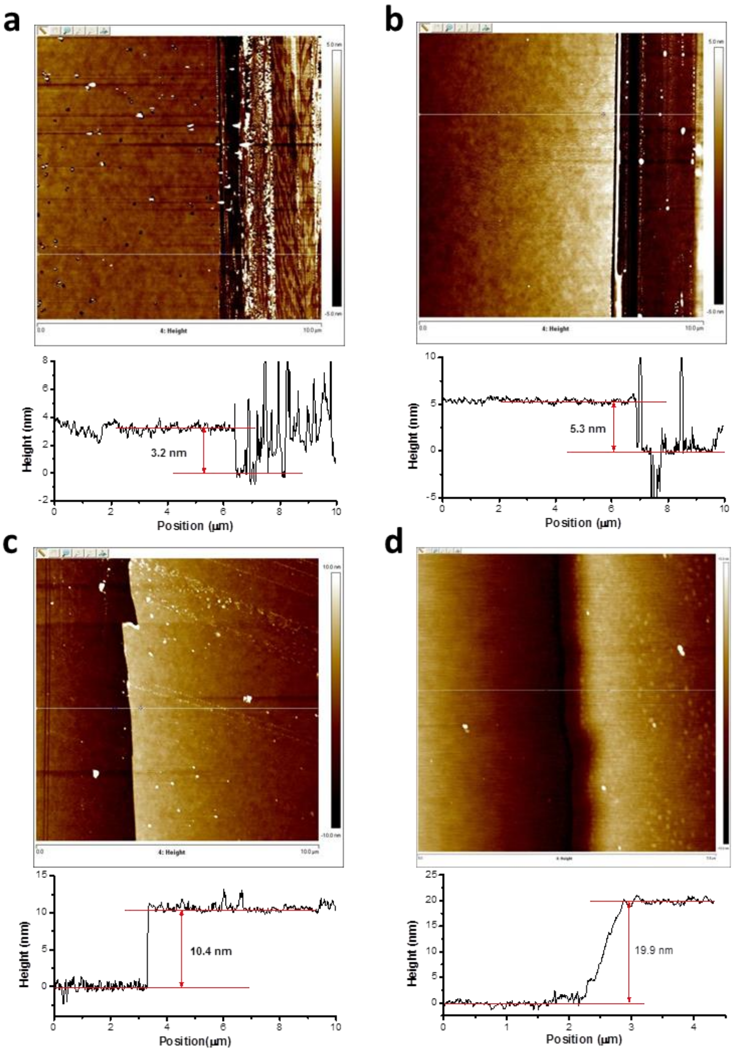

Figure 3.3 AFM images and height profiles of MoO_3 thin films with various thicknesses: (a) 3 nm, (b) 5 nm, (c) 10 nm, and (d) 20 nm. The oxide layer was deposited on the SiO_2-Si substrate with thickness control by the thermal evaporation.

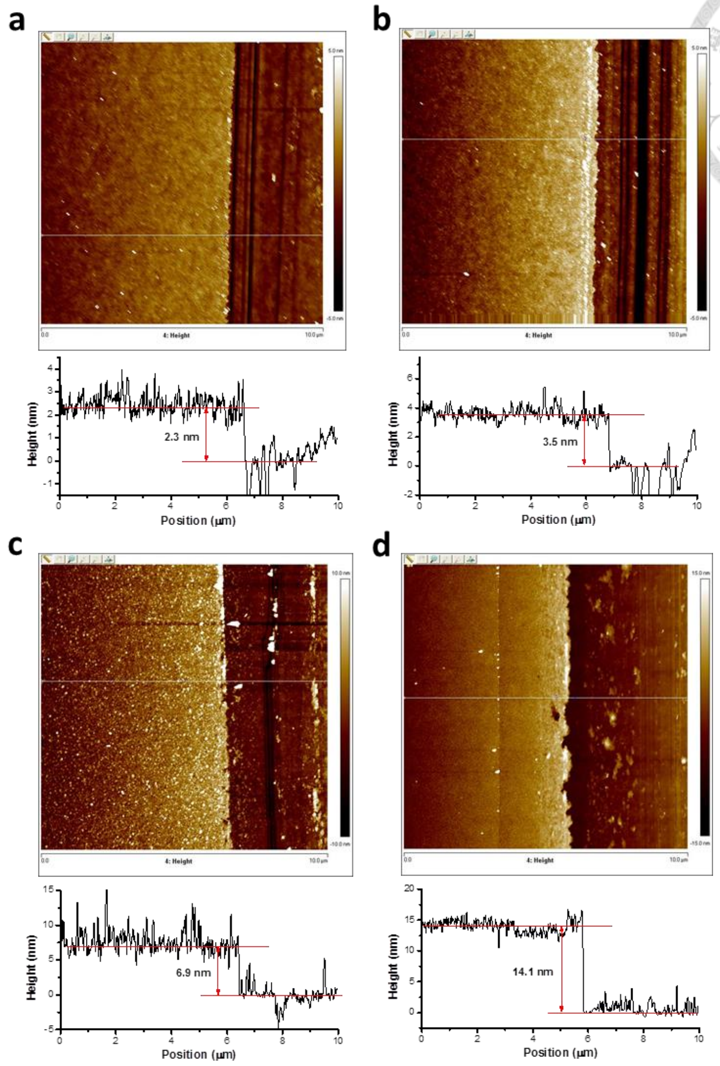

Figure 3.4 AFM images and height profiles of MoS_2 thin films with various thicknesses: (a) MS3, (b) MS5, (c) MS10, and (d) MS20.

AFM images with height profiles were analyzed to confirm the film thickness before and after the MoS_2 formation, as illustrated in Figure 3.3 and Figure 3.4. The oxide thickness is as our expectation ranging from 3 to 20 nm and is homogeneous on the SiO2-Si substrate. After sulfurization, the thickness of formed MoS2 reduces by around 30% compared to its oxide precursor; specifically, the resultant film thickness is 2.3, 3.5, 6.9, and 14.1 nm for MS3, MS5, MS10, and MS20, respectively, corresponding to around 3, 5, 10, and 20 layers of MoS_2.

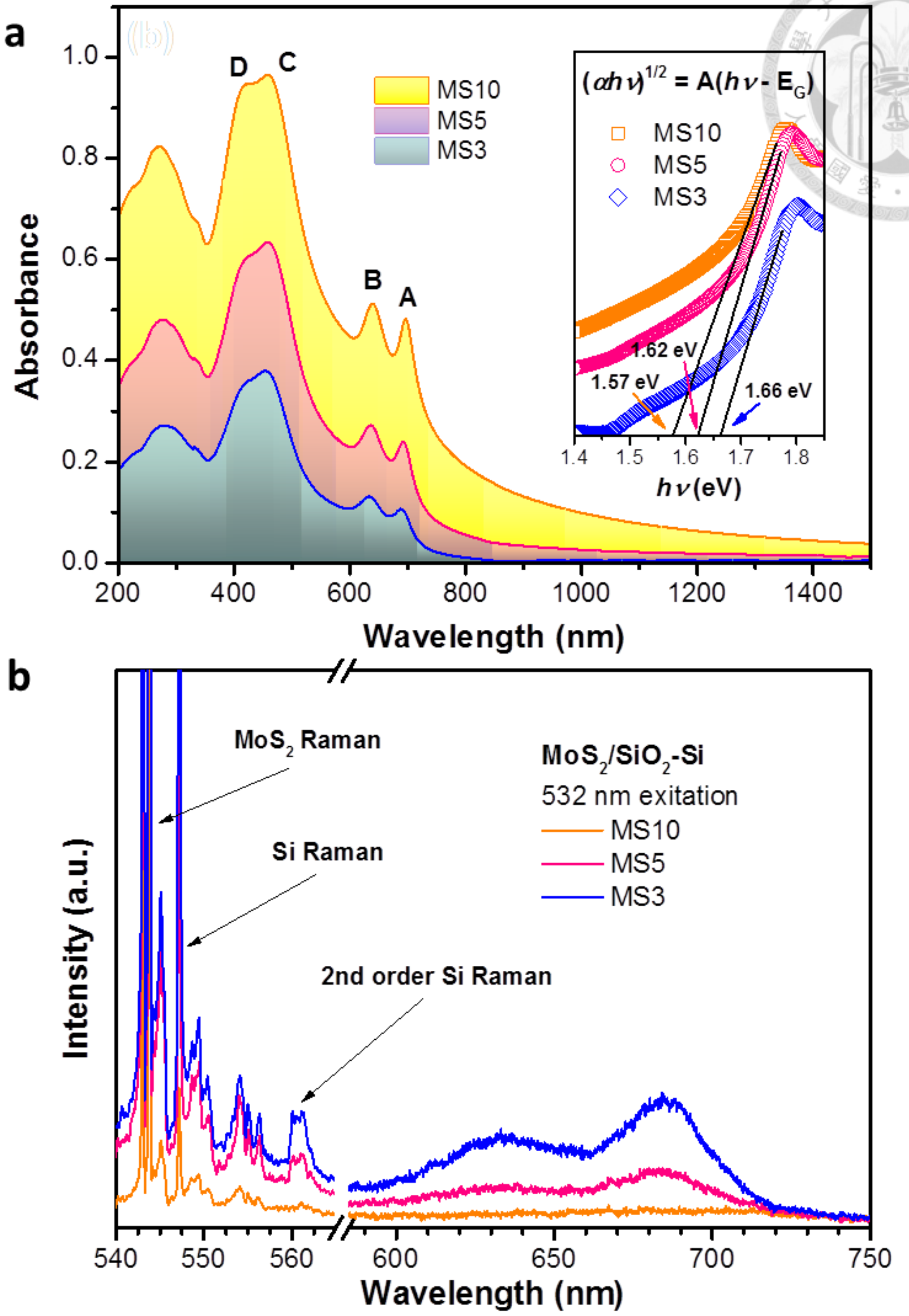

Figure 3.5 (a) Absorption spectra of MoS_2 with various film thicknesses. The inset figure illustrates the transformed tauc plot. (b) Photoluminescence spectra of MoS_2 thin films with various thicknesses.

In order to estimate the band gaps of prepared MoS_2 thin films, the absorption spectra were measured, as shown in Figure 3.5(a). The prominent A/B peaks (1.7 to 2.0

eV) are the spin-orbit-split pair arising from the band edge exitonic transitions at the Brillouin zone K point. The broad C/D peaks are interband transitions from the occupied d_{z2} orbital to unoccupied dxz, d_{yz}, d_{xy}, and d_{x2-y2} orbitals.[7, 8] As illustrated in Figure 3.5(a), the A/B peaks show a slight blue shift from MS10 to MS3, which can be attributed to the quantum confinement effect.[9] We estimated the optical band gap by the tauc plot with the indirect allowed transition for the few-layered MoS_2, as shown in the inset of Figure 3.5(a). The increase of the optical band gaps from 1.57 eV to 1.66 eV is apparent with the reduction of the film thickness from MS10 to MS3. PL spectra in Figure 3.5(b) exhibit similar results as the absorption spectra but different behaviors. Two distinct emission peaks are observed in MS3 and can be attributed to the direct exitonic transition corresponding to A/B pair in absorption spectra. The emission intensity dramatically diminishes and disappears in MS10, which is attributed to the direct to indirect transition of the bandgap energy. For ultrathin MoS_2 layers where local field effects are relative small, the Raman/Absorption and PL intensities show opposite layer dependence. The intensity evolution in PL also indicates MS3 has higher luminescence quantum efficiency than thicker MoS_2 films.[10]

3.1.3 Layer number, structure, and oxide-residual identification

To determine the layer number precisely, we performed the HRTEM and collected the cross-sectional images of our MoS_2 films. Figure 3.6(a) illustrates the photographs of the MoO_3 thin films with various thicknesses and the corresponding MoS_2 films after sulfurization. Our two-step process has successfully achieved large-area and homogeneous growth of MoS_2 film with good thickness control. Figure 3.6(b), 3.6(d), and 3.6(f) illustrate the cross-sectional TEM images of FIB-cutting MS10, MS5 and MS3 specimens, respectively, where it elucidates that our MoS_2 films are continuous and flat rather than discrete random-orientated particles. The corresponding HRTEM images of higher magnification, Figure 3.6(c), 3.6(e), and 3.6(g), clearly show that the layer number of MoS_2 for MS10, MS5, and MS3 is around 10, 5, and 3, respectively, which is consistent with the AFM and Raman results.

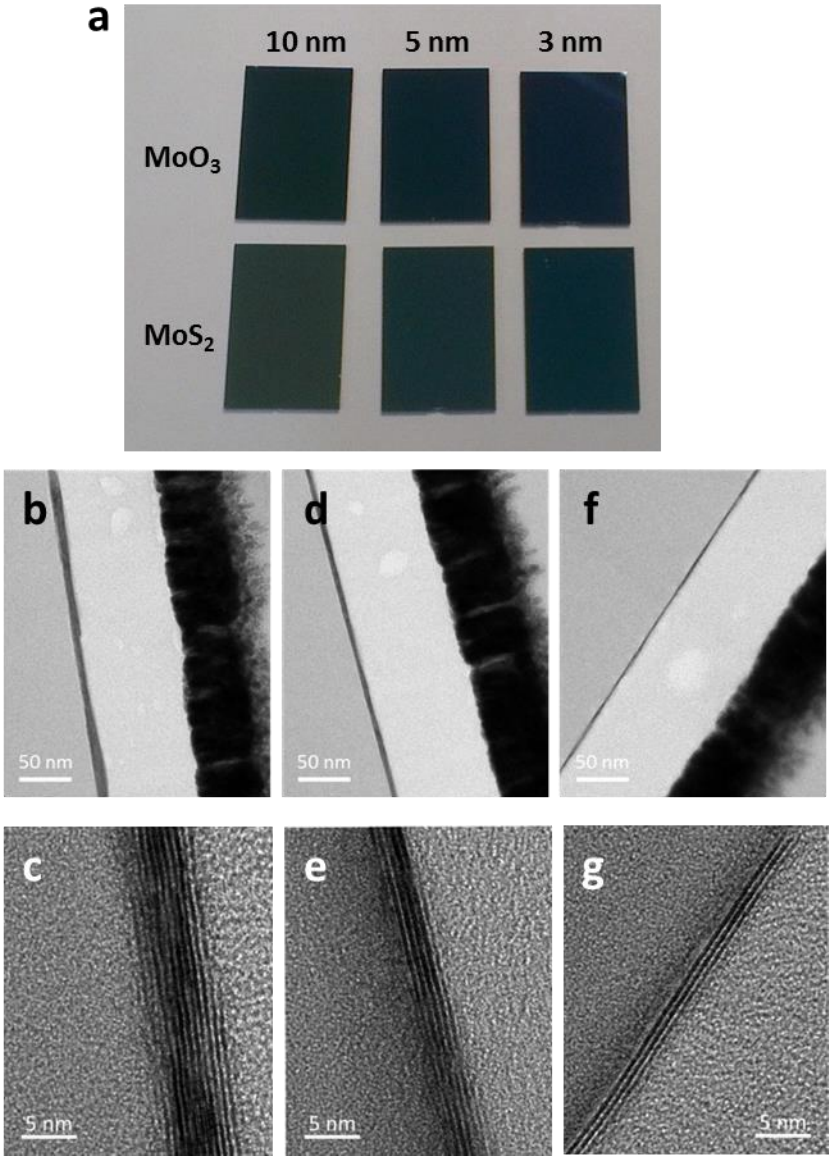

Figure 3.6 a) Photographs of the as-deposited MoO_3 films on 1 x 1.5 cm SiO_2-Si substrates, and the corresponding MoS_2 films after the oxides were sulfurized. The oxide thickness was controlled as 3 to 10 nm. Cross-sectional HRTEM images of MoS_2 films with thickness of (b), (c) MS10; (d), (e) MS5; and (f), (g) MS3.

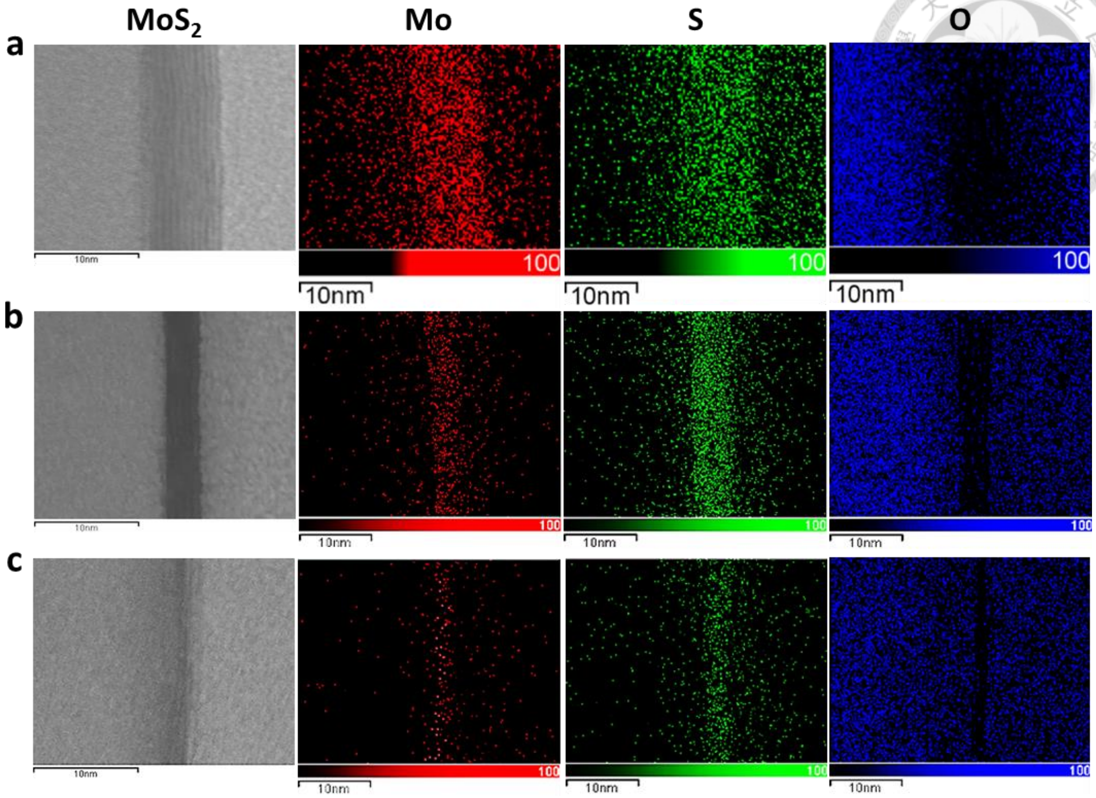

Figure 3.7 TEM-EDX mapping images of (a) MS10, (b) MS5, and (c) MS3. Red, green, and blue colors refer to the Mo, S, and O elements, respectively. The EDX images were adjusted by the Quantmap.

TEM-EDX mapping was performed to identify the existence of the oxygen impurities, as illustrated in Figure 3.7. Obviously, the oxygen signals dramatically decrease in the MoS_2 layers regardless the film thickness. This indicates the sulfurization process can turn MoO_3 into MoS_2 completely. The structures of our MoS_2 films were analyzed by XRD, as shown in Figure 3.8. Compared with the standard powder diffraction profile (ICDD:37-1492), our MoS_2 films exhibit strong (002) diffraction peaks, implying a *c*-axis prefer orientation. The reduced intensity and peak broadening in thinner films arise from the decrease in *z*-direction resolution in θ-2θ scan mode when the film thickness decreases. The XRD results have revealed that our MoS_2

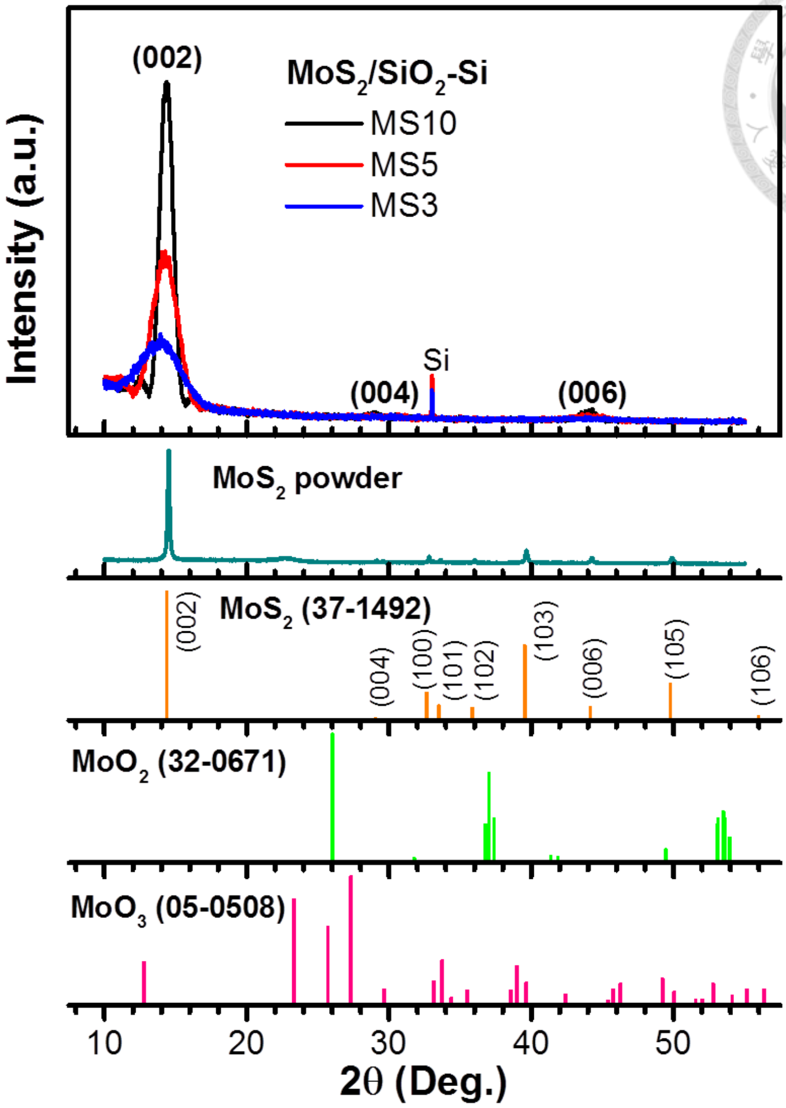

Figure 3.8 XRD profiles of MS10, MS5, and MS3. Commercial MoS_2 powder is utilized as a comparison. The standard patterns of MoS_2, MoO_2, and MoO_3 are also shown as references.

is hexagonal symmetry with *c*-axis perpendicular to the substrate, which is consistent with the observation in TEM images. Also, the XRD profiles only show (002) and related high index diffraction peaks. No oxide signal, such as MoO_2 or MoO_3, is found in the XRD profiles, which further examines there is no oxide residual in our CVD-grown MoS_2 thin films.

3.2 Binding energy analyses

3.2.1 Core level spectra

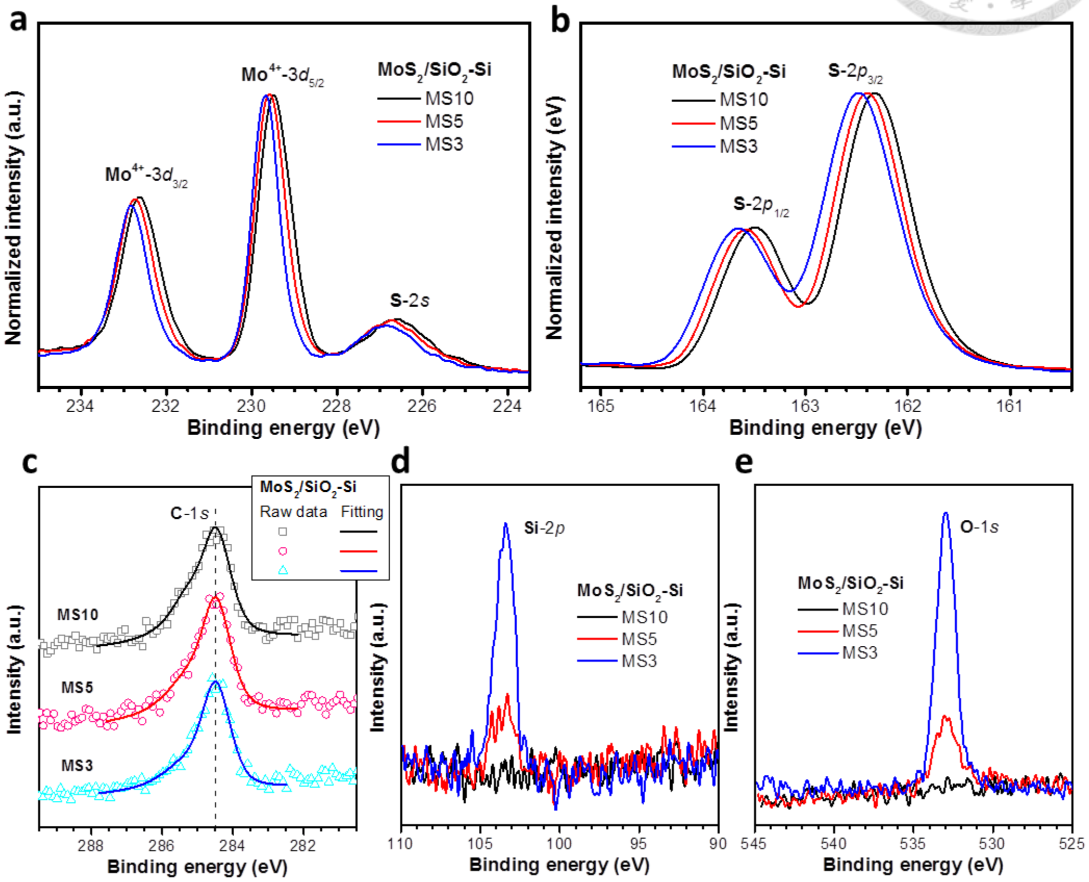

Figure 3.9 The XPS core-level spectra of (a) Mo-3d, (b) S-2p, (c) C-1s, (d) Si-2p, and (e) O-1s, collected from MoS$_2$ with various film thicknesses

Table 3.1 The energy values of Mo-3*d* and S-2*p* core levels obtained from Figure 3.9. All the values in the table are in the unit of eV

MoS$_2$	Mo		ΔSO	E_{CL}^{Mo}	ΔE_{CL}^{Mo}	S		ΔSO	E_{CL}^{S}	ΔE_{CL}^{S}	E_{CL}^{Mo}-E_{CL}^{S}	S/Mo
	3$d_{3/2}$	3$d_{5/2}$				2$p_{1/2}$	2$p_{3/2}$					
MS10	232.62	229.49	3.13	231.06	0.11	163.50	162.32	1.18	162.91	0.08	68.15	2.01
MS5	232.74	229.59	3.15	231.17	0.09	163.58	162.40	1.18	162.99	0.08	68.18	2.02
MS3	232.83	229.68	3.15	231.26		163.66	162.48	1.18	163.07		68.19	1.98

The surface chemical states of prepared MoS_2 thin films analyzed by XPS are shown in Figure 3.9. The detailed results are listed in the Table 3.1. The MoS_2 exhibits two characteristic peaks at around 229.6 and 232.7 eV, corresponding to the doublet Mo $3d_{5/2}$ and $3d_{3/2}$ for Mo^{4+}. There are one peak at around 226.7 eV and two peaks at around 162.4 and 163.6 eV assigned as S-2*s*, and the doublet S $2p_{3/2}$ and $2p_{1/2}$, respectively. After adjusting the energy by the C-1*s* position, both Mo-3*d* and S-2*p* core levels are found to shift ~0.2 eV toward high binding energy (BE) as the film thickness decreases. Meanwhile Si-2*p* and O-1*s* core levels from the substrate remain in the same positions and their peak intensities increase with reducing film thickness. On the other hand, the binding energy does not show obvious shift for thicker MoS_2 film (MS20) in either Mo-3*d* or S-2*p* compared to MS10, as shown in Figure 3.10. This indicates that the BE shift may relate to the surface effect on MoS_2 rather than the bulk.

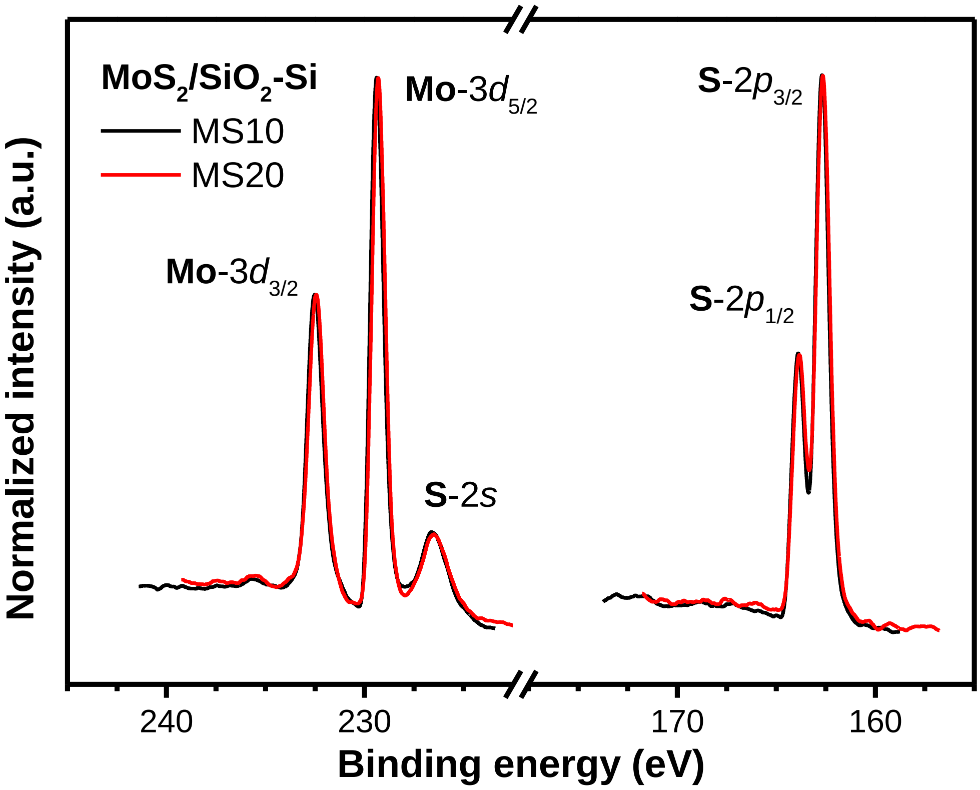

Figure 3.10 XPS core-level spectra of Mo-3*d* and S-2*p* in MS10 and MS20.

doi:10.6342/NTU201603487

To clarify the correlations for the unique BE shift with the film thickness, we discuss as follows. First, the BE shift may result from the variations in the chemical environment of the surface Mo and S atoms due to the improper control during the synthesis. This indicates the oxidation states of Mo and S may change with the film thickness. Originally they should be Mo^{4+} and S^{2-} in an ideal MoS_2. Since we prepared the MoS_2 from MoO_3, where it is Mo^{6+}, if part of the oxides is not fully sulfurized, especially in the thicker film, mixed valances of Mo will be observed in the Mo-3*d* core-level spectrum. However, TEM-EDX mapping (Figure 3.7) and XRD profiles (Figure 3.8) indicate that there is no detectable oxide impurity in our MoS_2 thin films. If the sulfur deficient sample is obtained, the zero valance Mo may appear ($MoS_x \rightarrow MoS_2 + Mo$), which will also contribute to the Mo-3*d* spectrum.[11, 12] During the sulfurization, sulfur-rich phase MoS_3 could form as an intermediate state, which can be considered as $Mo^{IV}(S^{2-})(S_2^{2-})$ and reflects on the changes in S-2*p* core level.[13] However, we do not observe the peak broadening, shape change, or shoulders in the spectra because of the average oxidation state of Mo or S increases or decreases. Therefore, we rule out the possibility that BE changes with valence states.

Second, the surface of MoS_2 could be charged positively when the photoelectrons leave the sample surface. The accumulated positive charges at the sample surface will trap the following photoelectrons leading to the increase in the measured BE. Although the electron flood gun was employed to neutralize the surface charges, we still observe the BE shift in Mo-3*d* and S-2*p* core-level spectra. As illustrated in Figure 3.5(a), the band gap energy of MoS_2 increases when the film thickness reduces, which intuitively implies the conductance of MoS_2 thin film decreases and results in surface charging. Nevertheless, it was reported that the conductance of MoS_2 has little dependence with the thickness.[14] On the contrary, the conductivity of MoS_2 increases as the film

doi:10.6342/NTU201603487

thickness decreases, which indicates that the surface of MoS_2 is more conductive than the bulk. In our work, the thicknesses of three MoS_2 thin films are all less than 10 nm, and get thinner from MS10 to MS3, which means the surface properties are dominant. Figure 3.11 depicts the electrical measurements of our MoS_2 thin films with van der Pauw configuration, where it shows all the MoS_2 films have the conductance in the same order of magnitude regardless of the film thickness. However, the conductivity of MS3 is more than 20 times higher than that of MS10, indicating that the surface is more conductive than the bulk. Thus, surface charging shall not account for the BE shift, especially for MS3 which exhibits the highest binding energy of Mo-3*d* and S-2*p* among these three samples.

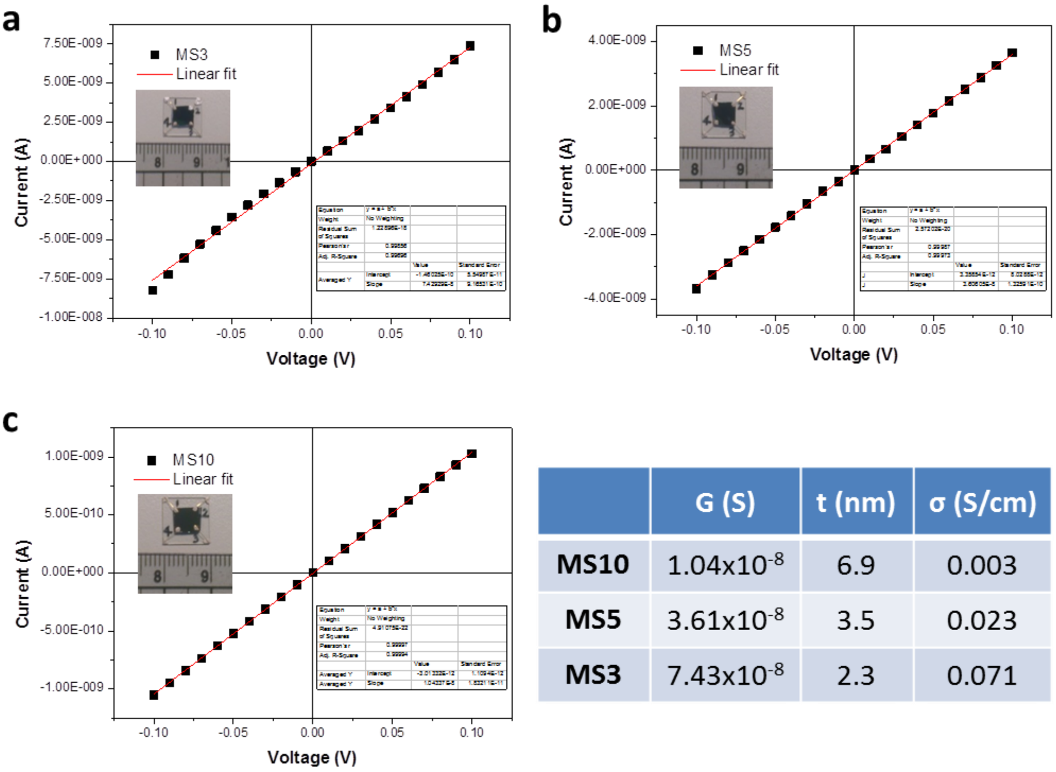

	G (S)	t (nm)	σ (S/cm)
MS10	1.04×10^{-8}	6.9	0.003
MS5	3.61×10^{-8}	3.5	0.023
MS3	7.43×10^{-8}	2.3	0.071

Figure 3.11 I-V curves of MS3, MS5, and MS10 measured by van der Pauw configuration. The device and the linearly fitting results are shown in the inset figures. The conductivities of MoS_2 films were calculated and listed in the table, where **G** is conductance, **t** is the film thickness obtained from AFM, and **σ** is conductivity.

To further confirm the surface charging effect, we also prepared reference samples, which are MoS_2 grown on the conducting substrate (graphene paper, GP) via the same processes as those grown on the SiO_2-Si substrates. As shown in Figure 3.12, the Raman results demonstrate that MoS_2 thin films were successfully grown on the conducting carbon material with similar qualities to MoS_2 grown on the SiO_2-Si. The XPS core-level spectra of MoS_2 grown on various substrates are illustrated in Figure 3.13. Comparatively, it is quite clear that the substrate will not influence the Mo-3*d* and S-2*p* core levels significantly, whereas the change of film thickness induces the BE shift. This result also suggests that there is no or negligible surface charging effect on our MoS_2 thin film.

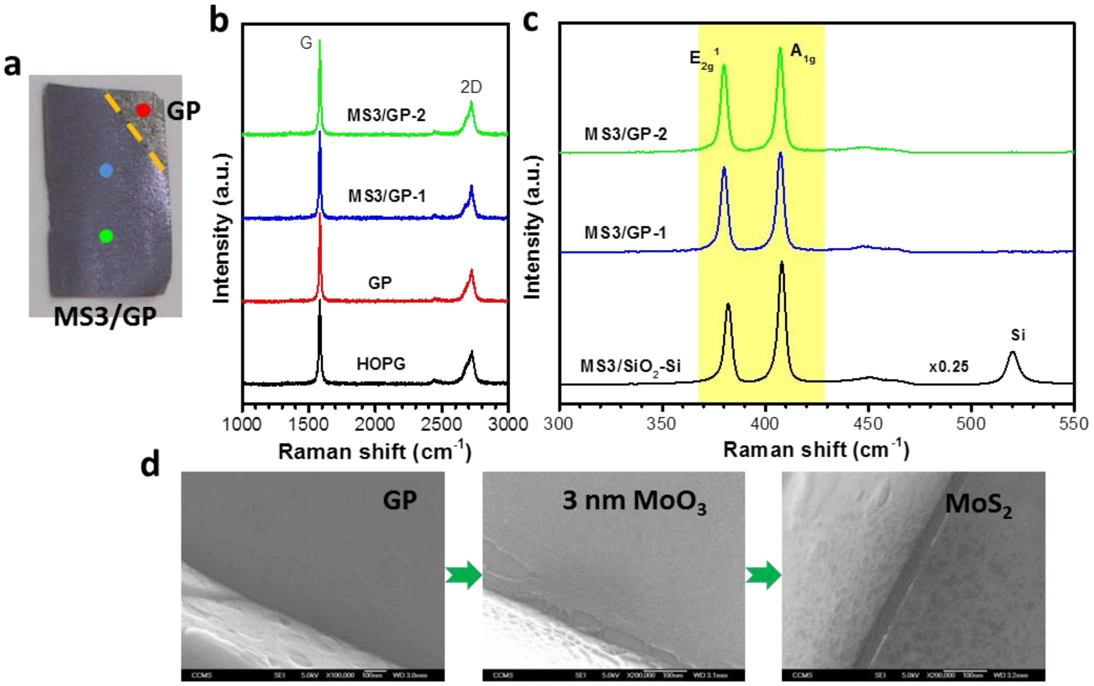

Figure 3.12 (a) The photo image of graphene paper (GP) and the MoS_2 grown on the top of it; (b) Raman spectra of HOPG, GP, and GP with MoS_2 grown on the top of it. The corresponding measured positions are illustrated in (a); (c) Raman spectra of MoS_2 grown on the GP and SiO_2/Si substrates; (d) SEM images of bare graphene paper, 3 nm MoO_3 deposited on the GP, and after sulfurization at 1000°C for 30 min.

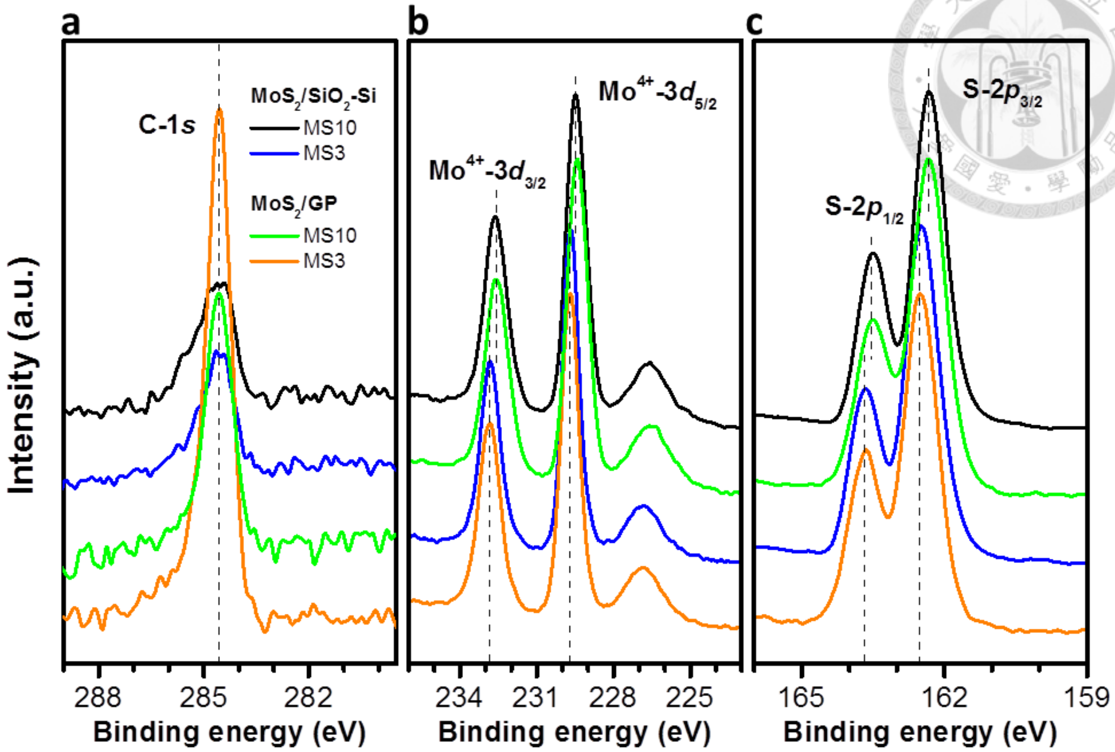

Figure 3.13 XPS core level spectra of (a) C-1*s*; (b) Mo-3*d*; (c) S-2*p* of MS10 and MS3 grown on SiO_2-Si and graphene paper (GP), respectively.

Third, the composition deviation from the stoichiometry at the MoS_2 surface may lead to the BE shift. It was demonstrated that the binding energy of Mo-3$d_{5/2}$ decreased progressively as the x in MoS_x decreased, while the binding energy of S was independent of the MoS_x stoichiometry.[12] Recent reports also elucidated that the variations in the S/Mo ratio would reveal the n-type or p-type behavior of MoS_2.[15] Sulfur-deficient MoS2 (S/Mo < 2) generally has n-type feature because the local formed sulfur vacancies act as electron donors, shifting the Fermi level toward the conduction band minimum (CBM). On the contrary, sulfur-rich or Mo-deficient (S/Mo > 2) will lead to the p-type feature, causing the Fermi level to move away from the CBM. Intentional surface treatment to turn the S/Mo ratio was also discovered to change the threshold voltage of MoS_2 field-effect transistors.[16] Since the BE detects the energy differences from core levels referenced to the Fermi level of the system, the variations in the Fermi level will influence the measured BE. However, it is noted that it seems no strong correlation between the film thickness and MoS_2 stoichiometry. In our work, both Mo-3*d* and S-2*p* core levels vary monotonically with film thickness, and the calculated S/Mo ratios are all closed to 2, as listed in Table 3.1. Thus, the deviations in composition shall not be blamed for the BE shift in our case.

Except for the chemical composition, the extrinsic doping may be another way to vary the Fermi level in two-dimensional materials. For example, impurities, like Na, at the MoS_2/SiO_2 interface will generate a defect-induced shallow donor level right below the Fermi level, resulting in n-type doping to the MoS_2 conduction band.[17] It has also been proposed that impurities in natural MoS_2, whose concentration is less than the detection limit of XPS, can have significant impacts on its electronic properties.[18] However, we prepared each MoS_2 film via the same CVD process, which is much different from the natural environment. The concentration and composition of impurities shall be similar in our MoS_2 films, and their effects on the material properties could be independent with the film thickness. When we changed the substrate from SiO_2-Si to graphene paper (GP), we still observed BE shifts with MoS_2 thickness (Figure 3.13). Thus, the impurity effects on the BE may not be the suitable answer in our case.

Moreover, recent study illustrated that the physically adsorbed O_2/H_2O at the MoS_2 surface reduces the Fermi level due to its hole-doping characteristic.[19] The competing screening effect between the surface- and the substrate-O_2/H_2O molecules was claimed for the work function variations with the MoS_2 thickness. However, it is not the scenario for the BE shift in our case. The characteristic peak of O-1*s* in Figure 3.9(e) is located at around 533.1 eV, corresponding to the SiO_2 from the substrate. Its intensity decreases with increasing the MoS_2 thickness, and becomes invisible for the MS10, which implies

doi:10.6342/NTU201603487

the oxygen signal in our case mainly originates from the substrate rather than the adsorbed O_2/H_2O.

3.2.2 Valence band spectra

The other possible reason for the BE shift is the variations in the measured valance band position and/or the core levels at the MoS_2 surface corresponding to the surface band bending (SBB). As shown in Table 3.1, both Mo-3*d* and S-2*p* core levels downshift as the film thickness increases, and the energy differences between Mo-3*d* and S-2*p* (E_{CL}^{Mo}-E_{CL}^{S}) are comparable, which imply that SBB would occur in our MoS_2 thin films. Addou *et al*. has proposed the concept of SBB on natural MoS_2, which was attributed to the influences of surface defects.[18] Mahatha *et al*. was also reported that the metallic edge steps and negative-charged dislocations would generate the electric field gradient on the MoS_2 surface, leading to the inhomogeneous SBB so as localized Fermi level pinning (FLP) which caused the BE shift in XPS.[20] Figure 3.14(a) to 3.14(c) are AFM images, where they exhibit the surface topographies of MoS_2 thin films. Within the 2 x 2 μm, the MoS_2 thin films prepared from the thermal-evaporated MoO_3 on the SiO_2-Si substrate show polycrystalline features with the grain size of ~100 nm. The high density of edges and grain boundaries (GBs) also reflects on the Raman results shown in Figure 3.2, where it demonstrates that the intensity of E_{2g}^1 is lower than that of A_{1g}. However, the edge densities among these three samples are so similar that the impacts on the BE shift may be ignored.

To further clarify the effect of SBB, the valance band spectra of MoS_2 thin films were collected by fine scanning near the Fermi level of the system, where the binding energy is 0. Figure 3.14(d) illustrates the valance band spectra of MoS_2 thin films and the details are listed in Table 3.2. The valance band maximum (VBM) of MoS_2 can be

doi:10.6342/NTU201603487

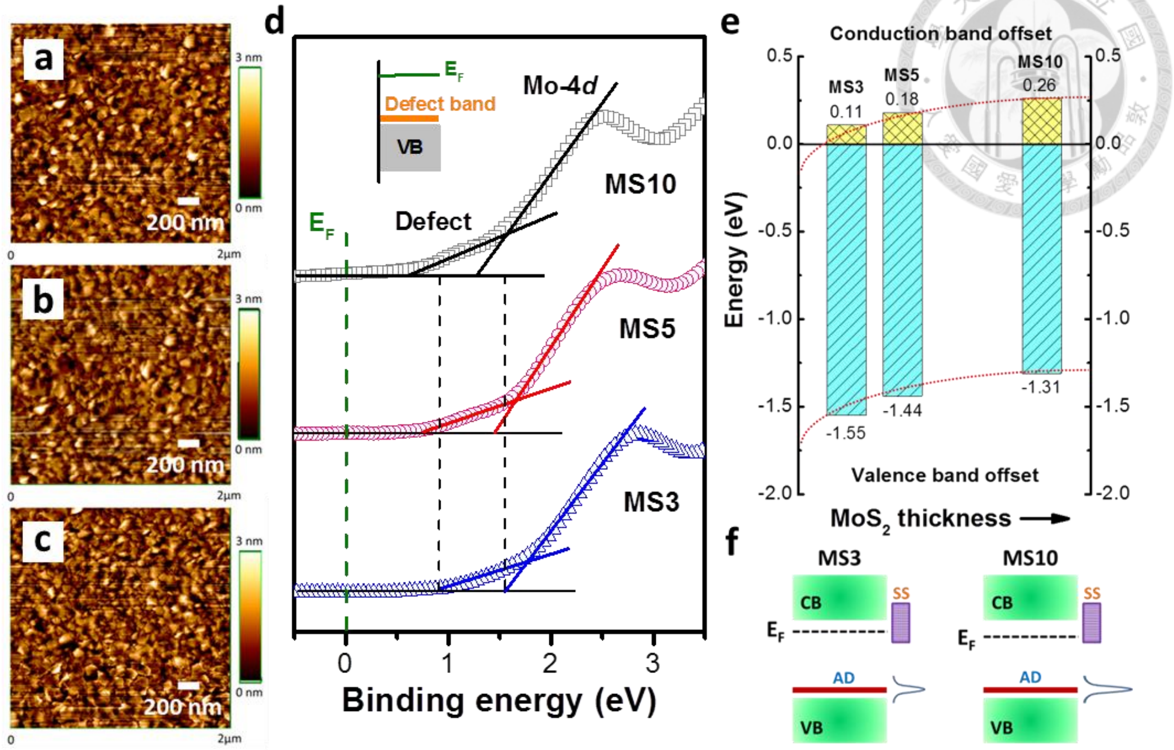

Figure 3.14 AFM topographies of (a) MS3, (b) MS5, and (c) MS10; (d) Valance band spectra of various MoS$_2$ film thicknesses; (e) Calculated band offsets in our MoS$_2$ films from (d) and Figure 3.5(a); (f) Schematic diagram for the band structures of MS3 and MS10.

Table 3.2 The valance band edges of various MoS$_2$ thicknesses obtained from Figure 3.14(d). All the values in the table are in the unit of eV.

MoS$_2$	**E_V ^{1}**	**E_V ^{2}**	**ΔE^{12}**	**ΔE_V^1**	**ΔE_V^2**	**$E_{CL}{}^{Mo}$-$E_V{}^2$**	**$E_{CL}{}^{S}$-$E_V{}^2$**	**$E_G{}^*$**
	defect	**Mo-4*d***	**E_V ^{2}-E_V ^{1}**					
MS10	0.65	1.31	0.66	0.12	0.13	229.75	161.60	1.57
MS5	0.77	1.44	0.67	0.12	0.11	229.73	161.55	1.62
MS3	0.89	1.55	0.68			229.71	161.52	1.66

regarded as the density-of-state (DOS) of Mo-4*d*, which locates at 1.55 eV relative to the Fermi level for MS3 and decreases the relative energy to 1.31 eV for MS10. According to the optical band gap estimated in Figure 3.5(a), it illustrates that our MoS_2 is n-type. It has been reported that the VBM of MoS_2 at the Γ point downshifts with respect to the local maximum at the K point as the layer number decreases.[10] However, based on the direct measurement of VBM by angle-resolved photoemission spectroscopy (ARPES), we can regard it as almost no variations in VBM when the MoS_2 is more than 3 layers.[21] The energy differences among the three samples at valence band edges are almost the same to those at core levels, indicating that the SBB does occur in our MoS_2. It is worth to note that there is a small band tail in front of the valance band edge, which could be regarded as a defect-induced gap states. Zhou *et al.*'s calculation proposed that the sulfur vacancies would create a shallow occupied defect level right adjacent to the VBM, and two deep unoccupied defect levels below the CBM in n-type MoS_2.[22] Thus, the small defect band that we observed in Figure 3.14(d) may be originated from the local sulfur vacancies due to the high edge densities and GBs in our MoS_2 thin films.

Since the defect bands are attributed to the sulfur vacancies, these positively charged defects may form donor-like (or metallic-like) surface states that contribute additional free electrons to the MoS_2 surface and generate an electric field pointing from the surface to the bulk.[15] The electrical potential formed near the surface will then bend the bands downward. Figure 3.14(e) illustrates the band offsets of MoS_2 films with various thicknesses, which clearly shows the consequence of band bending when the film thickness reduces. Although the BE refers to the energy difference between core levels and Fermi level at the MoS_2 surface, it is an average outcome of the detected volume in the real case rather than a single measured plane. Therefore, we obtain larger

doi:10.6342/NTU201603487

BE in thinner MoS_2 than the thicker one due to the bending down feature. The SBB we proposed also implies that thinner MoS_2 possesses higher conductivity because higher electron density at the surface leads to CBM close to Fermi level, which is consistent with our electrical measurement results (Figure 3.11). Other two-dimensional materials were also found to have such thickness-dependent variations in conductivity and might be explained by the SBB effect. Besides, MoS_2 has been demonstrated as a good piezoelectric material.[23-25] The electric field applied from the S site to the Mo site will stretch the Mo-2S dipole, creating tensile stress along the field direction and compressive stress at the orthogonal direction. Therefore, the built-in surface potential in our MoS_2 thin film could induce the piezoelectric effect to elongate its lattice constant in *c*-axis and reduce in *a*/*b*, corresponding to increasing E_{2g}^1 and decreasing A_{1g} in Raman. Similar phenomenon has been discovered on GaN nanorods.[26] This effect is proportional to the field strength; i.e., the thinner MoS_2, the lattice alters more. The frequency evolutions of E_{2g}^1 and A_{1g} with MoS_2 thickness in Figure 3.2 also reflect on the changes of lattice constants due to the piezoelectric effect in a certain extent.

Although SBB seems to match our observation, the variations of defect densities in our MoS_2 films may not be ignored, which would shift Fermi level as well. As shown in Figure 3.14(d), the DOS of defect bands slightly increases from MS3 to MS10, which implies that defects in the bulk may also contribute to the defect band near the VBM. The thicker MoS_2 films probably have higher defect number in between MoS_2 layers, such as the point defect of interstitial or the line defect of dislocation. Those bulk defects would form localized trap states in the band gap of MoS_2, and part of them locate near the VBM.[27, 28] Thus, the higher DOS of defect bands in MS10 might result from the formation of additional acceptor-like defect states in the bulk, as shown in the Figure 3.14(f). The bulk defects would capture free electrons leading to lower

doi:10.6342/NTU201603487

Fermi level.

However, sulfur vacancy is the main defect in MoS_2 due to its low formation energy so that it is expected to have the greatest impacts on the Fermi level compared to other structural defects.[22, 27] Addition to the defects, strain in our MoS_2 films, originated either from the substrate or the thermal treatment in CVD process, is also possible to alter the band structure leading to the BE shift. The largest direct band gap shift can be estimated to 300 meV per 1% biaxial compressive strain in a tri-layer MoS_2.[29] However, it is difficult to make such high strain difference among our MoS_2 films without bending the substrate. Part of the strain could also be relaxed by the GBs in our polycrystalline MoS_2 films. Thus, the effect of strain-induced band structure variations shall be limited in our case. Based on previous discussion, though slight quality variation can be observed among our MoS_2 films, which would affect the Fermi level so as the BE, surface states is still the dominant effect on the BE shift. In addition, the proposition of the donor-like surface states in the CVD-grown MoS_2 films could also explain the downward SBB observed in Figure 3.14(e).

3.3 Fermi level tuning

3.3.1 Au deposition

A thin layer of Au (~1 nm) was deposited by utilizing the e-beam evaporator under high vacuum to see how the BE varied at the MoS2 surface with a metal contact. Figure 3.15(a) to 3.15(c) illustrate the core-level spectra of Au-deposited MoS_2, where Mo-3*d* and S-2*p* core levels down shift after the Au deposition, while Au-4*f* shifts oppositely toward higher energy, implying the charge transfer between Au and MoS_2. The valance band spectrum of Au/MoS_2 shows three distinct edges, as labeled in (I), (II), and (III) in

doi:10.6342/NTU201603487

Figure 3.15(d). Compared to bare MoS_2 and pure Au, the energy positions of (I) and (III) are right consistent with the band edges of Au, while (II) is the contribution of Mo-4*d* with the energy position shifting ~0.3 eV toward the Fermi level. This indicates that the high work function metal (ϕ_{Au} = 5.1 eV) serves as a p-type material and attracts electrons from the n-type MoS_2 surface when they contact each other.[30] After reaching the thermal equilibrium, the accumulated electrons at the MoS_2 surface will be reduced so as the Fermi level position, leading to BE downshift.

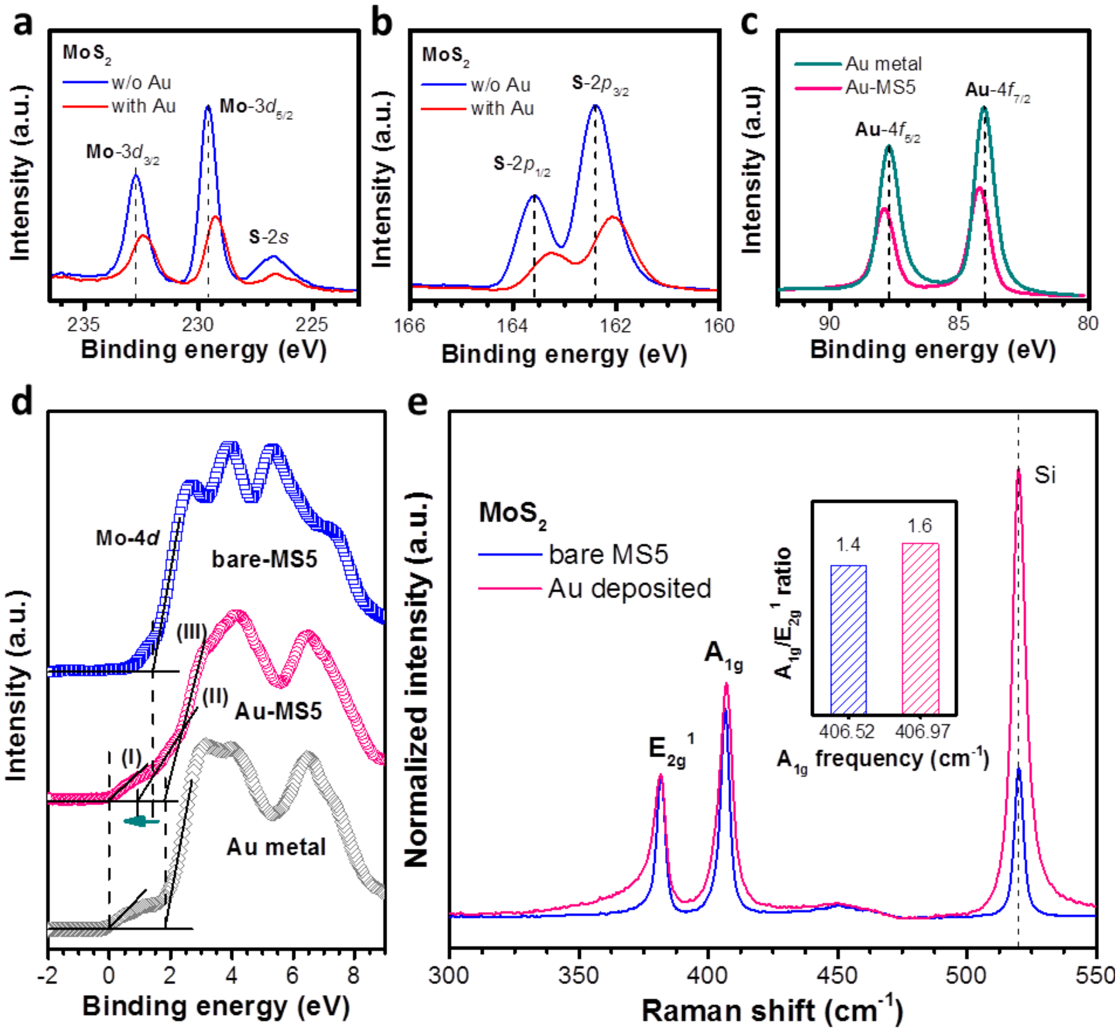

Figure 3.15 XPS core-level spectra of (a) Mo-3*d*, (b) S-2*p*, and (c) Au-4*f* of MS5 before and after Au deposition; (d) Valance band spectra of bare MS5, Au-deposited MS5, and pure Au; (e) Raman spectra of MS5 before and after Au deposition.

doi:10.6342/NTU201603487

It is worth to note that Mcdonnell *et al*. have shown if there is no chemical reaction occurring at the metal/MoS_2 interface, the BE will not shift.[15] In Figure 3.15(a) and 3.15(b), the core-level spectra exhibit no chemical reaction or surface damage at the Au/MoS_2 interface, indicating the BE shift after Au deposition in our case shall result from other factors. The metallic behavior of MoS_2 has been discovered at the Mo-terminated edges (sulfur-deficient sites) or two different types of 60^o GBs consisting of distinct 4-fold ring chains.[22, 31] These defects have been shown to transfer charges easily, leading to good catalytic performance.[22, 32] The Schottky barrier at MoS_2 and Au interface is also discovered lower than expectation because the metallic-like surface defects on MoS_2.[15] Since our MoS_2 thin films exhibit polycrystalline characteristics with many edges and GBs, they may provide free charges at the interface to realign the Fermi level after contact with metal and shift the BE. Furthermore, it has been reported that p-doped MoS_2 gives rise to the increase of relative intensity and frequency difference between A_{1g} and E_{2g}^1 modes.[30] The Raman spectra of MoS_2 before and after Au deposited were compared in Figure 3.15(e). After normalized the peak intensity of E_{2g}^1, the A_{1g} mode of Au-deposited MoS_2 shows higher intensity and blue-shift to higher frequency than bare MoS_2, which also illustrates the hole-doping characteristics of Au on our MoS_2 films.

3.3.2 HER application

Since our previous results show that Fermi level in our MoS_2 monotonically changes with film thickness and the polycrystalline feature may facilitate the charge transfer at the surface, we try to demonstrate its catalytic behavior by hydrogen evolution reaction (HER). Figure 3.16(a) shows the linear sweep voltammetry (LSV) curves of our MoS_2 grown on the GP. It is obvious that the onset potential dramatically

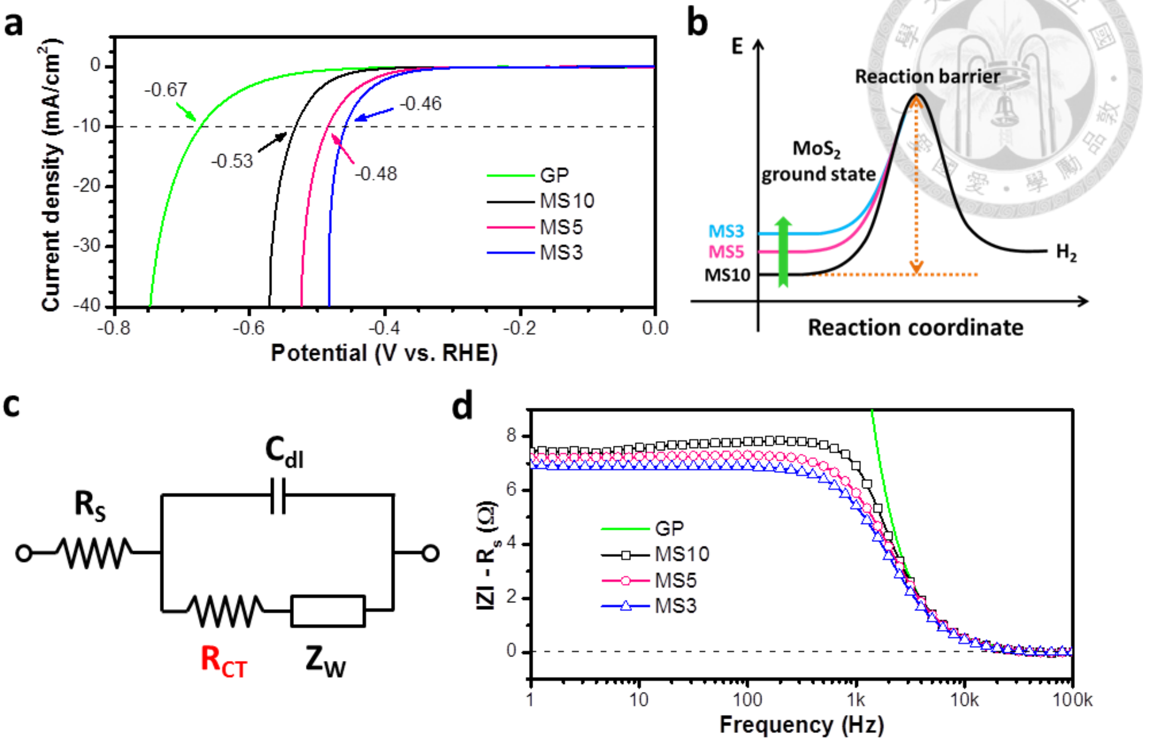

Figure 3.16 (a) LSV curves for the GP substrate and MoS_2/GP with various MoS_2 thicknesses; (b) Schematic diagram of potential energy surface vs. reaction coordination for HER; (c) Schematic diagram of the equivalent circuit in our electrochemical system for HER; (d) Corresponding Bode plot for HER at -10 mA/cm^2, obtained by the impedance measurement from 0.1 to 100k Hz with amplitude of 10 mV.

downshifts when there is MoS_2 on the GP surface, and further decreases when the MoS_2 thickness reduces. The corresponding potential at -10 mA/cm^2 decreases 140 mV between GP and MS10, and 70 mV between MS10 and MS3, respectively. The onset potential here represents the potential that is required to drive HER, which is related to the Fermi level of our MoS_2 film and the chemical potential of HER. As a result of the identical electrolyte we used for each specimen, the lower onset potential indicates lower reaction barrier required to be overcome for HER, as shown in Figure 3.16(b). The evolution of the onset potential with the MoS_2 film thickness in Figure 3.16(a) implies that MS3 has the highest ground state in the potential energy surface for HER, i.e. the highest Fermi level near the CBM, which is consistent with the trends we observed in the XPS.

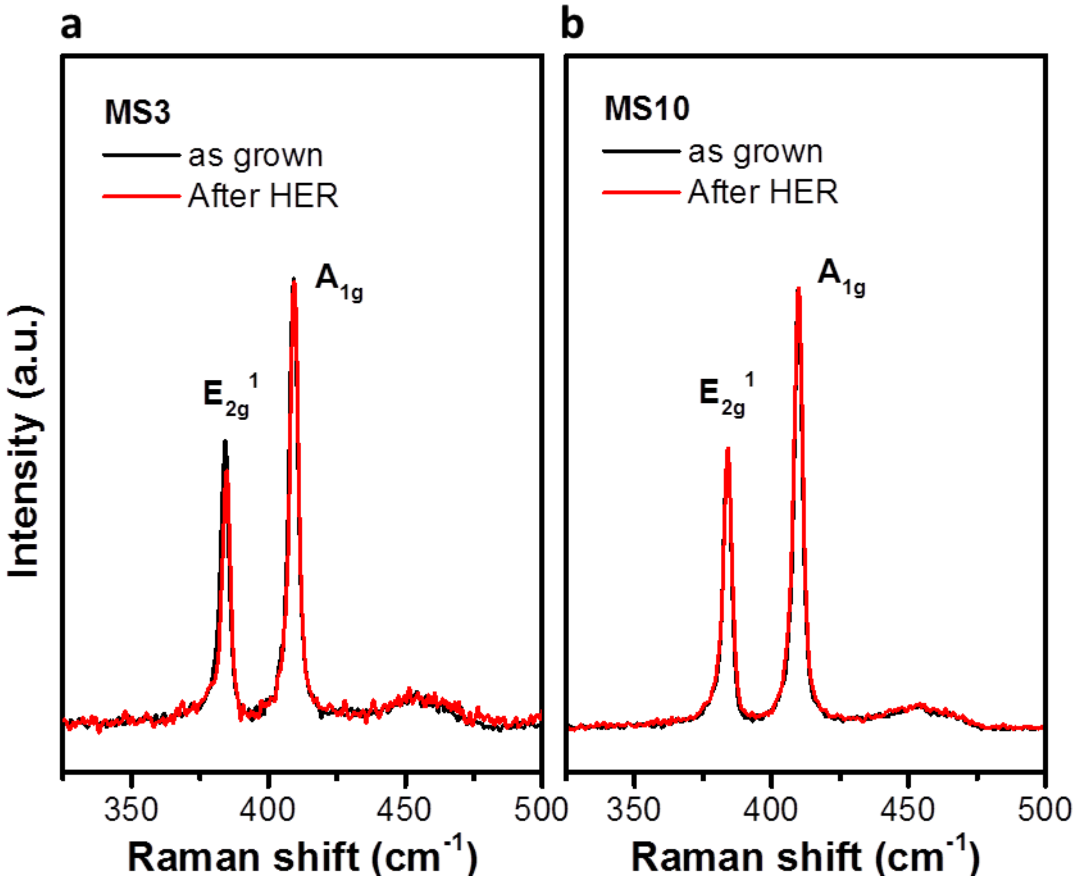

Figure 3.17 Raman spectra of (a) MS3 and (b) MS10 before and after HER.

To further illustrate the charge transfer between our MoS_2 films and the reactants (protons) in the electrolyte, the impedance measurements of the electrochemical system were carried out. Figure 3.16(c) shows the equivalent circuit in our electrochemical system, where R_S is the resistance including the electrode resistance and the electrolyte resistance, C_{dl} is the double layer capacitance near the MoS_2 surface, R_{CT} is the charge transfer resistance between our MoS_2 and reactants in the electrolyte, and Z_W is the Warburg impedance related to the mass transfer of the protons from the electrolyte to

doi:10.6342/NTU201603487

the MoS_2 surface. R_{CT} can be extracted from the Bode plot because it is independent of applied frequencies. Figure 3.16(d) shows the Bode plot for bare GP and MoS_2/GP specimens at -10 mA/cm^2. After subtracting the effect from R_S, R_{CT} decreases monotonically from MS10 to MS3, indicating the charge transfer from MoS_2 surface to the protons becomes faster and more efficient when the MoS_2 thickness reduces. This result is consistent with our electrical measurement, which exhibits higher conductivity for thinner MoS_2. Moreover, comparing the Raman spectra of MoS_2 films before and after HER for more than 100 cycles (Figure 3.17), it is interesting to note that the profiles clearly overlap for either thin (MS3) or thick (MS10) MoS_2 indicating the high chemical stability of our MoS_2 under a catalytic reaction.

3.4 Summary

We prepared MoS_2 thin films on SiO_2-Si with thickness ranging from 3 to 10 layers via CVD process, and observed the BE of Mo-3d and S-2p monotonically downshift ~0.2 eV with an increase in film thickness by XPS analyses. Defect-induced Fermi level variation is suggested to explain the thickness-dependent behaviors. Polycrystalline features shown in the AFM images and the defect bands appeared adjacent to the VBM of MoS_2 which indicates the sulfur vacancies exist in our MoS_2 thin films. A downward band bending is proposed based on the defect-induced surface states to explain the BE shift with MoS_2 thickness. Meanwhile, the bulk defects appearing in the thicker MoS_2 may form acceptor-like trap states in the band gaps, giving rise to lower Fermi level. The thickness-dependent Fermi level variation can also be applied on other two-dimensional materials where the conductivity increases with a decrease in film thickness. The electrical field generated at the MoS_2 surface might

doi:10.6342/NTU201603487

trigger the piezoelectric effect to alter the lattice constants, which is consistent to our frequency evolutions of E_{2g}^1 and A_{1g} in Raman. Depositing Au on the MoS_2 is found to reduce the BE ~0.3 eV because of its hole-doping characteristics, which implies the Fermi level can be tuned by the surface treatment. The Fermi level in the MoS_2 films affects the interfacial transport properties in MoS_2-related applications. We have also demonstrated here that the onset potential for HER evolves with MoS_2 film thickness, which is related to the Fermi level variation in our MoS_2 films. The lower charge transfer resistance in thinner MoS_2 is also an indirect support for the thickness-dependent conductivity and SBB effect. The tunable Fermi level and the high chemical stability make MoS_2 a potential material for catalytic reactions. We believe our discoveries will also stimulate novel concepts in designing new catalyst systems and flexible electronic devices based on the two-dimensional materials.

References

[1] T. J. Wieting and J. L. Verble, Phys. Rev. B **3** (12), 4286-4292 (1971).

[2] Q. Li, E. C. Walter, W. E. van der Veer, B. J. Murray, J. T. Newberg, E. W. Bohannan, J. A. Switzer, J. C. Hemminger and R. M. Penner, J. Phys. Chem. B **109** (8), 3169-3182 (2005).

[3] C. Lee, H. Yan, L. E. Brus, T. F. Heinz, J. Hone and S. Ryu, ACS Nano **4** (5), 2695-2700 (2010).

[4] S. Sahoo, A. P. S. Gaur, M. Ahmadi, M. J. F. Guinel and R. S. Katiyar, J. Phys. Chem. C **117** (17), 9042-9047 (2013).

[5] Y. Cheng, Z. Zhu and U. Schwingenschlögl, RSC Adv. **2** (20), 7798 (2012).

[6] H. Li, Q. Zhang, C. C. R. Yap, B. K. Tay, T. H. T. Edwin, A. Olivier and D. Baillargeat, Adv. Funct. Mater. **22** (7), 1385-1390 (2012).

[7] R. V. Kasowski, Phys. Rev. Lett. 30 (23), 1175-1178 (1973).

[8] L. A. King, W. Zhao, M. Chhowalla, D. J. Riley and G. Eda, J. Mater. Chem. A **1** (31), 8935 (2013).

[9] K. F. Mak, C. Lee, J. Hone, J. Shan and T. F. Heinz, Phys. Rev. Lett. **105** (13) (2010).

[10] A. Splendiani, L. Sun, Y. Zhang, T. Li, J. Kim, C. Y. Chim, G. Galli and F. Wang, Nano Lett. **10** (4), 1271-1275 (2010).

[11] J. R. Lince, D. J. Carré and P. D. Fleischauer, Phys. Rev. B **36** (3), 1647-1656 (1987).

[12] M. A. Baker, R. Gilmore, C. Lenardi and W. Gissler, Appl. Surf. Sci. **150**, 255-262 (1999).

[13] T. Weber, J. C. Muijsers, J. H. M. C. Van Wolput, C. P. J. Verhagen and J. W.

Niemantsverdriet, J. Phys. Chem. **100** (33), 14144-14150 (1996).

[14] R. S. Chen, C. C. Tang, W. C. Shen and Y. S. Huang, Nanotechnology **25** (41), 415706 (2014).

[15] S. McDonnell, R. Addou, C. Buie, R. M. Wallace and C. L. Hinkle, ACS Nano **8** (3), 2880-2888 (2014).

[16] W. S. Leong, Y. Li, X. Luo, C. T. Nai, S. Y. Quek and J. T. Thong, Nanoscale **7** (24), 10823-10831 (2015).

[17] K. Dolui, I. Rungger and S. Sanvito, Phys. Rev. B **87** (16) (2013).

[18] R. Addou, L. Colombo and R. M. Wallace, ACS Appl. Mater. Interfaces **7** (22), 11921-11929 (2015).

[19] J. H. Kim, J. Lee, J. H. Kim, C. C. Hwang, C. Lee and J. Y. Park, Appl. Phys. Lett. **106** (25), 251606 (2015).

[20] S. K. Mahatha and K. S. Menon, J. Phys. Condens. Matter. **24** (30), 305502 (2012).

[21] W. Jin, P.-C. Yeh, N. Zaki, D. Zhang, J. T. Sadowski, A. Al-Mahboob, A. M. van der Zande, D. A. Chenet, J. I. Dadap, I. P. Herman, P. Sutter, J. Hone and R. M. Osgood, Phys. Rev. Lett. **111** (10) (2013).

[22] W. Zhou, X. Zou, S. Najmaei, Z. Liu, Y. Shi, J. Kong, J. Lou, P. M. Ajayan, B. I. Yakobson and J. C. Idrobo, Nano Lett. **13** (6), 2615-2622 (2013).

[23] W. Wu, L. Wang, Y. Li, F. Zhang, L. Lin, S. Niu, D. Chenet, X. Zhang, Y. Hao, T. F. Heinz, J. Hone and Z. L. Wang, Nature **514** (7523), 470-474 (2014).

[24] H. Zhu, Y. Wang, J. Xiao, M. Liu, S. Xiong, Z. J. Wong, Z. Ye, Y. Ye, X. Yin and X. Zhang, Nat. Nanotechnol. **10** (2), 151-155 (2015).

[25] K.-A. N. Duerloo, M. T. Ong and E. J. Reed, J. Phys. Chem. Lett. **3** (19), 2871-2876 (2012).

doi:10.6342/NTU201603487

[26] W. S. Su, T. T. Chen, C. L. Cheng, S. P. Fu, Y. F. Chen, C. L. Hsiao and L. W. Tu, Nanotechnology **19** (23), 235401 (2008).

[27] H.-P. Komsa and A. V. Krasheninnikov, Phys. Rev. B **91** (12) (2015).

[28] A. N. Enyashin, M. Bar-Sadan, L. Houben and G. Seifert, J. Phys. Chem. C **117** (20), 10842-10848 (2013).

[29] Y. Y. Hui, X. Liu, W. Jie, N. Y. Chan, J. Hao, Y. T. Hsu, L. J. Li, W. Guo and S. P. Lau, ACS Nano **7** (8), 7126-7131 (2013).

[30] Y. Shi, J. K. Huang, L. Jin, Y. T. Hsu, S. F. Yu, L. J. Li and H. Y. Yang, Sci. Rep. **3**, 1839 (2013).

[31] M. V. Bollinger, J. V. Lauritsen, K. W. Jacobsen, J. K. Nørskov, S. Helveg and F. Besenbacher, Phys. Rev. Lett. **87** (19) (2001).

[32] T. F. Jaramillo, K. P. Jorgensen, J. Bonde, J. H. Nielsen, S. Horch and I. Chorkendorff, Science **317** (5834), 100-102 (2007).

doi:10.6342/NTU201603487

Chapter 4 Modulation of Sulfurization Kinetics for Orientation Control

In this chapter, the sulfurization kinetics in two general MoS_2 precursors is compared. Different sulfurization mechanisms are discussed which make the orientation control in MoS_2 become possible. An electronic device based on dual-oriented MoS_2 is also demonstrated.

4.1 Sulfurization rates of Mo metal and MoO_3 in H_2S

4.1.1 Thermodynamic information

In this work, we used H_2S gas as the sulfur source. The sulfurization reactions for Mo metal and MoO_3 can be written as follows:

$$Mo_{(s)} + 2H_2S_{(g)} \rightarrow MoS_{2(s)} + 2H_{2(g)} \tag{4.1}$$

$$MoO_{3(s)} + 3H_2S_{(g)} \rightarrow MoS_{2(s)} + 3H_2O_{(g)} + 1/2S_{2(g)} \tag{4.2}$$

To compare the sulfurization rates of Mo metal and MoO_3, we first analyzed the thermodynamic information for the sulfurization reactions. Table 4.1 shows the standard Gibbs free energies of formation for the reactants and products in Eq. (4.1) and Eq. (4.2).[1] The Gibbs free energies of Eq. (4.1) and Eq. (4.2) at 800K were then calculated as -150.82 kJ/mol and -178.545 kJ/mol, corresponding to the equilibrium constants of 7.05×10^9 for Eq. (4.1) and 4.55×10^{11} for Eq. (4.2), respectively. Both reactions exhibit

doi:10.6342/NTU201603487

negative free energy of reaction, indicating the reactions occur spontaneously at 800K. The equilibrium constant for Eq. (4.2) is two orders of magnitude higher than that of Eq. (4.1), implying that MoO_3 is more easily sulfurized than Mo under H_2S atmosphere at 800K.

Table 4.1 Standard Gibbs free energy of formation for reactants and product compounds in the sulfurization reaction. Free energy of sulfurization reactions at 800K and 1300K are also calculated. The energy values in this table are collected from ref. [1]

Compound	**ΔG_f (kJ/mol)***		
	300k	800k	1300k
MoO_2 (s)	-531.7	-440.5	-354.1
MoO_3 (s)	-667.6	-542.1	-423.7
MoS_2 (s)	-267.1	-242.2	-161.8
H_2O (g)	-228.5	-203.5	-175.8
H_2S (g)	-3.41	-45.69	-26.18
S_2 (g)	79.38	10.03	0
S_4 (g)	91.04	23.6	72.42
S_6 (g)	53.4	5.32	128.6
S_8 (g)	48.26	3.368	185.1
(4.1) $Mo + 2H_2S \rightarrow MoS_2 + 2H_2$		-150.82	-109.44
(4.2) $MoO_3 + 3H_2S \rightarrow MoS_2 + 3H_2O + 1/2S_2$		-178.545	-186.96
(4.4) $4S_2 \rightarrow S_8$		-36.752	185.1
(4.5) $H_2 + 1/2S_2 \rightarrow H_2S$		-50.705	-26.18
(4.6) $MoO_3 + 2H_2S + H_2 \rightarrow MoS_2 + 3H_2O$		-219.22	-213.14
(4.7) $MoO_3 + H_2 \rightarrow MoO_2 + H_2O$		-101.9	-106.2
(4.8) $MoO_2 + 2H_2S \rightarrow MoS_2 + 2H_2O$		-117.32	-106.94

doi:10.6342/NTU201603487

4.1.2 Comparison of sulfurization rates

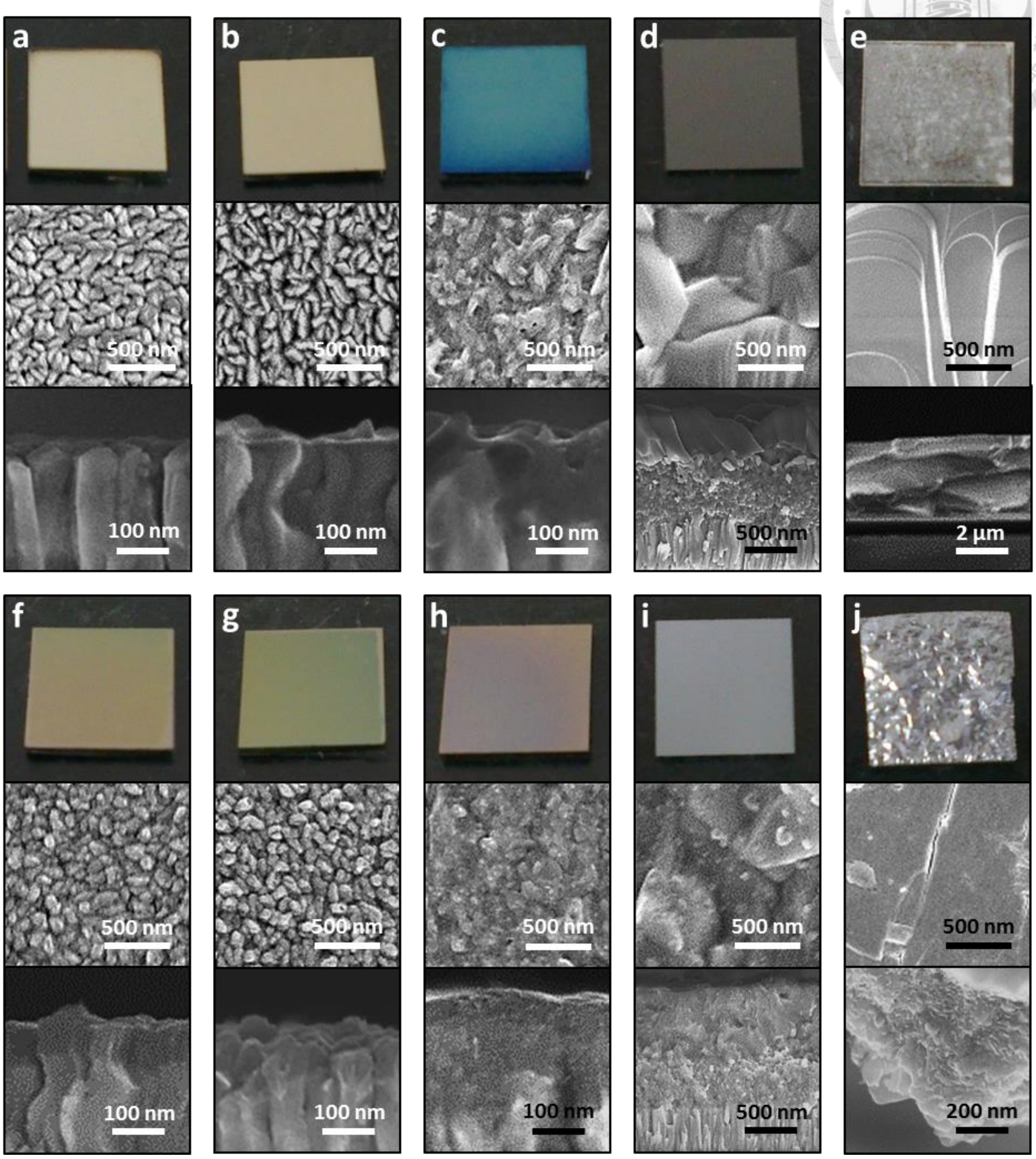

Figure 4.1 Photographs, top-view and cross-section SEM images of Mo-glass oxidized at 500^{o}C for various time in O_2/N_2 mixture. (a) pristine Mo-glass (MG), (b) MOG-15min, (c) MOG-30min, (d) MOG-1h, (e) MOG-2h. Corresponding photos and SEM images of specimens after sulfurization at 500^{o}C for 2h in H_2S. (f) MG-S, (g) MSG-15min, (h) MSG-30min, (i) MSG-1h, (j) MSG-2h.

To further confirm the difference of sulfurization rates between MoO_3 and Mo, we oxidized the Mo-glass (MG) in O_2/N_2 mixture (1:4) at 500^{o}C for various time to obtain films of different oxide to metal ratios. Figure 4.1(a) to 4.1(e) illustrate the photographs of MGs oxidized for 0~2h. The corresponding top-view and cross-section SEM images are also shown underneath the photos. The significant changes of the film color indicate various thicknesses of oxide layer formed, which interfere the reflection lights from the surface of the oxide layer and the oxide/Mo interface. When elongating the oxidation time, from the top-view images, the uniform grainy Mo particles gradually turn into large and dense oxides.

The thickness of the oxide layer is almost undetectable for 15 min oxidation, but is ~200 nm for 30 min oxidation. It is interesting that the cross-section image shows tri-layer structure for 1h oxidation (Figure 4.1(d)): top is the micro-grain oxide, nano-grain oxide is in the middle, and the bottom remains the Mo metal. It seems that the top oxide hinders the oxygen diffusion to the bottom, leading to the size gradient in the oxide layers. Moreover, the residual Mo metal is ~500 nm, but the total film thickness expands significantly to ~1.5 μm. This refers that ~500 nm of top Mo metal is responsible for the ~1 μm oxide layer. Figure 4.1(e) shows that the oxide is layered structure, and the thickness expands to ~3 μm with negligible residual Mo metal. Figure 4.2 is Raman spectra of oxidized MG for various oxidation time at 500^{o}C. It exhibits that the oxide formed on the Mo surface is MoO_3 rather than MoO_2. The enhancement of peak intensity with oxidation time indicates the oxide thickness increases.

The pristine MG and oxidized MGs were all sulfurized at 500^{o}C (773K) for 2h in 10% H_2S/Ar to produce MoS_2. To simplify the descriptions to the specimens, the oxidized MG is named as MOG-**t**, and sulfurized specimen is named as MSG-**t**, where **t** is oxidation time. Figure 4.1(f) to 4.1(j) are photos and SEM images of sulfurized

doi:10.6342/NTU201603487

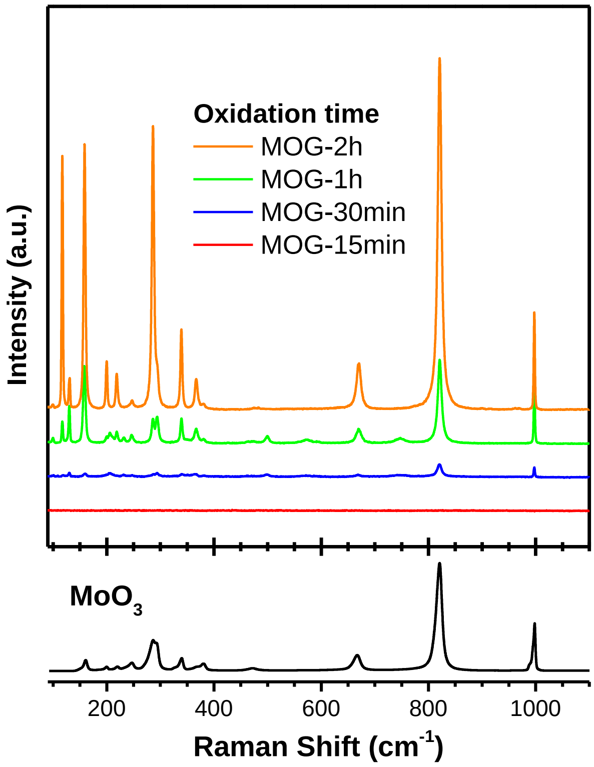

Figure 4.2 Raman spectra of Mo-glass oxidized at 500°C for various time in O_2/N_2 mixture.

specimens corresponding to Figure 4.1(a) to 4.1(e). The film colors of sulfurized specimens further change and also have evolution with MoS_2 thickness. The whole film of MSG-2h (Figure 4.1(f)) peeled off from the bottom glass substrate, which may be attributed to the weak interaction between MoS_2 and glass, and different thermal expansions between them.[2] The top-view images of the sulfurized specimens show surprisingly similar surface morphology and particle size to those corresponding un-sulfurized specimens. The cross-section image in Figure 4.1(f) clearly shows that top Mo metal has been sulfurized, and the thickness of MoS_2 is ~100 nm. With increasing the MoO_3/Mo ratio, the thickness of obtained MoS_2 increases. From the edge image in Figure 4.1(j), the MoS_2 film shows polycrystalline features with the grain size in nanometer scale.

There are several interesting findings in Figure 4.1. First, after the oxidation of Mo metal, the thickness of the oxide layer is more than two times of the consumed Mo. The volume expansion is reasonable because Mo is body-centered cubic (bcc) structure with lattice constant of 3.147 Å, while MoO_3 is orthorhombic structure with much larger unit cell (a = 3.962 Å, b = 13.858 Å, c = 3.697 Å), where Mo is octahedral coordinated surrounding by six oxygen atoms. Second, after sulfurized at 500^{o}C for 2h, the surface morphology of MoS_2 seems to follow the shape of oxide, but the grain size is still within nanometer scale. This indicates that the roughness of the MoS_2 film could be controlled by modulating the surface morphology of the oxide precursor. Third, compared Figure 4.1(f) and Figure 4.1(j), it reveals that MoO_3 has much higher sulfurization rate than Mo metal, which is consistent to the thermodynamic expectation. From the cross-section image in Figure 4.1(f), MoS_2 derived from the Mo metal is ~100 nm. Considering the volume expansion, the consumed Mo shall be less than 50 nm in thickness. On the other hand, in Figure 4.1(j), the oxide layer (~3 μm) transforms into MoS_2 completely, indicating the sulfurization rate of MoO_3 is at least 60 times higher than that of Mo metal.

4.1.3 Sulfurization mechanism

It is worth to note that MoO_3 is the most stable compound compared to MoS_2 and Mo metal according to the Gibbs free energies in Table 4.1 (MoO_3 < MoS_2 < Mo). However, the free energy of sulfurization in H_2S for MoO_3 is smaller than that for Mo metal. To understand the physical meanings behind the energy difference, we first consider the molecular/atomic interactions in MoO_3 and Mo metal. Compared the melting points of MoO_3 (795^{o}C) and Mo (2623^{o}C), the latter is significantly higher than the former, implying that the interactions among Mo atoms are much stronger than that

doi:10.6342/NTU201603487

among MoO_3 molecules. At the sulfurization temperature (500^oC), the molecular interactions in MoO_3 may be reduced especially between the van der Waal connected layers because it is close to the melting point of MoO_3, whereas Mo metal may not be affected as much as MoO_3. Moreover, Weber *et al*. has proposed that in the beginning of sulfurization, H_2S is favor to protonate the terminal $–Mo{=}O_t$ groups that weakens the Mo-O and S-H bonds, and facilitates the subsequent substitution of sulfur for oxygen to form the $MoOS_2$ oxysulfide as the intermediate product.[3] For Mo metal, H_2S will directly react with the surface Mo and release the hydrogen to form Mo-S during the sulfurization. The adsorption of sulfur atoms seems no preference to the Mo atoms because the difference in the electronegativity between Mo (2.16) and S (2.58) is small. This implies the activation energy for Eq. (4.2) is smaller than Eq. (4.1), leading to faster sulfurization. It also gives us a hint that if the kinetic parameters of sulfurization can be well-controlled, it is possible to directly grow MoS_2 on Mo surface from a thin layer of MoO_3 without sacrificing the Mo metal.

4.2 Orientation evolution of MoS_2

4.2.1 Raman analyses

Figure 4.3 shows Raman spectra of sulfurized specimens. Three distinct characteristic peaks are observed at ~408.6 cm^{-1}, ~383.2 cm^{-1}, and ~285.5 cm^{-1}, representing A_{1g}, E_{2g}^1, and E_{1g} vibration modes of MoS_2, respectively.[4] A_{1g} and E_{1g} refer to the symmetric vibration of sulfur atoms along the *c*-axis and basal plane of MoS_2, respectively. E_{2g}^1 involves both Mo and sulfur atoms vibrating oppositely along the basal plane. It is noticed that after normalized the E_{2g}^1 peaks, the peak intensities of A_{1g} to E_{1g} dramatically decrease with increasing the oxidation time, i.e. MoO_3/Mo ratio

doi:10.6342/NTU201603487

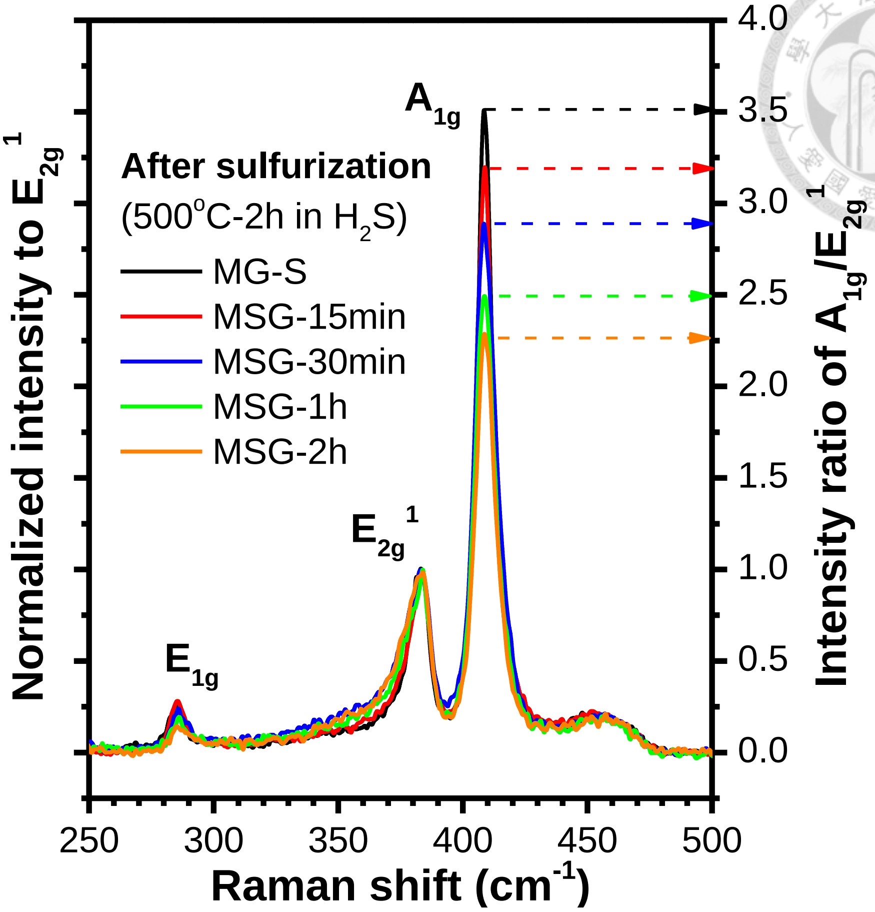

Figure 4.3 Raman spectra of oxidized Mo-glass after sulfurization at 500°C for 2h in H_2S. MSG-**t**, **t** denotes various oxidation time before sulfurization.

before sulfurization. The intensity ratio of A_{1g} to E_{2g}^1 can be estimated from approximate 3.5 decreasing to 2.3 when the oxidation time increases from 0 to 2h. During the sulfurization, except for MoO_3, part of the Mo metal underneath the MoO_3 may also be sulfurized. Since the sulfurization rate of MoO_3 is much higher than that of Mo metal, it is expected that the ratio of MoO_3-derived MoS_2 to Mo-derived one shall increase with the oxidation time, and be responsible for the evolution of Raman modes in Figure 4.2(b). Generally, E_{1g} mode is forbidden for the plane perpendicular to the *c*-axis (basal plane) in a backscattering geometry.[5] The decreasing intensity of E_{1g} with increasing oxidation time implies that MoS_2 turns to expose terraces. The

doi:10.6342/NTU201603487

significant variations of A_{1g}/E_{2g}^1 ratio can also be attributed to the stacking tendency of MoS_2. Kong *et al*. has demonstrated that edge-terminated MoS_2 film preferentially excited A_{1g} mode due to the polarization dependence, whereas E_{2g}^1 mode is preferentially excited for terrace-terminated film.[6] Thus, we may regard that MoS_2 derived from Mo metal prefers to expose edges with respect to the substrate in our sulfurization conditions. In contrast, MoS_2 sulfurized from MoO_3 tends to expose terraces on the substrate.

4.2.2 XANES analyses

Figure 4.4 illustrate the Mo K-edge XANES before and after sulfurization of oxidized MG specimens. Absorption spectra of MoO_2 and MoO_3 powders were also collected as references. The fluorescence mode was adopted to reveal the bulk information of the target element. The absorption edge of MOG-2h in Figure 4.4(a) locates at higher energy than Mo metal and MoO_2, and close to MoO_3, indicating the valance state of Mo is 6+ in MOG-2h. It also shows a clear pre-edge feature representing an allowed 1*s* to 4*d* transition in Mo of a distorted octahedral coordination,[7] which is similar to the spectrum of MoO_3. These results confirm that the oxide layer derived from the Mo metal is MoO_3. On the other hand, the absorption edge of MOS-1h locates between Mo^0 (Mo metal) and Mo^{4+} (MoO_2), and shows a small pre-edge feature. According to the results in Figure 4.1(d), which exhibit that nearly half of the Mo metal was oxidized to MoO_3, the average valance of Mo in MOS-1h is then estimated as ~3+, which is consistent to the result in Figure 4.4(a). The absorption profile of MOS-1h can also be regarded as the superposition of Mo metal and MoO_3. After sulfurization, MG-S in Figure 4.4(b) does not show clear difference with the un-sulfurized Mo-glass, indicating few Mo was sulfurized. MSG-1h and MSG-2h,

doi:10.6342/NTU201603487

however, show progressively shift of the absorption edges to the higher energy, indicating the changes in the average valence of Mo due to the formation of MoS_2.

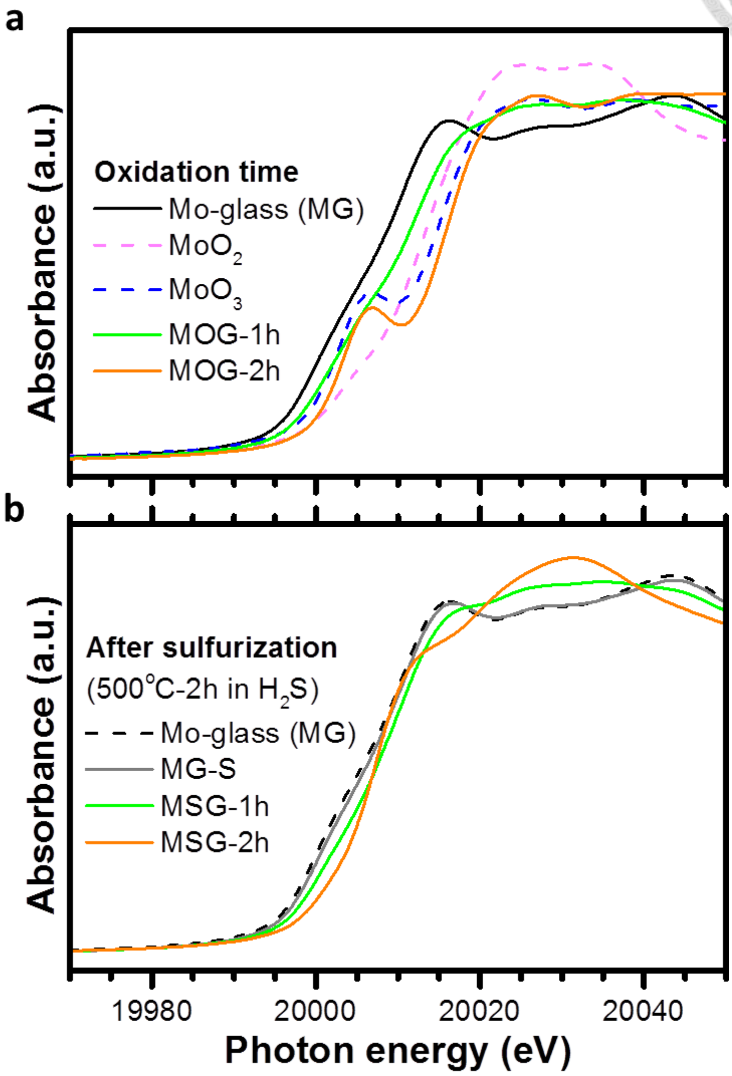

Figure 4.4 Mo K-edge XANES of (a) Mo-glass oxidized at 500°C for various time, and (b) corresponding specimens in (a) after sulfurization at 500°C for 2h in H_2S.

Figure 3(c) illustrates the sulfur K-edge XANES of sulfurized specimens, which qualitatively reveal density-of-states (DOS) of unoccupied sulfur 3*p* states in the conduction band.[27] Here, we collected the signals with fixed incident angle of x-ray photons at 45° with respect to the specimen. In Fig. 3(c), it is obvious that the white line

doi:10.6342/NTU201603487

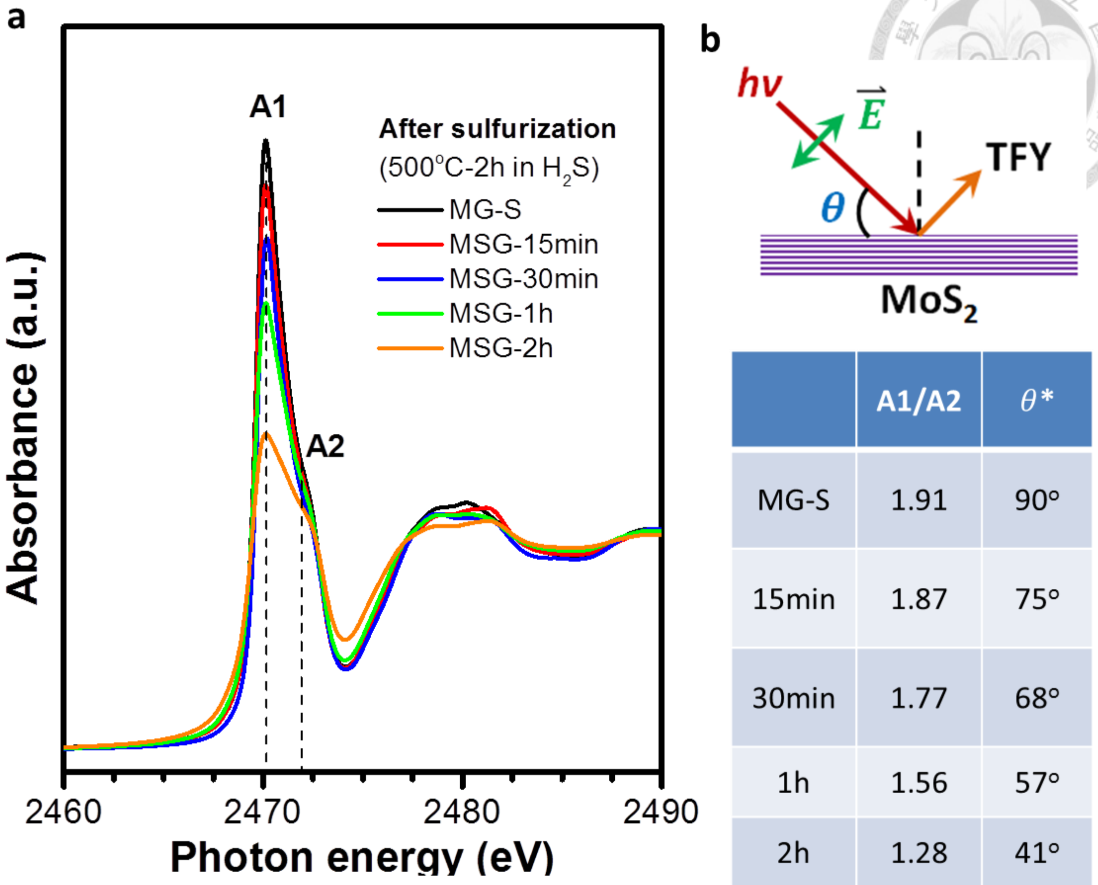

	A1/A2	θ*
MG-S	1.91	90°
15min	1.87	75°
30min	1.77	68°
1h	1.56	57°
2h	1.28	41°

Figure 4.5 (a) S K-edge XANES of oxidized Mo-glass after sulfurization at 500°C for 2h in H_2S; (b) Schematic illustration of polarization-dependent XAS on MoS_2. Calculated A1/A2 ratios from (a) are listed in the table. The angles (θ) between incident photons and the basal plane of MoS_2 are estimated from Figure 3 in ref. [8]

(peak A) decreases with increasing the oxidation time. It has been demonstrated that the x-ray absorption coefficient μ varies angle-dependently due to interactions between the E-field vector (**E**) of the incident photons and the oriented MoS_2 orbitals, which can be written as:[8]

$$\mu(\theta) = \mu_{\parallel} + (\mu_{\perp} - \mu_{\parallel})cos^2\theta \tag{4.3}$$

where θ is defined as the angle between the incident photons and the basal plane of MoS_2. $\mu_{\parallel}$ is the absorption coefficient with **E** parallel to the basal planes of MoS_2 ($\theta = 90^o$), which excites electrons to the states of $p_{x,y}$ character; while $\mu_{\perp}$ is the absorption coefficient with **E** perpendicular to the MoS_2 layers ($\theta = 0^o$) giving rise to transitions to p_z states. It was reported that the Mo 4*d* bands split into the lowest d_{z2} states at the valance band maximum, d_{x2-y2}, d_{xy} states at the conduction band minimum, and d_{xz}, d_{yz} at higher energy levels in the conduction band due to the ligand-field effect of the hexagonal MoS_2 with the trigonal prismatic coordinated Mo.[9-11] The splitting of peak A into A1 at ~2470.2 eV and A2 at ~2471.9 eV is observed in Figure 4.5(a), and is attributed to the hybridization of the unoccupied Mo 4*d* sub-bands with different DOS of sulfur $p_{x,y}$ and p_z states.[8]

As a result of the fixed incident angle (45^o) for the x-ray photons, the evolutions of peak A shall originate from the variations of MoS_2 orientation on the MG. The angles (θ) of photon-MoS_2 interaction were estimated by calculating the A1/A2 ratio and tabulated in the Fig. 3. As the table shows, the higher MoO_3/Mo ratio before sulfurization, the smaller A1/A2 ratio and the angle θ are. This implies that less electrons are excited to the sulfur $p_{x,y}$ states for specimens of higher MoO_3/Mo ratio before sulfurization due to the **E** becomes less horizontal to the MoS_2 layers. Noted that MG-S possesses the highest A1/A2 ratio, and the angle θ is ~90^o, indicating the MoS_2 stands ~45^o on the MG. In contrast, A1/A2 ratio is the smallest in MSG-2h, and the angle θ is ~41^o, which is close to the incident angle, implying the MoS_2 layers are in-plane oriented on the MG. Therefore, the results in Figure 4.5 illustrate that MoO_3-derived MoS_2 prefers to expose terrace on the substrate, but Mo-derived MoS_2 has vertically aligned tendency, which is consistent to the Raman results in Figure 4.3.

doi:10.6342/NTU201603487

Since the rate-limiting process of sulfurization has been proposed as the sulfur diffusion,[6] the crystal structure of the precursors may play an important role to determine the orientation of formed MoS_2. MoO_3 is a layered material with the stacking tendency parallel to the substrate, as shown in Figure 4.1(e). During the sulfurization, H_2S may not only react with the surface-terminated oxygen of MoO_3, but also has possibilities to react from the edges of the MoO_3 layers into the van der Waal gaps due to the reduction of the interlayer interaction at high temperature. This could be the reason that MoO_3 is sulfurized fast and the formed MoS_2 tends to expose terraces on the substrate as MoO_3 does. It also implies that if the crystal orientation of MoO_3 can be controlled, the orientation of oxide-derived MoS_2 may be manipulated like Mo metal precursor. On the other hand, it was reported that quick sulfurization of Mo metal gave rise to the vertically aligned MoS_2.[6] The metal-derived MoS_2 was able to retain its orientation even after further annealing at the same sulfurization temperature (550^oC), but it preferred to restack and lie down at high annealing temperature (800^oC) to reduce the total surface energy. In our work, we are able to obtain MoS_2 with edge-exposed tendency by slowly sulfurizing Mo metal at 500^oC in H_2S environment. As previous discussed, Mo metal is bcc structure, and H_2S has no preferential sites to react with. This implies that the orientation of Mo-derived MoS_2 may be dominated by the diffusion path of H_2S into the Mo metal, which is normal to the substrate in principle, at relatively low sulfurization temperature (500^oC) rather than the sulfurization kinetics.

4.3 Introduction of H_2 with H_2S

Higher sulfurization rate of MoO_3 than Mo metal has been demonstrated based on both the thermodynamic analyses and the experimental results. To enlarge the rate

doi:10.6342/NTU201603487

difference, we further examine the Eq. (4.2) from the thermodynamic points of view. As listed in Table 4.1, when MoO_3 reacts with H_2S, it produces S_2 gas except for MoS_2 and H_2O. At the sulfurization temperature, in fact, S_2 tends to form larger sulfur molecules, such as S_8 (Eq. (4.4)), because it is energetically favored (Free energy is -36.752 kJ/mol at 800K).

$$4S_{2(g)} \rightarrow S_{8(g)} \tag{4.4}$$

However, once the large sulfur molecule forms, the substitution for oxygen of MoO_3 will be affected. Meanwhile, it may also hinder the H_2S diffusion from the surface to the bulk, which reduces the efficiency of MoS_2 formation. Moreover, it is well known that H_2S will decompose into H_2 and S_2 at high temperature (reverse reaction of Eq. (4.5)). According to the Le Chatelier's principle, losing S_2 will promote the decomposition of H_2S, leading to more large sulfur molecules form and less MoS_2 produces. To improve the situation, introducing H_2 is required, and Eq. (4.2) will become Eq. (4.6).

$$H_{2(g)} + 1/2S_{2(g)} \rightarrow H_2S_{(g)} \tag{4.5}$$

$$MoO_{3(s)} + 2H_2S_{(g)} + H_{2(g)} \rightarrow MoS_{2(s)} + 3H_2O_{(g)} \tag{4.6}$$

Both Eq. (4.5) and Eq. (4.6) show negative free energy, indicating the reactions prefer to move toward right hand side, especially for Eq. (4.6), whose free energy (-219.22 kJ/mol) is much lower than Eq. (4.2) (-178.545 kJ/mol). It implies that introducing H_2 in H_2S may further accelerate MoS_2 formation from MoO_3, whereas Eq.

doi:10.6342/NTU201603487

(4.1) may be retarded according to the Le Chatelier's principle. Since the H_2 is introduced, it is inevitable that MoO_3 will undergo two-step sulfurization:

$$MoO_{3(s)} + H_{2(g)} \rightarrow MoO_{2(s)} + H_2O_{(g)} \tag{4.7}$$

$$MoO_{2(s)} + 2H_2S_{(g)} \rightarrow MoS_{2(s)} + 2H_2O_{(g)} \tag{4.8}$$

However, compared the free energy of Eq. (4.7) (-101.9 kJ/mol) with Eq. (4.2) (-178.545 kJ/mol), it shows that MoO_3 is favor to react with H_2S as the first step. Therefore, enlarging the difference in sulfurization rate between MoO_3 and Mo metal seems achievable by feeding H_2 with H_2S.

In Table 4.1, we also discover that at higher sulfurization temperature (1300K), the free energy of Eq. (4.1) decreases (-109.44 kJ/mol), but the free energy of Eq. (4.2) increases (-186.96 kJ/mol), resulting in the larger energy difference than that at 800K. It is noted that the free energy of Eq. (4.4) becomes positive at 1300K, indicating that S_2 does not favor to form large molecules at such high temperature. On the other hand, at 1300K, the decomposition of H_2S becomes more severe that withdraws Eq. (4.1) from moving toward right hand side. This implies that we may also achieve larger rate difference between MoO_3 and Mo metal by raising sulfurization temperature, but the introduction of H_2 is still suggested to suppress the H_2S decomposition. In our work, we fed H_2 at 500^oC in the subsequent experiments to carry out large rate difference rather than increasing the temperature because MG cannot survive at 1300K.

4.4 Dual-oriented MoS_2 for electronic device

4.4.1 Control of MoO_3/Mo ratio

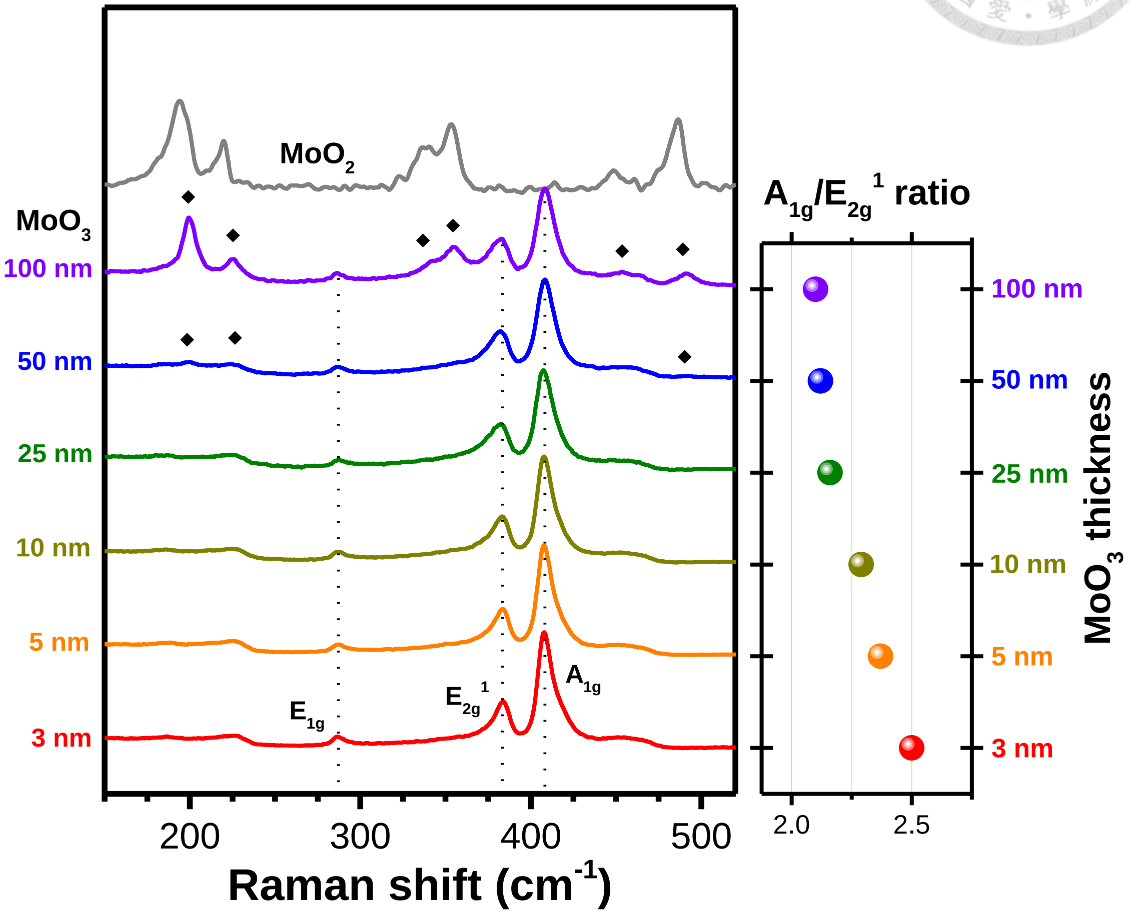

Figure 4.6 Raman spectra of sulfurized Mo-glass with various thicknesses of MoO_3 deposited on the surface by thermal evaporation before sulfurization.

To have better control in the thickness and roughness of the oxide layer on the MG, we deposited MoO_3 by thermal evaporation with the film thickness ranging from 3 nm to 100 nm rather than oxidizing the MG. The following sulfurization proceeded at 500°C in $H_2S/H_2/Ar$ mixture (1:2:9) for 10 min. Figure 4.6 illustrates the Raman spectra of the sulfurized MoO_3/MG composites with various MoO_3 thicknesses. The sulfurized specimens are named as MS**d** (d = 3~100 referring to the thickness of MoO_3 in nm) for simplicity. All specimens exhibit distinct A_{1g}, E_{2g}^1, and E_{1g} characteristic peaks of MoS_2, but several additional peaks appear as the MoO_3 thickness larger than 50 nm, which can be assigned as MoO_2. The A_{1g}/E_{2g}^1 ratio is ~2.5 for MS3, and gradually decreases as the MoO_3 thickness increases. After the MoO_3 thickness reaches 25 nm, the A_{1g}/E_{2g}^1 ratio seems to keep at ~2.1. The evolution of A_{1g}/E_{2g} ratios implies that part of Mo metal was sulfurized to MoS_2 that possesses different orientation with oxide-derived MoS_2. The thicker is deposited MoO_3, the larger ratio of oxide-derived MoS_2 to Mo-derived MoS_2 is, giving rise to reducing A_{1g}/E_{2g}^1 ratio. Therefore, to obtain a MoS_2 thin film with terrace-terminated tendency on Mo metal, we can either deposit MoO_3 for more than 10 nm to prevent Mo metal from sulfurization, or reduce the sulfurization time.

4.4.2 ZnO/MoS_2 heterostructure device

Kang *et al.* addressed that Mo is a suitable contact metal for MoS_2 because of the ultra-low resistance in between, and edge contact in multilayer MoS_2 can metallize all the MoS_2 layers and contact all the conducting channels.[12] Since the orientation of MoS_2 can be manipulated by selecting the precursor of Mo and utilizing a proper sulfurization process, a vertical device with edge-terminated MoS_2 on the Mo bottom contact can be carried out. Here, we grew ZnO via ALD process on two different oriented MoS_2 for electronic devices as comparison: One of the MoS_2 films derived from directly sulfurizing MG for 30 min, and the other derived from sulfurizing MoO_3-deposited MG for 10 min (MS5). Figure 4.7(a) illustrates the x-ray diffraction spectra of ZnO grown on these two MoS_2 thin films. Compared with the standard diffraction pattern of powder ZnO (ICDD: 36-1451), ALD-ZnO grown on the MoO_3-derived MoS_2 exhibits preferred orientation along [002] direction (*c*-axis), while it randomly stacks on the Mo-derived MoS_2.

doi:10.6342/NTU201603487

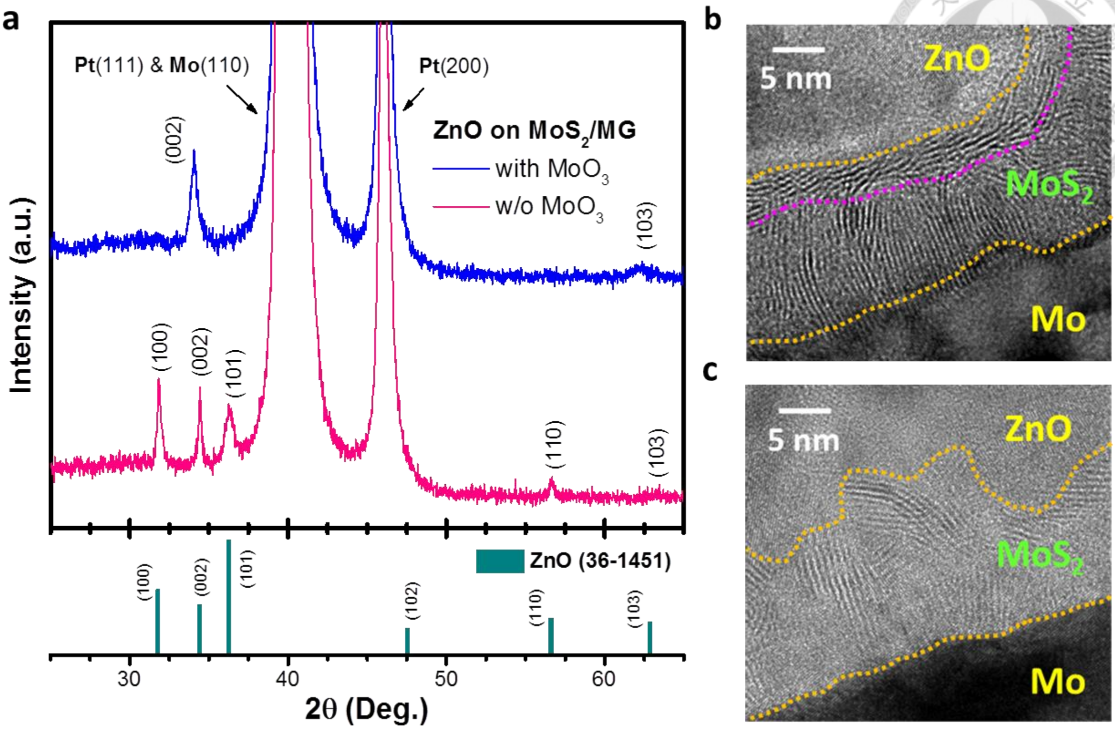

Figure 4.7 (a) XRD patterns of ALD-ZnO grown on the MoS_2/MG, where the MoS_2 derived from the Mo-glass with MoO_3 (top) and without MoO_3 (bottom). High resolution TEM images of ZnO/MoS_2/Mo interfaces, where the MoS_2 derived from the Mo-glass (b) with MoO_3 and (c) without MoO_3.

Figure 4.7(b) and 4.7(c) show the TEM images of ALD-ZnO grown on the MoO_3-derived MoS_2 and on the Mo-derived MoS_2, respectively. It is obvious that there are two orientations of MoS_2 in the MS5 (Figure 4.7(b)): the one connecting to the Mo metal is perpendicular to the substrate, and the other connecting to ZnO is parallel to the substrate. The thickness of former one is ~10 nm, and that of latter one is ~4 nm, which corresponds to 5~6 layers of MoS_2. On the other hand, Mo-derived MoS_2 (Figure 4.7(c)) shows single orienting tendency perpendicular to the substrate.

MoS_2 is a two-dimensional hexagonal material with lattice constants a = 3.16 Å and c = 12.3 Å, and ZnO can also be regarded as a three-dimensional hexagonal material with lattice constants *a* = 3.25 Å and *c* = 5.2 Å. Thus, the lattice mismatch between MoS_2 and ZnO at the *ab* plane can be calculated as ~2.8%. The TEM image in Figure 4.7(b) demonstrates that MoO_3-derived MoS_2 has the orientation parallel to the substrate, which may facilitate the following epitaxial growth of ZnO, resulting in the (002) preferred orientation. However, the high surface energy of edge-terminated MoS_2 in Figure 4.7(c), and large lattice mismatch (~57.7%) between MoS_2 and ZnO at planes orthogonal to *ab* plane may complicate the nucleation and growth mechanism of ZnO in ALD process giving rise to random orientation.

It is worth to note that Mo-glass is a common-used substrate in CZTS-based thin film solar cell. One of the key issues to deteriorate the cell performance is the formation of MoS_2 at the surface of Mo back contact.[13-15] The thickness of the unwanted MoS_2 in-between the CZTS/Mo interface can be few hundred nm,[16] but numerical simulation showed that 50 nm is sufficient enough to induce adverse effect.[17] Recent report showed that the oxygen content in the Mo layer is beneficial to reduce the MoS_2 thickness.[18] This implies that the oxide on the Mo surface may play a role in suppressing MoS_2 formation. In our case, the MoS_2 derived from the Mo metal in MS5 is ~10 nm, which is much thinner than the MoS_2 layer formed in the general CZTS system. The intentionally deposited MoO_3 thin layer on MG may serve as a sacrificing layer, and form MoS_2 faster than the bottom Mo metal. Once the oxide-derived MoS_2 layer forms, it may become a diffusion barrier for sulfur diffusing into Mo metal due to its in-plane orienting feature, which suppresses the sulfurization of bottom Mo metal. Since the formation of MoS_2 layer seems inevitable in CZTS-base solar cell, intentionally formed MoS_2 from MoO_3 may impede further MoS_2 formation from Mo back contact, and reduce the series resistance in the device.

doi:10.6342/NTU201603487

4.4.3 I-V behaviors

To illustrate the interface properties between ZnO and two different terminated MoS_2, the I-V curves were measured by fabricating devices A and B, as shown in Fig. 6, with the ohmic metal (Ti/Au) on the top surface of ZnO. The I-V measurements were performed by sweeping the voltage between +2V to -3V with the sequence from (I) to (IV) for 10 cycles. Both devices exhibit an obvious turn-on behavior with a small hysteresis loop at positive bias, while a smaller current response with a distinct hysteresis loop at negative bias. The turn-on behavior at positive bias is attributed to the carriers transporting through a barrier at MoS_2/ZnO interface, which is similar to the diode feature. The hysteresis loop at negative bias, originating from the synergy effect of ZnO/MoS_2, can be divided into a low resistance state (LRS) and a high resistance state (HRS), which can be applied as a memory.

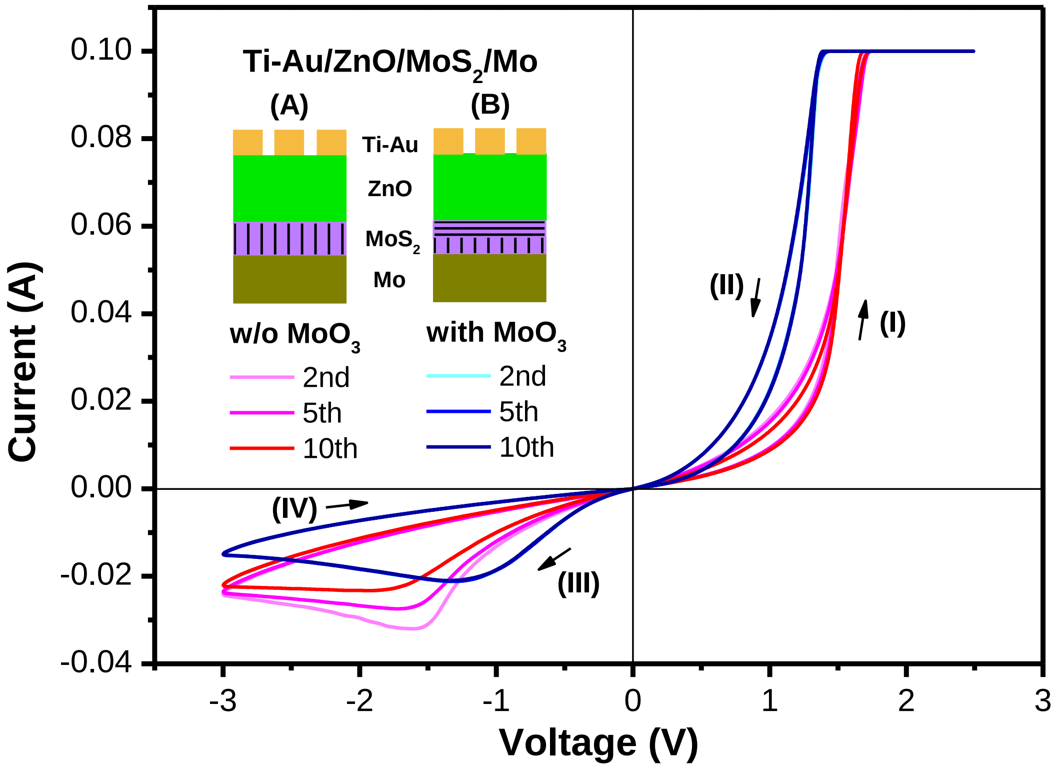

Figure 4.8 I-V behaviors of Ti-Au/ZnO/MoS_2/Mo devices, where the MoS_2 derived from the Mo-glass with MoO_3 (red) and without MoO_3 (blue).

However, the interface with the single, vertically-oriented MoS_2 (w/o MoO_3 on the MG before sulfurization) in device A shows unstable I-V behavior during cycling, especially at the negative bias. The ON/OFF ratio degrades with cycles, and the current at LRS is smaller than that in device B. In contrast, the interface with dual-oriented MoS_2 (in-plane MoS_2 from MoO_3 and out-of-plane one from Mo metal) in device B shows much stable I-V curves, and larger ON/OFF ratio.

The MoS_2/Mo interface in both device A and B is expected as ohmic contact due to the MoS_2 is edge-connected. The top Ti/Au electrode is also an ohmic metal to ZnO. Thus, the different I-V behaviors between device A and B shall mainly result from the variations in the MoS_2/ZnO interface. Although the MoS_2 layer in device A is edge-terminated, the high surface energy could bring about chemical reactions at the MoS_2/ZnO interface during the ZnO growth and I-V measurement, leading to the formation of oxysulfides where the valance of Mo could be 5+.[3, 19, 20] The oxysulfides at the MoS_2/ZnO interface act as a transport barrier for carriers, and may grow thicker with sweeping cycles, leading to the increase of series resistance and degradation of the ON/OFF ratio. On the other hand, basal plane of MoS_2 is relatively chemical inert from both molecular orbital and experimental points of view.[21] The stable I-V performance in device B is attributed to the terrace-terminated MoS_2 at the MoS_2/ZnO interface. However, further investigations are required to confirm the interface properties.

4.5 Summary

We have demonstrated that MoO_3 has much higher sulfurization rate than Mo at 500^{o}C in H_2S environment based on both thermodynamic analyses and experimental

doi:10.6342/NTU201603487

	Mo	MoO_3
1. Crystal structure	Body centered cubic 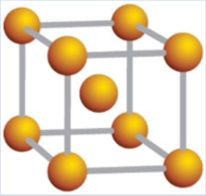 *a* = 3.147 Å	Orthorhombic, layered structure 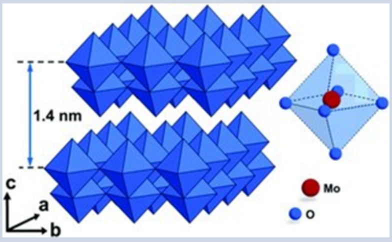 *a* = 3.962 Å, *b* = 13.858 Å, *c* = 3.697 Å
2. Molecular/Atomic interaction	Strong (m.p.=2623°C)	Weak (m.p.=795°C) with van der Waal gaps
3. Sulfurization route	No preferential adsorption of H_2S on Mo 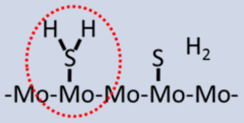 Electronegativity: Mo (2.16) vs. S (2.58)	Protonation of surface terminal oxygen to form oxysulfide as intermediate 
4. Sulfurization rate 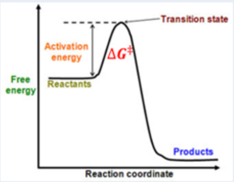 $rate \propto \exp(\frac{-\Delta G^\ddagger}{RT})$	Slow (high activation energy) ↓ H_2 Slower	Fast (low activation energy) ↓ H_2 Faster
5. MoS_2 orientation	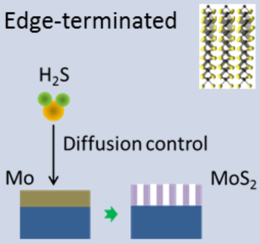	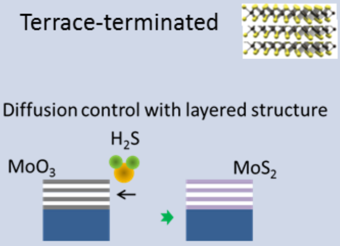
6. ZnO orientation on MoS_2	Random	(002) Preferred orientation
7. ZnO/MoS_2 interface	Unstable	Stable

Figure 4.9 Comparisons of Mo and MoO_3 as the MoS_2 precursors in the sulfurization process and device characteristics.

observations. The comparison of two MoS_2 precursors is summarized in Figure 4.9. Raman and XAS results reveal that MoO_3-derived MoS_2 tends to expose terraces, while Mo-derived MoS_2 prefers to expose edges. The orientation discrepancy in MoS_2 could be attributed to the different crystal structures of the precursors and the reaction routes of H_2S. Introducing H_2 with H_2S is expected to enlarge the difference in sulfurization rate between MoO_3 and Mo; thus, the pre-deposited MoO_3 thin layer on MG can form terrace-terminated MoS_2 in a short time. This intentionally grown MoS_2 layer with in-plane orientation may suppress further MoS_2 formation from Mo metal, which is beneficial for CZTS-based solar cell. ALD-grown ZnO on the edge-terminated MoS_2 exhibits random orientation, and the fabricated device shows unstable I-V behaviors due to the probably formed oxysulfides at the MoS_2/ZnO interface. In contrast, Terrace-terminated MoS_2 promotes ZnO to grow along *c*-axis on its top. The device performs stable I-V characteristics at MoS_2/ZnO interface which can be applied as a memory. It is interesting that large difference in sulfurization kinetics between oxide and metal makes it possible to develop diverse combinations of MoS_2 with different orientations on various substrates for either electronics or catalysts. Similar characteristics may also occur on producing other TMD materials.

doi:10.6342/NTU201603487

References

[1] M. W. Chase Jr., *NIST-JANAF Thermochemical Tables 4th Ed.* (American Institute of Physics).

[2] G. Plechinger, A. Castellanos-Gomez, M. Buscema, H. S. J. van der Zant, G. A. Steele, A. Kuc, T. Heine, C. Schüller and T. Korn, 2D Mater. **2** (1), 015006 (2015).

[3] T. Weber, J. C. Muijsers, J. H. M. C. Van Wolput, C. P. J. Verhagen and J. W. Niemantsverdriet, J. Phys. Chem. **100** (33), 14144-14150 (1996).

[4] C. Lee, H. Yan, L. E. Brus, T. F. Heinz, J. Hone and S. Ryu, ACS Nano **4** (5), 2695-2700 (2010).

[5] S. Sahoo, A. P. S. Gaur, M. Ahmadi, M. J. F. Guinel and R. S. Katiyar, J. Phys. Chem. C **117** (17), 9042-9047 (2013).

[6] D. Kong, H. Wang, J. J. Cha, M. Pasta, K. J. Koski, J. Yao and Y. Cui, Nano Lett. **13** (3), 1341-1347 (2013).

[7] T. Ressler, O. Timpe, T. Neisius, J. Find, G. Mestl, M. Dieterle and R. Schlögl, J. Catal. **191** (1), 75-85 (2000).

[8] D. Li, G. M. Bancroft, M. Kasrai, M. E. Fleet, X. H. Feng and K. H. Tan, Phys. Chem. Minerals **22**, 123-128 (1995).

[9] L. F. Mattheiss, Phys. Rev. B **8** (8), 3719-3740 (1973).

[10] C. Gong, H. Zhang, W. Wang, L. Colombo, R. M. Wallace and K. Cho, Appl. Phys. Lett. **103** (5), 053513 (2013).

[11] L. F. Mattheiss, Phys. Rev. Lett. **30** (17), 784-787 (1973).

[12] J. Kang, W. Liu and K. Banerjee, Appl. Phys. Lett. **104** (9), 093106 (2014).

[13] J. J. Scragg, T. Kubart, J. T. Wätjen, T. Ericson, M. K. Linnarsson and C.

Platzer-Björkman, Chem. Mater. **25** (15), 3162-3171 (2013).

[14] F. Liu, K. Sun, W. Li, C. Yan, H. Cui, L. Jiang, X. Hao and M. A. Green, Appl. Phys. Lett. **104** (5), 051105 (2014).

[15] J. J. Scragg, J. T. Watjen, M. Edoff, T. Ericson, T. Kubart and C. Platzer-Bjorkman, J. Am. Chem. Soc. **134** (47), 19330-19333 (2012).

[16] P. A. Fernandes, P. M. P. Salomé, A. F. da Cunha and B.-A. Schubert, Thin Solid Films **519** (21), 7382-7385 (2010).

[17] P. Chelvanathan, M. I. Hossain, J. Husna, M. Alghoul, K. Sopian and N. Amin, J. J. Appl. Phys. **51**, 10NC32 (2012).

[18] K.-J. Yang, J.-H. Sim, B. Jeon, D.-H. Son, D.-H. Kim, S.-J. Sung, D.-K. Hwang, S. Song, D. B. Khadka, J. Kim and J.-K. Kang, Prog. Photovoltaics: Research and Applications **23** (7), 862-873 (2015).

[19] J. C. Dupin, D. Gonbeau, I. Martin-Litas, P. Vinatier and A. Levasseur, Appl. Surf. Sci. **173**, 140-150 (2001).

[20] G. L. Frey, K. J. Reynold, R. H. Friend, H. Cohen and Y. Feldman, J. Am. Chem. Soc. **125**, 5998-6007 (2003).

[21] J. R. Lince, D. J. Carré and P. D. Fleischauer, Phys. Rev. B **36** (3), 1647-1656 (1987).

doi:10.6342/NTU201603487

Chapter 5 Oxide and Chalcogenide Heterojunction

In this chapter, the resistive switching behavior of Pt/ZnO/MoS_2/Mo heterojunction device is demonstrated. The interfacial properties are crucial to the switching behavior. Carrier transport is studied at room temperature and low temperature, and a switching mechanism is then proposed.

5.1 Device structure

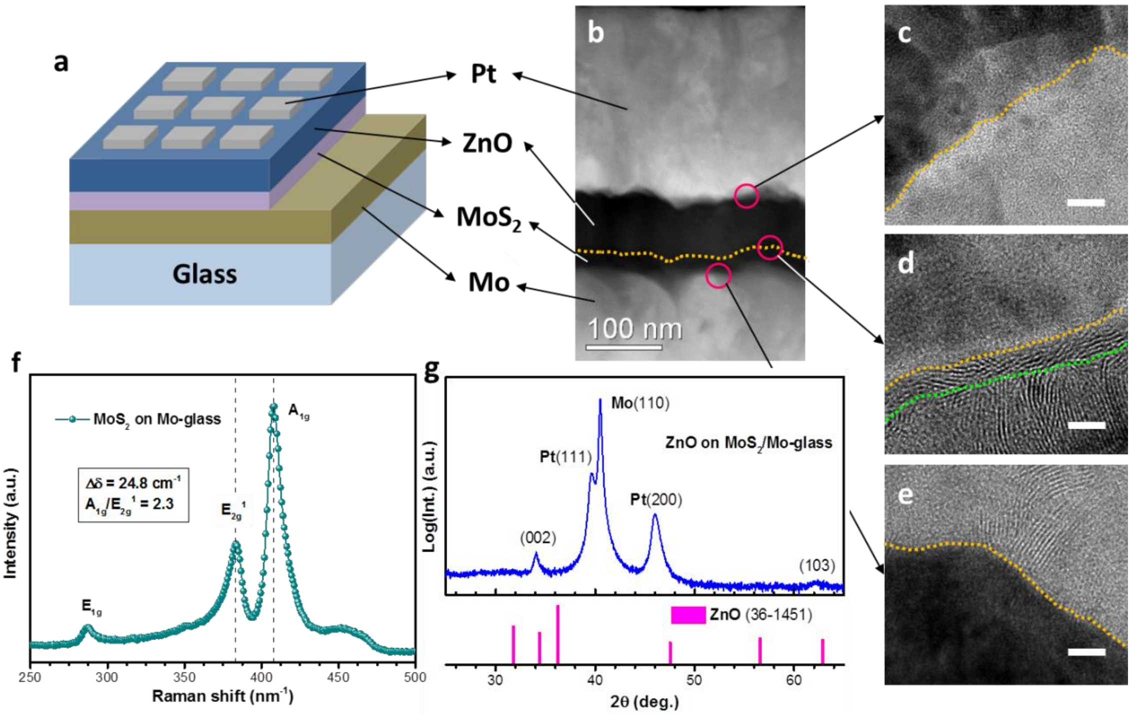

Figure 5.1 (a) Schematic diagram and (b) cross-sectional HRTEM image of the Pt/ZnO/MoS_2/Mo heterostructure device. Corresponding HRTEM images of the red circles in (b) illustrate three interfaces in the device: (c) Pt/ZnO interface, (d) ZnO/MoS_2 interface, and (e) MoS_2/Mo interface. The scale bar in (c) to (e) is 5 nm. (f) Raman spectrum of the dual-oriented MoS_2 thin films on Mo-glass. (g) XRD profile of ALD-ZnO gown on MoS_2/Mo-glass.

Pt/ZnO/MoS_2/Mo heterojunction devices were fabricated to study the resistive switching properties, as illustrated in Figure 5.1(a). The detailed fabrication process is described in previous chapter (Figure 2.4). Figure 5.1(b) shows the cross-sectional HRTEM image of the device, where the thicknesses of ZnO and MoS_2 are around 100 and 20 nm, respectively. A Pt layer of 200 nm in thickness and 100 μm x 100 μm in area was deposited as the top electrode (TE). The interfacial images of Pt/ZnO, ZnO/MoS_2 and MoS_2/Mo are illustrated with higher magnification in Figure 5.1(c) to 5.1(e), respectively. Pt/ZnO and MoS_2/Mo show sharp interfaces without any alloys or intermediates. MoS_2 exhibits dual orientations in the device, where edge-terminated MoS_2 (e-MoS_2) of around 15 nm in thickness contacts with the Mo bottom electrode (BE), and terrace-terminated one (t-MoS_2) of around 5 nm contacts with ZnO. The formation of dual-oriented MoS_2 is discussed in previous chapter. This configuration is benefit for ohmic contact with Mo and chemically stable interface with ZnO. The Raman spectrum in Figure 5.1(f) and XRD profile in Figure 5.1(g) reveal that ZnO layer is grown on dual-oriented MoS_2 with *c*-axis preferred orientation.

5.2 Resistive switching behaviors

5.2.1 I-V characteristics

The I-V curve of the Pt/ZnO/MoS_2/Mo device was performed in the ambient and dark environment at room temperature by sweeping the voltage between +2 V to -5 V with the compliance current (C.C.) of 0.1 A. An asymmetric I-V curve including five steps is observed in Figure 5.2(a). Initially (step (I)), the system is at a high resistance state (HRS). With increasing the applied voltage, the system suddenly switches into a low resistance state (LRS) at around 2 V and reaches the C.C. of 0.1 A (step (II)).

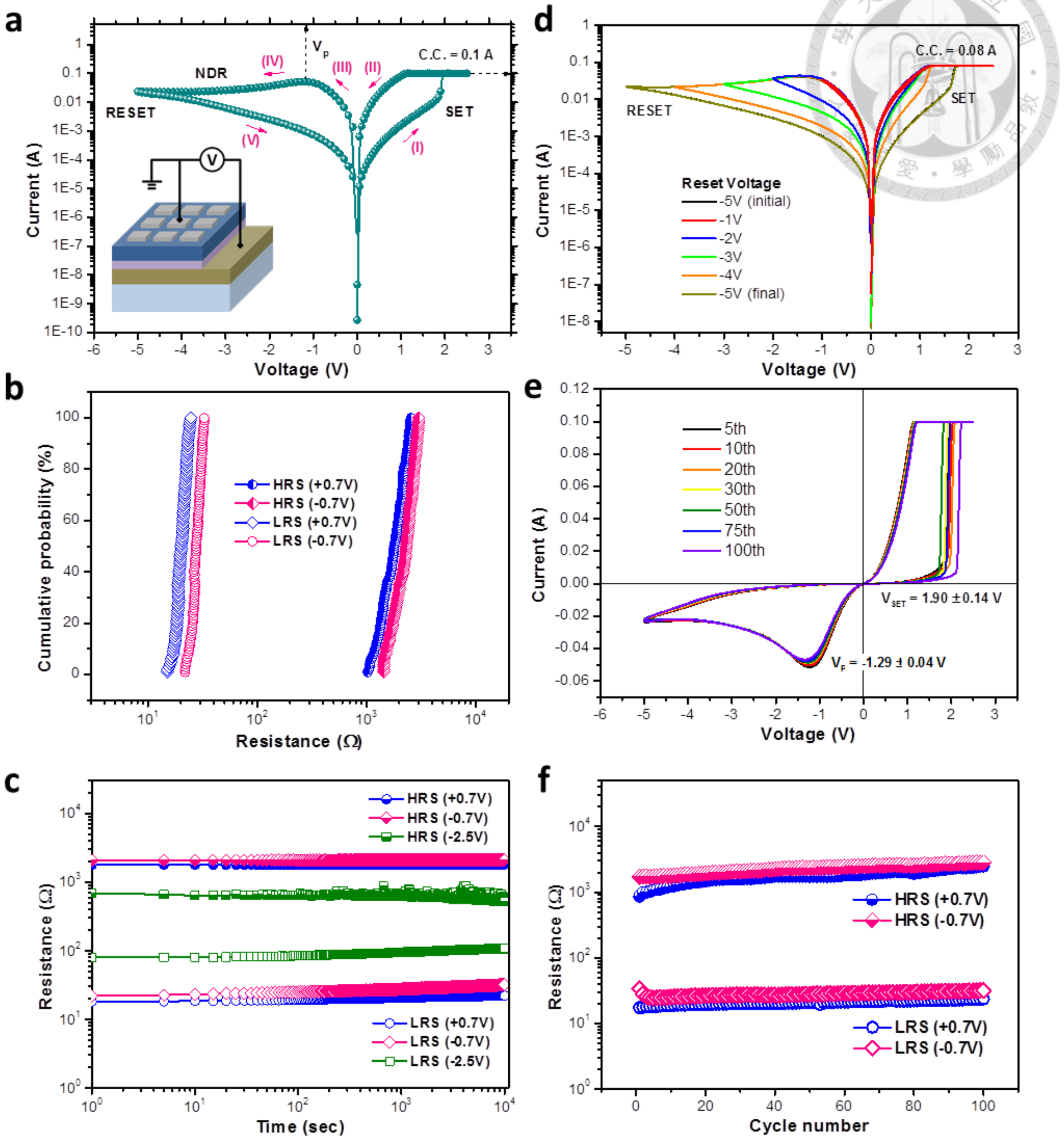

Figure 5.2 (a) I-V characteristics of a Pt/ZnO/MoS_2/Mo heterojunction device, where C.C. denotes compliance current and NDR refers to negative differential resistance; (b) Cumulative distribution of the HRS/LRS for the Pt/ZnO/MoS_2/Mo devices at both forward and reverse biases; (c) Retention test of a Pt/ZnO/MoS_2/Mo device at both forward and reverse biases; (d) I-V characteristics of a Pt/ZnO/MoS_2/Mo device with lower C.C. (0.08A) and various RESET voltages; (e) and (f) Endurance test of a Pt/ZnO/MoS_2/Mo device for 100 cycles.

This process is named as a SET or forming process. The resistance changes can be attributed to the formation of the conducting channels in the active material.[1] When reversing the bias, the system remains at LRS and continues to increase current to the maximum value where the voltage reaches V_P (step (III)). After V_P, the current gradually decreases (step (IV)), and the system performs a negative differential resistance (NDR). When the voltage sweeps back from -5 V to 0 V, the system follows a HRS path (step (V)). It is obvious that our system obeys a bipolar switching behavior because the resistance changes with changing the electric-field direction. It is noted that there is no distinct RESET process and no electroforming step in our case, which is different from most of the ZnO-based RRAM devices.[2-4]

Figure 5.2(b) shows cumulative probability distributions of resistances at HRS/LRS by a read voltage of 0.7 V at both forward and reverse biases. The statistic distributions of the resistances for 100 cells are nearly vertical with a slight fluctuation, indicating the switching behavior is very uniform. The ON/OFF current ratio at 0.7 V is calculated as $\sim 10^2$. The retention test was carried out to evaluate the ability of nonvolatile data storage, as illustrated in Figure 5.2(c). At the read voltage of 0.7 V, HRS/LRS for both forward and reverse biases show good retention characteristics up to 10^4 sec without obvious degradation. However, the system becomes unstable when we read the device at NDR region (-2.5 V). This implies the NDR could be a dynamically metastable state rather than a thermodynamic stable state.

Figure 5.2(d) shows the I-V curve of a Pt/ZnO/MoS_2/Mo device with lower C.C. (0.08 A) compared to Figure 5.2(a) and various RESET voltages (V_{RESET}). When the C.C. decreases from 0.1 A to 0.08 A, the HRS is found to decrease while the LRS increases, resulting in smaller ON/OFF current ratio. If the V_{RESET} is further reduced from -5 V to -2 V, it is obvious that the current at LRS does not change so as the V_P, but

doi:10.6342/NTU201603487

the HRS dramatically evolves with the V_{RESET}. Noted that SET voltage (V_{SET}) is also strongly affected by the V_{RESET}. There is no distinguishable V_{SET} when the $V_{RESET} < -3$ V. The V_{RESET}-dependent V_{SET} property could be related to the interfacial properties at ZnO/MoS_2 in the device. The endurance test is illustrated in Figure 5.2(e) and 5.2(f), where it exhibits the switching behavior is stable for at least 100 cycles. The variations in the V_{SET} reveal that the conducting channels formed in the active material vary with cycles, whereas V_P corresponding to the rupture of the conducting channels shows a relatively stable value at around 1.29 V.

5.2.2 Junction properties in Pt/ZnO/MoS_2/Mo

Interface properties have been considered as the dominant factor in most of the transition-metal-oxide based memristors. Since our device has multi-junctions, the junction properties need to be clarified for the resistive switching behavior. Figure 5.3(a) illustrates the I-V curves of the Pt/ZnO/Mo device, where a bipolar behavior is observed. Distinct resistance switching from HRS to LRS occurs in the SET process. At the LRS, the device exhibits an ohmic-like behavior. When we change the potential sweeping, high C.C. (0.1 A and 0.05 A) case gives rise to unstable RESET process. The dielectric breakdown could be attributed to the thermal effects induced by the high current density. Operating the device at low C.C. (0.01 A) can obtain a stable resistive switching behavior with clear SET and RESET features. However, the electroforming process is required. The ON/OFF current ratio ($\sim 10^2$) and the V_{SET} in the Pt/ZnO/Mo device are similar to those of the Pt/ZnO/MoS_2/Mo device, implying the SET process in the later device may relate to the Pt/ZnO interface.

Figure 5.3(b) illustrates the I-V curves of the Pt/MoS_2/Mo device, where the MoS_2 is dual-oriented and derived from 5 nm MoO_3 (MS5). The device also exhibits a bipolar

doi:10.6342/NTU201603487

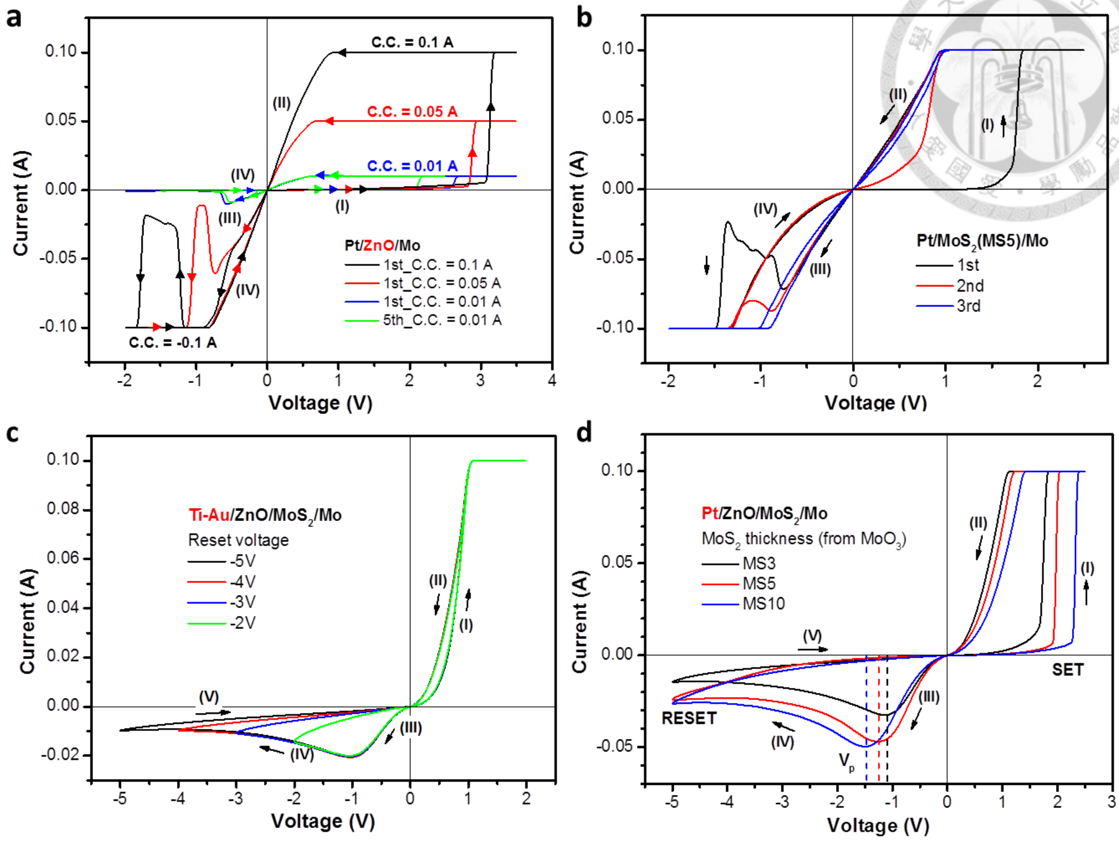

Figure 5.3 (a) I-V characteristics of a Pt/ZnO/Mo device with various compliance currents; (b) I-V characteristics of a Pt/MoS_2/Mo device; (c) I-V characteristics of a Ti-Au//ZnO/MoS_2/Mo device with various V_{RESET}; (d) I-V characteristics of Pt/ZnO/MoS_2/Mo devices with various MoS_2 thicknesses.

character with ohmic-like LRS as Pt/ZnO/Mo, but dramatic degradation occurs within few cycles under C.C = 0.1 A. Figure 5.3(c) illustrates the I-V curves of the Ti-Au//ZnO/MoS_2/Mo device, where the Ti-Au is an ohmic metal to ZnO. This configuration allows us to explore the ZnO/MoS_2 junction. At forward bias, the device exhibits unclear SET process with small hysteresis, while the curve features are quite similar to Pt/ZnO/MoS_2/Mo device at reverse bias (Figure 5.2(d)). It is worth to notice that devices of only ZnO or MoS_2 show ohmic-like LRS, but combining those two brings about the non-linear curve at LRS, indicating a junction barrier probably exists at the interface. Utilizing Ti-Au as the TE does not show V_{RESET}-dependent V_{SET} behavior, which could be owing to unclear SET process. This also implies Pt is a better TE to obtain high ON/OFF current ratio in the device.

Since the MoS_2 in our devices is dual-oriented, different ratio of t-MoS_2 to e-MoS_2 may lead to various behaviors in I-V measurement. Figure 5.3(d) illustrates the I-V curves of Pt/ZnO/MoS_2/Mo devices with various MoS_2 thicknesses, where the MoS_2 thickness is controlled by the deposited MoO_3. It is obvious that thicker MoS_2 exhibits larger V_{SET} and V_P at HRS, while the conductivity at LRS is also lower. Among these three thicknesses, MS5 has the largest ON/OFF current ratio at low read voltage, especially under reverse bias, which probably arises from it compromises the conductivity and the ZnO/MoS_2 junction properties. Thus, the following analyses will focus on this specimen.

5.3 Transport properties

5.3.1 Effects of carrier trapping

Trapping and detrapping of the charge carriers at the metal-semicondoctor interface or in the bulk of the semicondoctor has been considered as the main mechanism on the electronic conduction in the ZnO-based memristor.[5] This trapping/detrapping character is based on the space-charge-limited (SCL) conduction with filled or unfilled traps.[6] SCL conduction with no traps can be described by Child's law:

$$J = \frac{9\epsilon_0\epsilon_r\mu V^2}{8d^3} \tag{5.1}$$

where J is the current density, ϵ_0 is the permittivity of free space, ϵ_r is the static

doi:10.6342/NTU201603487

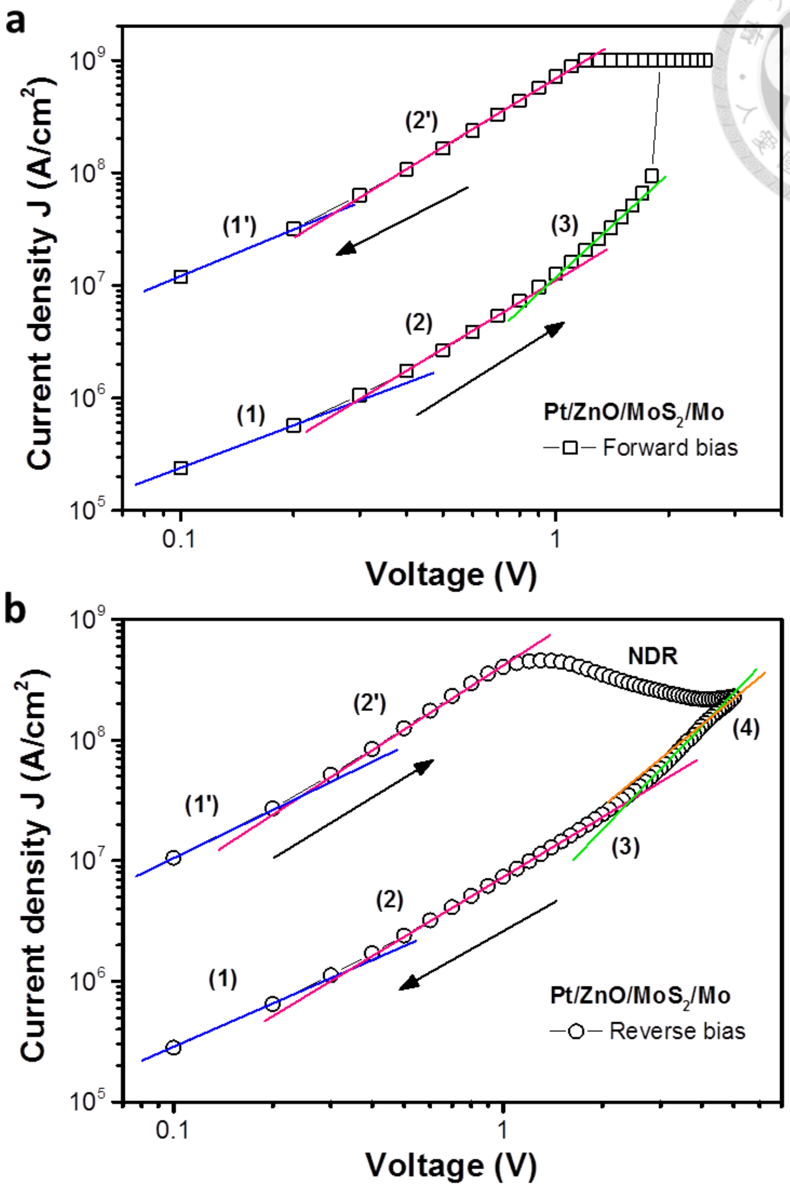

Figure 5.4 I-V characteristics of a Pt/ZnO/MoS_2/Mo device in a double-logarithmic plot: (a) forward bias and (b) reverse bias. Arrow indicates sweeping directions.

Table 5.1 Fitting slopes in Figure 5.4.

Bias	HRS				LRS		E_t (from (3))
$J \propto V^{\alpha}$	(1)	(2)	(3)	(4)	(1′)	(2′)	(meV)
	Ohmic	SCL	TFL	SCL	Ohmic	SCL	
Forward	1.26	2.02	3.08		1.43	2.04	53.8
Reverse	1.2	1.67	2.83	2.29	1.36	1.78	47.3

dielectric constant of the semiconductor, μ is the carrier mobility, and d is the semiconductor thickness. When the traps are confined in single or multiple discrete energy levels locating near the conduction band edge (called shallow traps), the form of SCL conduction is given by:

$$J = \frac{9\epsilon_0\epsilon_r\mu V^2}{8d^3}\theta \tag{5.2}$$

in which $\theta = \mathrm{P}/(\mathrm{P} + \mathrm{P}_t)$, where P is the density of free carriers and P_t is the density of the trapped carriers. When the traps distributed exponentially within the forbidden energy gap, at high injection current, the filling traps results in the current being governed by the density and energy distribution of the traps.[7] Then, the SCL conduction can be expressed as:

$$J = q^{1-l}\mu N_C\left(\frac{2l+1}{l+1}\right)^{l+1}\left(\frac{l}{l+1}\frac{\epsilon_0\epsilon_r}{N_t}\right)^{l}\frac{V^{l+1}}{d^{2l+1}} \tag{5.3}$$

with $l = T_C/T$, where T_C is a characteristic temperature related to the trap distribution and is given by $T_C = \mathrm{Et}/k$. $\mathrm{N_C}$ is the density of states in the conduction band and k is the Boltzmann constant. Et is the characteristic energy of the exponential distribution and marks the width of the exponentially distributed traps. Small Et leads to trap distributions varying rapidly with energy, while large Et approximates a slowly varying trap distribution.

Figure 5.4 illustrates the I-V curves of a Pt/ZnO/$\mathrm{MoS_2}$/Mo heterojunction device in a double-logarithmic plot. The linear fitting results are listed in Table 5.1. At low current injection in forward bias (Figure 5.4(a)), both HRS and LRS show ohmic-like conduction. With increasing applied bias, it will become SCL conducting mode. Under

doi:10.6342/NTU201603487

high current injection, trap-filled limit (TFL) conduction is observed at HRS. The filled traps with electrons will lead to the sudden current jump corresponding to the SET process. The trapping/detrapping behavior in the reverse bias (Figure 5.4(b)) is similar to that in the forward bias, but the calculated slopes are smaller for the SCL conduction. The smaller slopes indicate the SCL conduction is controlled by single shallow traps which is close enough to the conduction band to be in thermal equilibrium with electrons in the conduction band.[7] The additional trap-free SCL conduction at high voltage implies the saturated hysteresis and resistance change when all the traps are filled by the injected carriers into exponentially distributed energy. Thus, the shifts in the conduction modes at the HRS for the reverse bias case depend on the carrier trapping level. When reducing the sweep voltage, the trapping level decreases with the injecting carrier density. The lower Et at reverse bias indicates the narrower energy distribution resulting in rapid switch of the conduction mode.

5.3.2 Effects of ion migration

Except for the electronic conduction, ionic transport is another dominant factor for the resistive switching behavior in ZnO-based memristors.[8] The resistance switching between HRS and LRS is attributed to the formation and rupture of the conduction channels in the dielectric layer, which has been directly observed by in-situ TEM images.[9] The conducting channel in ZnO originates from its intrinsic defect, which is oxygen vacancy (V_O). The positive charged V_O will migrate in the ZnO bulk toward the interface under high electric field. The contribute current can be described as:[10]

$$i_{VO} \propto \frac{FA\mu_{VO}C_{VO}\Delta E}{d} \propto \nabla E \tag{5.4}$$

doi:10.6342/NTU201603487

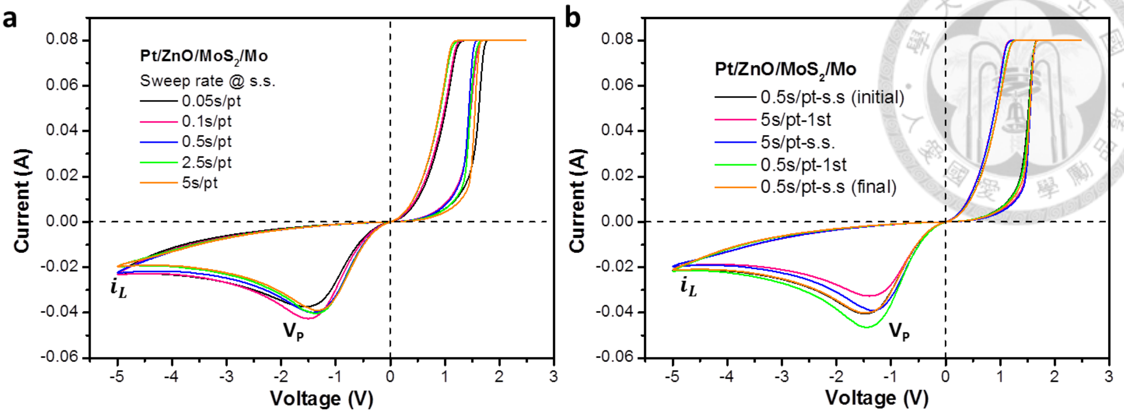

Figure 5.5 I-V characteristics of a Pt/ZnO/MoS$_2$/Mo device (a) with various sweep rates and (b) with switching sweep rate between 0.5 s/pt and 5 s/pt. S.S. denotes the steady state.

where F is the Faraday constant, A is the cross-section area, μ_O is the mobility of V_O in the bulk ZnO, and C_O is the concentration of V_O. From Eq. (5.4), the current at steady state is proportional to the potential gradient within the ZnO, which implies that changing the sweeping rate (dV/dt) may lead to the fluctuation of the migration current. This strategy has been adopted to study the NDR properties in Cu_2S/ZnO, where Cu^+ is responsible for the migration ion.[11]

Figure 5.5(a) illustrates the I-V curves of a Pt/ZnO/MoS$_2$/Mo device performed with various sweep rates at steady state. The sweep rate of 0.5 s/pt is the parameter that we generally adopt for recording I-V curves. When the sweet rate reduces, V_P at reverse bias and the current at $1/2V_P$ decrease, while the limiting current (i_L) slightly increases. Increasing the sweep rates will obtain opposite results. Same behavior can be observed when we suddenly switch the sweep rate between slow (5 s/pt) and fast (0.5 s/pt), as illustrated in Figure 5.5(b). This sweep-rate dependent current and V_P characteristics reveal the relations between NDR and the V_O migration.

5.3.3 Temperature-dependent I-V measurement

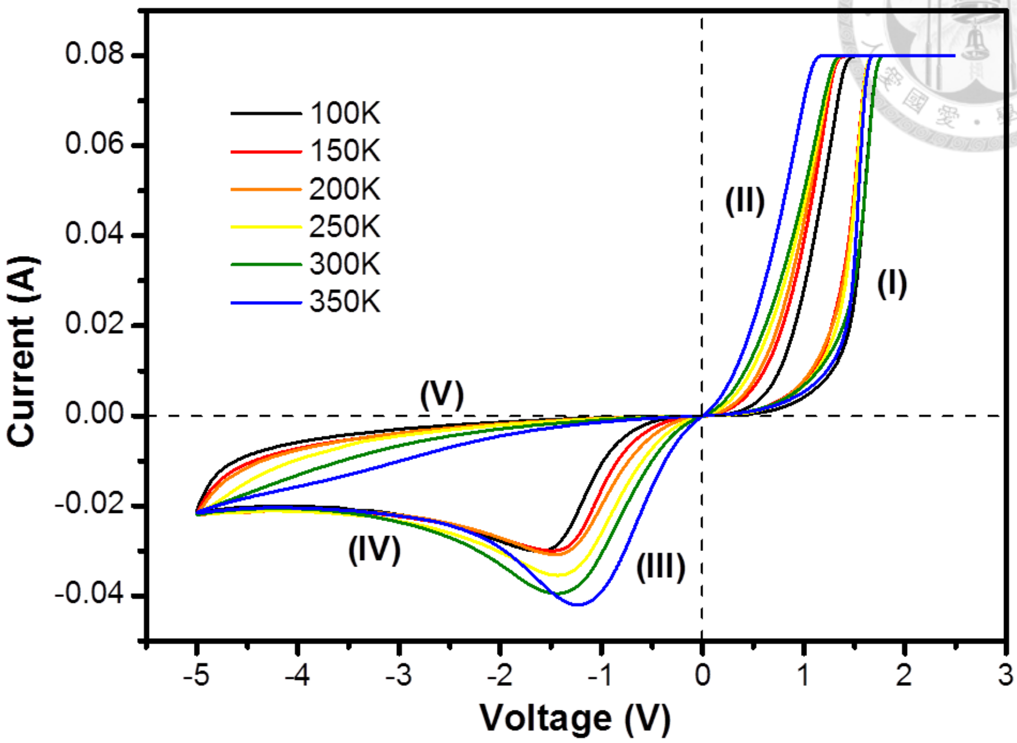

Figure 5.6 I-V characteristics of a Pt/ZnO/MoS_2/Mo device at various temperatures

To further explore the transport properties in the Pt/ZnO/MoS_2/Mo heterojunction device, the temperature-dependent I-V curves were performed, as illustrated in Figure 5.6. It is obvious that among the five steps in a full cycle, step (I) and (IV) are less dependent on the temperature change, while step (II), (III), and (V) are highly temperature dependent. Step (I) is a SET process and is related to the Pt/ZnO interface. The formation of the conducting channels due to the migration of V_O toward the Pt/ZnO interface assists the filled trap conduction of electrons, which switch the resistance from HRS to LRS at forward bias. Although the conductivity of ZnO and the mass transport of V_O will be degrades with increased temperatures, sufficient concentration of V_O in the ZnO may decoupled the relation between V_{SET} and temperature.

Step (II) and (III) are LRS at forward and reverse biases, respectively. The I-V

doi:10.6342/NTU201603487

behavior at this state can be correlated to the ZnO/MoS_2 interface, which is expected to have a barrier based on the band alignment. The electronic conduction at LRS is dominated by the ohmic behavior at low current injection and SCL conduction (with single shallow traps) at higher applied voltage. Both ZnO and MoS_2 are semiconductors. The conductivity will decrease as temperature decreases, which also affects the conduction at low bias. SCL conduction is in principle independent of temperature (Eq. (5.2)). However, the SCL conduction here accompanies with the mass transport of VO, which will be retarded at the low temperature due to the lower mobility leading to slow current response. Moreover, part of the carriers transport across the ZnO/MoS_2 junction barrier through thermionic emission will also be reduced at low temperature.

Step (IV) is the NDR region with the limiting current of around 0.02 A. At the limiting condition, the positive and negative charge carriers are highly separated in the ZnO, which induced a strong electric field opposite to the applied direction. The inverse E-field will limit the carrier transport like the trap-free SCL conduction mode. The highly accumulated electrons at the Pt/ZnO interface under reverse bias may follow the Fwoler-Nordheim (F-N) tunneling path way to overcome the high Schottky barrier at the interface. However, the number of electrons that are available for tunneling may be limited by the space charge distribution. Both SCL conduction and F-N tunneling are temperature independent, and the dynamic balance between them gives rise to the stable limiting current. At step (V),

The highly polarized ZnO at high reverse bias in step (IV) will act like a capacitor (electrons at Pt/ZnO interface and V_O at ZnO/MoS_2 interface). When the voltage further sweeps back from -5 V to 0 V (step (V)), high concentration gradient of the carriers will detached from the interface to the bulk by the diffusion. At low temperature, diffusion rate is low. The capacitance effect induced by the polarized carriers will lead to the

doi:10.6342/NTU201603487

current drop when the $\partial V/\partial t$ switches from positive to negative. At high temperature, high mobility of the carriers will reduce the polarization effect and have high current at HRS.

5.3.4 Origin of the NDR in Pt/ZnO/MoS_2/Mo

It is worth to note that the RESET process in the Pt/ZnO/MoS_2/Mo is not distinct as pure ZnO or pure MoS_2 based devices.(ref) The unique V_{RESET}-dependence of V_{SET} is also first observed in our system (Figure 5.2(d)). Thus, exploring the origin of the NRD at reverse bias is required to understand the full picture of the resistive switching mechanism. Figure 5.7(a) illustrates the evolution of the peak current (I_P) and voltage (V_P) with temperature at reverse bias. When the operating temperature increases, I_P increases, but V_P decreases. V_P originates from the max current before the rupture of the conducting channels, which is related to the migration of the V_O from Pt/ZnO interface toward the bulk ZnO. Lower V_P indicates the faster rupture of the conducting channels due to the higher V_O migration rate at high temperature. This circumstance becomes more severe as the temperature higher than 300 K. The increase of the max current with temperature can be attributed to the increase of material conductivity and more carriers transport through the barrier at ZnO/MoS_2 due to the thermal effect. The black dash line in Figure 5.7(a) represents the tolerable power output at various temperatures, where 300 K has the maximum value implying the high ON/OFF current ratio can be obtained at this temperature. High I_P and proper V_P make 300 K as the better operation temperature for the Pt/ZnO/MoS_2/Mo device.

From Figure 5.6, we can calculate the activation energy (Ea) at HRS and LRS by the Arrhenius equation, as illustrated in Figure 5.7(b). Regardless the direction of potential sweep, LRS has larger Ea than HRS, and Ea decreases as voltage increases.

doi:10.6342/NTU201603487

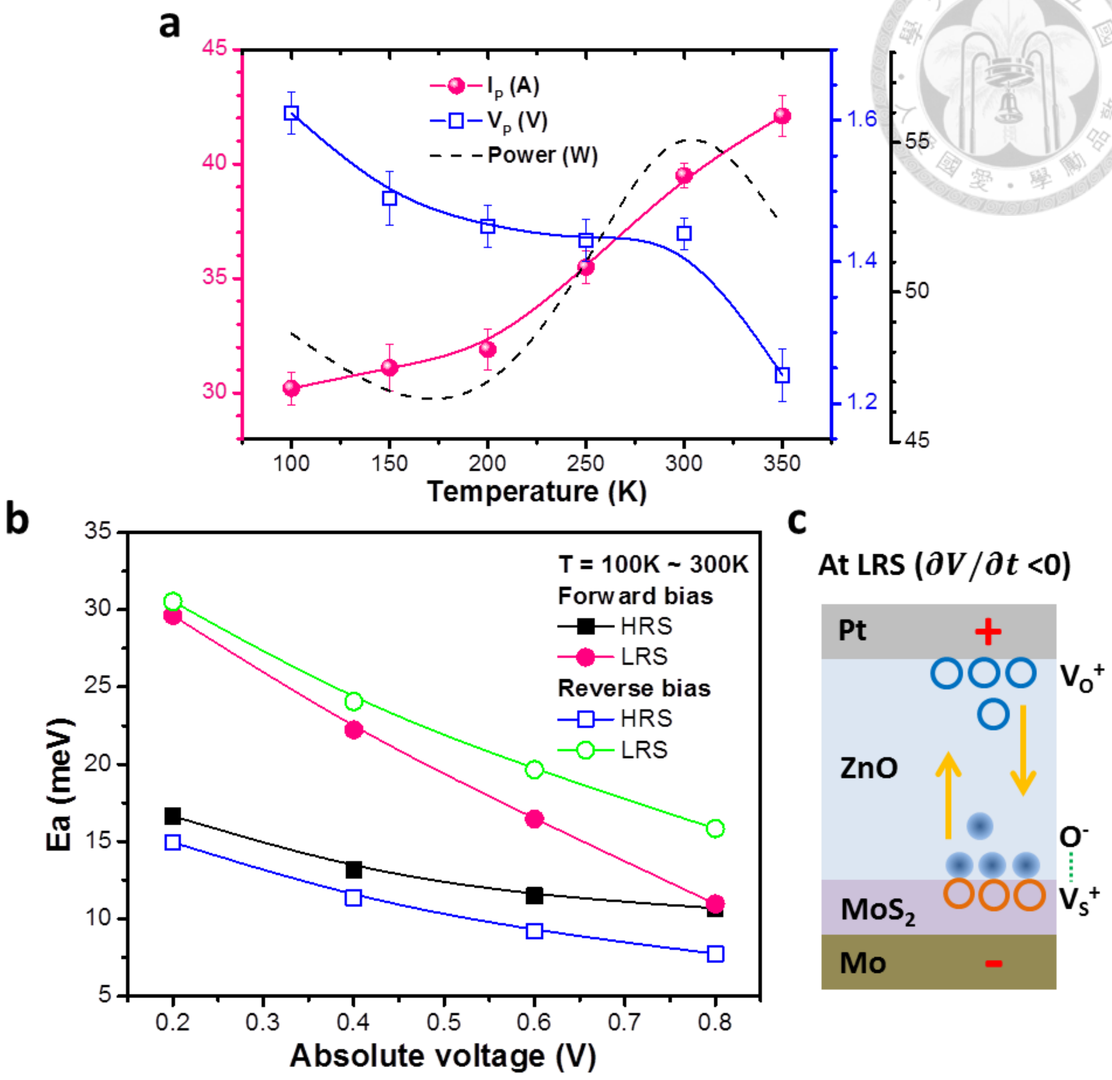

Figure 5.7 (a) Evolutions of peak current and peak voltage with temperature at reverse bias; (b) Evolution of estimated activation energy at HRS and LRS with absolute voltage; (c) Schematic illustration of interaction between sulfur vacancies from MoS_2 surface and oxygen atoms from ZnO under reverse bias.

In general, Ea at LRS shall much less than that at HRS due to the injected electrons move in the conduction band of the dielectric layer after the trap sites are filled.[12] However, we obtain an opposite results in our device, which indicates the switching mechanism in the Pt/ZnO/MoS_2/Mo is different from other system.

The low values of Ea in our system represents that the traps in ZnO or MoS_2 can be easily filled, implying the electronic conduction is not the main cause for the different I-V behavior. On the other hand, the transport of V_O is the key factor to switch the resistance in the ZnO-based memristor. If the transport scheme is disturbed, it will lead to different I-V response. As a result of the thin MoS_2 layer, our system can be regarded as a ZnO-based memristor with the interface modified by a MoS_2 layer. Thus, the ZnO/MoS_2 interface plays an important role to alter the ionic transportation.

A lot of defects have been discovered at the MoS_2 surface, especially the sulfur vacancies, which will create the donor-like surface states, as described in Chapter 3. When ZnO contacts with the MoS_2 surface, the oxygen atoms from ZnO may be bound with these surface states physically or probably partially oxidize surface MoS_2 due to the high electron negativity, as shown in Figure 5.7(c). If this circumstance occurs, migration of V_O in the ZnO toward ZnO/MoS_2 interface at reverse bias might be retarded, resulting in a wide RESET process (step (IV)). At LRS, it presumably accompanies the chemical reduction of the surface MoS_2, while it is an oxidation process for MoS_2 surface at HRS. The lower Ea at HRS may be attributed to the easier oxygen adsorption on the surface defect sites of MoS_2. The decrease of Ea with voltage can be imagined like climbing the potential surface with increasing applied bias. The reduction and oxidation rates may approach comparable values at high bias, which results in less difference in Ea. The V_{RESET}-dependent V_{SET} feature may also be explained by the surface reduction of MoS_2. The less reduction of the MoS_2 surface at low V_{RESET} indicates less V_O reaches the ZnO/MoS_2 interface and most V_O stays at Pt/ZnO interface, which facilitates the SET process and reduce the V_{SET}. Since the redox reaction may take place at the ZnO/MoS_2 interface, our device shall belong to a valence change memory.

doi:10.6342/NTU201603487

5.4 ZnO/MoS$_2$ interface

Based on our previous proposition, the adsorption and desorption of oxygen from the ZnO/MoS$_2$ interface dominates the I-V behavior in the Pt/ZnO/MoS$_2$/Mo device. This process will change the chemical states of MoS$_2$ surface so we measured the XPS spectra for the MoS$_2$ specimens with and without ZnO deposition, as illustrated in Figure 5.8(a). To carry out the XPS measurements, the ZnO was deposited by ALD with 20 cycles for around 2 nm in thickness on MoS$_2$ surface. It is obvious that the binding energies of both Mo-3*d* and S-2*p* core levels downshift for around 0.4 eV after few nm of ZnO grown on the MoS$_2$ surface. The downshift in BE can be attributed to the charge transfer between MoS$_2$ and ZnO. In addition, there is a small peak at around 231 eV in the Mo-3*d* spectra after ZnO deposition, which can be assigned as the Mo^{5+} indicating slightly oxidation of the MoS$_2$ surface may take place.[13] The PL spectrum of ALD-ZnO was also identified to confirm the quality as shown in Figure 5.8(b). The

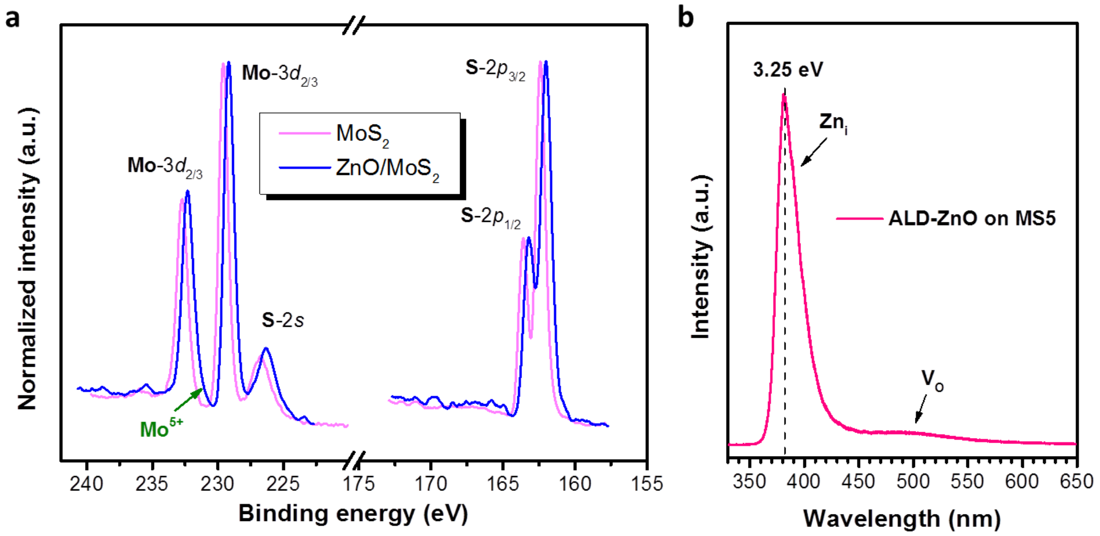

Figure 5.8 (a) XPS spectra of Mo-3*d* and S-2*p* before and after ZnO deposition; (b) PL spectrum of ALD-ZnO grown on the MoS$_2$ (MS5).

main peak at ~382 nm arises from the bandgap emission of ZnO, corresponding the to the optical bandgap energy of 3.25 eV. The side shoulder peak at ~390 nm and a broad peak located at ~500 nm can be referred to the Zn interstitial (Zn_i) and the oxygen vacancy (V_O), respectively, which implies the ALD-ZnO is n-type.[14, 15]

Since both MoS_2 and ZnO are n-type semiconductors, the junction barrier between them shall depend on their band positons and the Fermi level positions. The schematic band diagram of ZnO and MoS_2 before contact is depicted in Figure 5.9(a). In our case, ALD-ZnO has Zn_i and V_O as the electron donors (Figure 5.8(b)). The carrier concentration in the ALD-ZnO could be higher than that in the MoS_2, leading to higher Fermi level position. Accordingly, when they contact each other, it may form an ideal n-n^+ heterojunction with a small barrier at ZnO conduction band and an electron trap at MoS_2 side as illustrated in Figure 5.9(b). However, the XPS results reveal the charge transfer between MoS_2 and ZnO, and the oxidation of MoS_2 surface (Figure 5.8(a)). This will result in the smaller band bending at the ZnO/MoS_2 junction, and the formation of the interface states, as shown in Figure 5.9(c). The lower barrier at the ZnO/MoS_2 interface facilitates the electron conduction, while the interface states may

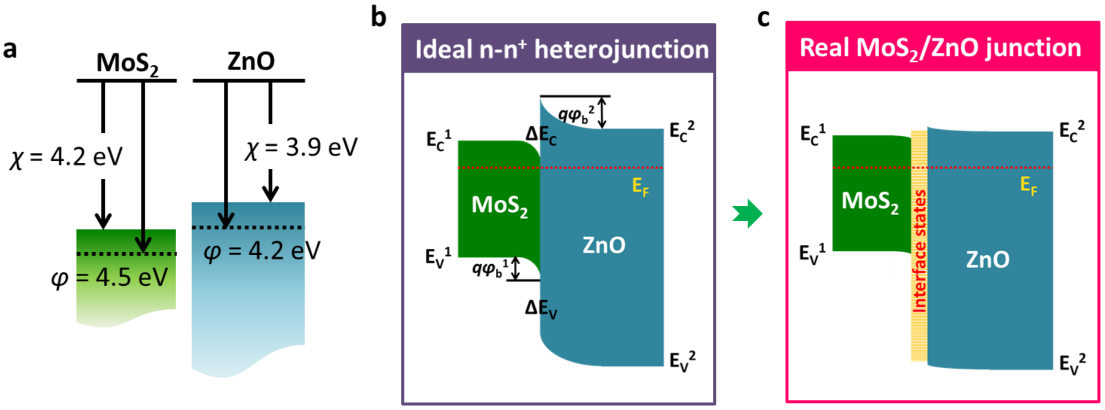

Figure 5.9 Schematic band diagrams of MoS_2 and ZnO: (a) before contact, (b) ideal junction, and (c) real junction.

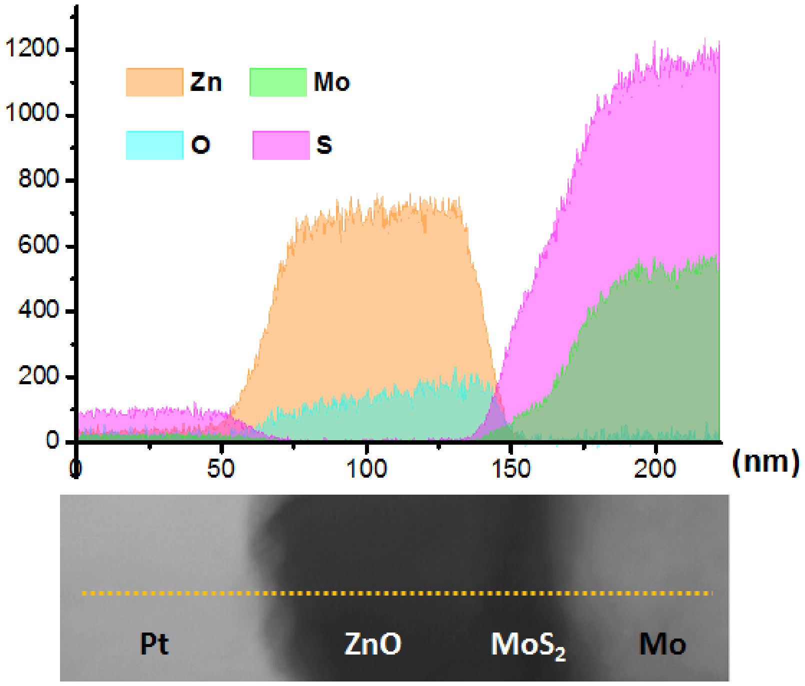

Figure 5.10 STEM-EDX line scan profiles of a Pt/ZnO/MoS$_2$/Mo heterojunction device.

become the trap centers, leading to the non-linear I-V behavior at LRS.

To further examine the composition at the ZnO/MoS$_2$ interface, the EDX analysis in the STEM mode was performed with the line-scan, as illustrated in Figure 5.10. It is obvious that the oxygen has the concentration gradient in the ZnO, which elucidates the existence of the V_O in the ZnO and it is responsible for the resistive switching. The oxygen-rich feature at ZnO/MoS$_2$ interface also supports the proposition that oxygen favors to bind with MoS$_2$ due to the donor-like surface states, which increases the Ea at LRS and extends the RESET process at NDR region.

5.5 Switching mechanism

Resistive switching in the Pt/ZnO/MoS$_2$/Mo heterojunction device is not a purely electronic behavior, but also involves the ionic transportation for the conduction. Figure

5.11 shows simplified diagrams of the proposed switching mechanism. Generally, the I-V feature at HRS is dominated by the ZnO and Pt/ZnO interface, while ZnO/MoS_2 dominates the LRS.

According to previous discussions, the mechanism can be described by the trapping/detrapping controlled (SCL) transport at HRS, where the traps are easily filled due to the low Ea. Meanwhile, the Vo transport in the ZnO will cause formation and rupture processes of the conducting channels, which assist to the resistance switches between HRS and LRS. The transition of the charge trapping modes at HRS corresponds to fill the trap sites from shallow to deep in the energy level. The ZnO in our device has revealed two donor defects of Zn_i and V_O from the PL spectrum (Figure 5.8(b)). The former one is a shallow defect, while the later one is in a deep energy level.[15] At low injection current, the shallow defect (Zn_i) may contribute to the SCL conduction. With increasing the applied voltage, V_O tends to move toward Pt/ZnO side, which may produce more deep defects in ZnO at the interface. The distribution characteristic of these defects in energy could be expressed by Et. Once these deep traps start being filled at high forward bias, trap-filled limit (TFL) behavior will exhibit.

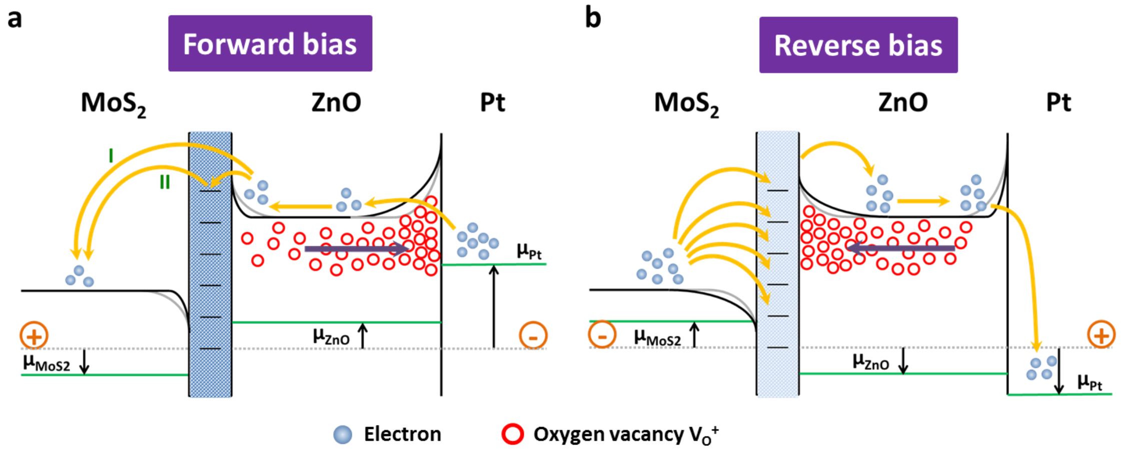

Figure 5.11 Schematic diagrams illustrate the proposed resistive switching mechanism at (a) forward bias and (b) reverse bias.

After all the traps are filled and the V_O conducting channels form at the Pt/ZnO interface, SET process takes place leading to resistance drop suddenly, when the electron mainly transports in the ZnO conduction band.

On the other hand, the transport barrier formed at ZnO and MoS_2 interface after the band alignment results in nonlinear I-V behavior at LRS when applied low bias. Carriers will transport through the barrier by either thermal effect or trap assisted hopping (scheme I and II in Figure 5.11(a)) At forward bias, the trap states in the ZnO/MoS_2 are filled. Electronic conduction will then be dominated by Pt/Zn, especially for HRS. The formation of the interface states at the ZnO/MoS_2 results in the NDR feature corresponding to the desorption of oxygen from MoS_2 at the interface and high Ea. The RESET potential determines the reduction reaction at ZnO/MoS_2 or the oxidation reaction at Pt/ZnO. The less amount of V_O (or more stoichiometric ZnO) left at Pt/ZnO, the more stable junction properties leading to stable SET process. At reverse bias, the trap states in the ZnO/MoS_2 are refilling (Figure 5.11(b)). The highly separated carriers at Pt/ZnO and ZnO/MoS_2 generates opposite E-field to limit the further charge separation. Electrons transport through Pt/ZnO may follow F-N tunneling, which is independent with temperature variation.

5.6 Summary

A hybrid 2D-MoS_2 and 3D-ZnO hexagonal material has been applied as a memory. Pt/ZnO/MoS_2/Mo heterojunction device were successfully fabricated. The I-V characteristics illustrate the bipolar behavior with ON/OFF current ratio ~10^2. Good endurance and retention at read voltage of 0.7 V are also demonstrated which could be attributed to the dual orientation of MoS_2. E-MoS_2 offer good conduction between Mo

doi:10.6342/NTU201603487

BE and t-MoS_2, and t-MoS_2 has better chemical stability for ZnO/MoS_2 interface. Three unique characteristics are observed in our I-V curves: non-linear LRS, long RESET process, and V_{RESET}-dependent V_{SET}. At positive potential sweep (HRS, $\partial V/\partial t > 0$), Pt/ZnO controls the electronic conduction, where trapping/detrapping and the V_O migration are the major mechanism. At negative potential sweep (LRS, $\partial V/\partial t < 0$), the interface states formed at ZnO/MoS_2 dominate the RESET and NDR properties, which further influences V_{SET}. The Pt/ZnO/MoS_2/Mo device has shown the dual-oriented MoS_2 can be applied in electronics. Since both ZnO and MoS_2 have good photo-response, our device may create additional states for multi-bits by shining light or for other optoelectronic applications. Other oxide-MoS_2 or TMD-based heterojunction devices may also exhibit unique properties for novel applications.

doi:10.6342/NTU201603487

References

[1] R. Waser and M. Aono, Nat. Mater. **6**, 833-840 (2007).

[2] J. Qi, M. Olmedo, J. Ren, N. Zhan, J. Zhao, J. G. Zheng and J. Liu, ACS Nano **6** (2), 1051-1058 (2012).

[3] C. H. Huang, J. S. Huang, S. M. Lin, W. Y. Chang, J. H. He and Y. L. Chueh, ACS Nano **6** (9), 8407-8414 (2012).

[4] X. Zhu, W. Su, Y. Liu, B. Hu, L. Pan, W. Lu, J. Zhang and R. W. Li, Adv. Mater. **24** (29), 3941-3946 (2012).

[5] C. H. Huang, J. S. Huang, C. C. Lai, H. W. Huang, S. J. Lin and Y. L. Chueh, ACS Appl. Mater. Interfaces **5** (13), 6017-6023 (2013).

[6] K.-C. Kao and W. Hwang, *Electrical transport in solids : with particular reference to organic semiconductors*. (Pergamon Press, New York, 1981).

[7] D. S. Shang, Q. Wang, L. D. Chen, R. Dong, X. M. Li and W. Q. Zhang, Phys. Rev. B **73** (24) (2006).

[8] X. Huang, K. C. Chang, T. C. Chang, T. M. Tsai, C. C. Shih, R. Zhang, S. Y. Huang, K. H. Chen, J. H. Chen, H. J. Wang, W. J. Chen, F. Zhang, C. Chen and S. M. Sze, IEEE Electron. Device Lett. **35** (2), 1227-1229 (2014).

[9] J. Y. Chen, C. L. Hsin, C. W. Huang, C. H. Chiu, Y. T. Huang, S. J. Lin, W. W. Wu and L. J. Chen, Nano Lett. **13** (8), 3671-3677 (2013).

[10] A. J. Bard and L. R. Faulkner, *Electrochemical methods : fundamentals and applications*. (Wiley, New York, 2001).

[11] X. Liu, M. T. Mayer and D. Wang, Appl. Phys. Lett. **96** (22), 223103 (2010).

[12] K. M. Kim, B. J. Choi, M. H. Lee, G. H. Kim, S. J. Song, J. Y. Seok, J. H. Yoon, S. Han and C. S. Hwang, Nanotechnology **22** (25), 254010 (2011).

doi:10.6342/NTU201603487

[13] T. Weber, J. C. Muijsers, J. H. M. C. Van Wolput, C. P. J. Verhagen and J. W. Niemantsverdriet, J. Phys. Chem. **100** (33), 14144-14150 (1996).

[14] M. D. McCluskey and S. J. Jokela, J. Appl. Phys. **106** (7), 071101 (2009).

[15] S. Al-Hilli and M. Willander, Sensors (Basel) **9** (9), 7445-7480 (2009).

doi:10.6342/NTU201603487

Chapter 6 Substrate Effects on MoS$_2$ Growth and ALD Process

In this chapter, MoS$_2$ thin films grown on various substrates in previous results are compared. The surface properties of MoS$_2$ are found to influenced by the growth substrate and further affect the ZnO deposition during the ALD process. Surface treatment is adopted to modify the MoS$_2$ surface and eventually improves the ALD efficiency.

6.1 Growing MoS$_2$ on various substrates

In our previous results, we have demonstrated MoS$_2$ thin film can be easily grown on various substrates by two-step CVD process, such as a substrate with a dielectric layer on the surface (SiO$_2$-Si in chapter 3), or a conducting substrate (graphene paper in chapter 3 and Mo-glass in chapter 4). Among these substrates, SiO$_2$-Si and graphene paper (GP) can survive at high temperature sulfurization (1000^{o}C), but Mo-glass (MG) can only tolerant sulfurization at relatively low temperature (~500^{o}C). Here, we adopt SiO$_2$/Si as a standard to compare the substrate effect for MoS$_2$ growth.

Figure 6.1(a) to Figure 6.1(c) show the photographs and corresponding AFM or SEM images of MoS$_2$ grown on various substrates at 500^{o}C and 1000^{o}C, respectively. From the AFM images in Figure 6.1(a), it is clear that MoS$_2$ grown at 1000^{o}C has much larger grain size (~200 nm) than that at 500^{o}C (~50 nm). It also depicts that MoS$_2$ can be grown in a large scale with a smooth surface topography regardless the type of substrates.

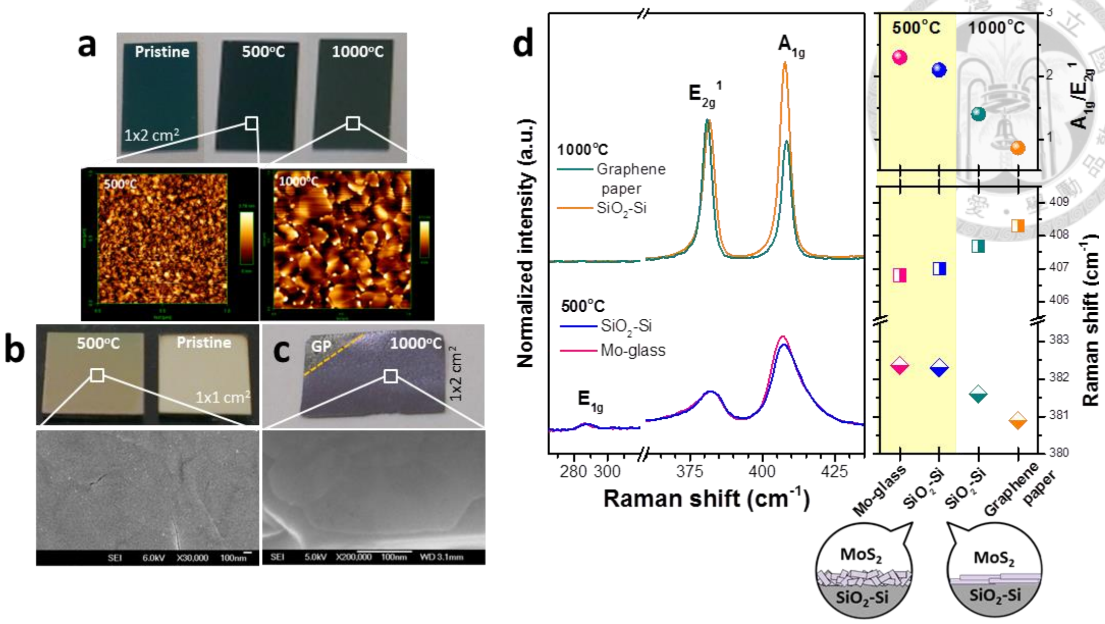

Figure 6.1 MoS_2 thin film grew on (a) SiO_2-Si, (b) Mo-glass (MG), and (c) graphene paper (GP); (d) Raman spectra of MoS_2 grown on various substrates. The MoS_2 thin film was derived from 10 nm MoO_3.

Figure 6.1(d) illustrates the Raman spectra of MoS_2 grown on various substrates, where MoS_2 was derived from 10 nm MoO_3. Compared to SiO_2-Si, MoS_2 grown on MG at 500°C has similar A_{1g}/E_{2g}^1 ratio and frequency difference (~24.6 cm^{-1}) between them. The slight deviation may result from the sulfurization of bottom Mo metal in MG which possesses vertically aligned orientation. When the sulfurization temperature increases to 1000°C, the Raman peaks become sharper, indicating improved crystallinity of MoS_2 which is consistent with the AFM results in Figure 6.1(a). The A_{1g}/E_{2g}^1 ratio decreases a lot and the frequency difference between A_{1g} and E_{2g}^1 increases obviously. The lower A_{1g}/E_{2g}^1 ratio in high temperature MoS_2 refers to higher *c*-axis oriented MoS_2 lying on the substrate. The increase in frequency difference between A_{1g} and E_{2g}^1 from low to high temperature indicates improvement on MoS_2 stacking order.[1] It is noticed that MoS_2 grown on GP has even lower A_{1g}/E_{2g}^1 ratio and larger frequency difference

doi:10.6342/NTU201603487

between A_{1g} and E_{2g}^1 than MoS_2 on the SiO_2-Si substrate. The lower A_{1g}/E_{2g}^1 ratio could be attributed to the similar hexagonal structure of MoS_2 and the graphere sheets in GP top surface, which assists MoS_2 to grow along the same direction with GP. Monolayer MoS_2 grown on the few-layer graphene (FLG) has been reported to have similar E_{2g}^1 position and larger A_{1g} frequency with respect to that on the SiO_2 due to the substrate doping effect.[2] In Figure 6.1(d), our MoS_2 grown on GP shows both downshift in E_{2g}^1 and upshift in A_{1g} in Raman spectrum, indicating the substrate doping is not the cause for the peak shift. On the other hand, substrate-induced tensile strain is proposed to vary the lattice constants of MoS_2 and to shift the Raman peaks. The expansion in a/b and shrinkage in c would give rise to higher A_{1g} and lower E_{2g}^1, which is consistent with our observation. Lower A_{1g}/E_{2g}^1 ratio and higher order in MoS_2 stacking on the GP substrate also imply larger grain size of MoS_2 on GP or stronger interaction between MoS_2 and GP, which enhances the strain induced from the substrate.

6.2 Growing ZnO on MoS_2 via ALD process

To fabricate a MoS_2-based heterostructure device, ZnO is selected to grow on the MoS_2 surface because its small lattice mismatch and synergistic optoelectronic properties. Here, we adopt atomic layer deposition (ALD) process to grow ZnO on the MoS_2 due to its highly precise thickness control and the high aspect ratio deposition. Figure 6.2 illustrates the results of ZnO grown on various substrates. It is obvious that ZnO can be successfully grown on the MoS_2/SiO_2-Si and MoS_2/MG. However, we found it is difficult to grow ZnO on MoS_2/GP.

GP is an ultra-light and flexible substrate, which means it requires to be fixed on other support to prevent from sucking by the pump. Besides, we have tried vacuum tap,

doi:10.6342/NTU201603487

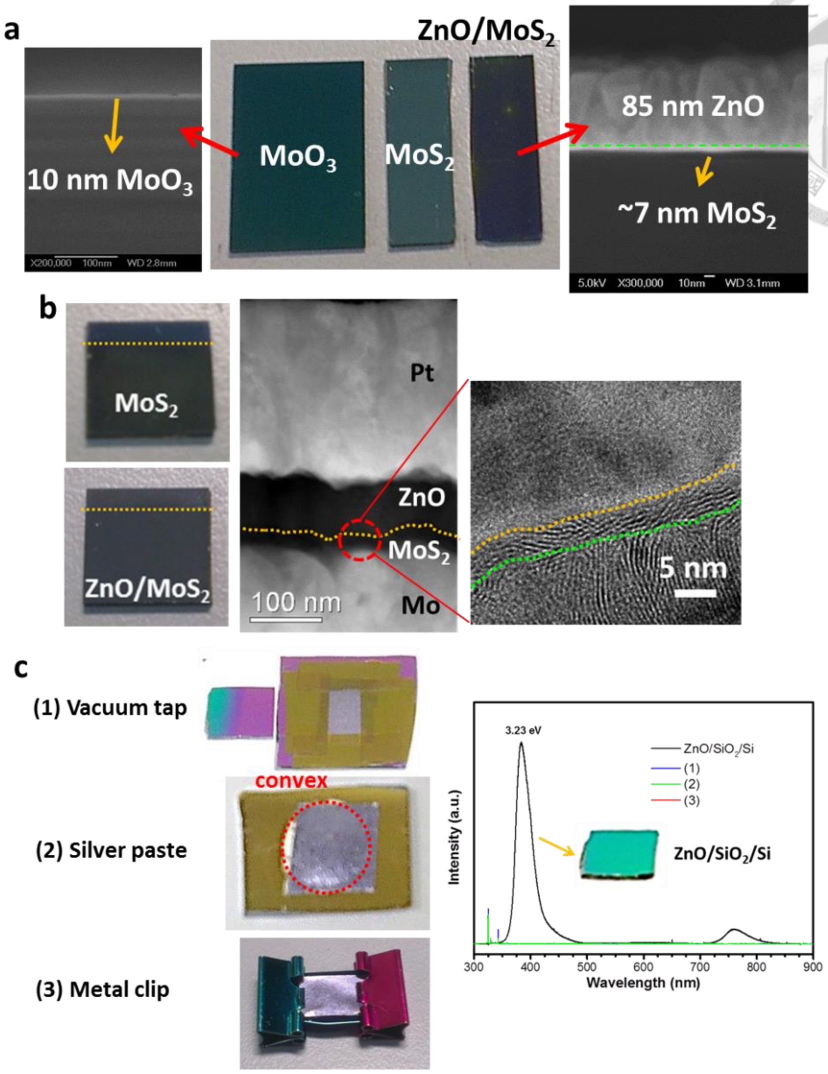

Figure 6.2 ALD-ZnO grew on (a) MoS_2(MS10)/SiO_2-Si, (b) MoS_2(MS5)/MG, and (c) MoS_2(MS5)/GP.

silver paste, and metal clips to fix MoS_2/GP on the Si-SiO_2. However, none of them can successfully grow ZnO on the MoS_2 surface, as shown in PL spectra in Figure 6.2(c).

ALD process for growing ZnO can be generally divided into two half cycles. First is H_2O adsorption on the MoS_2 surface, and second is DEZn react to the adsorbed H_2O molecule, as shown in Figure 6.3(a). Growing oxide on clean MoS_2 surface via ALD process was reported to be difficult because the lack of nucleation sites on the basal plane.[3] However, we can still grow ZnO on the MoS_2/SiO_2-Si and MoS_2/MG

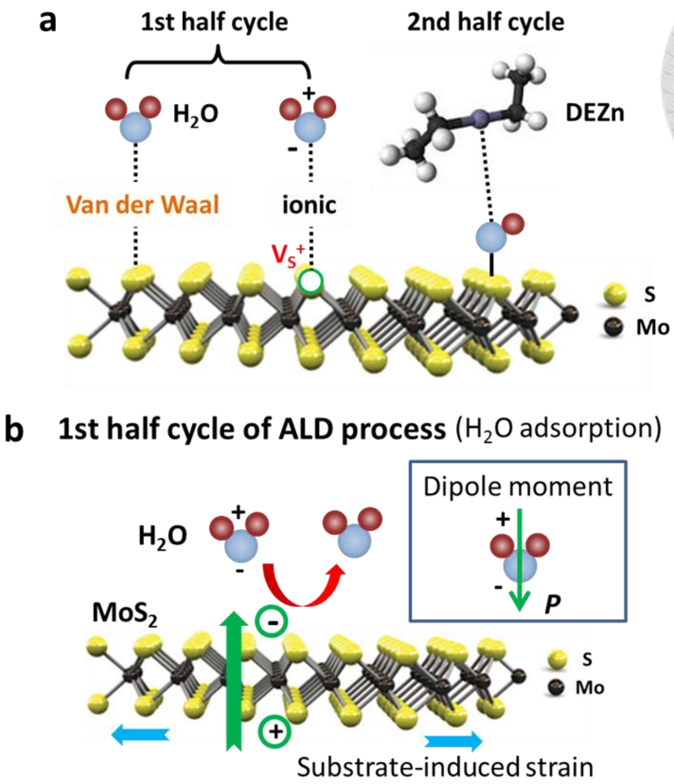

Figure 6.3 (a) Schematic illustrate of two half cycles in the ALD process for growing ZnO; (b) Schematic illustration of H_2O adsorption in the strained MoS_2 during the first half cycle in the ALD process.

uniformly. In Chapter 3, we have demonstrated that there are sulfur vacancies at our polycrystalline MoS_2 surface, which may facilitate the H_2O adsorption as the first step in the ALD process due to the dipole-dipole interaction (Figure 6.3(a)). Based on this inference, MoS_2/GP shall have sufficient sulfur vacancies to proceed ALD process, while it failed to grow ZnO on the top surface. The reason may result from the difficulty in H_2O adsorption via van der Waal interaction (physisorption).

Since the GP provides tensile strain to the MoS_2, the MoS_2 lattice will stretch at in-plane direction and shrink at cross-plane direction, as shown in Figure 6.3(b). The compressive transformation in the *z* direction would trigger piezoelectric effect to generate electric field pointing from bottom to the top surface,[4] which might impede the H_2O adsorption due to the opposite dipole moment to the induced electric field. The difficult in H_2O adsorption on the strained MoS_2 surface leads to uneasy growth of ZnO in the ALD process.

6.3 Surface treatment

To grow a uniform ZnO thin film on the strain MoS_2/GP via ALD process, two main problems need to be overcome. One is to fix the ultra-light sample on the support without the aid of any organic material or metal. The other is to improve the H_2O adsorption on the strained MoS_2 surface.

Wang *et al*. has discovered that graphene can be clean transferred without coating the organic supporting layer, such as PMMA.[5] Electrostatic force is introduced on the target substrate and then graphene can be easily and clean transferred on it with the attractive force. Since GP is composed of graphene sheets, we tried to adopt similar method to attach MoS_2/GP on the SiO_2-Si, as illustrated in Figure 6.4(a). We first supplied negative charges onto the SiO_2-Si surface by the electrostatic generator. Afterwards, the MoS_2/GP with relatively positive bottom surface was put on the negatively charged SiO_2-Si surface and automatically attached well due to the attractive force. This clean attachment of MoS_2/GP on SiO_2-Si can sustain in the whole ALD process without detachment.

Lee *et al*. has reported that ozone treated graphene present uniform hydrophilic groups on the graphene basal plane, which improve the oxide growth homogeneity in ALD process.[6] The ozone adsorption on graphene surface is gentle and reversible due to the small reaction barrier that will not damage graphene surface. Here, we adopted

doi:10.6342/NTU201603487

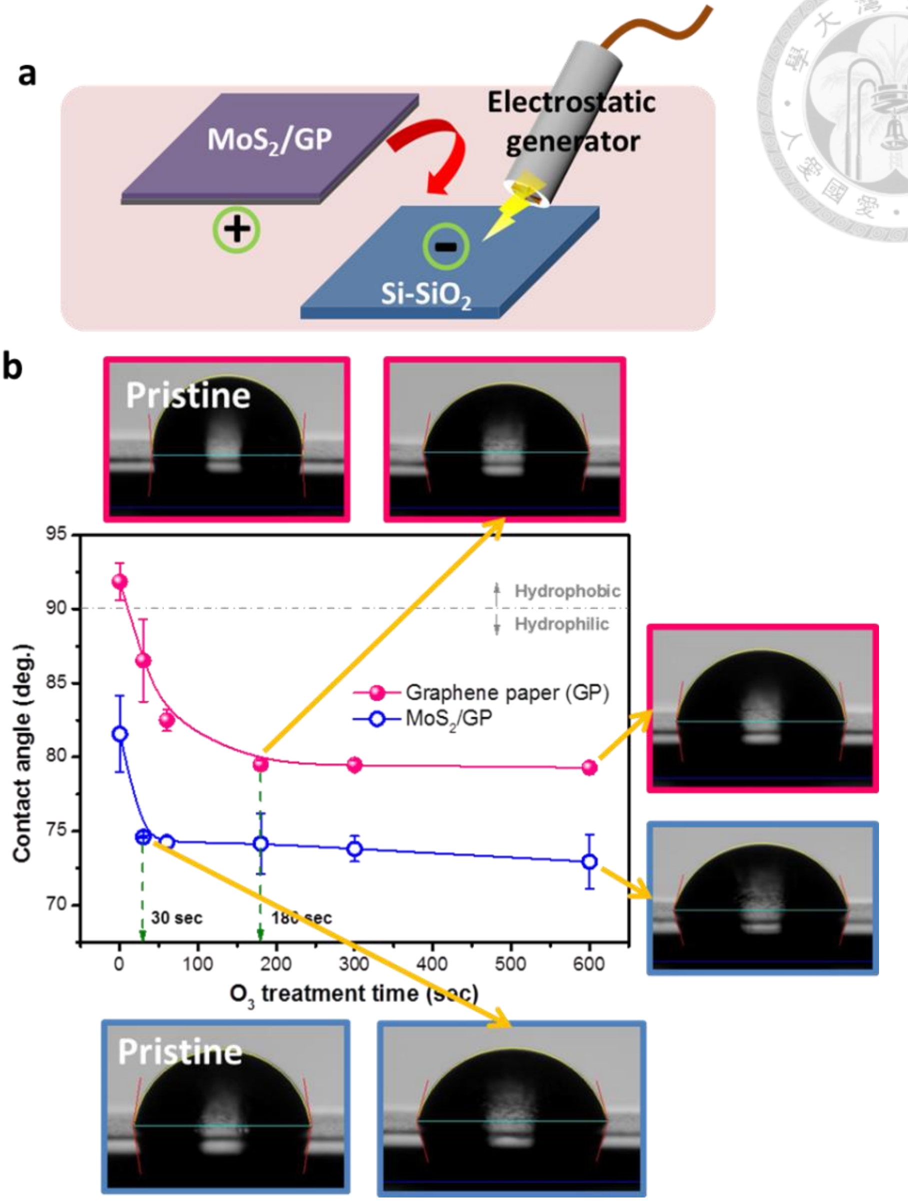

Figure 6.4 (a) Schematic illustrate of electrostatic-assisted attachment of MoS$_2$/GP on SiO2/Si; (b) Contact angles of GP and MoS$_2$/GP respectively with various O$_3$ treatment time.

similar treatment on both bare GP and MoS$_2$/GP, and measured the contact angles with various O$_3$ treated time, as shown in Figure 6.4(b). Bare GP originally is the hydrophobic. After 30 sec O$_3$ treatment, it becomes hydrophilic. Further treatment with O$_3$, the contact angle continues to decrease and saturates after 180 sec, when the contact

doi:10.6342/NTU201603487

angle is ~79^o. Compared to bare GP, the surface of MoS$_2$/GP is already hydrophilic (contact angle ~ 82^o), which could be attributed to the sulfur vacancies at the surface. After O$_3$ treatment for 30 sec, the contact angle reduces to ~74^o and almost saturates when elongating the treatment time. Thus, we select 30 sec as the best condition for the O$_3$ treatment time.

Figure 6.5 illustrates the photographs, PL spectra and SEM images of the MoS$_2$/GP after ZnO deposition by ALD process. Compared to the untreated specimen, ZnO can grow homogeneously on the MOS$_2$/GP after O$_3$ treatment. The higher PL intensity indicates thicker ZnO film on the MoS2 surface. The SEM images also illustrate high uniformity of ZnO deposited with good aspect ratio even at the edge steps of GP.

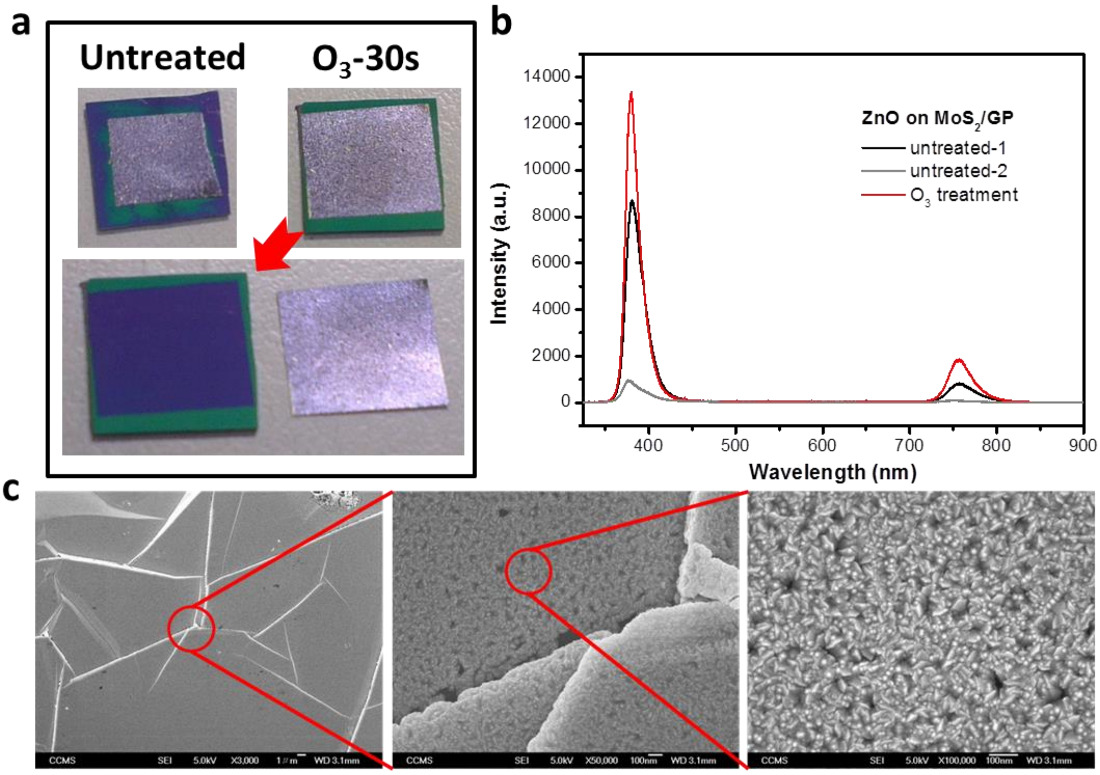

Figure 6.5 (a) Compared photographs of untreated and O$_3$-treated MoS$_2$/GP after ZnO deposition via ALD process; (b) Photoluminescence spectra of ZnO on untreated and O$_3$-treated MoS$_2$/GP respectively; (c) SEM images of ZnO on O$_3$-treated MoS$_2$/GP.

6.4 Summary

MoS_2 thin film can be successfully grown on SiO_2-Si, MG, and GP by two-step CVD process. Among different substrates, MoS_2 encountered tensile stress when it grew on the GP, which may be attributed to the large grain size and strong interaction between MoS_2 and the graphene sheets at GP top surface. The strained MoS_2 may also affect the H_2O physisorption in the first half cycle of ALD process because the piezoelectric effect induced E-field is opposite to the H_2O dipole moment, which leads to ZnO difficult to nucleate at the surface. Applying electrostatic force provides a clean procedure to fix MoS_2/GP on a solid support. O_3 treatment for 30 sec further modifies the surface chemistry of MoS_2 to more hydrophilic, especially the basal plane, giving rise to homogeneous deposition of ZnO thin film with good aspect ratio even at the step-edge of GP. Our findings provide an easy, clean and gentle treatment on the surface of two-dimensional materials, which can be applied on other TMDs for fabricating heterostructure configuration.

doi:10.6342/NTU201603487

References

[1] Q. Li, E. C. Walter, W. E. van der Veer, B. J. Murray, J. T. Newberg, E. W. Bohannan, J. A. Switzer, J. C. Hemminger and R. M. Penner, J. Phys. Chem. B **109** (8), 3169-3182 (2005).

[2] M. Buscema, G. A. Steele, H. S. J. van der Zant and A. Castellanos-Gomez, Nano Res. **7** (4), 561-571 (2015).

[3] S. McDonnell, B. Brennan, A. Azcatl, N. Lu, H. Dong, C. Buie, J. Kim, C. L. Hinkle, M. J. Kim and R. M. Wallace, ACS Nano **7** (11), 10354-10361 (2013).

[4] H. Zhu, Y. Wang, J. Xiao, M. Liu, S. Xiong, Z. J. Wong, Z. Ye, Y. Ye, X. Yin and X. Zhang, Nat. Nanotechnol. **10** (2), 151-155 (2015).

[5] D. Y. Wang, I. S. Huang, P. H. Ho, S. S. Li, Y. C. Yeh, D. W. Wang, W. L. Chen, Y. Y. Lee, Y. M. Chang, C. C. Chen, C. T. Liang and C. W. Chen, Adv. Mater. **25** (32), 4521-4526 (2013).

[6] G. Lee, B. Lee, J. Kim and K. Cho, J. Phys. Chem. C **113**, 14225-14229 (2009).

doi:10.6342/NTU201603487

Chapter 7 Conclusions

In this thesis, I have successfully produced MoS_2 thin films on various substrates ($Si-SiO_2$, graphene paper, and Mo-glass) by a two-step CVD process. The thickness of MoS_2 can be well-controlled by thermal evaporation of MoO_3 precursor. The surface properties of MoS_2 are found to strongly correlate with the thickness. Surface defects, especially sulfur vacancies, will generate donor-like surface states that will bend the surface bands downward leading to higher conductivity in thinner MoS_2. This surface band bending feature, corresponding to the Fermi level variation, can be tuned by the surface treatment. Higher Fermi-level position near conduction band minimum in thinner MoS_2 has shown its better catalytic performance for hydrogen evolution reaction due to the lower activation energy.

I have also demonstrated that two common precursors (Mo metal and MoS_2) have different sulfurization kinetic response. Applying this characteristic with well-controlled sulfurization conditions, different orientations of MoS_2 can be obtained, which makes combining two orientations of MoS_2 in an electronic device with vertical configuration become possible. Edge-terminated MoS_2 can serve as the conduction media bridging the metal contact and terrace-terminated MoS_2. This configuration can be the base for heterostructure applications with better interface properties than edge-terminated MoS_2 only. ZnO, grown by ALD process, is selected for the hybrid hexagonal material with MoS_2. A Pt/ZnO/MoS2/Mo heterojunction device is fabricated as a memristor, which exhibits unique resistive switching behaviors related to the ZnO/MoS_2 interface properties, and the switching mechanism has been thoroughly discussed.

My thesis has illustrated a simple, effective, and easily controlled growth process

doi:10.6342/NTU201603487

for MoS_2. The strain (from different substrates), orientations (from different precursors), and surface properties (from different thicknesses and surface treatments) of CVD-grown large area MoS_2 can be manipulated by tuning the growth conditions. Two applications related to the surface (HER) and interfacial (RRAM) properties are also demonstrated. The physical concepts of surface states induced Fermi level variations and the strategy for orientation control may be applied for other TMD materials. The unique properties in oxide-MoS_2 heterojunction device also show the possibility for designing novel TMD-based heterostructure applications.

doi:10.6342/NTU201603487

Publications

1. **Yu-Kai Lin**, Ruei-San Chen, Tsu-Chin Chou, Yi-Hsin Lee, Yang-Fang Chen, Kuei-Hsien Chen, and Li-Chyong Chen, “Thickness-Dependent Binding Energy Shift in Few-Layer MoS_2 Grown by Chemical Vapor Deposition”, *ACS Appl. Mater. Interfaces*, Manuscript ID: am-2016-066158.R1 (accepted) [IF = 6.723]
2. Ching-Hsuan Lin, Ruei-San Chen, **Yu-Kai Lin**, Sheng-Bo Wang, Li-Chyong Chen, Kuei-Hsien Chen, Meng-Chieh Wen, Mitch Ming-Chi Chou, and Liuwen Chang,”Photoconduction Properties and Anomalous Power-dependent Quantum Efficiency in non-polar ZnO Epitaxial Films Grown by Chemical Vapor Deposition”, *ACS Photonics*, Manuscript ID: ph-2016-00615f (submitted) [IF = 5.404]
3. Chin-Hsuen Lin, Ruei-San Chen, **Yu-Kai Lin**, Seng-Bo Wang, Li-Chyong Chen, Kuei-Hsien Chen, M. C. Wen, Mitch Ming-Chi Chou, and Liuwen Chang,” Photoconductivities in *m*-plane and *c*-plane ZnO Epitaxial Films Grown by Chemical Vapor Deposition on $LiGaO_2$ Substrates: A Comparative Study” *RSC Advances*, Manuscript ID: RA-ART-07-2016-018344 (submitted) [IF =3.289]
4. Cheong-Wei Chong, Meng-Jie Huang, Hsien-Cheng Han, **Yu-Kai Lin**, Jien-Ming Chiu, Yi-Fang Huang, Hong-Ji Lin, Tun-Wen Pi, Jauyn Grace Lin, Li-Chyong Chen, Kuei-Hsien Chen, and Yang-Fang Chen, “Resistance Memory Device of $La_{0.7}Sr_{0.3}MnO_3$ on Si Nanotips Template”, *Appl. Phys. Lett*. **103**, 211606 (2013). [IF = 3.515]
5. Ying-Chu Chen, Yu-Kuei Hsu, Yan-Gu Lin, **Yu-Kai Lin**, Ying-Ying Horng, Li-Chyong Chen, and Kuei-Hsien Chen, “Highly Flexible Supercapacitors with

Manganese Oxide Nanosheet/Carbon Cloth Electrode", *Electrochim Acta* **56**, 7124-7130 (2011). [IF = 3.832]

6. Chien-Cheng Li, Ran-Jin Lin, Hong-Ping Lin, **Yu-Kai Lin**, Yan-Gu Lin, Ching-Chun Chang, Li-Chyong Chen, and Kuei-Hsien Chen, "Catalytic Performance of Plate-type Cu/Fe Nanocomposites on ZnO Nanorods for Oxidative Steam Reforming of Methanol", *Chem. Commun.* **47**, 1473-1475 (2011). [IF = 6.169]
7. **Yu-Kai Lin**, Yi-Han Su, Yun-Hsin Huang, Chia-Jung Hsu, Yu-Kuei Hsu, Yan-Gu Lin, Ko-Hsiung Huang, San-Yuan Chen, Kuei-Hsien Chen, and Li-Chyong Chen, "Efficient Hydrogen Production Using Cu-based Catalysts Prepared via Homogeneous Precipitation", *J. Mater. Chem.* **19**, 9186-9194 (2009). [IF = 4.795]
8. Yan-Gu Lin, Yu-Kuei Hsu, San-Yuan Chen, **Yu-Kai Lin**, Li-Chyong Chen, and Kuei-Hsien Chen, "Nanostructured Zinc Oxide Nanorods with Copper Nanoparticles as a Microreformation Catalyst", *Angew. Chem. Int. Ed.* **48**, 7586-7590 (2009). [IF = 11.829]

Manuscripts in preparation

1. **Yu-Kai Lin**, Yang-Fang Chen, Kuei-Hsien Chen, and Li-Chyong Chen, "*Modulating Sulfurization Kinetics in Mo Precursors to Grow Large-scale MoS$_2$ with Dual Orientations for Electronic Devices*".
2. **Yu-Kai Lin**, Yang-Fang Chen, Kuei-Hsien Chen, and Li-Chyong Chen, "*A 2D-3D Hybrid Material for Memory: Resistive Switching Behavior at MoS$_2$/ZnO Heterojunction*".
3. **Yu-Kai Lin**, Oliver Ming-Ren Chyan, Chen-Kai Chang, Yang-Fang Chen,

Li-Chyong Chen, and Kuei-Hsien Chen,” *Visualization of Surface Energy Topography on Large-scaled Graphene by Electrochemical Approach*”.

Appendix A

Visualization of Surface Energy Topography on Large-scaled Graphene by Electrochemical Approach

Abstract

Toward a good junction between CVD-graphene and adjacent materials without contamination of unwanted chemicals in a multi-leveled electronic or spintronic device, directly growing materials on graphene was adopted. The growth mechanism is highly influenced by the surface properties of the substrate, namely graphene. In the present study, the surface energy topology of the large-scaled, untransferred CVD-graphene was successfully reified by utilizing the electrochemical technique to selectively deposit MoO_2 onto the graphene surface. Our results show that the better discrimination of the graphene domains is obtained at -0.75 V (vs. Ag/AgCl) for seconds in the 0.2 mM MoO_4^{2-} solution which is a diffusion-controlled electrodeposition near the threshold potential. The nucleation of MoO_2 and its distribution were explained by the modified classical nucleation theory which is related to the local properties of the substrate. Both the defect density of graphene and the surface states of the Cu-foil substrate were also proposed to affect the topology of surface energy. By visualize the surface energy topology, it helps understand the surface properties of graphene and is beneficial for using graphene as a substrate to grow materials on top of it.

doi:10.6342/NTU201603487

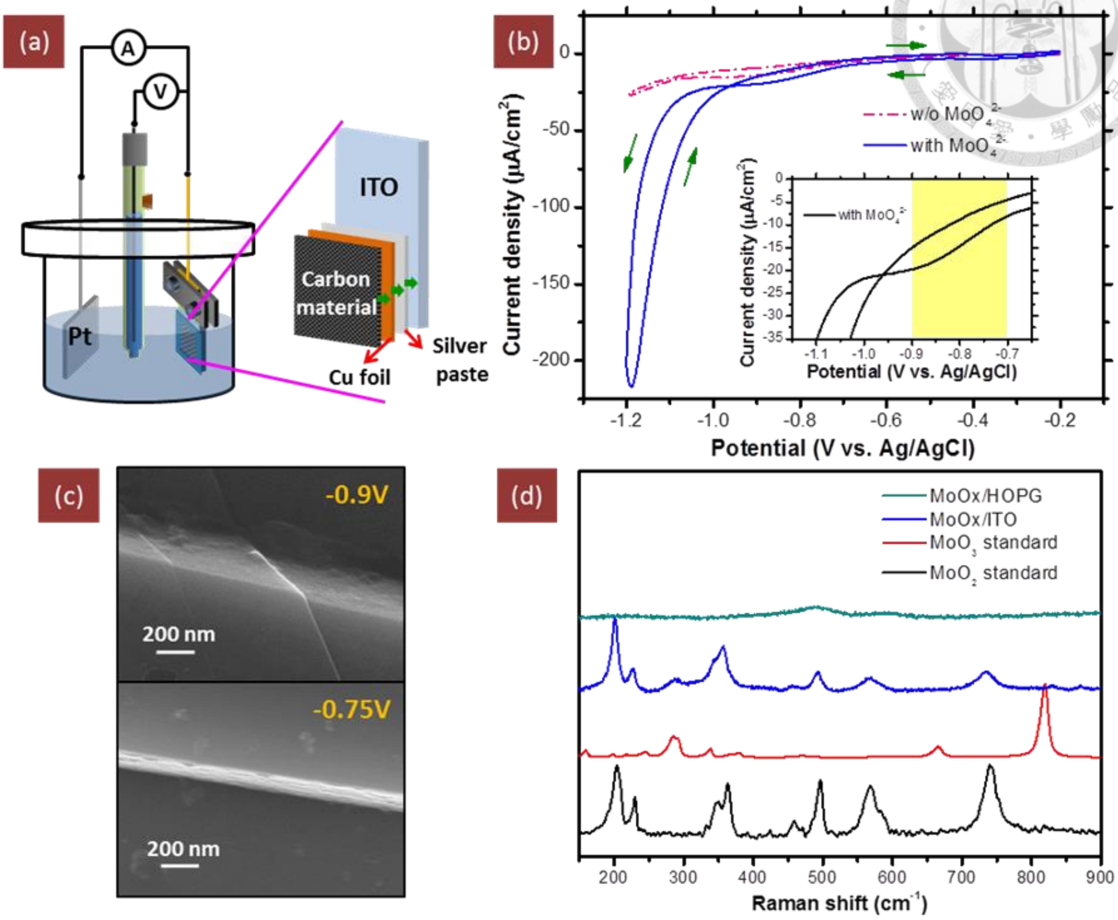

Figure A.1 (a) the sketch of the electrochemical system used in this study; (b) cyclic voltammetry (CV) curves measured at 5 mV/s in the electrolyte with and without 1 mM MoO_4^{2-} for HOPG electrode; (c) SEM images of MoO_2 nanowires grown at different applied bias for 5 min on the step-edge of the HOPG electrode; (d) Raman analyses of the electrodeposited MoO_2.

doi:10.6342/NTU201603487

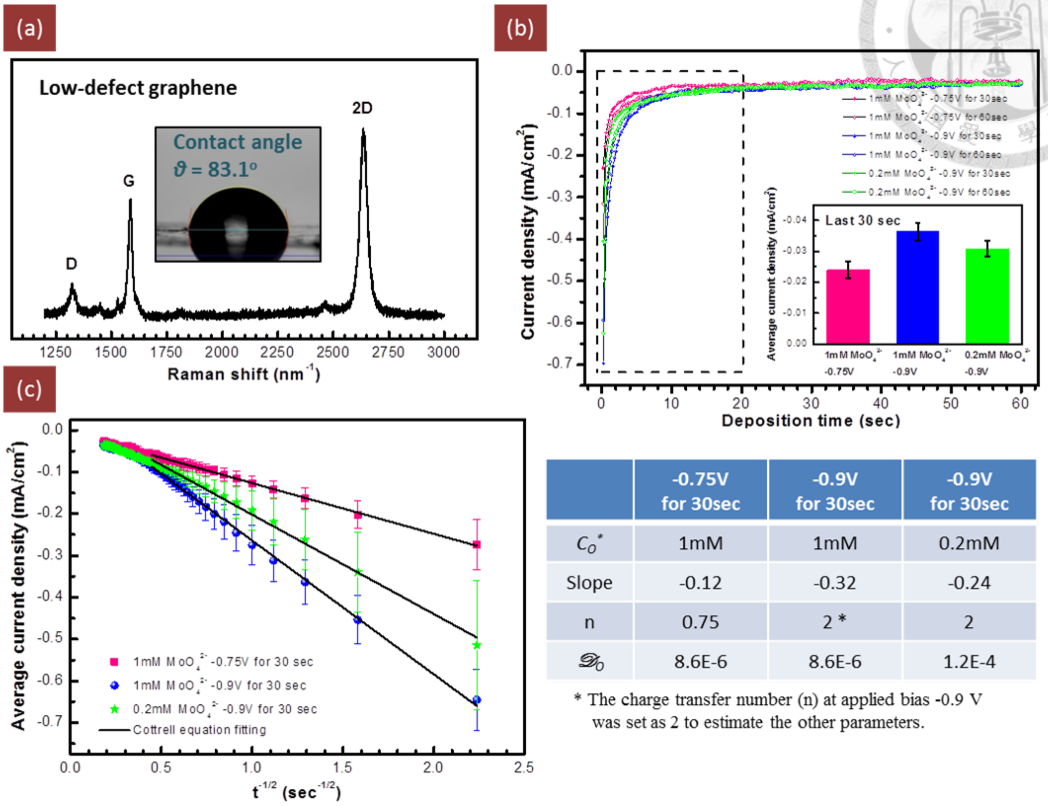

	-0.75V for 30sec	-0.9V for 30sec	-0.9V for 30sec
C_O^*	1mM	1mM	0.2mM
Slope	-0.12	-0.32	-0.24
n	0.75	2 *	2
$\mathscr{D}_O$	8.6E-6	8.6E-6	1.2E-4

* The charge transfer number (n) at applied bias -0.9 V was set as 2 to estimate the other parameters.

Figure A.2 (a) The Raman spectrum of the selected low-quality graphene for MoO_2 deposition. (b) The measured current densities with the evoluted deposition time of various growth conditions. The inset is the average current densities calculated from the deposition time of 30 to 60 sec. (c) Plot of the average current density of the first 30 sec in (b) as a function of the inverse square root of the deposition time. The table listed left is the estimated charge transfer numbers and diffusion coefficients of MoO_4^{2-} by the Cottrell equation fitting (Eq. 3) in (c).

doi:10.6342/NTU201603487

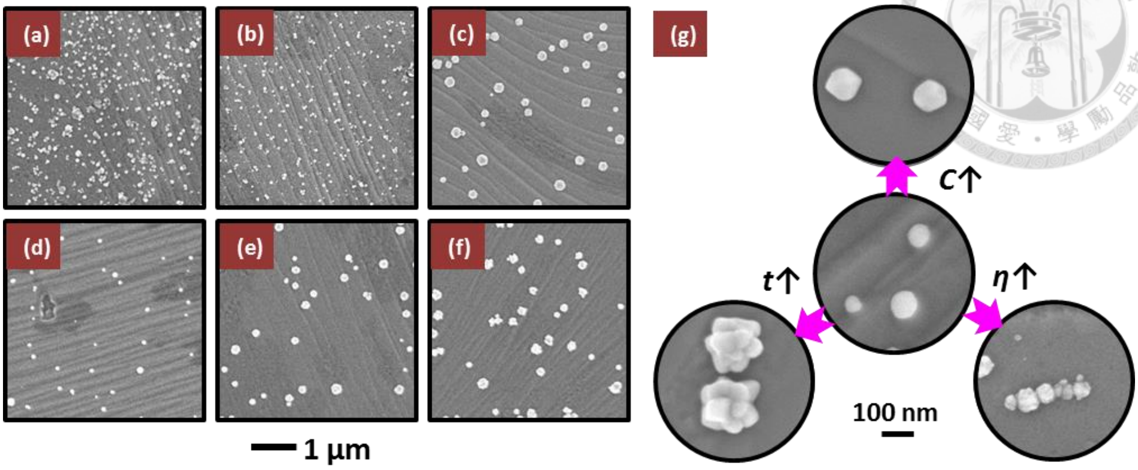

Figure A.3 The SEM images of the MoO_2 nanoparticles deposited on the graphene/Cu surface at (a) -0.9 V for 30 sec in 1 mM MoO_4^{2-} , (b) -0.9 V for 30 sec in 0.2 mM MoO_4^{2-}, (c) -0.75 V for 30 sec in 1 mM MoO_4^{2-}, (d) -0.75 V for 10 sec in 0.2 mM MoO_4^{2-}, (e) -0.75 V for 30 sec in 0.2 mM MoO_4^{2-}, (f) -0.75 V for 90 sec in 0.2 mM MoO_4^{2-}, (g) The morphological evolutions of the MoO_2 under different controlled parameters, i.e. concentration of MoO_4^{2-}, C_O^*; overpotential, η; deposition time, t_d.

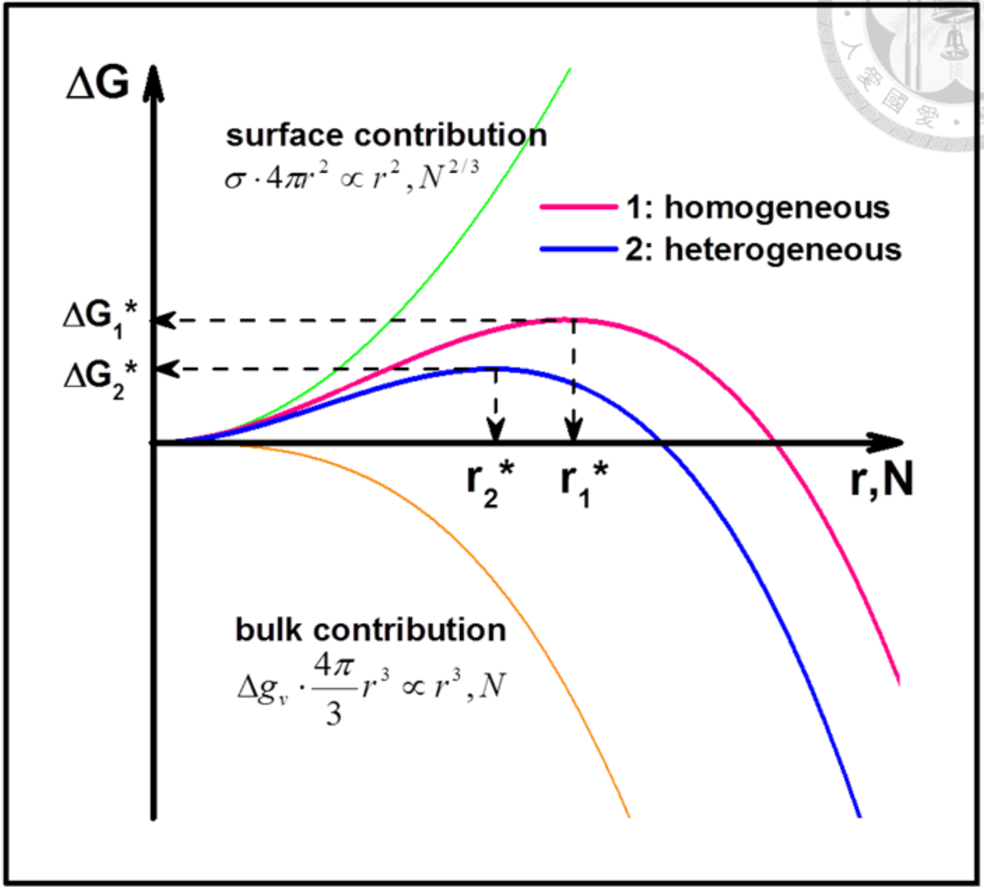

Figure A.4 The sketch of the formation energy of the nuclei as a function of the nuclei size.

doi:10.6342/NTU201603487

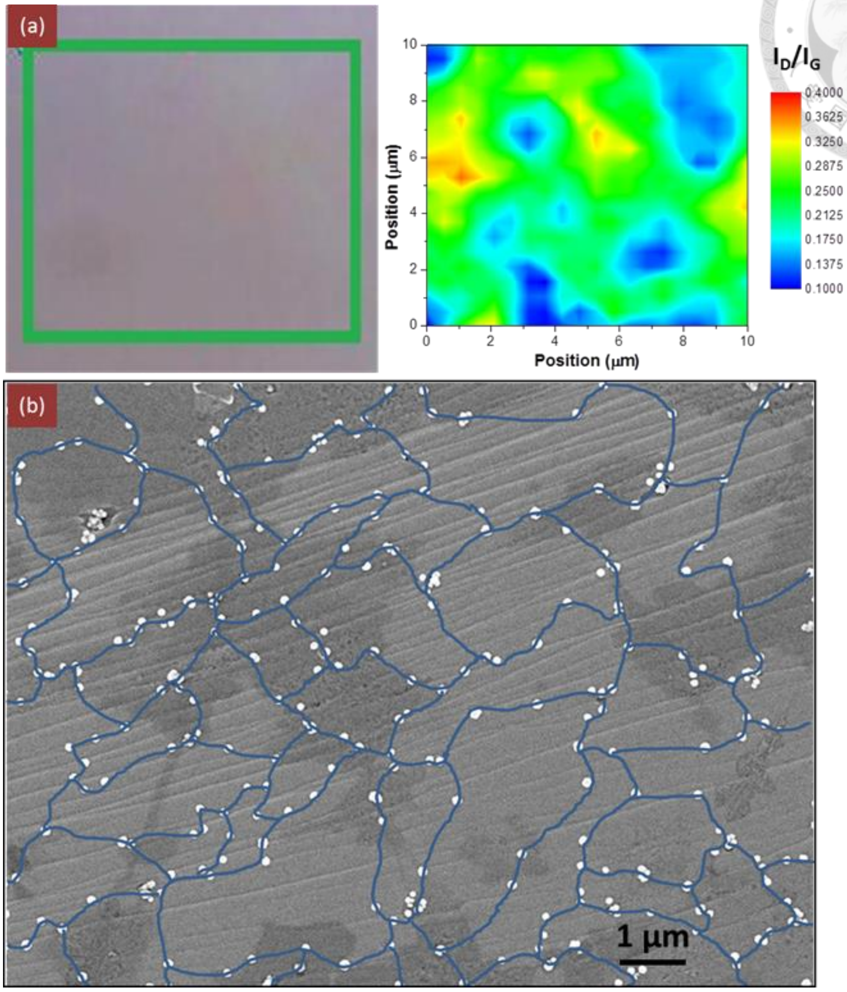

Figure A.5 (a) The optical image of the graphene transferred onto the SiO_2 substrate and the corresponding Raman mapping image of I_D/I_G ratio. (b) The distribution of the MoO_2 nanoparticles on the graphene/Cu which were deposited at -0.75 V for 30 sec in 0.2 mM MoO_4^{2-}.

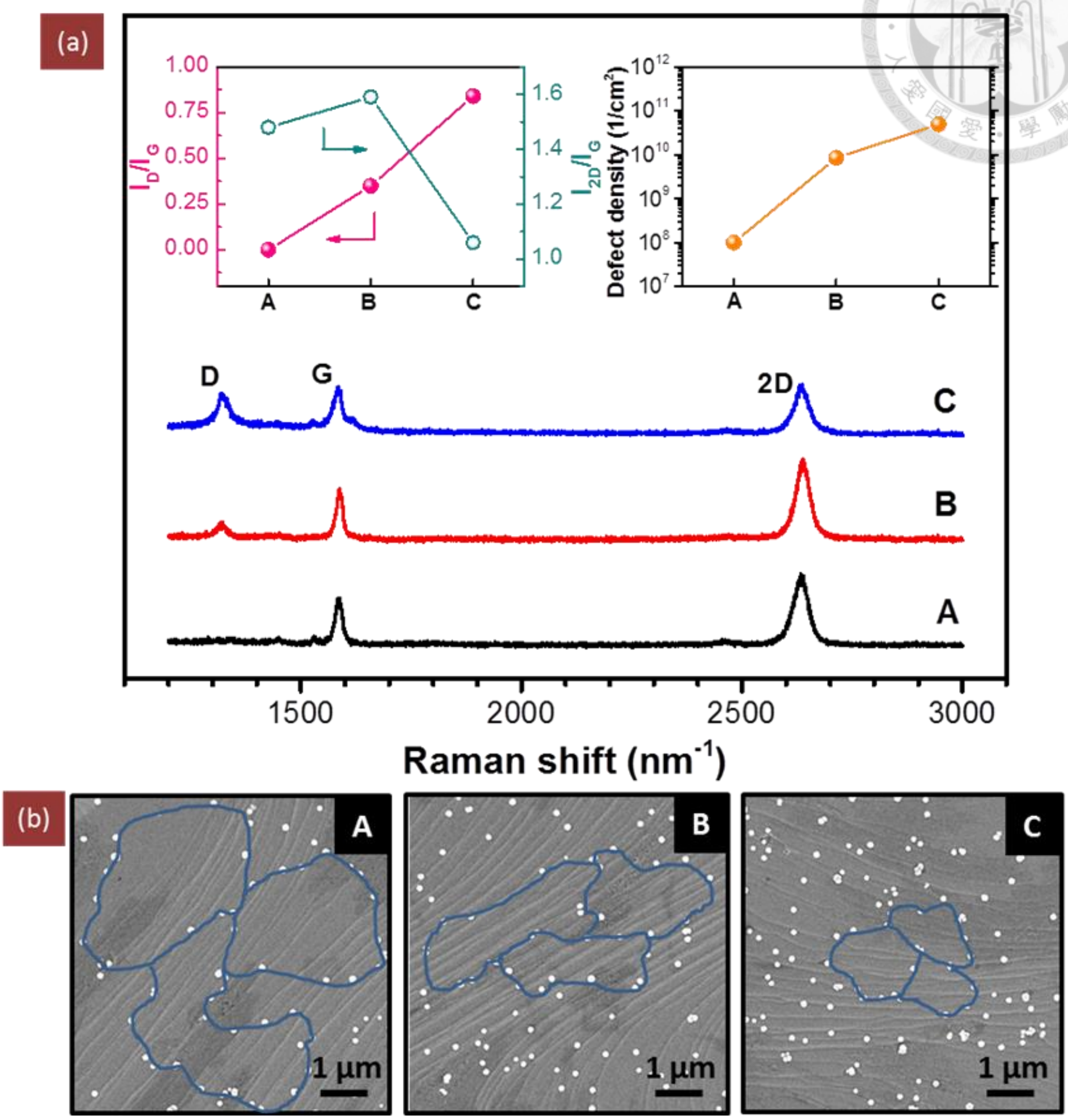

Figure A.6 (a) The Raman spectra of the graphenes with different defect densities. (b) The distribution of MoO_2 nanoparticles on the graphene/Cu with different defect densities.

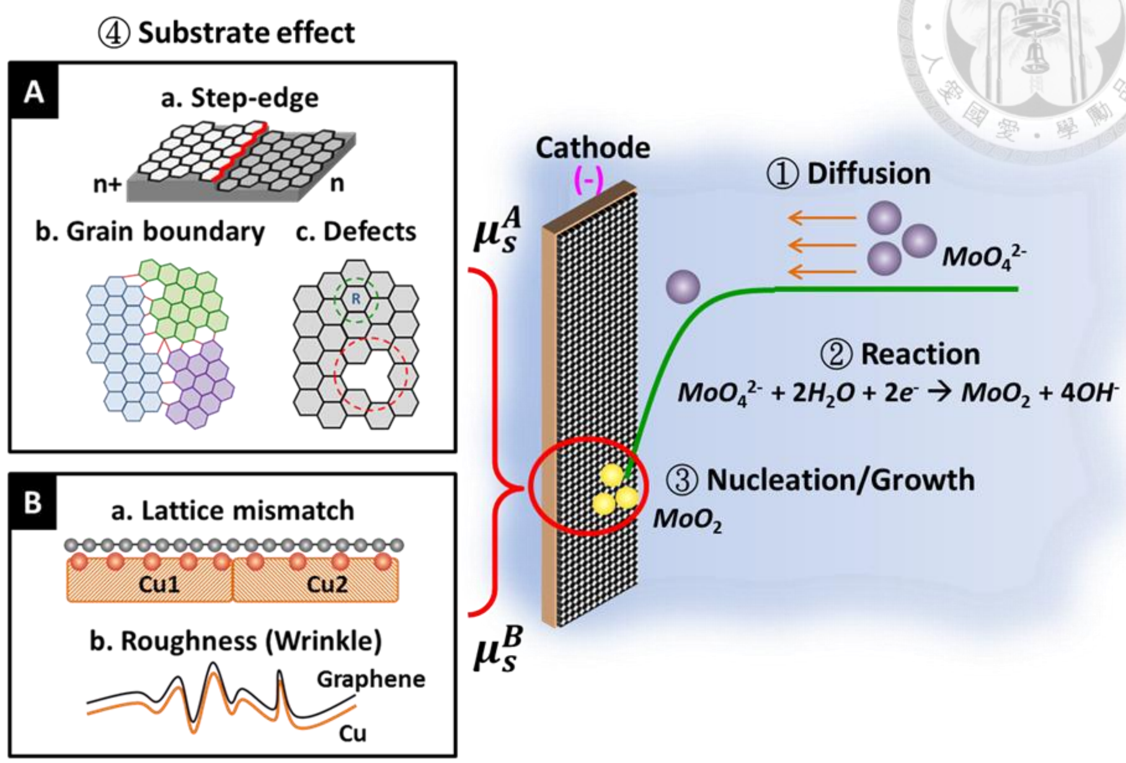

Figure A.7 Schematic diagram of the electrodeposition process of MoO_2 nanoparticles.

Appendix B

Defect Modulation and Morphology Evolution of Copper-doped ZnO Nanorods via Electrochemical Method

Abstract

ZnO has been attracted considerable interests to the optical and electronic industries, because of its electrical, optical, and acoustic characteristics. As in many semiconductors, defects in ZnO influence its electric and optical properties greatly. ZnO with a wurtzite structure is naturally an n-type semiconductor because of a deviation from stoichiometry due to the presence of intrinsic defects such as O vacancies (Vo) and Zn interstitials (Zni). Moreover, copper was chosen as a dopant in this study due to its characteristic of hole acceptor and its potential for band-gap engineering to ZnO. This additional modification of ZnO was expected to change its crystal structure as well as the electronic structure which can broaden the application of ZnO. The types and the densities of the defects in ZnO are strongly correlated to the growth conditions. Here we adopt electrochemical method to deposit ZnO nanorods on FTO substrate. By varying solution compositions and tuning the applied bias in the electrodeposition process, the defects in ZnO can be modulated. XRD and SEM were first analyzed to check the crystal structure and the morphology evolution of Cu-doped ZnO after electrodeposition. The mechanism of electrodeposition process was also discussed. We found that the pH value at the electrode surface would play an important role on the deposition rate, and the anions in the solution would affect the morphologies of ZnO:Cu. X-ray absorption spectroscopic (XAS) techniques were employed to analyze the electronic structures of

doi:10.6342/NTU201603487

ZnO:Cu. Based on the results of XAS, we found that some defects, such as Vo and anion impurities, in the ZnO:Cu lattice can be reduced or rearranged after post annealing treatment. This alteration of defects was not only observed in the photoluminescence, but also affected the magnetic properties of ZnO:Cu. In this regard, we expect that ZnO:Cu can be a potential material for optoeletronic and spintronic application by controlling its defects and morphologies well.

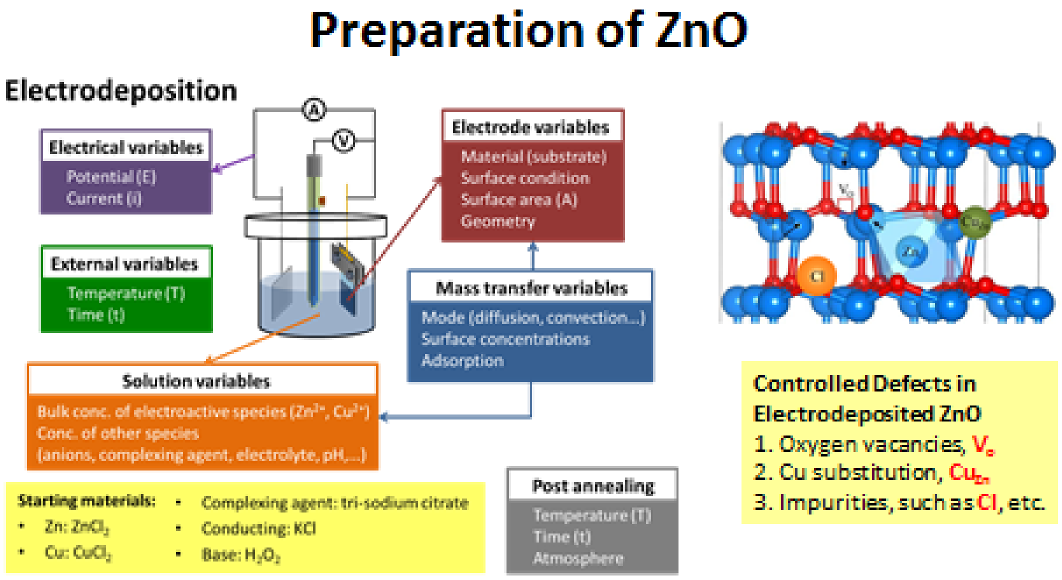

Figure B.1 Preparation of ZnO-based nanostructures via electrochemical deposition.

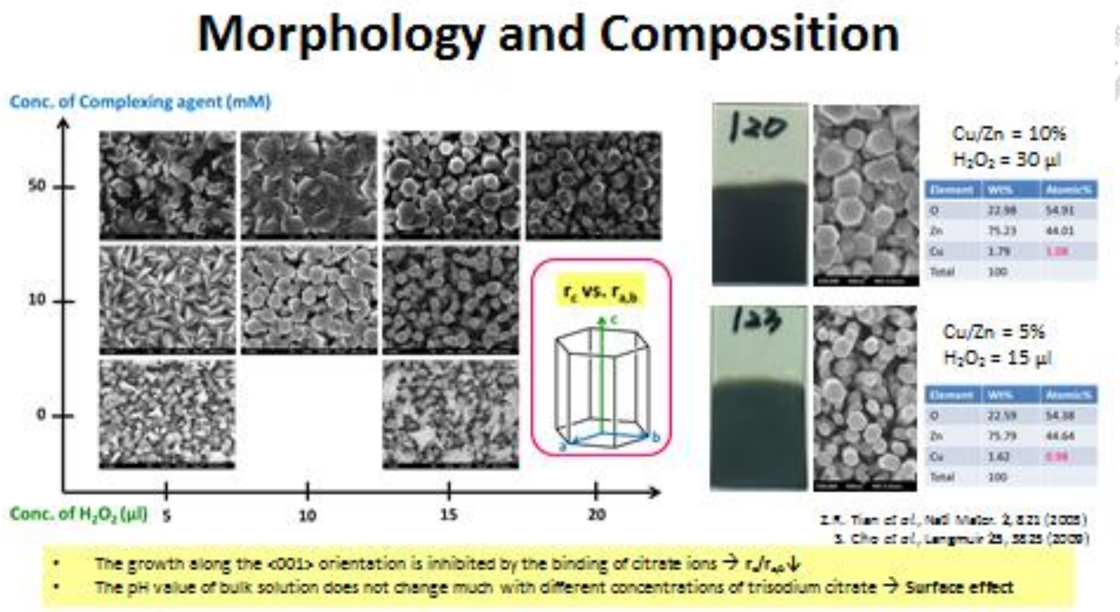

Morphology and Composition

Cu/Zn = 10%
H_2O_2 = 30 μl

Element	Wt%	Atomic%
O	22.98	54.91
Zn	75.23	44.01
Cu	1.79	1.08
Total	100	

Cu/Zn = 5%
H_2O_2 = 15 μl

Element	Wt%	Atomic%
O	22.59	54.38
Zn	75.79	44.64
Cu	1.62	0.98
Total	100	

2. R. Tian *et al.*, Nat Mater. 2, 821 (2003)
3. Cho *et al.*, Langmuir 25, 3825 (2009)

- The growth along the <001> orientation is inhibited by the binding of citrate ions → $r_c/r_{a,b}$↓
- The pH value of bulk solution does not change much with different concentrations of trisodium citrate → **Surface effect**

Figure B.2 Morphology and composition of EC-prepared ZnO:Cu nanorods.

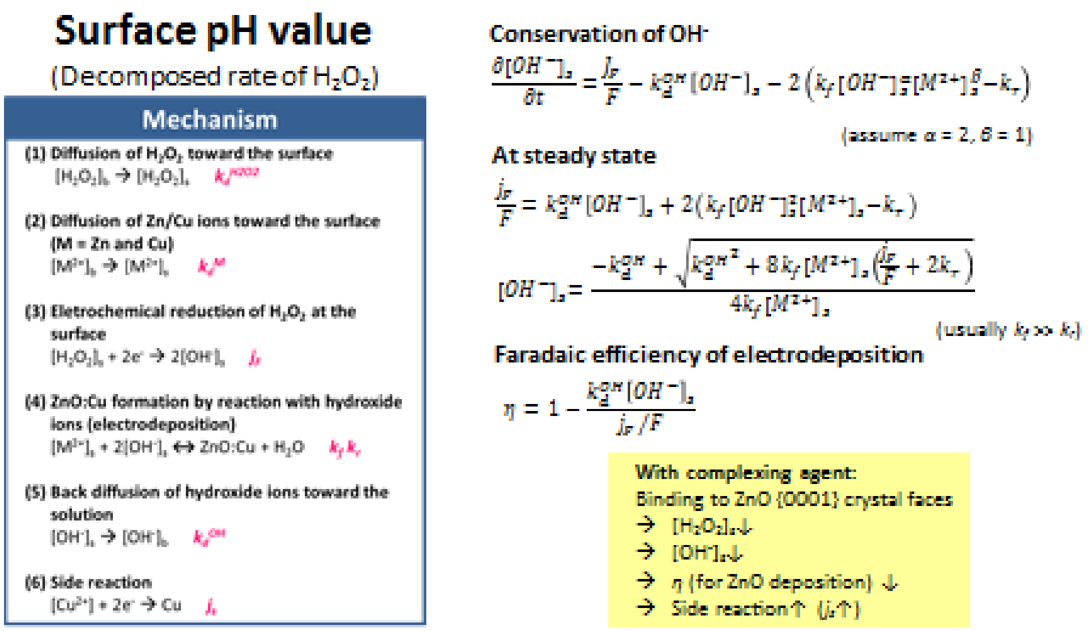

Surface pH value

(Decomposed rate of H_2O_2)

Mechanism

(1) Diffusion of H_2O_2 toward the surface
$[H_2O_2]_b \rightarrow [H_2O_2]_s$ k_d^{H2O2}

(2) Diffusion of Zn/Cu ions toward the surface (M = Zn and Cu)
$[M^{2+}]_b \rightarrow [M^{2+}]_s$ k_d^{M}

(3) Eletrochemical reduction of H_2O_2 at the surface
$[H_2O_2]_s + 2e^- \rightarrow 2[OH^-]_s$ j_F

(4) ZnO:Cu formation by reaction with hydroxide ions (electrodeposition)
$[M^{2+}]_s + 2[OH^-]_s \leftrightarrow ZnO{:}Cu + H_2O$ $k_f\ k_r$

(5) Back diffusion of hydroxide ions toward the solution
$[OH^-]_s \rightarrow [OH^-]_b$ k_d^{OH}

(6) Side reaction
$[Cu^{2+}] + 2e^- \rightarrow Cu$ j_s

Conservation of OH^-

$$\frac{\partial [OH^-]_s}{\partial t} = \frac{j_F}{F} - k_d^{OH}[OH^-]_s - 2\left(k_f[OH^-]_s^{\alpha}[M^{2+}]_s^{\beta} - k_r\right)$$

(assume α = 2, β = 1)

At steady state

$$\frac{j_F}{F} = k_d^{OH}[OH^-]_s + 2\left(k_f[OH^-]_s^2[M^{2+}]_s - k_r\right)$$

$$[OH^-]_s = \frac{-k_d^{OH} + \sqrt{{k_d^{OH}}^2 + 8k_f[M^{2+}]_s\left(\frac{j_F}{F} + 2k_r\right)}}{4k_f[M^{2+}]_s}$$

(usually $k_f \gg k_r$)

Faradaic efficiency of electrodeposition

$$\eta = 1 - \frac{k_d^{OH}[OH^-]_s}{j_F/F}$$

With complexing agent:
Binding to ZnO {0001} crystal faces
→ $[H_2O_2]_s$↓
→ $[OH^-]_s$↓
→ η (for ZnO deposition) ↓
→ Side reaction↑ (j_s↑)

Figure B.3 Analysis of surface pH value in our electrodeposition system.

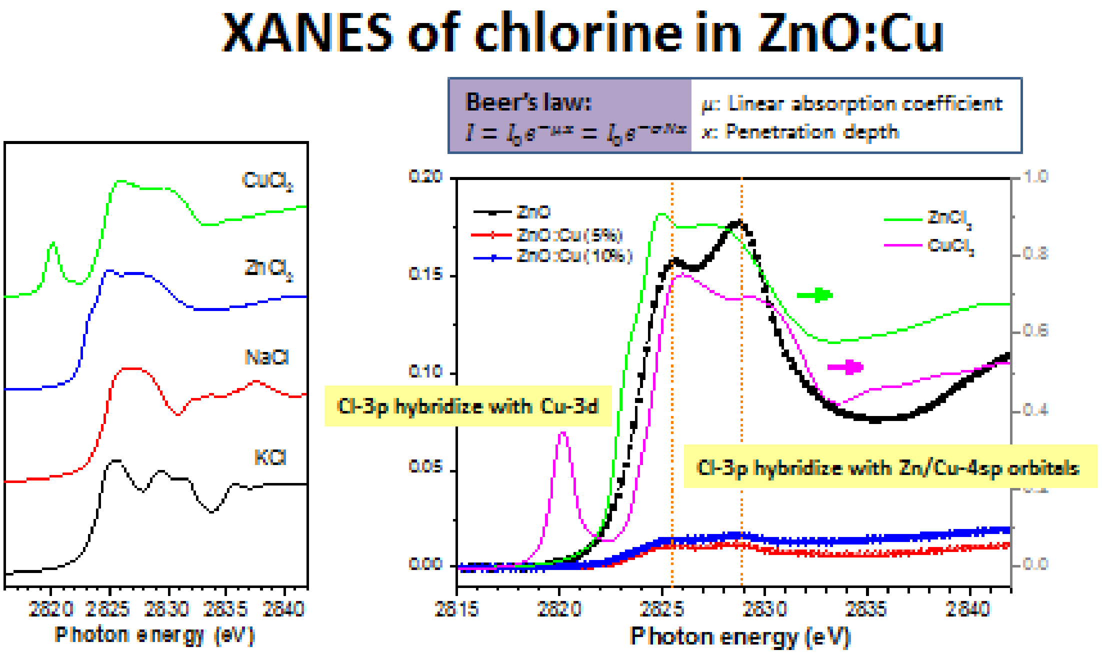

Figure B.4 XANES of Cl K-edge in EC-prepared ZnO:Cu.

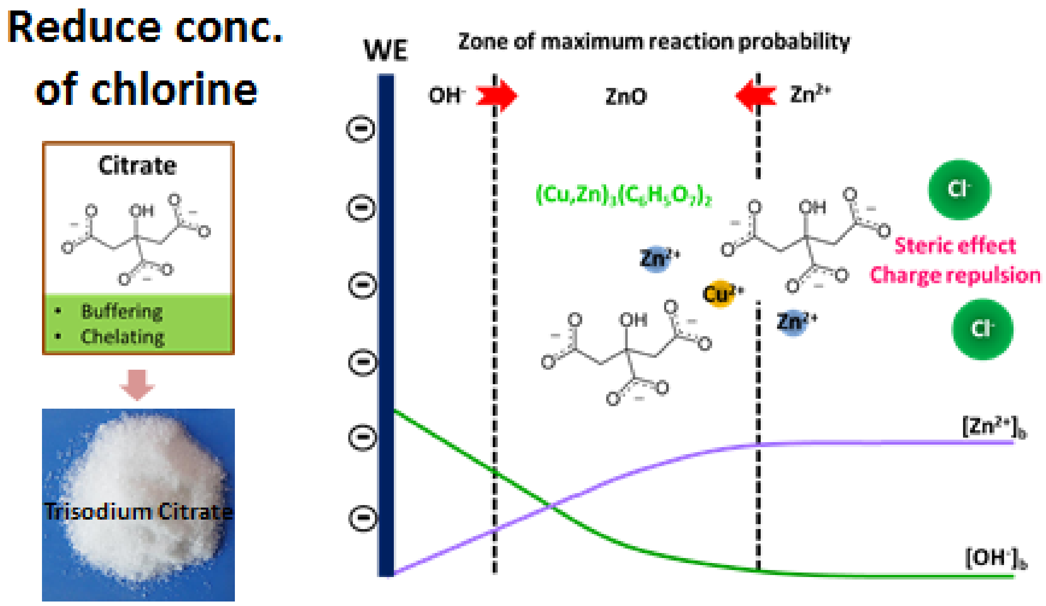

Figure B.5 Schematic illustration of decrease in concentration of chlorine due to the addition of trisodium citrate.

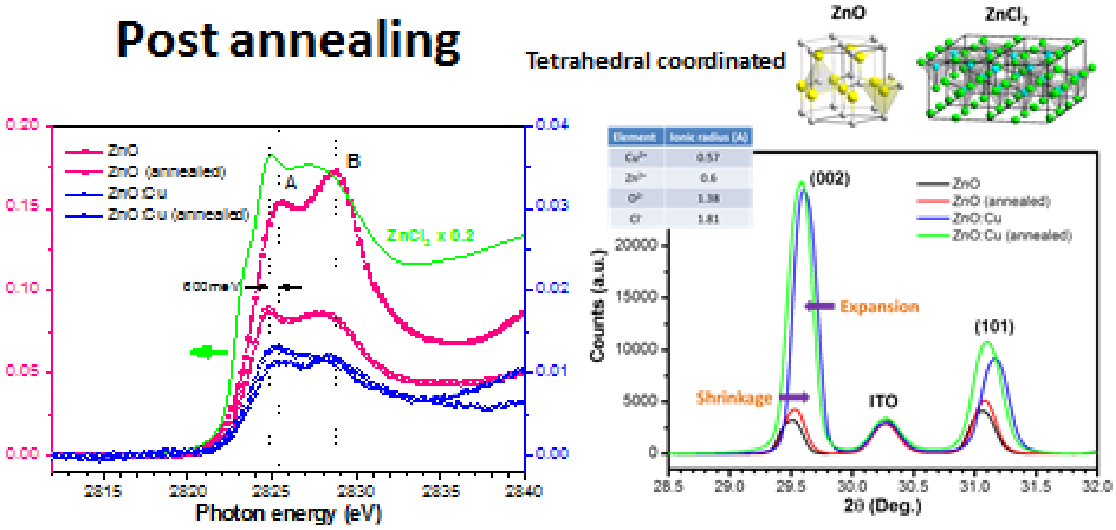

Element	Ionic radius (Å)
Cu^{2+}	0.57
Zn^{2+}	0.6
O^{2-}	1.38
Cl^{-}	1.81

Figure B.6 K-edge XAS and XRD patterns show the effects of post annealing on ZnO nanorods.

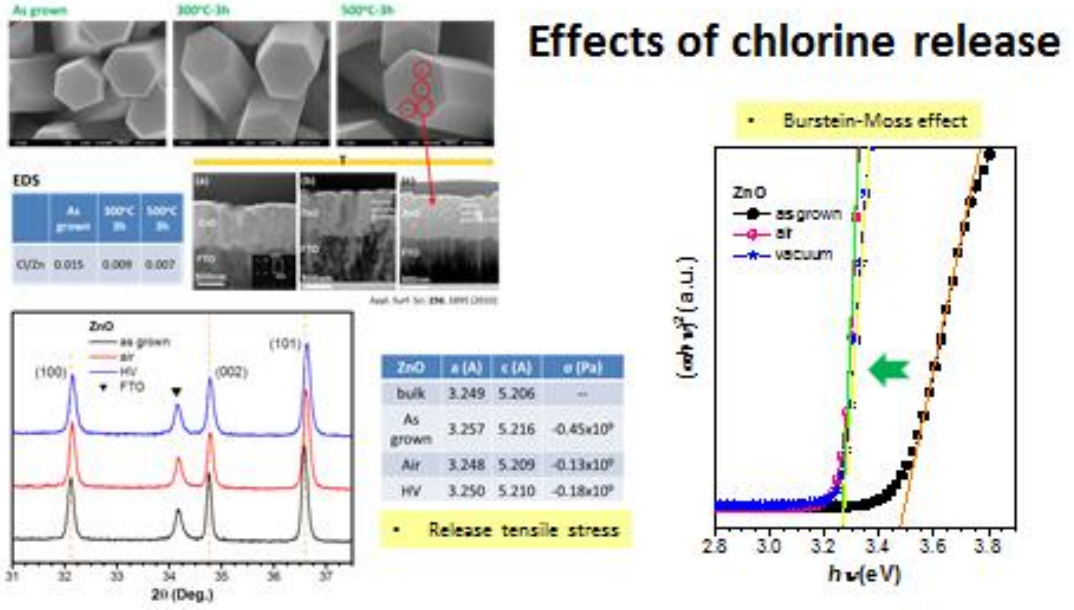

EDS

	As grown	300°C 3h	500°C 3h
Cl/Zn	0.015	0.009	0.007

ZnO	a (Å)	c (Å)	σ (Pa)
bulk	3.249	5.206	--
As grown	3.257	5.216	-0.45x10^9
Air	3.248	5.209	-0.13x10^9
HV	3.250	5.210	-0.18x10^9

Figure B.7 SEM, XRD, and UV-Vis. spectra show the effects of releasing chlorine in ZnO nanorods.

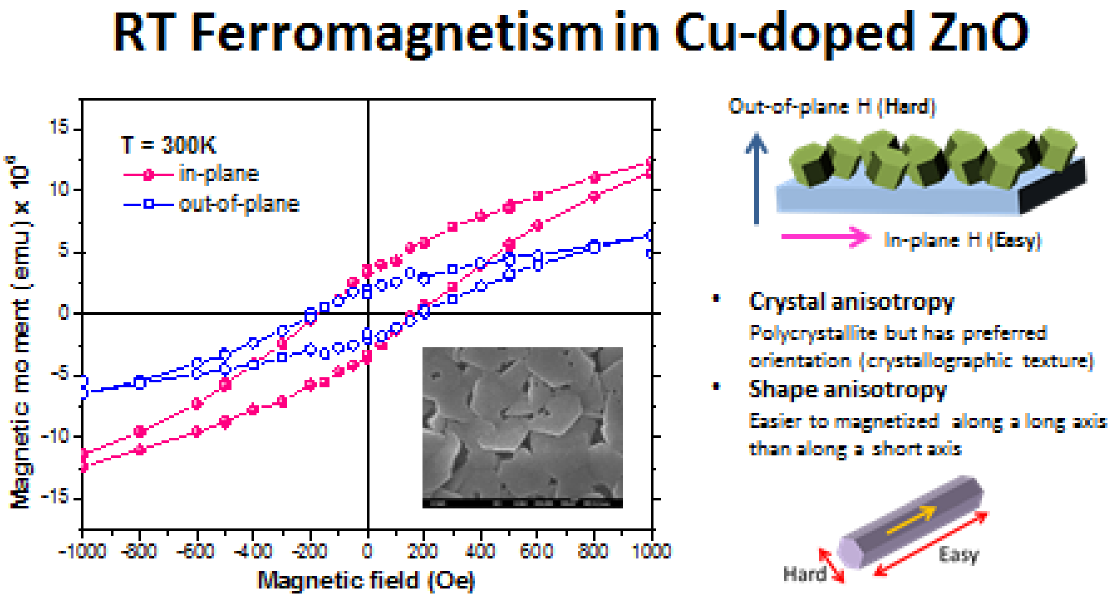

RT Ferromagnetism in Cu-doped ZnO

- Crystal anisotropy
  Polycrystallite but has preferred orientation (crystallographic texture)
- Shape anisotropy
  Easier to magnetized along a long axis than along a short axis

Figure B.8 Magnetic moment of ZnO:Cu nanostructures at room temperature.

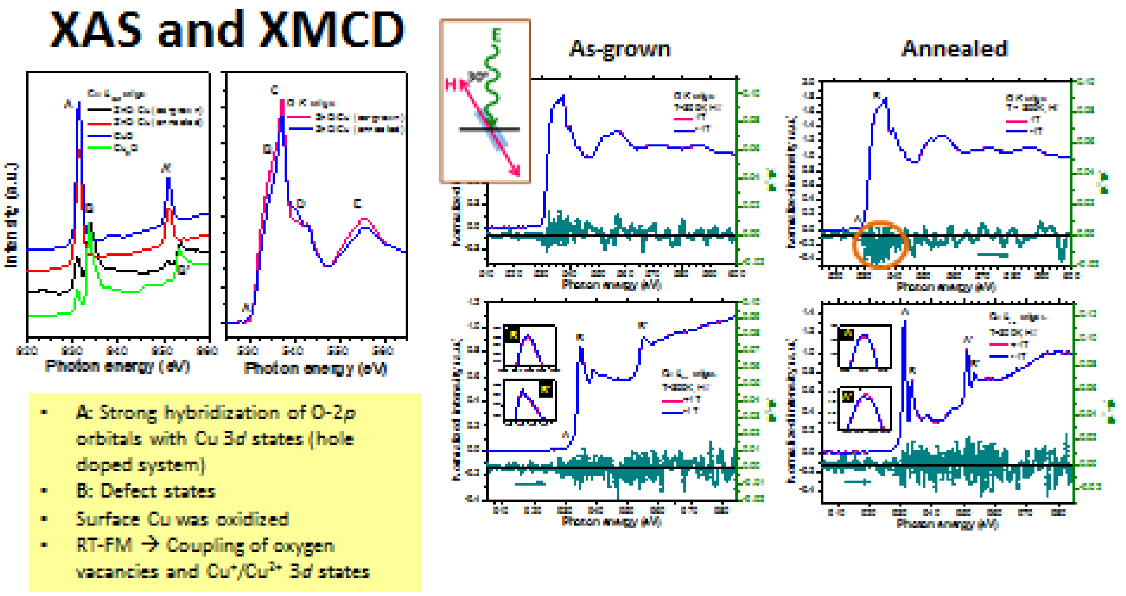

XAS and XMCD

- A: Strong hybridization of O-2*p* orbitals with Cu 3*d* states (hole doped system)
- B: Defect states
- Surface Cu was oxidized
- RT-FM → Coupling of oxygen vacancies and Cu^{+}/Cu^{2+} 3*d* states

Figure B.9 Cu and O K-edge XAS and XMCD spectra.

doi:10.6342/NTU201603487